EVAPOTRANSPIRATION AND ITS PARTITIONING IN TALLGRASS PRAIRIE UNDER WOODY PLANT ENCROACHMENT

A Dissertation

by

XIANGMIN SUN

Submitted to the Office of Graduate and Professional Studies of
Texas A&M University
in partial fulfillment of the requirements for the degree of

DOCTOR OF PHILOSOPHY

Chair of Committee,	Bradford P. Wilcox
Committee Members,	James L. Heilman
	Binayak Mohanty
	Jason B. West
	Chris B. Zou
Head of Department,	Cliff Lamb

December 2019

Major Subject: Ecosystem Science and Management

ABSTRACT

Evapotranspiration (ET) drives the energy and mass exchanges between ground and atmosphere. Partitioning of ET into evaporation from both bare soil (E) and vegetation interception (I) and plant transpiration (T) is essential for quantifying water use efficiency and evaluating ecosystem functioning under climate change and land cover change.

First, we carried out a worldwide meta-analysis on 31 *in situ* ET–partitioning studies reported in drylands. Over the long-term scale, E and T are roughly equivalent for most natural ecosystems, while T/ET is relatively higher for irrigated agroecosystems. Leaf area index is a significant variable than fractional cover to explain T/ET variations across dryland ecosystems.

Secondly, a paired treatment-control configuration was set up in tallgrass prairie, with the treated denuded of vegetation, while the adjacent, control site kept undisturbed. Results showed that the incorporation of the soil heat storage (within 8 cm-depth) was indispensable for energy balance closure analysis. The yearly ET was 728 ± 3 mm and 547 ± 2 mm for the control and treated site, respectively.

Thirdly, we applied a two-source isotopic mixing model to partition the ET flux. Two field campaigns were carried out to sample waters in various ecohydrologic pools during two wetting–drying episodes, with high antecedent soil moisture across the profile for Campaign 1, but soil moisture was only partially replenished in shallow layers prior to Campaign 2. We found that deuterium (^{2}H) is preferable to ^{18}O for Keeling-plot regression analysis. The mean ± standard deviation of T/ET was 0.80 ± 0.06 and 0.90 ± 0.06 during Campaign 1 and 2, respectively. When shallow soil moisture (especially within 10-cm depth) had been substantially depleted, the deep soil layer (up to 1 m) increasingly became the major source.

Lastly, we investigated the effects of woody plants encroachment on the ET fluxes and isotopic processes. An intensive field campaign was carried out with rotatory isotopic sampling among tallgrass prairie grassland, oak woodland, and eastern redcedar woodland. The dual-isotope plots revealed that the trees had access to deeper soil moisture than grass did. During the peak growing

season, ET and xylem water had similar isotopic composition across all these three ecosystems, indicating a convergent dominance of T in ET flux regardless of ecosystem types.

DEDICATION

To my mother, my father, and my sisters.

ACKNOWLEDGMENTS

Firstly, I would like to state my sincere gratitude to my advisor Prof. Bradford P. Wilcox for his strong support during my Ph.D study and research, for his patience, motivation, and extensive knowledge. His direction and helpful suggestions helped me in all the time of research and writing of this thesis. I could not have imagined having a better advisor and mentor for my Ph.D study.

Besides my advisor, I would like to thank the rest of my thesis committee: Prof. James L. Heilman, Prof. Binayak Mohanty, Dr. Jason B. West, and Dr. Chris B. Zou, not only for their generous agreement on my access to their laboratory and research facilities, but also for their insightful comments and encouragement for widening my research from various perspectives.

My deep-rooted gratitude also goes to Elaine Stebler, Dr. Ayumi Hyodo, Chris Stansberry, who provided me informed assistance on multiple practical procedures in field work and laboratory operation. Opportunity to gain these experiences and skills was indispensable for me to complete this research.

I also want to express my appreciation to fellow graduate students, both in Texas A&M University and Oklahoma State University, for the stimulating discussions either at field work or during writing this dissertation. The list includes Briana Wyatt, Patricia Torquato, Giovanne Serrau, Cynthia Wright, Shishir Basant, and Pedro Afonso Leite.

Last but not the least, I would like to thank my family: my parents, my sisters, and my two little nieces for supporting me spiritually during my study in this Ph.D program and my life in general.

CONTRIBUTORS AND FUNDING SOURCES

Contributors

This work was supported by a dissertation committee consisting of Professor Bradford P. Wilcox and Associate Professor Jason B. West of Department of Ecosystem Science and Management, Professor James L. Heilman of Department of Soil and Crop Sciences, Professor Binayak Mohanty of Department of Biological and Agricultural Engineering from Texas A&M university, and Professor Chris B. Zou of Department of Natural Resource Ecology and Management from Oklahoma State University.

All work in data analysis and research conducted for the dissertation was completed by the student independently.

Funding Sources

This research was funded by the National Science Foundations Dynamics of Coupled Natural and Human Systems (CNH) program (DEB-1413900). The graduate study was supported by the Sid Kyle Graduate Merit Assistantships in the Department of Ecosystem Science and Management at Texas A&M University, and the Mills Scholars Program from the Texas Water Resources Institute.

NOMENCLATURE

R_g	$\mathrm{W\,m^{-2}}$	Incoming global radiation
R_e	$\mathrm{W\,m^{-2}}$	Reflectance and emittance
R_n	$\mathrm{W\,m^{-2}}$	Net radiation
H	$\mathrm{W\,m^{-2}}$	Sensible heat flux
LE	$\mathrm{W\,m^{-2}}$	Latent heat flux
S_{above}	$\mathrm{W\,m^{-2}}$	Heat storage above ground
G_0	$\mathrm{W\,m^{-2}}$	Ground surface heat flux
S_{soil}	$\mathrm{W\,m^{-2}}$	Soil heat storage above the heat-flux plates
G_s	$\mathrm{W\,m^{-2}}$	Soil heat flux through the heat-flux plates
A_d	$\mathrm{W\,m^{-2}}$	Advective heat flux below the anemometer
e	Pa	Ambient water vapor partial pressure
e_s	Pa	Saturated water vapor partial pressure
u	$\mathrm{m\,s^{-1}}$	Mean wind speed
u_*	$\mathrm{m\,s^{-1}}$	Friction velocity
β		Bowen ratio
x_i	m	Along-wind distance contributing to i of turbulent fluxes
x_{peak}	m	Along-wind distance with the highest contribution
ΔT_s	$^\circ\mathrm{C}$	Change in soil temperature
C_s	$\mathrm{J\,kg^{-1}\,K^{-1}}$	Heat capacity of moist soil
ρ_a	$\mathrm{kg\,m^{-3}}$	Air density
c_p	$\mathrm{J\,kg^{-1}\,K^{-1}}$	Specific heat of air at constant pressure
γ	$\mathrm{kPa\,K^{-1}}$	Psychrometric constant

g_a	$\mathrm{m\,s^{-1}}$	Aerodynamic conductance of the air layer
g_s	$\mathrm{m\,s^{-1}}$	Surface conductance to water vapor
Ω		Decoupling factor
E	mm	Bare soil evaporation
T	mm	Plant transpiration
ET	mm	Bulk evapotranspiration
δ	‰	Stable isotopic composition of water (δ^2H and δ^{18}O)
δ_E	‰	δ of E
δ_T	‰	δ of T
δ_{ET}	‰	δ of bulk ET
δ_{soil}	‰	δ of soil water in the top 15 cm layer
δ_{Se}	‰	δ of liquid soil water at the evaporating site
δ_{Le}	‰	δ of liquid water at the evaporating site under ISS
δ_{leaf}	‰	δ of bulk leaf water
δ_V	‰	δ of atmospheric water vapor
δ_X	‰	δ of xylem water
δ_a	‰	δ of ambient water vapor
w	$\mathrm{mmol\,mol^{-1}}$	Water vapor mixing ratio
$R^2_{Keeling}$		R^2 for Keeling-plot regression
RH, h	%	Relative humidity or normalized relative humidity
VPD	kPa	Water vapor pressure deficit
α_{eq}		Equilibrium isotopic fractionation factor (>1)
α_k		Kinetic isotopic fractionation factor
ϵ_{eq}	‰	Equilibrium isotopic fractionation
ϵ_k	‰	Kinetic isotopic fractionation

T'_{soil}	K	Soil temperature at the evaporating front (5 cm)
T_{soil}	°C	Soil temperature at the evaporating front
T_{air}	°C or K	Air temperature at measuring height (3 m)
D	$\mathrm{m^2\,s^{-1}}$	Diffusion coefficient for the common isotopologue
D_i	$\mathrm{m^2\,s^{-1}}$	Diffusion coefficient for the rarer isotopologue
n		Aerodynamic parameter for adjusting diffusivity ratios
θ_{soil}	$\mathrm{m^3\,m^{-3}}$	Volumetric water content at the evaporating front
θ_{sat}	$\mathrm{m^3\,m^{-3}}$	Saturated volumetric water contents
θ_{res}	$\mathrm{m^3\,m^{-3}}$	Residual volumetric water contents

TABLE OF CONTENTS

Page

LIST OF FIGURES

FIGURE Page

LIST OF TABLES

TABLE Page

1. INTRODUCTION ON EVAPOTRANSPIRATION PARTITIONING IN DRYLAND ECOSYSTEMS *

1.1 Introduction

Drylands cover about 40% of the global landmass and up to 44% of cultivated lands, supporting 35% of the global population [1]. Drylands can be grouped into four categories, according to level of aridity: hyper-arid, arid, semiarid, and (dry) subhumid [2]. Sustainable and efficient management of these ecosystems requires an in-depth understanding of the water cycle, and especially of the evapotranspiration (ET) component, which typically accounts for 90%–95% of annual precipitation [3, 4, 5]. The bulk ET flux consists of interception evaporation (I), soil evaporation (E), and plant transpiration (T). Partitioning of ET—determination of the relative importance of these constituent fluxes, usually expressed as a ratio (T/ET or E/ET)—is a challenging exercise but is essential for understanding dryland ecohydrology [6, 7, 8]. This rationale is well supported, considering the following facts:

- Partitioning of ET is critical for quantifying (1) water-use efficiency [9, 10], (2) ecosystem productivity [11, 12] and sustainability [13], (3) biological water demand and its influence on the hydrologic cycle [7], and (4) the coupling of hydrologic and biogeochemical cycles [14, 15, 16].

- Partitioning of ET is essential for calibrating and validating surface–plant–atmosphere transfer models [17, 18, 19], land surface models [20, 21], and the land –atmosphere interaction in climate models [22, 23].

- The processes of I, E, and T differ not only in timing and duration [24] but also with respect to the mechanisms involved in phase changethe latter differences being responsible for the dissimilarities in stable isotope composition among these constituent fluxes [25].

*A version of this chapter has been published as: Sun, X., Wilcox, B.P. and Zou, C.B., 2019. Evapotranspiration partitioning in dryland ecosystems: a global meta-analysis of *in situ* studies. *Journal of Hydrology* 576:123-136. Adapted with permission. Copyright 2019 Elsevier B.V.

A clear understanding of ET partitioning is especially crucial for sustainable management of water resources in drylands, which are expected to be increasingly limited under climate change, mounting demographic pressures, and competition from many other socio-economic sectors. A fundamental strategy for reaching a sustainable level of agricultural water consumption is that of enhancing the productive component (T) and curtailing the unproductive component (E) [26].

Topics on ET partitioning have been summarized in a few studies: a comprehensive review on methodologies available for ET partitioning, including both *in situ* measurement and modeling, on the basis of 52 publications [6]; a review on the isotopic approach for measuring gas exchange at the ecosystem level [27]; based on 81 ecosystem–scale studies worldwide, a compiled ET partitioning study found that T/ET is relatively lower in semiarid ecosystems (51 ± 15% for steppe, desert, and shrublands) than in wet climates (e.g., 70 ± 14% for tropical forests) [28]; on the basis of 48 published studies, a synthesis study investifgated the relationship between T/ET and leaf area index (LAI) at a global scale [29]; and this relationship was further refined for different vegetation types [30].

To our knowledge, however, there has been no synthesis of what is known about ET partitioning particularly in drylands. In this paper, on the basis of a meta-analysis of the pertinent *in situ* studies, we discuss four topics relevant to ET partitioning: (1) the approaches and methodologies commonly used for field studies; (2) the general trends in ET partitioning in dryland ecosystems; (3) emerging themes from the literature; and (4) challenges and opportunities for future investigations.

1.2 Literature collection

Using the Web of Science Core Collection (http://apps.webofknowledge.com), we searched for relevant peer-reviewed journal articles published in English from 1987 to June of 2018. We used mutated combinations of the following inquiry terms: "evapotranspiration" AND "partition*"), ("evaporation" AND "transpiration"), ("dryland" OR "water-limited"), and ("semiarid" OR "semi-arid" OR "arid"). We filtered the retrieved raw records ($\sim$ 200) with the following criteria: (1) quantitative separation of the ET flux, whether into two constituents (E and T) or three (E, T,

and I); (2) major results obtained from *in situ* studies at the site or plot scale, rather than from modeling or remote sensing at the regional scale; and (3) at least two independent measurements, in parallel, of the three variables ET, E, and T.

The outcome was the selection of 31 *in situ* studies from drylands across the world (Fig. 1.1), which yielded 38 datasets (Tables 1.1 and 1.2). Some studies [31, 32] encompassed multiple ecosystems and/or different treatments, in which case we labeled each ecosystem/treatment as a separate dataset. If exact numeric values relevant to ET partitioning were given only in graphs, we extracted those values with Engauge Digitizer (10.4, Mark Mitchell, Engauge Digitizer, https://github.com/markummitchell/engauge-digitizer).

As shown in Figs. 1.1 and 1.2, the great majority (about 80%) of the retrieved studies were conducted in semiarid climates, whereas those done in hyper-arid and subhumid climates account for only about 10% (5% each category). On the basis of the information provided in the original records, we grouped the dryland ecosystems into the following eight types: grassland, savanna, shrubland, open woodland, forest, orchard, cropland, and marshland. Semiarid-climate grasslands and shrublands are the two most common natural ecosystems (each representing more than 15%). Agro-ecosystems (including croplands and orchards, usually irrigated) are also well represented (38%) across the spectrum of climatic aridity. The most common crops were winter wheat and maize (Table 1.2).

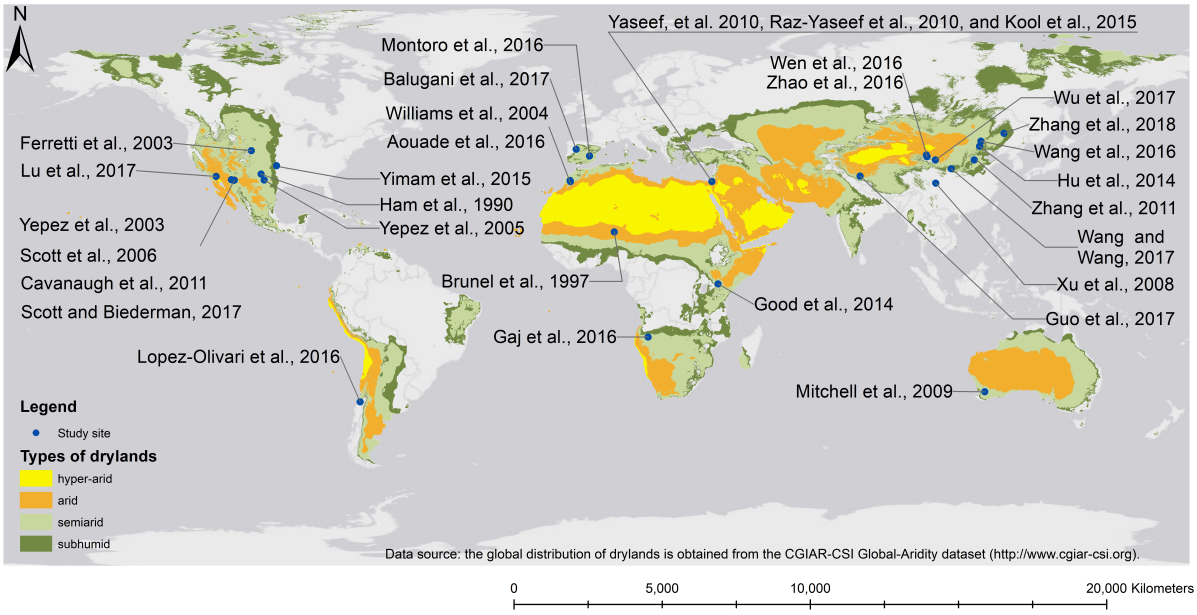

Figure 1.1: Distribution of drylands and locations of study sites.

Table 1.1: Results of ET partitioning via the hydrometric approach (15 studies)

Location	Climate	MAP[1]	Ecosystem	Plant Canopy		Soil	Study Period	Measuring methods[2]				T/ET[3]	Source
				Cover%	*LAI*			ET	E	T	I		
Texas, USA	semiarid		cotton cropland		2.39	sandy clay loam	Aug. 8–15, 1989	BREB	lysimeter	sap		0.57	[33]
Arizona, USA	subhumid	322	Chihuahuan desert shrubland	51%		gravelly –sandy loams	summer growing season, 2003	BREB		sap		0.58	[34]
Southwestern Australia	semiarid	361	open eucalyptus woodland		0.66	sandy loams to clay	Nov. 2005 — Mar. 2007		chamber	sap	rain gauge & stem collars	(0.22 –0.53)	[35]
Southern Israel	semiarid	285	open forest	60%	1.5	clay-loam	2003–2007	EC	soil chambers	sap	empirical	0.45	[36]
Southern Israel	semiarid	285	open forest	65%	1.5	clay–loam	Oct.2004 — May 2007	EC	chamber	sap	empirical	(0.49)	[13]

Continued on next page

Table 1.1 Continued

Location	Climate	MAP[1]	Ecosystem	Plant Canopy		Soil	Period	Measuring methods[2]				T/ET[3]	Source
				Cover%	*LAI*			ET	E	T	I		
Southeastern Arizona, USA	semiarid	340–345	shrublands	24–27%	0.45 –0.46	sandy loam	summer 2008	EC		sap		0.42–0.47	[37]
Oklahoma, USA	subhumid	880	cropland	0–95%		loam	growing seasons of 2011–2013	Mass (soil)	FAO-56		tray	(0.72 vs 0.58)	[32]
Central Spain	semiarid	320	grape vineyard		1.4 –2		2011–2014	lysimeter		lysimeter		0.19 –0.69	[38]
Region del Maule, Chile	semiarid	602	olive orchard (irrigated)	30%	1.32	clay loam	growing seasons of 2009 –2011	EC	lysimeter	sap		0.64–0.74	[39]
Negev highlands, Israel	hyper-arid	<100	wine grape vineyard		<1.71		growing season 2012	EC	energy balance & lysimeter			0.89–0.91	[40]

Continued on next page

Table 1.1 Continued

Location	Climate	MAP[1]	Ecosystem	Plant Canopy		Soil	Period	Measuring methods[2]				T/ET[3]	Source
				Cover%	*LAI*			ET	E	T	I		
Northwestern China	arid	117	desert shrub	15–20%	1.0	unconsolidated sand	growing seasons of 2008–2010	BREB	lysimeter	sap	Stemflow funnel & throughfall container	-0.639	[41]
Inner Mongolia, China	semiarid	286	steppe grassland		0 –1.2		growing seasons of 2005–2008	EC	Flux variance — similarity —			0.50–0.74	[42]
Spain	semiarid	586	open woodland	7%		sandy	dry summers of 2009–2010	EC	HYDRUS1D	sap		0.06	[43]
Southern Arizona, USA	semiarid		shrubland, savanna, grasslands		0.2 –0.8		summer growing seasons of 2004–2015	EC	—– ET/GEP regression —–			0.44	[31]

Continued on next page

Table 1.1 Continued

Location	Climate	MAP[1]	Ecosystem	Plant Canopy		Soil	Period	Measuring methods[2]				T/ET[3]	Source
				Cover%	*LAI*			ET	E	T	I		
Northwest China	semiarid	584	orchard (apple)		1.4 –2.2		May– Sept. 2012–2014		lysimeter	sap	throughfall & stemflow collector	(0.39–0.49)	[44]

[1] Mean annual precipitation (mm);

[2] The ET flux and its constituents can be measured with the following methods: eddy covariance (EC), Bowen Ratio Energy Balance (BREB), soil moisture mass balance [Mass (Soil)], micro-lysimeter (lysimeter), simulation with the HYDRUS1D model, sap flow meter (sap), the Food and Agriculture Organization crop ET formula (FAO-56). The flux variance similarity method and regression analysis using ET and Gross Ecosystem Production (GEP) are used to partition ET for EC measurement.

[3] Numbers in parentheses indicate measurement of $T/(E+T+I)$ including measured or calculated interception (I); numbers without parentheses indicate measurement of $T/(E+T)$ without explicit consideration of interception (I).

Table 1.2: Results of ET partitioning via the isotopic approach (16 studies)

Location	Climate	MAP	Ecosystem	Plant Canopy		Soil	Period	Sampling			Calculation methods[3]						T/ET	Source
				Cover%	*LAI*			Soil depth	Plant	Air[2]	ET	E	T	δ_{ET}	δ_E	δ_T		
Niger, West Africa	semiarid	550	bushland, woody shrubs	20%		sand	Early in the rainy season	0-12 m(c)	twigs	3–12 m(c)				iso-mass	CG	ISS	0.21	[45]
South-eastern Arizona, USA	semiarid	343	savanna woodland	70%	1.6[o][1]		Jul. & Sep., 2001	0-0.1 m		0.1-1 m, 3-14 m(c)	EC			Keeling	CG	ISS	0.85	[12]
North-eastern Colorado, USA	semiarid	320	shortgrass steppe			sandy loam	May 1999 — Oct. 2001	0.03 – 0.5 m			BREB & Mass			—- iso-mass (soil) —-			0.93	[46]

Continued on next page

Table 1.2 Continued

Location	Climate	MAP	Ecosystem	Plant Canopy		Soil	Period	Sampling			Calculation methods[3]						T/ET	Source
				Cover%	*LAI*			Soil depth	Plant	Air[2]	ET	E	T	δ_{ET}	δ_E	δ_T		
Marrakech, Morocco	semiarid	253	olive orchard				Oct.27 – Nov.11, 2002	0-0.3 m	twigs	0.1-8.9 m(c)	EC		sap	Keeling	CG	ISS	1.00 – 0.69	[10]
South-eastern Arizona, USA	semiarid		grassland		0.66 – 0.37	loamy sand	Jun. 12–27, 2003	0-0.3 m	shoot bases	chamber (c)	Mass		photo	Keeling	CG	NSS	0.33 – 0.18	[47]
Western China	semiarid	710	subalpine shrubland	>90%	2.05[o]	sandy loam	June 21,24, 25, 2006	0-0.1 m	oak branches & grass stems	0.1 – 3 m(c)				Keeling	CG	ISS	0.66 – 0.97	[48]

Continued on next page

Table 1.2 Continued

Location	Climate	MAP	Ecosystem	Plant Canopy		Soil	Period	Sampling			Calculation methods[3]						T/ET	Source
				Cover%	*LAI*			Soil depth	Plant	Air[2]	ET	E	T	δ_{ET}	δ_E	δ_T		
Northern China	semiarid	480	winter wheat		2.6 (well–watered)	loam	growing season, 2009	0.05 -1m	stem	0.1 – 10 m(c)	EC	lysimeter		Keeling	CG	ISS	>0.70	[5]
Central Kenya	arid	600	perennial grass field	0 – 10%	≤ 0.1	sandy loam	Feb. 7–21, 2011	0.01 – 0.2 m		0.1 – 10 m(l)	EC & lysimeter	photo	Keeling	CG	chamber	0.29	[49]	
Inner Mongolia, China	semiarid	383	temperate grassland		≤ 0.5	sandy	DOY 178-224, 2009	0.05 – 0.25 m	leaf & stem	0.7 – 1.7 m(l)	EC			FG	CG	iso-mass	0.83	[50]

Continued on next page

Table 1.2 Continued

Location	Climate	MAP	Ecosystem	Plant Canopy		Soil	Period	Sampling			Calculation methods[3]						T/ET	Source
				Cover%	*LAI*			Soil depth	Plant	Air[2]	ET	E	T	δ_{ET}	δ_E	δ_T		
Northern -central Namibia	semiarid	250 – 600	forest			sandy	Jun. 9-15, Nov. 15-22, 2014			0.02 – 1 m within the vadose zone (l)	EC			–	iso-mass (soil)	–	0.81	[51]
Morocco	semiarid	240	winter wheat	85%	0-4	clayey to loamy	5 days in 2011 – 2013	0-0.7 m	stem	0 – 3 m (c)	EC			Keel-ing	CG	ISS	0.69 – 0.80	[20]

Continued on next page

Table 1.2 Continued

Location	Climate	MAP	Ecosystem	Plant Canopy		Soil	Period	Sampling			Calculation methods[3]						T/ET	Source
				Cover%	*LAI*			Soil depth	Plant	Air[2]	ET	E	T	δ_{ET}	δ_E	δ_T		
North-western China	arid	129	spring maize		5.6		May 27 – Sep. 22, 2012	0-0.8 m	leaf & root crown	0.6 – 3.6 m (l)	EC	lysi-meter		FG	CG	iso-mass & ISS	0.87	[52]
Southern California, USA	hyper–arid	80	forage sorghum		0.5 – 1.9	silty clay	Jul. 24 – Aug. 20, 2014			Cham-ber (l)				– Keeling & iso-mass –			0.46	[9]
North-western China	arid	164	maize		0-4.1	loam & sandy loam	Grow-ing season 2015	0-0.1 m	stem	1 – 4 m (c)	EC	lysi-meter		Keel-ing	CG & cham-ber	cham-ber	0.78	[53]

Continued on next page

Table 1.2 Continued

Location	Climate	MAP	Ecosystem	Plant Canopy		Soil	Period	Sampling			Calculation methods[3]						T/ET	Source
				Cover%	*LAI*			Soil depth	Plant	Air[2]	ET	E	T	δ_{ET}	δ_E	δ_T		
Tibetan Plateau, China	arid	82	catchment dominated by bare soil or grassland	11%			2012 – 2015				GLDAS			–	iso-mass (watershed)	–	0.41 (annual)	[54]
Northeastern China	semiarid	392	marshland		1.02		Jun. 18-19, 2013	0 – 0.1 m	stem and leaf	0.2 – 1.9 m(c)	EC	lysimeter		Keeling	CG	NSS & ISS	0.41	[55]

[1] For *LAI* ($\mathrm{m^2\ m^{-2}}$), o in brackets stands for overstory or upper canopy.

[2] (c) = cryogenic vapor trapping method (cold bath); (l) = laser spectrometer (direct *in situ* measurement).

[3] ET fluxes can be measured via a remote sensing data (GLDAS) or a mass balance (mass) method. Leaf-level transpiration can be measured with a portable photosynthesis system (photo). Isotopic compositions of δ_{ET}, δ_E, and δ_T can be analyzed via two major methods: (1) the isotopic mass balance (iso-mass), either at the soil column scale (soil) or at the watershed scale (watershed); and (2) the two-source mixing model, utilizing the Keeling-plot method (Keeling), the flux-gradient method (FG), the Craig-Gordon (CG) model, or the chamber method (chamber). For δ_T, two hypotheses have been developed: the isotopic steady state (ISS) assumption and non-isotopic steady state (NSS) assumption.

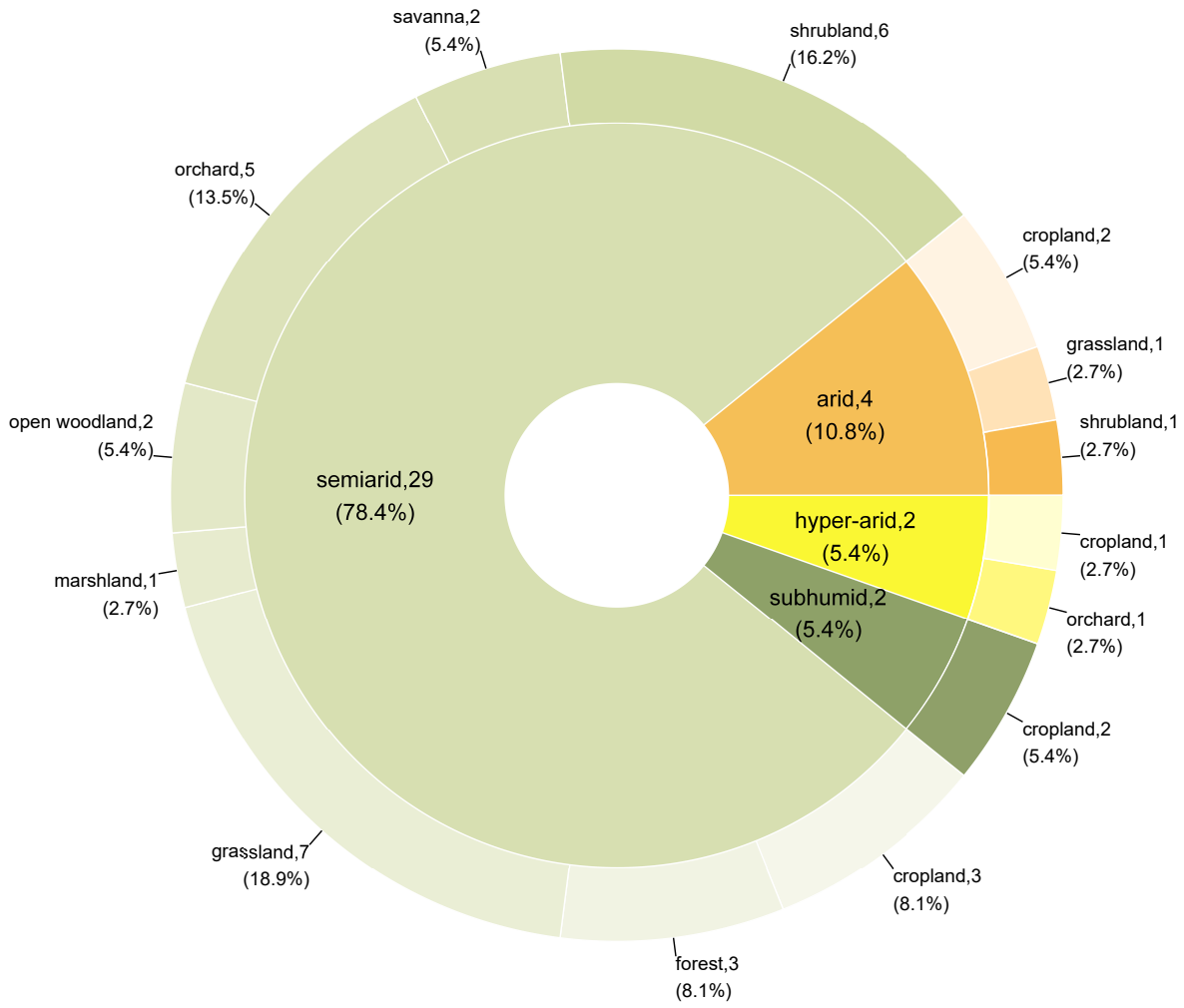

Figure 1.2: Dryland climate categories and ecosystem types represented by the retrieved studies. The number following each climate category and ecosystem type indicates the number of studies from which data was drawn, and the number in parentheses indicates the corresponding percentage of the retrieved 37 records from the 30 studies done at the ecosystem level (the study done on a regional watershed [54] is not included).

1.3 Approaches and methods used in the ET partitioning studies

Following the practice of previous studies [56, 19], we grouped the widely used *in situ* measurement methods for ET partitioning into two overarching approaches: hydrometric and isotopic (Fig. 1.3). Of the 31 published studies in our meta-analysis, 15 used mainly the hydrometric approach (Table 1.1) and 16 used mainly the isotopic approach (Table 1.2). However, these two approaches are usually integrated for ET partitioning, especially at the ecosystem or larger scales [49, 10, 57].

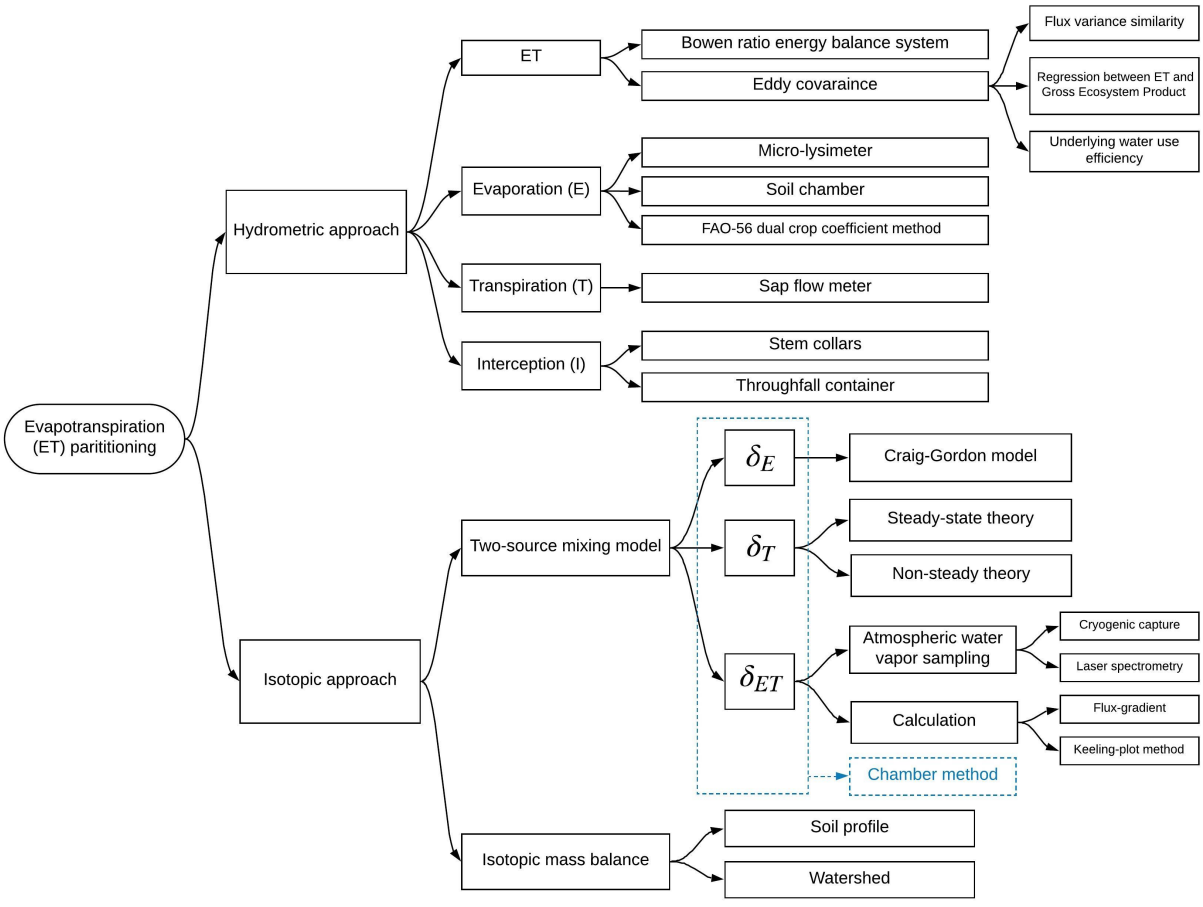

Figure 1.3: Hydrometric and isotopic approaches for partitioning of *ET*.

1.3.1 Hydrometric approach

Multiple hydrometric methods are available for measuring the bulk ET flux or its constituents individually. Micro-meteorological techniques—such as Bowen ratio energy budget and eddy covariance—provide only an aggregate of ET fluxes based on energy balance. However, multiple algebraic methods have been proposed that are capable of partitioning ET via additional measurements, such as ground surface temperature [58] or gross ecosystem photosynthesis [31]. Another recently proposed method for partitioning ET is based on the assumption of flux variance similarity in high-frequency eddy covariance data [59, 60, 61]. In addition, a concept called underlying water use efficiency ($uWUE$) have been proposed [62]. This concept estimates T/ET as a ratio of average over potential $uWUE$, by assuming that potential $uWUE$ is related to T and average $uWUE$ is related to ET.

To obtain transpiration (T), xylem sap flow is commonly measured by various thermic techniques [63, 64, 65, 66]. Gas-exchange chambers are also widely used to measure transpiration at smaller scales, such as leaf or stem [67, 68, 47]. For soil evaporation (E), the micro-lysimeter is an inexpensive and reliable tool when roots are excluded from the sampling soil column [49]; this tool is especially popular and convenient for loose and shallow soils in irrigated croplands.

Evaporation from canopy interception (I) is obtained by subtracting the sum of throughfall and stemflow from the measured above-canopy precipitation. Five of our retrieved studies explicitly included measurements or calculations of interception [49, 35, 69, 44, 36, 32]. These hydrometric methods are often used in combination to measure different constituents of the ET flux at the site or plot scale (Table 1.1) or used for comparison with and validation of other methods [70, 71].

1.3.2 Isotopic approach

Water vapor from soil evaporation is usually lighter in isotopic composition than that from transpiration, because during soil evaporation, the liquid–vapor phase change involves a strong fractionation process. Being a substantial factor in dryland ecosystems, the isotopically lighter soil evaporation contrasts strongly with the isotopically heavier transpiration, which facilitates the

practical application of the isotopic approach [49].

There are two major methodologies by which the isotopic approach is used. One is the two-source mixing model, expressed as

$$\frac{T}{ET} = \frac{\delta_{ET} - \delta_E}{\delta_T - \delta_E}, \tag{1.1}$$

where δ_{ET} is the isotopic composition of the aggregated ET flux, and δ_E and δ_T are the isotopic compositions of evaporation and transpiration, respectively. Various techniques and measuring methods have been developed to quantify these three isotopic values (Table 1.2) and (Fig. 1.3). For $\delta_E T$, the Keeling plot method [72, 27] and the flux-gradient method [73], both based on isotopic sampling of atmospheric water vapor within the ecosystem boundary layer, are widely used. For δ_E, the Craig–Gordon method [74, 75] has become a quasi-standard method. For δ_T, both steady-state theory and non-steady-state theory are often used, depending on the temporal resolution [76, 77, 78].

The second methodology is isotopic mass balance. Under steady-state conditions, it can be simplified as

$$P\delta_P = Q\ \delta_Q + E\ \delta_E + T\ \delta_T, \tag{1.2}$$

where P and δ_P represent precipitation and its isotopic composition, while Q and δ_Q represent runoff and its isotopic composition. This method has been applied at scales ranging from that of soil profile [46, 51] to that of regional watershed [54]. The development of the isotopic approach has been thoroughly discussed elsewhere [6, 19, 16, 57, 27, 79].

The isotopic approach requires extensive sampling of water from different reservoirs within the ecohydrologic cycle. To study the isotopic dynamics of atmospheric water vapor, cryogenic trapping systems [80, 81, 82, 5] have often been used; however, the trapping method involves a slow (a few hours) and laborious process of sample collection, resulting in low temporal resolution and discreteness of the data series. In contrast to such discrete snapshots, field-deployable laser spectroscopy has become increasingly popular for its ability to directly sample atmospheric wa-

ter vapor and to measure its isotopic composition with high temporal resolution and an accuracy comparable with that of traditional isotope ratio mass spectroscopy [83]. These laser instruments greatly expand the applicability of stable water isotopologues in ecohydrologic studies [16].

For the 16 studies using the isotopic approach (Table 1.2), seven used the single-isotope method (either ^{2}H or ^{18}O) and only two [51, 12] used the double-single isotope method (^{2}H and ^{18}O simultaneously). The ^{2}H method is preferable for estimating $\delta_E T$, owing to its high sensitivity [20]. In terms of labeling, two studies used artificially labeled water for ET partitioning [49, 47], and one used injection of deuterated water into the groundwater to separate the sourcing depths for transpiration [43].

1.3.3 Application of the hydrometric and isotopic approaches in dryland ecosystems

The *in situ* studies reported on in our 31 retrieved publications made extensive use of the hydrometric and isotopic approaches (Fig. 1.4a). The measurement periods vary dramatically from one study to anotherranging from one day [12, 5] to the length of the growing season or even a full year (Tables 1.1 and 1.2). The shorter-term investigations (most not exceeding 10 days) were classified as intermittent studies; these typically were carried out with the isotopic approach, owing to the need for extensive sampling and close human monitoring. In only two isotopic studies (in croplands) were measurements taken throughout the growing season [9, 52]. Long-term investigations, at either the growing season or the annual scale, are typically carried out with the hydrometric approach. One hydrometric study even used climatic records covering more than a decade [31].

1.4 General trends in ET partitioning in dryland ecosystems

Comparison of long-term annual mean precipitation (Fig. 1.4b), soil texture (Fig. 1.4c), and ecosystem types (Fig. 1.5a) reveals no clear trends in ET partitioning. Results from longer-term investigations (growing season or annual scale) show that in natural ecosystems, evaporation and transpiration are largely equivalent, whereas in agro-ecosystems (usually irrigated) the transpiration fraction is relatively higher (Fig. 1.5a). Results for T/ET from the longer-term studies in natural ecosystems showed less variability (0.37–0.84 [mean value ± standard deviation of 0.52 ±

0.13, n = 13]) than those from the intermittent studies (0.06–0.85 [mean value ± standard deviation of 0.47 ± 0.34, n = 9]). The 0.06 minimum value for one of the intermittent studies was observed in an open woodland (7% plant coverage) under dry summer conditions [43], indicating that T/ET is lower for woodlands with sparse vegetation canopies. Agro-ecosystems showed higher T/ET, with intermittent measurements ranging from 0.46 to 0.78 (mean value of 0.65 ± 0.13, n = 5) and longer-term measurements from 0.44 to 0.90 (mean value of 0.66 ± 0.17, n = 9). Maximum T/ET values are similar for natural ecosystems and agro-ecosystems (with the exception of open woodlands)—namely, around 0.75–0.85, which agree with the maximum values of 0.72–0.90 found at the global scale for natural and agricultural systems characterized by low LAI [29].

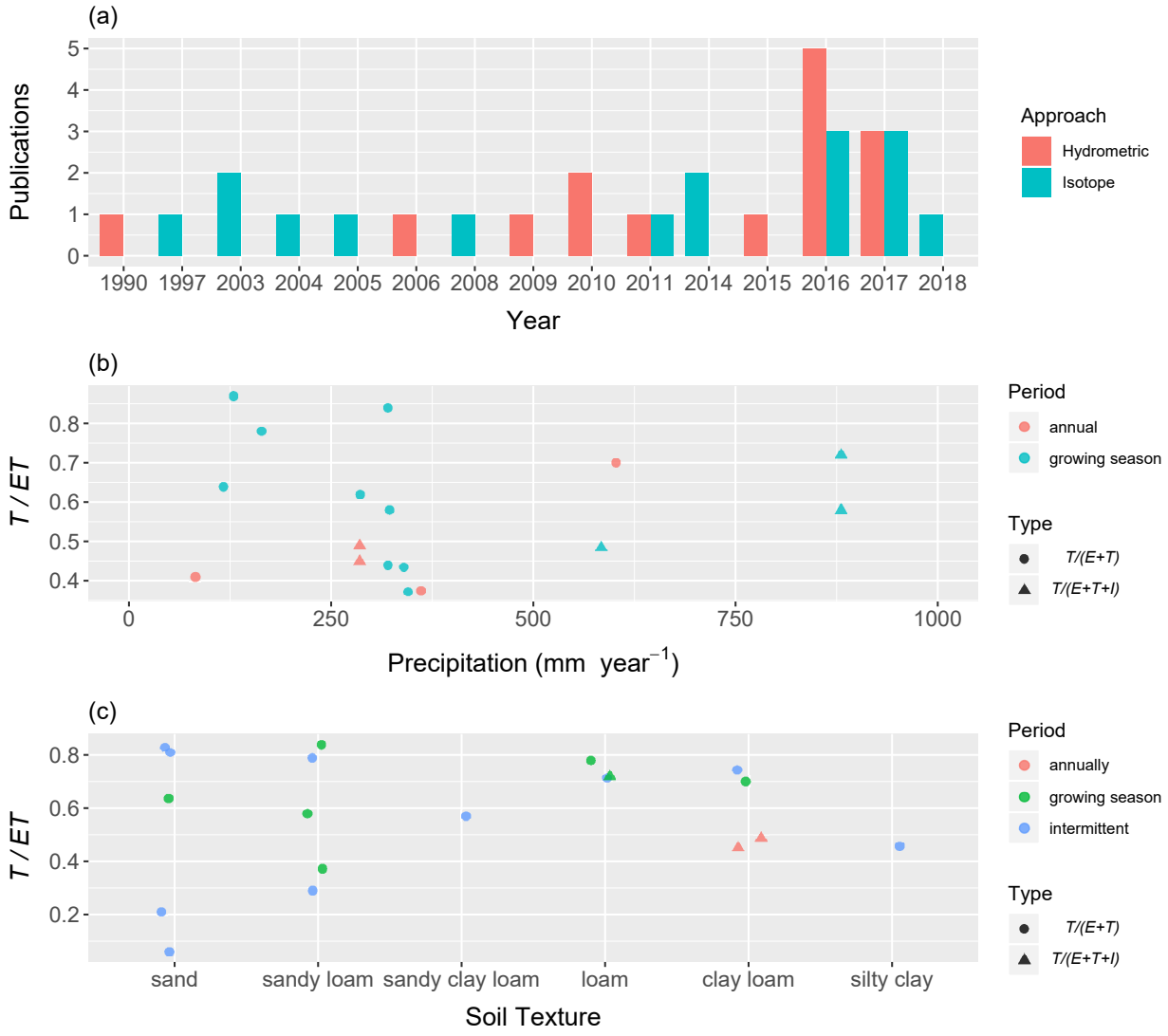

Figure 1.4: Approaches used and results of the retrieved studies on ET partitioning: (a) hydrometric vs isotopic approach; (b) and (c) dependency of T/ET on long-term annual precipitation and soil texture, respectively. Mean values are used for results reported as ranges in Tables 1.1 and 1.2.

No general trends were identified in the relationship between plant fractional cover and ecosystem type (Fig. 1.5b), whereas LAI (means and maximums) showed higher values in agro-ecosystems than in natural ones (Fig. 1.5c). The linear regression between converted T/ET and plant canopy characteristics revealed that mean and maximum LAI values explained 45% and 37%, respectively, of the variations in T/ET, whereas plant fractional cover failed to be an effective explanatory variable (Fig. 1.6). (All values in Fig. 1.6 are log-transformed because of the power-law relationship

between T/ET and the vegetation-canopy parameters—see Eq. 1.3 in Section 1.5.6.) Statistically, the regression was strongly significant for mean LAI (p-value ≤ 0.01) and significant for maximum LAI (p-value ≤ 0.05). However, the coefficient of determination (R^2) reported in this analysis is relatively low (Table 1.3), implying that the explanatory power of LAI for T/ET variability is constrained in dryland ecosystems.

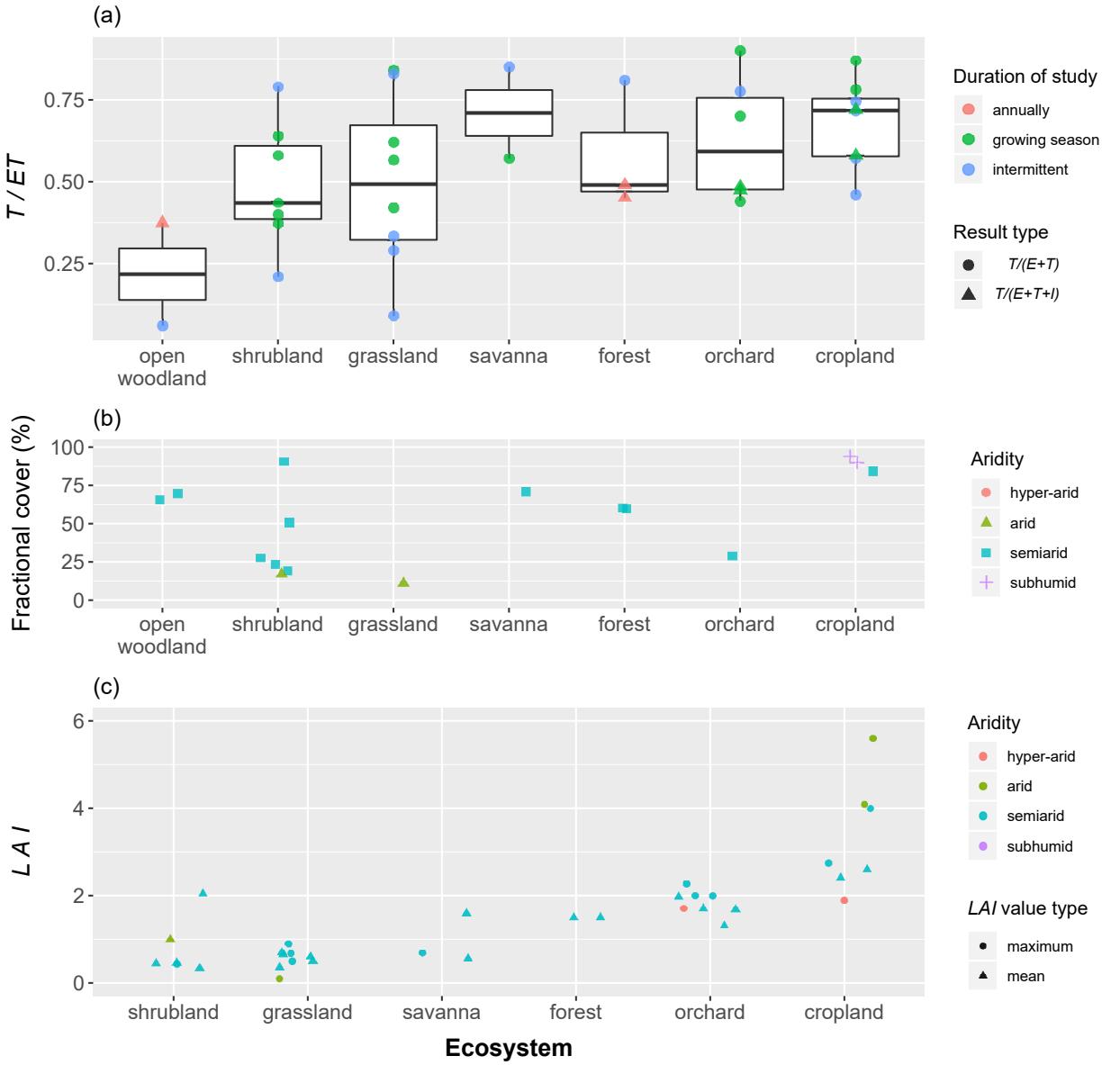

Figure 1.5: ET partitioning and canopy characteristics for the different types of ecosystems. Note: The studies done on a regional watershed ([54]) and a marshland ([55]) are not included. Mean values are used for results reported as ranges in Tables 1.1 and 1.2.

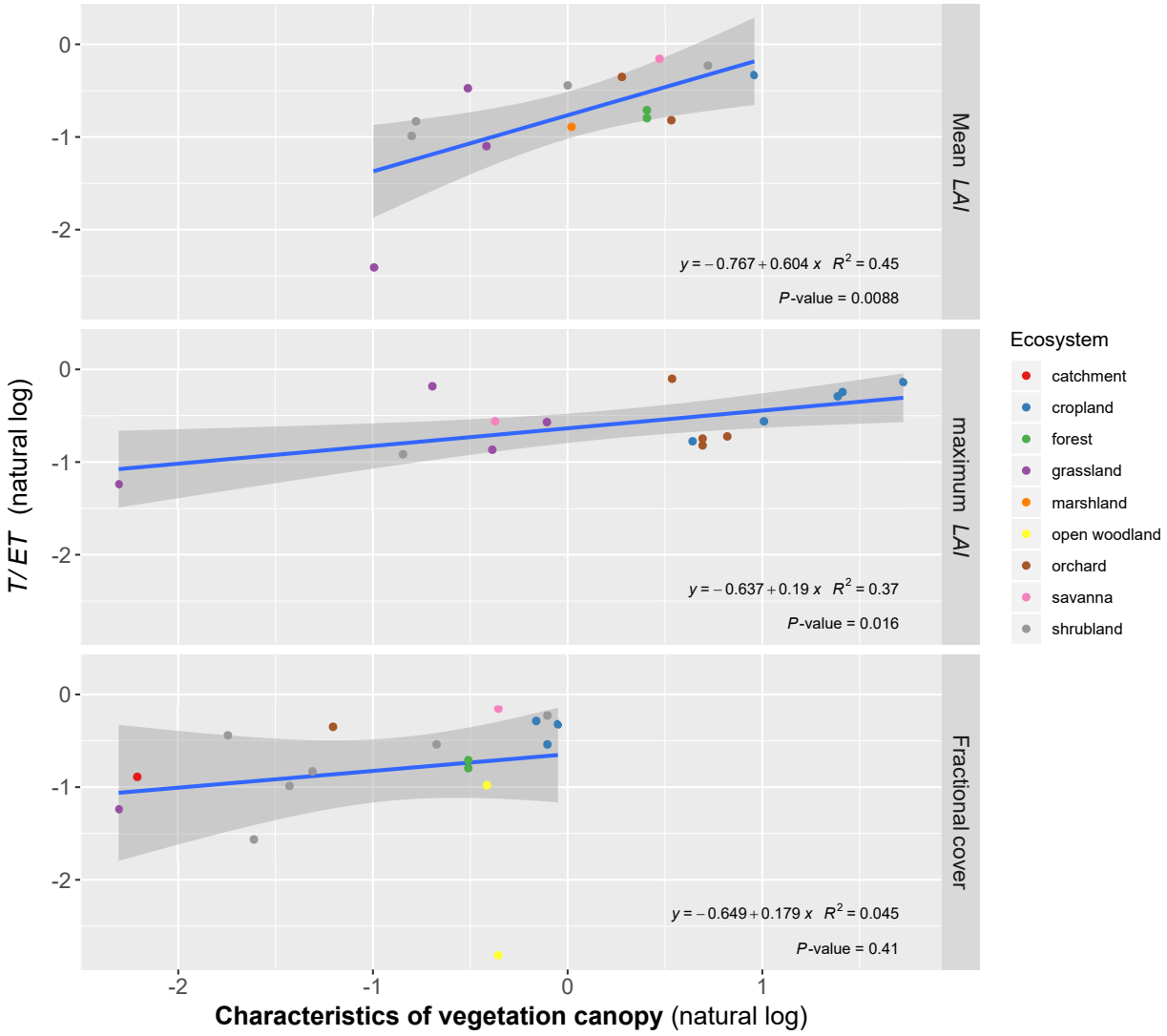

Figure 1.6: Relationship between T/ET (natural log) and vegetation canopy characteristics (natural log). This analysis did include the regional catchment study (Guo et al., 2017) and the marshland study (Zhang et al., 2018). Mean values are used for results reported as ranges in Tables 1.1 and 1.2.

Table 1.3: Results of regression analyses for T/ET and LAI.

Ecosystem Type	Regression	Note	Citation
Winter wheat	$T/ET = 1 - e^{-0.3442LAI}$	$R^2 = 0.7879$	[84]
Summer corn	$T/ET = 1 - e^{-0.4046LAI}$	$R^2 = 0.7444$	[84]
Cotton and grain sorghum	$T/ET = -0.21 + 0.70LAI^{0}.5$	$0.1 \leq LAI \leq 2.7$	[85]
Cowpeas	$T/ET = 1 - e^{-0.79LAI}$	—	[86]
Maize	$T/ET = 0.71LAI^{0}.14$	$R^2 = 0.868$	[53]
Forage sorghum	$T/ET = 0.45LAI^{0}.19$	—	[9]
Desert ecosystems*	$T/ET = 0.76LAI^{0}.70$	$R^2 = 0.75$	[31]
Global agricultural systems	$T/ET = 0.91LAI^{0}.07$	95% quantile regression	[29]
Global natural systems	$T/ET = 0.77LAI^{0}.10$	Same as above	[29]
Global (overall)	$T/ET = 0.91LAI^{0}.08$	Same as above	[29]
Drylands (this review)	$T/ET = 0.46LAI^{0}.60$	$R^2 = 0.45$	

* Desert ecosystems in southern Arizona, USA, including shrubland, savanna, and grassland.

1.5 Major themes identified via the meta-analysis

1.5.1 *ET* partitioning during dynamic wetting–drying episodes

The pattern of rare and irregular precipitation events that characterizes dryland ecosystems creates pulses of high and low biotic activity [87]. Consequently, during the dynamic wetting and drying cycles, both plant transpiration and soil evaporation can undergo rapid changes [47]. Soil evaporation is negligible when soils are dry, but after precipitation it becomes significant within a short period (usually a few days) [50, 42, 88]; then, once it has peaked, evaporation declines rapidly. Transpiration, which is suppressed during rainfall [89], peaks more slowly and also declines more gradually after precipitation [34].

Because of the differences in temporal dynamics between soil evaporation and transpiration, the pattern of ET partitioning varies significantly during these wetting–drying episodes. As examples, a study of a semiarid forest found that soil evaporation dominated ET shortly after a rain event, with E/ET ranging between 49% and 65% [51]; a study of a semiarid shrubland with more than 90% coverage showed that daily average E/ET decreased from 34% to 3% during the first two sunny days after precipitation [48]; and in a Chihuahuan desert, evaporation dominated ET at the onset of summer rains, but 2–4 weeks after the occurrence of large precipitation events, shrub vegetation recovered and began to transpire at peak rates [37, 31, 34].

Similar phenomena were often observed for irrigated agro-ecosystems. Examples include a winter wheat field, where E/ET was 0.20 before irrigation and 0.31 after irrigation [20]; an olive (*Olea europaea* L.) orchard, where E/ET was nearly 0 prior to irrigation, then reached 0.31 by midday on the sixth day following irrigation [10]; and a cotton cropland, where E/ET equaled or exceeded T/ET for four days after irrigation, but began a dramatic decrease from the fifth day [33]. In contrast to this trend of increasing E/ET shortly after irrigation, an exception was reported for a semiarid sparse grassland (*Eragrostis lehmanniana*) with loamy-sandy soil, where E/ET dropped following the irrigation pulse. In such environments, soil evaporation is typically the dominant flux and transpiration the minor flux; but with the rapid infiltration of irrigation water, causing a

short period of plant-available soil water in the rooting zone, transpiration increased briefly. The corresponding decrease in E/ET, to 0.57–0.65, occurred within three days after irrigation. By day 7, E/ET had again risen, to 0.78 [47].

1.5.2 Factors controlling evaporation and transpiration are different

Evaporation and transpiration are controlled by different factors. Soil evaporation is a physical process, mostly affected by abiotic factors, including vapor pressure deficit (VPD), water availability in the surface soil, and the shading effect of the vegetation canopy. Plant transpiration, on the other hand, takes place through the soil–plant–atmosphere continuum and is controlled by both abiotic and biotic factors—including plant-available soil water in the rooting zone, VPD, and physiological regulation of leaf stomata.

A study of an olive orchard (*Olea europaea* L.) showed that during wetting–drying cycles, daily rates of soil evaporation correlated positively with daily VPD, but transpiration did not [10]. Seasonal-scale investigations in a semiarid eucalyptus woodland found that daily rates of transpiration tracked seasonal changes in radiation and drainage, whereas daily rates of evaporation correlated positively with surface soil moisture content [35]. Similar results were found in a semiarid shrubland [37] and a pine forest [13], where soil evaporation was closely correlated with solar radiation and surface soil moisture, whereas transpiration was correlated with soil moisture in the deeper layers. This differencethe dependence of evaporation on shallow soil moisture and of transpiration on deeper soil moisturewas also observed in agro-ecosystems [5].

1.5.3 Controlling factors differ according to temporal scale

The factors controlling ET partitioning vary at different temporal scales. Ambient atmospheric conditions show high variability at the diurnal scale, whereas plant phenology exhibits great variations across the growing season, especially with changes in the precipitation pattern (dry vs wet). For example, in a study of a semiarid grassland, VPD was a significant factor at the diurnal scale, resulting in a U-shaped diurnal pattern of T/ET [50]. A similar diurnal T/ET pattern was found in another dryland grassland, but over the longer timescale of a two-week period of green-up and

senescence, green LAI and available soil water were the controlling factors for T/ET dynamics [49]. For semiarid sites characterized by summer rainfall, T/ET reached a peak coincident with the maximum LAI, suggesting the strong effect of plant phenology and precipitation pattern on ET partitioning [31]. Similarly, a modeling study in grassland ecosystems concluded that T/ET was controlled by canopy stomatal conductance at the diurnal scale, and by LAI at the seasonal and annual scales [90].

1.5.4 Effects of precipitation and soil moisture dynamics on ET partitioning

How ET is partitioned in a given ecosystem depends on the temporal pattern of precipitation distributionwhether precipitation is concentrated into a few big events or scattered among many smaller ones [91, 31]. For example, a study conducted in a semiarid forest found that annual T/ET was more influenced by large storms (>$30\,\mathrm{mm}$) than by the annual precipitation totals [13]—probably because only intense storms can result in deep inltration and thus plant–available soil moisture for trees. A similar phenomenon was observed in semiarid grasslands and shrublands in Arizona, USA, where seasonal T/ET was found to be relatively insensitive to precipitation patterns when precipitation was near- to below-normal [58] —conditions under which deep soil water infiltration probably rarely occurred.

1.5.5 Effects of interception on ET partitioning

Uncertainty concerning the contribution of interception is the largest source of bias in ET partitioning [30]. The amount of rainfall intercepted by the vegetation canopy and the debris layer depends on rainfall frequency and the structural characteristics and physiological properties of the vegetation. In arid and semiarid climates, sporadic and short precipitation events coupled with high VPD could result in a substantial amount of evaporation via interception [92]. Examples include a semiarid eucalyptus (*E. capillosa*) woodland, where 8%–15% of the rainfall was intercepted—of which 69% evaporated and 31% was yielded as stem flow [35]; and a semiarid pine forest, where interception accounted for 10%–12% of annual precipitation and more than 20% during the rainy season [69, 13]. In contrast, interception could be negligible in sparsely vegetated dryland ecosys-

tems, such as a desert shrubland in northern China, where interception accounted for only 3.2% of precipitation during the growing season [41].

1.5.6 Effects of vegetation canopy on ET partitioning

Several researchers noted that patterns of ET partitioning are influenced by the various characteristics of the vegetation canopy, such as LAI and fractional cover [8], phenological development during the growing season [38], and tree age [44]. Studies of the relationship between LAI and T/ET at the global scale [29, 30] suggest that LAI can be the first-order controlling factor for T/ET, as expressed in the following power-law function:

$$T/(E+T) = aLAI^b, \tag{1.3}$$

where coefficients a and b are specific to vegetation types (see Table 1.3) for results from the retrieved studies and several other pertinent investigations). It has been argued that this power-law function applies only to situations in which LAI is below a certain threshold (below that threshold, T/ET increases quickly and proportionally in response to increases in LAI; but above it, T/ET is no longer sensitive to changes in LAI). For example, an LAI threshold of 4 was found for a cropland of winter wheat and summer corn [84], and a threshold of approximately 2.7 for a cotton and sorghum site [85]. This threshold phenomenon may be attributable to suppression of transpiration per unit of LAI for well-developed or thickened plant canopy. A simulation based on tree mosaics also revealed that as LAI increased, T/ET gradually fell below a 1:1 proportionality [93].

The retrieved datasets show a high variability in T/ET—a range of 0.06–0.90 (Figs. 1.4 b & c and Fig. 1.5 a). Wide variations in T/ET were also reported at a global scale for ecosystems with low LAI (*e.g.* ≤ 0.5), indicating the possibility of high T/ET even under low LAI conditions [29]. A modeling study of grassland ecosystems also revealed that the relationship between T/ET and LAI is more erratic in semiarid and subhumid sites than in humid sites [90]. This greater variation in T/ET for low-LAI ecosystems implies that other biological or meteorological factors

might play a substantial role. For example, in a semiarid steppe region of Inner Mongolia, China, in a year with normal precipitation, T/ET decreased under grazing because of the reduction in *LAI* [42]. In contrast, in a dry year the grazing-induced reduction in *LAI* did not influence T/ET because plant physiological functions were suppressed by the drought conditions.

1.5.7 Effects of groundwater on *ET* partitioning

For sites with shallow groundwater (depths of 0–10 m), groundwater evaporation and root water uptake should be explicitly considered. For example, in an oak savanna, groundwater uptake by blue oak accounted for 70%–90% of total ET during the dry summer [94]. In a semiarid floodplain woodland, the ability of the dominant deep-rooted velvet mesquite (*Prosopis velutina*) to access groundwater contributed to an unusually high T/ET ratio (0.90) for the duration of the growing season [95]. Similarly, in a desert shrubland, groundwater lying some $5.7\,\mathrm{m}$ below the surface became the main source for both evaporation and transpiration [41]. And in a semiarid open woodland, evaporation of shallow groundwater accounted for up to one-third of total ET, but only after soil moisture in the vadose zone had been depleted [43].

1.6 Emerging technologies, challenges, and opportunities

Our understanding of ET fluxes and partitioning of ET in drylands has advanced dramatically in the past few decades, owing to enhanced capabilities in measurement technologies, data availability, and numerical modeling. At the same time, the particular nature of ecohydrologic processes in drylandsespecially the heterogeneity in spatial–temporal scalesmeans that ET partitioning in these regions remains challenging.

1.6.1 Field-deployable isotopic laser spectroscopy for water vapor analysis

The isotopic approach for ET partitioning is continuing to evolve. The methods traditionally used for sampling water from soils and plants have major limitations, such as (1) the destructive nature of sampling and (2) the laborious and time-consuming procedure of cryogenic vacuum distillation. In addition, the isotopic representativeness of plant samples remains debatable [96, 97, 98]. For drylands, a special challenge is that under very dry conditions, the negligible flux of soil

evaporation might prevent reliable calculation of δ_{ET}, because of the absence of detectable vertical gradients in vapor concentrations and in the isotopic compositions of water vapor [47]. Extreme conditions of heat and aridity will decrease the equilibrium fractionation factor [75], rendering the end-members (δ_E and δ_T) insufficiently distinguishable [9], which translates to a high degree of uncertainty for the isotopic approach.

A critical question in quantifying the isotopic composition of soil evaporation is how fractionation processes affect the isotopic composition of soil water [51]—which, under conditions of intense evaporation, exhibits high variability across the profile [50]. During the dry season, vapor transport can dominate water diffusion in the vadose zone and plays a key role in mass and energy transfer within soils [99, 100]. To determine the effects of fractionation processes, then, isotopic sampling of water vapor across the soil profile is essential [43].

A promising tool for sampling of soil water vapor in the vadose zone is field-deployable laser isotope spectroscopy, which enables direct, continuous, and non-destructive measurement [51, 101, 102]. *In situ* sampling of soil water vapor has been performed both to study water vapor dynamics [51, 102, 103, 104] and to derive the isotopic composition of liquid soil water based on the water–vapor equilibrium assumption [101]. This assumption is supported by a case study in a semiarid African savanna, where the liquid–vapor interface was measured from the *in situ* soil profile [103]. The major concern during sampling of soil water vapor for isotopic analysis is fractionation caused by either inducing evaporation of liquid soil water or condensation of vapor inside the sampling apparatus [103]. At present, standard sampling protocols with wide applicability are still under development [105].

1.6.2 Water diffusion pathways from ground to atmosphere

To be consistent and comparable, *in situ* studies on ET partitioning must identify and take into account the various diffusive pathways by which water moves from terrestrial ecosystems to the near-surface atmosphere. In the past, many field studies ignored the role of evaporation underneath the canopy, considering it to be negligible because of the shading effect [43]. An accurate quantification of under-canopy evaporation necessitates the application of either an extinction coefficient

for radiation diffusion or a threshold LAI value [84]. For two-layered ecosystems (e.g., savannas and shrublands), even though transpiration fluxes can be combined to simplify analysis [48], transpiration from the upper tree/shrub layer and from the understory herbaceous layer should be measured separately [30]. Such detailed *in situ* studies are essential for quantifying the different diffusive pathways for plant transpiration and for identifying the biophysical factors that control transpiration from different functional types [106].

1.6.3 Scaling and modeling

Dryland ecosystems, characterized by scarce and sporadic precipitation as well as low vegetation coverage, exhibit considerable spatial heterogeneity along with high temporal variability in plant physiological activity [107, 13, 108]. For these reasons, upscaling of measurements from the stand or plot scale is quite challenging. For example, upscaling of sap flow is highly uncertain and error-prone—first, because the scaling relationships for different parameters (basal area, plant density, canopy height, canopy coverage, sapwood area, LAI) vary widely [66]; and second, because plants of different functional types have different phenological stages [29, 12]. When sap flow is being compared with ET fluxes obtained by eddy-covariance measurement, the upscaling needs to be confined to the contributing footprints of the turbulent fluxes [10].

Coupling of the eddy-covariance method with laser isotope spectroscopy could make it possible for ecosystem-level ET partitioning to be accomplished without the need for scaling [46, 10, 57]. In addition, this combined methodology can be expanded to measurement of carbon isotopes, thereby enabling the partition of CO_2 dynamics and calculation of water-use efficiency [49], both of which are essential for parameterizing and validating physical-based ecosystem models [109].

1.7 Conclusions

In dryland ecosystems, although ET is the largest water-loss flux, it is poorly quantifiedespecially at fine temporal scales. Despite the importance of accurately quantifying ET, its partitioning remains a major challenge for ecohydrologic studies in drylands. To review and summarize the current state of knowledge on this topic, we retrieved 31 publications on *in situ* studies of ET

partitioning covering the past nearly three decades. We classified these studies by the length of time over which measurements were taken, ranging from intermittent (typically less than 10 days, and usually done with the isotopic approach) to long-term (done at the growing season or annual scale, and usually with the hydrometric approach). For natural ecosystems, results from the intermittent studies showed higher variability than those from the longer-term studies. Longer-term T/ET varied over a narrow range, with a mean value of 0.52—implying that soil evaporation and plant transpiration are largely equivalent in natural drylands over the long term. Agro-ecosystems (usually irrigated) exhibited a relatively higher T/ET and showed greater variability in the longer-term measurements. Maximum values of T/ET were roughly similar for natural ecosystems and agro-ecosystems. Soil evaporation and plant transpiration responded differently during dynamic wetting–drying episodes, both in timing and duration. Soil evaporation is more controlled by meteorological processes and shallow soil water, whereas transpiration is more controlled by plant phenology and water availability in the rooting zone.

The patterns of ET partitioning in drylands are influenced by multiple biometeorological factors, including the temporal distribution of precipitation, rainfall interception, soil moisture recharging, groundwater depth, and vegetation development. Atmospheric conditions and stomatal conductance dominate ET partitioning at diurnal scales, while canopy phenology (or LAI) and soil moisture dominate over longer timescales. Our regression analyses revealed that LAI (especially its mean values) is an essential factor controlling T/ET variability in dryland ecosystems, but its explanatory power might be curtailed by stomatal control under dry climatic conditions.

On the basis of our findings, we suggest three promising areas of investigation to help meet the challenges of ET partitioning in drylands: (1) employment of laser spectroscopy for intensive isotopic sampling of water vapor in the vadose zone; (2) improved identification and accurate quantification of the various pathways of water diffusion; and (3) development of methods for upscaling measurements taken at incongruent spatial/temporal scales owing to different research approaches (hydrometric vs isotopic).

2. EFFECT OF VEGETATION ON THE ENERGY BALANCE AND EVAPOTRANSPIRATION IN TALLGRASS PRAIRIE *

2.1 Introduction

Covering 37% of the Earth's surface, the grassland biome is a key component of the terrestrial biosphere, and is crucial for agriculture production, biodiversity conservation, and climate regulation [110, 111]. In the Southern Great Plains of the USA, tallgrass prairie is the major type of grassland, especially in the state of Oklahoma [112], but this prairie is considered a globally endangered resource [113], with agricultural conversion having consumed all but about 13% of its historical extent [114]. Recently, this endangered prairie has been threatened by the rapid encroachment of woody plants, particularly juniper (*Juniperus virginiana* L.) [115, 116], owing mainly to changes in land-use practices that have led to altered fire regimes [117]. Further encroachment by woody plants could substantially affect the water cycle, primarily through altering evapotranspiration (ET), which is the largest component of the water budget in this region [116]. Understanding ET and the underlying ecohydrologic responses of grassland to extreme events in a changing climate, such as during drought, is an essential consideration for studies of ecosystem services, the management of water resources, and the understanding of climate change [118].

Energy and water are tightly coupled. A major portion of the incoming solar radiation is converted to fluxes of sensible (H) and latent heat [LE, where E ($\mathrm{kg\,m^{-2}\,s^{-1}}$) is evaporation from the surface and L ($\mathrm{J\,kg^{-1}}$] is the latent heat of vaporization, which determine the energy exchange and water-vapor flux of the near-surface atmosphere, respectively, and the partitioning between H and LE determines many climatological processes and physical properties of the planetary boundary layer, with the latent heat flux also affecting the soil moisture, runoff, and biogeochemical cycles [119]. The most direct method of measuring these vertical turbulent fluxes is through the eddy-covariance (EC) method [120], which is widely used in micrometeorology [121].

*A version of this chapter has been published as: Sun, X., Zou, C.B., Wilcox, B. and Stebler, E., 2019. Effect of vegetation on the energy balance and evapotranspiration in tallgrass prairie: A paired study using the eddy-covariance method. *Boundary-layer meteorology*, 170(1), pp.127-160. Adapted with permission. Copyright 2018 Springer Nature.

However, the energy imbalance or closure problem remains an unsolved problem with the use of the EC method, namely the available energy is 10%–30% larger than the sum of the H and LE fluxes over various vegetation types [122, 123, 124, 125, 126, 127, 128, 129, 130, 131]. Correcting for these discrepancies is challenging because many of the involved causes are difficult to quantify [122, 123, 124], including the energy storage [132, 127, 128, 130], energy advection and mesoscale eddies generated in heterogeneous landscapes [133, 124, 126, 134, 135], and measurement uncertainties related to sonic anemometers [136, 137, 138]. For low canopies such as grassland, studies have found that the degree of energy-balance discrepancy differs between sites with high vegetation coverage and those having a greater exposure of soils, owing to the effects of the heat storage in the upper soil layer and the fractional coverage of vegetation [123, 139]. For a semi-arid grassland, integration of the soil heat storage (S_{soil}) measured above heat-flux plates significantly improves the surface-energy balance [140]. In contrast, an analysis on a subset of European FLUXNET stations indicated that the storage terms do not play a major role in the overall closure of the energy balance [125]. Given these uncertainties, experiments using two collocated plots, one of them denuded of vegetation, could help disentangle the influences of vegetation and soil heat storage on the closure problem.

The low measurement height and associated relatively small fetch of grassland flux towers facilitate the design of classical, paired ecological experiments, which combine the strength of near-continuous, spatially-integrated, EC monitoring with the explanatory power of causal analysis [141]. With the use of identical equipment on sites having similar land-use histories and nearly identical environmental conditions, confounding factors are minimized, increasing the confidence in the results of different treatments of the vegetation [142, 141]. Collocated measurements for contrasting vegetation types in tallgrass prairie region include burning versus no burning [143, 144], cultivation versus natural cover [145, 146], shrub versus grassland [147, 148, 149], and well-watered versus drought conditions [150]. The energy balance has been investigated in a boreal jack pine forest with clearcutting versus no treatment [151] but, to our knowledge, no one has experimentally compared treated and untreated sites in grasslands to examine the difference in

energy balance. The high variability of precipitation in grasslands and the resultant high intra-annual variations in primary production [152, 153] make these ecosystems a prime setting for the study of ecosystem physiology and ET through the experimental manipulation of the vegetation cover [154]. To accurately quantify the effects of vegetation canopy on surface energy fluxes, the best methodology would be to remove the vegetation from one of two sites, with the second one serving as a control site.

We have selected a pair of collocated tallgrass prairie sites having similar soil, topographic, and vegetation conditions. One site was treated with herbicide and subject to mowing early in the growing season, with the control site left undisturbed. Using one year of continuous EC measurements, we investigated and compared the energy balance, energy partitioning, diurnal and seasonal patterns of ET, and the key meteorological or biological factors controlling ET for the two sites. Specifically, our objectives were to answer the following questions:

- Influence of the soil heat storage (S_{soil}) on the energy-balance closure: how do the values of S_{soil} and the sub-surface soil heat flux (G_s as measured by heat-flux plates) compare under two different vegetation coverages? If the value of S_{soil} is integrated into the ground surface heat flux (G_0), does the degree of energy-balance closure differ between the two sites?

- Influence of photosynthetically active vegetation on energy partitioning: how different are the seasonal and diurnal patterns of energy partitioning between the two sites, owing to the presence of active vegetation at the control site and its absence at the treated site?

- Evapotranspiration variation and the key controlling factors: how does ET vary, temporally and in magnitude, under contrasting vegetation coverages? How does the cumulative ET compare with the precipitation? Does the difference in vegetation cover between the paired sites translate to a difference in controlling factors for ET?

2.2 Study Sites

The study was conducted at the Range Research Station ($36°3'24.6''$N, $97°11'28.3''$W, elevation about 330 m above sea level), which is a research and extension facility administered

by the Oklahoma Agricultural Experiment Station, Oklahoma State University, and is located about $11\,\mathrm{km}$ south-west of Stillwater in Payne County, Oklahoma, USA. The terrain is mostly flat, with slopes of 3%–8%, and the soil type is mainly Stephenville–Darnell complex [155]. This tallgrass prairie is dominated by perennial, warm-season (C4) grasses, including little bluestem (*Schizachyrium scoparium* [Michx.] Nash), big bluestem (*Andropogon gerardii* Vitman), Indiangrass (*Sorghastrum nutans* [L.] Nash), switchgrass (*Panicum virgatum* L.), and tall dropseed (*Sporobolus asper* [Michx.] Kunth) [156]. According to Mesonet long-term average climate data (2002–2015), this site has a sub-humid climate with an average air temperature of $15.5\,^{\circ}\mathrm{C}$, a mean annual precipitation of $852\,\mathrm{mm}$, an average wind speed of $4\,\mathrm{m\,s^{-1}}$ (maximum gusts of $7.6\,\mathrm{m\,s^{-1}}$), an average relative humidity of 66%, an average atmospheric pressure of $97.7\,\mathrm{kPa}$, an average daily global radiation of $192\,\mathrm{W\,m^{-2}}$, and an average daily net radiation of $98\,\mathrm{W\,m^{-2}}$ [157, 158, 159].

2.3 Materials and Methods

From 2014–2015, two EC towers separated by a distance of $250\,\mathrm{m}$ were installed in the Range Research Station, with one in the north of the grassland tract, and the other in the south. In 2016, we delineated two collocated experimental sites, with one surrounding the northern EC tower, and the other surrounding the southern tower (Fig.2.1). The northern site was sprayed with herbicide on May 12, 2016, mowed on May 29. A large amount of the remaining cover of dried standing stems was left, so that little bare ground was visible. And we sprayed herbicide again on July 20. Having been thus treated for vegetation removal, this site is hereafter referred to as Site T. The southern site was left as natural, undisturbed grassland, to serve as a control, and thus is hereafter referred to as Site C. At each of the two sites, the EC tower was located at the north-western or northern end, facing the greatest fetch as determined by the prevailing wind direction (south or south-south-east; see Fig. 2.2).

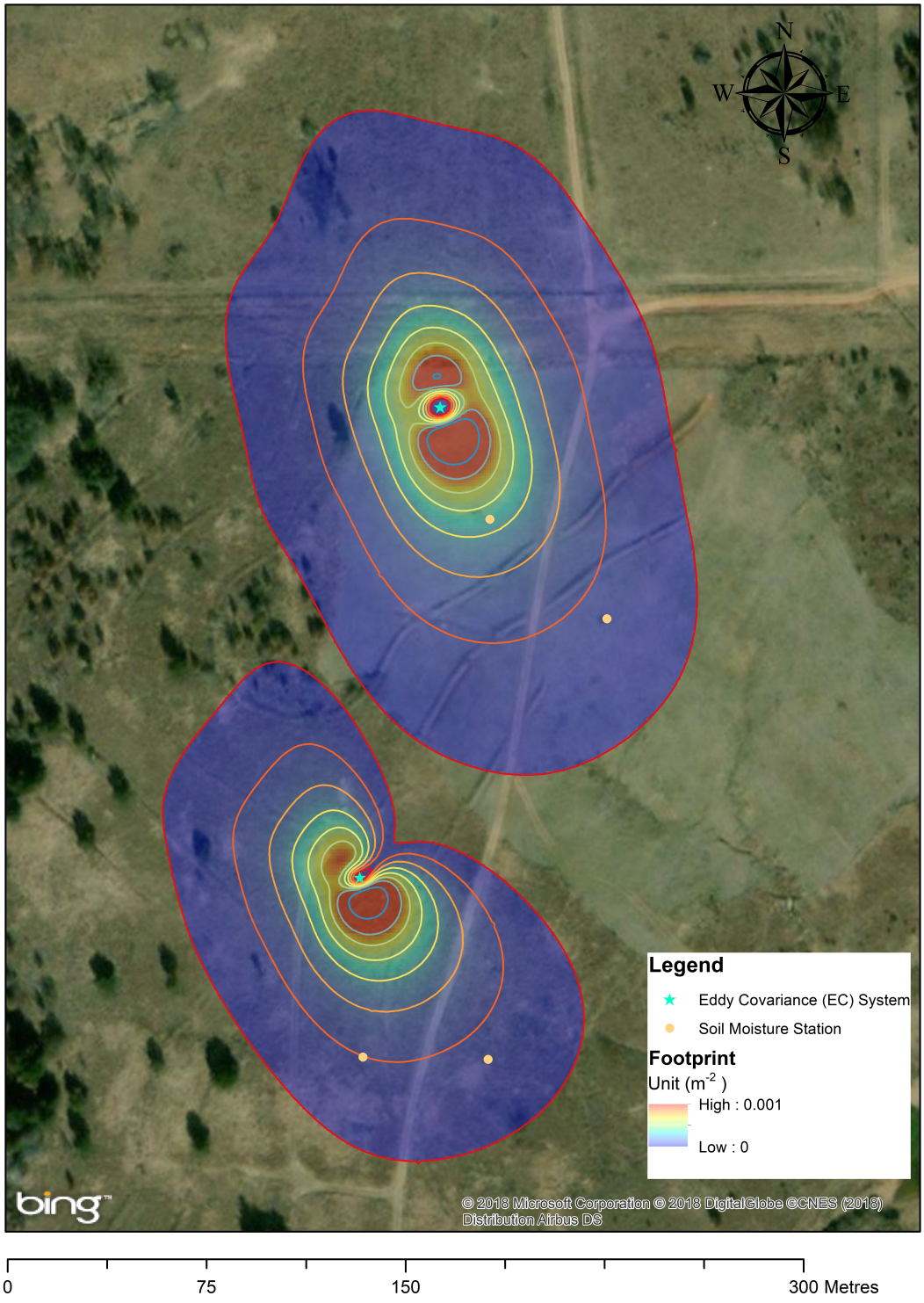

Figure 2.1: Configuration of the study sites with superimpositions of the flux-footprint climatology. Except for the space immediately surrounding each EC tower, the contour lines from inner to outer are the yearly cumulative footprint climatology boundaries from 10% to 80%, with an interval of 10%. The EC devices were mounted $3\,\mathrm{m}$ above the ground.

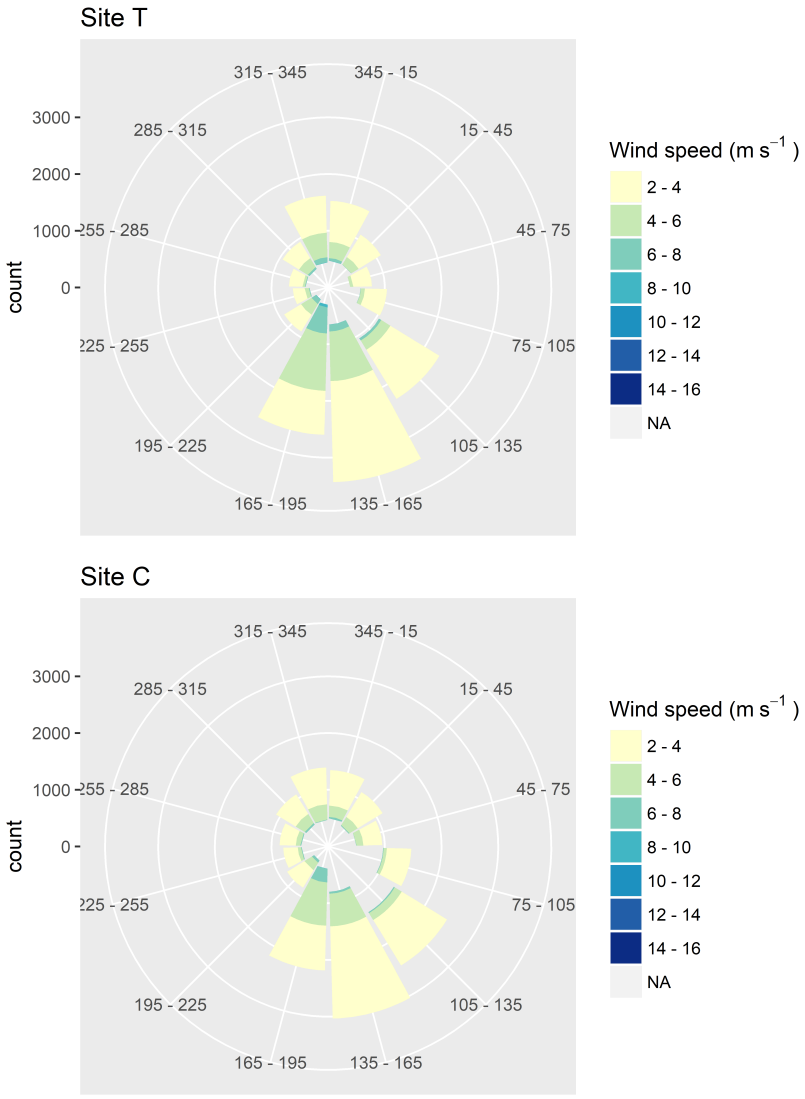

Figure 2.2: Wind rose maps for the two sites.

2.3.1 Eddy-Covariance Systems and Biometeorological Sensors

Each EC tower was equipped with an integrated CO_2 and H_2O open-path gas analyzer and three-dimensional sonic anemometer (EC100, IRGASON, Campbell Scientific Inc., Logan, Utah) mounted $3\,\mathrm{m}$ above the ground. A standard set of sensors for measuring biometeorological variables was also installed at each tower, including two heat-flux plates (HFP01, Hukseflux, Delft, Netherlands) set $8\,\mathrm{cm}$ below the ground, one averaging soil thermocouple (TCAV, Campbell Scien-

tific Inc., Logan, Utah), with the two members of each pair set at $2\,\mathrm{cm}$ and $6\,\mathrm{cm}$ below the ground, with a distance of $1\,\mathrm{m}$ between the two pairs, one water-content reflectometer (CS616, Campbell Scientific Inc., Logan, Utah) set $2.5\,\mathrm{cm}$ below the ground, a net radiometer (NR-Lite2, Kipp and Zonen, Delft, Netherlands), and a temperature probe for the ambient air (107, Campbell Scientific Inc., Logan, Utah) with a solar radiation shield. All the biometeorological sensors sampled every $5\,\mathrm{s}$, and 30-min averages were calculated and stored with a datalogger (CR3000, Campbell Scientific Inc., Logan, Utah). To measure the normalized difference vegetation ($NDVI$), we installed spectral reflectance sensors (SRS, Decagon Inc., Pullman, Washington) in close proximity to the two EC towers. The pair mounted Site T was operational only for 24 days (May 12 to June 4) following the initial herbicide spraying, while the other pair, in Site C, was operational beginning in February. A rain gauge (HOBO RG3, Onset Inc., Bourne, Massachusetts) was mounted above the canopy at Site C to record precipitation (precipitation events were assumed to be the same for both sites). Finally, soil-moisture probes (ECH_2O EC-5, Decagon, Pullman, Washington) were inserted at two soil-moisture stations at each site at depths of $0.05\,\mathrm{m}$, $0.2\,\mathrm{m}$, $0.45\,\mathrm{m}$, and $0.8\,\mathrm{m}$, to measure the volumetric soil water content (θ) of four depth intervals across the soil profile: 0–0.1 m, 0.1–0.3 m, 0.3–0.6 m, and 0.6–1.0 m (Fig. 2.1). All the measurements described above were recorded in terms of the local time (LT = UTC –6 h; no daylight saving time).

Surface turbulent-flux measurements were collected at a frequency of $10\,\mathrm{Hz}$, and computed for an average of $30\,\mathrm{min}$ with biometeorological data via the EddyPro software (version 6.2.1, LI-COR Biosciences, Lincoln, Nebraska). We adopted dynamic canopy heights from previous observational results [160]. The key processing steps included despiking and the statistical screening of raw data [161], tilt correction with the double rotation method [162], spectral corrections [163, 164, 165], and the compensation for density fluctuations [166]. Subsequently, EddyPro quality flags were calculated for all fluxes on the basis of the steady state test and the test for developed turbulent conditions, and combined into a 0–1–2 system [167].

2.3.2 Footprint Analysis, Quality Control, and Gap Filling

To determine whether the flux footprints of the two sites overlapped spatially, we estimated the climatology boundaries of the two-dimensional footprint with yearly cumulative contributions from 10% to 80% (with an interval of 10%) to the measured turbulent fluxes (Fig. 2.1). We used the Flux Footprint Prediction model [168] for these estimates, because of its ability to accurately predict the maximum footprint boundary [169]. The planetary boundary-layer height, which is used by the Flux Footprint Prediction model for crosswind-integrated scaling, was obtained from the North American Regional Reanalysis data provided by the National Oceanic and Atmospheric Administrations Physical Sciences Division, Boulder, Colorado, USA (https://www.esrl.noaa.gov/psd/). The sample code employed for extracting time series of the planetary boundary-layer height based on the geographical location is provided in Appendix A. As for the footprint analysis, we calculated two matrices along the wind direction [170] (Kljun et al., 2004): X_i (i = 10%–90%, with an interval of 20%), provided by the along-wind distance contributing i cumulative turbulent fluxes, and X_{peak}, which is the upwind distance providing the highest contribution. Fetches extending beyond the boundaries of the two sites (as defined by the $X_{70\%}$) footprint criterion) were discarded after the first treatment (May 12, 2016). Following footprint filtering, the median values of $X_{70\%}$ and X_{peak} were $92.5\,\mathrm{m}$ and $48.6\,\mathrm{m}$ for Site T, and $88.9\,\mathrm{m}$ and $39.2\,\mathrm{m}$ for Site C.

The EC results produced by the EddyPro software were subject to further filtering and quality testing. Under conditions of stable stratification and low turbulent mixing (primarily during the night), a routine filtering criterion for the friction velocity u^* was applied on a monthly basis (with thresholds ranging between 0.06 and 0.18 $\mathrm{m\,s^{-1}}$ for Site T, and between 0.09 and 0.25 $\mathrm{m\,s^{-1}}$ for Site C) via the moving-point test [171]. Poor-quality data (those having quality flags = 2) and outliers (values beyond three times of the standard deviations) were screened for values of the H and LE fluxes. The FREddyPro package (https://cran.r-project.org/web/packages/FREddyPro/index.html) was employed for all despiking, the filtering of monthly u_*, and other general post-processing of EddyPro output files.

After all the filtering operations, data coverage for the remaining 30-min H and LE fluxes are

55.3% and 46.5%, respectively, for Site T, and 72.6% and 59.5%, respectively, for Site C. Gap-filling [172, 173] was implemented with the R package REddyProc developed at the Max Planck Institute of Biogeochemistry (https://www.bgc-jena.mpg.de/bgi/index.php/Services-/REddyProcWebRPackage). Records of ancillary environmental factors, such as global radiation and air temperature, were used to separately fill gaps in the time series of the sensible and latent heat fluxes via the default routines of the gap filling algorithm after u_* filtering within seasons, with the u^* thresholds based on 50% of the bootstrap re-sampling. Bowen ratios calculated during the night (for global radiation <$20\,\mathrm{W\,m^{-2}}$) were filtered, and Bowen-ratio outliers during the daytime were removed (outside the range 5 to 15, which accounted for less than 1% at each site), and then filled by the linear method [174] with the imputeTS package (https://cran.r-project.org/web/packages/imputeTS/index.html).

Uncertainties in H and LE fluxes were integrated from 30-min random errors of fluxes [175], including the errors in gap-filling estimates. The uncertainty in the 30-min ET propagates from that in the 30-min LE flux, and uncertainties in yearly budgets and monthly averaged values of ET were calculated by integrating the additive variance of random measurement errors and gap-filling uncertainties. We present aggregated uncertainty estimates with 95% confidence intervals.

2.3.3 Energy-Balance Closure

Whether the EC method has underestimated the surface turbulent fluxes is usually assessed by checking the energy-balance closure [176, 131]. As shown in Fig. 2.3, the surface energy budget can be formulated as

$$R_n - G_0 - S_{above} = LE + H + A_d, \tag{2.1}$$

with all terms having units of $\mathrm{W\,m^{-2}}$, where R_n is the net radiation (the balance between incoming global radiation and outgoing reflection and thermal radiation), S_{above} is the above-ground heat storage, consisting of heat stored in the above-ground biomass and photosynthetic heat storage flux, A_d is the advective heat flux beneath the EC sensors, G_0 is the ground surface heat flux, consisting of sub-surface heat flux (G_s) measured by heat-flux plates at a depth of $0.08\,\mathrm{m}$ in this

study, and the soil heat storage (S_{soil}) above the plates [177],

$$S_{soil} = \frac{\Delta T_s C_s d}{t}, \tag{2.2}$$

where ΔT_s is the change in soil temperature above the fixed depth d ($0.08\,\mathrm{m}$) during the measuring time interval t ($30\,\mathrm{min}$), and C_s is the heat capacity of moist soil ($\mathrm{J\,kg^{-1}\,K^{-1}}$). More details on the value of C_s can be found in Campbell Scientific (https://s.campbellsci.com/documents/us/-miscellaneous/old-manuals/HFP01%20Soil%20Heat%20Flux%20Plate.pdf, page 5-6, accessed in 2016).

In calculating the energy-balance closure, we have omitted the above-ground heat storage because, in the case of a low vegetation canopy, the magnitude of the photosynthetic flux is small [178], and the storage in the above-ground biomass is insignificant [131]. Advection was omitted as well, not only because it is considered to be insignificant over flat terrain [179], but also because its direct measurement is technically challenging [124, 171]. Thus, the calculation of the energy balance (at yearly and monthly scales) involves the linear regression between the instantaneous turbulent-flux measurements [$H + LE$ (before gap-filling)] from the EC method, and the measurements of the available energy (R_n –G_0) from the independent biometeorological sensors, assuming

$$R_n - G_0 = LE + H \tag{2.3}$$

Lastly, we coerced the energy-balance closure using the Bowen ratio method [178].

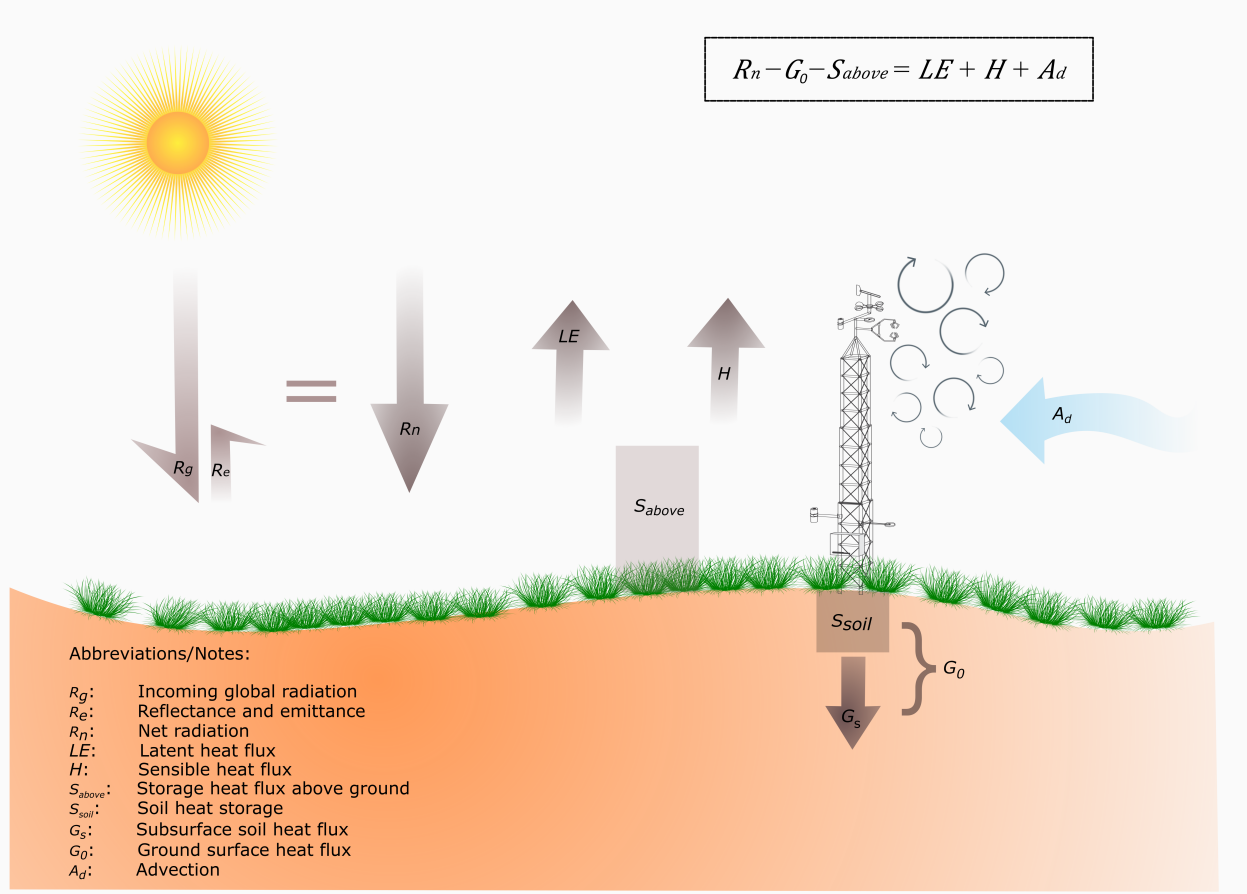

Figure 2.3: Diagram of surface-energy budget and energy-balance closure. The net radiation (R_n) is the source of all energy fluxes within the boundary layer, including the latent heat flux (LE) consumed in the process of evapotranspiration (ET), the sensible heat flux (H) associated with temperature variations, the below-ground heat flux (G_0), consisting of the soil heat storage above the heat-flux plate (S_{soil}), the sub-surface soil heat flux at the measurement depth (G_s), the above-ground heat storage (S_{above}), and the advective heat flux from all directions (A_d).

2.3.4 Parametrization of the Bulk Surface Characteristics

To interpret the influence of meteorological and biological factors on the ET variations, we calculated the surface conductance to water vapor (g_s, $\mathrm{m\,s^{-1}}$) during daytime periods (a global radiation > $20\,\mathrm{W\,m^{-2}}$) based on the inversion of the Penman–Monteith equation [180],

$$g_s = \frac{g_a}{\frac{\Delta(R_n - G) + \rho_a c_p VPD g_a}{\gamma LE} - \frac{\Delta}{\gamma} - 1} \tag{2.4}$$

where g_a ($\mathrm{m\,s^{-1}}$, described below) is the aerodynamic conductance of the air layer between the canopy top and the measurement height, Δ ($\mathrm{kPa\,K^{-1}}$) is the slope of the saturation vapor pressure versus air temperature, ρ_a ($\mathrm{kg\,m^{-3}}$) is the air density, c_p ($\mathrm{J\,kg^{-1}\,K^{-1}}$) is the specific heat of air at constant pressure, VPD (kPa) is the vapor pressure deficit, and γ ($\mathrm{kPa\,K^{-1}}$) is the psychrometric constant,

$$\gamma = 0.665 \times 10^{-3} P \tag{2.5}$$

where P (kPa) is the atmospheric pressure. The aerodynamic conductance g_a ($\mathrm{m\,s^{-1}}$) is defined as

$$\frac{1}{g_a} = \frac{u}{\mu_*^2} + 6.2\mu_*^{-0.67} \tag{2.6}$$

where u ($\mathrm{m\,s^{-1}}$) is the wind speed [181]. Leaf stomata and soil spaces are the major paths for surface water-vapor conductance, and thus the value of g_s is proportional to the leaf area index or the $NDVI$ and water-vapor conductance through the soil profile. The main factors controlling the value of g_a are the surface characteristics and the wind speed u.

The Penman–Monteith model [181] includes the effects of surface resistance ($r_s = g_s^{-1}$) and the above-canopy aerodynamic resistance ($r_a = g_a^{-1}$) on the potential ET,

$$LE = \frac{\Delta(R_n - G) + \frac{\rho c_p VPD}{r_a}}{\Delta + \gamma(1 + \frac{r_s}{r_a})} \tag{2.7}$$

As $r_a \to \inf$ or zero, the latent heat flux can be converted to either the equilibrium latent heat flux (LE_{eq}) or the imposed latent heat flux (LE_{im}) [182], which implies that the Penman–Monteith equation can be transformed as

$$LE = \Omega LE_{eq} + (1 - \Omega) LE_{im} \tag{2.8}$$

where Ω is the decoupling factor,

$$\Omega = \frac{\Delta + \gamma}{\Delta + \gamma(1 + \frac{g_a}{g_s})} \tag{2.9}$$

These calculations show that the latent heat flux lies between the two limits defined by the values of LE_{eq} and LE_{im}. When the energy budget is dominated by a diabatic process or available energy, Ω approaches unity, so that the ET rate is then effectively independent of the value of g_s and the vapor pressure deficit VPD, and may thus be viewed as decoupled from the prevailing weather conditions [181]. Conversely, Ω approaches zero when the ET is controlled by g_s and VPD, indicating greater coupling between the surface and near-surface atmosphere.

2.4 Results

2.4.1 Comparison of Environmental Conditions

While our paired adjacent sites exhibited similar meteorological conditions in general, there were differences in the net radiation and wind speed. Total rainfall for the year was $721\,\mathrm{mm}$, amounting to 85% of the 15-year mean (Mesonet, https://www.mesonet.org/index.php/weather/-mesonet_averages_maps#y=average&m=ann&p=rnet_sm&d=false, accessed in 2016), with $604\,\mathrm{mm}$ (84%) received during the growing season (April through October). However, during those months there were several dry intervals, including June 1–17 and August 1–24 with rainfall <$10\,\mathrm{mm}$ (Fig. 2.4a). In late May (about one week after the first herbicide application to Site T), the daily mean R_n began to diverge between the two sites. The difference in daily mean R_n for the period June–October was 13 ± 1 $\mathrm{W\,m^{-2}}$ (Fig. 2.4b), where, unless explicitly stated otherwise, mean values are expressed as ± the 95% confidence interval hereafter. The daily mean air temperature T_{air} and the VPD at the two sites were nearly identical, and showed the same seasonal patterns, reflecting the general seasonal pattern in the value of R_n (Figs. 2.4c, e). The yearly mean wind speed was $3.0\,\mathrm{m\,s^{-1}}$ at Site T and $2.7\,\mathrm{m\,s^{-1}}$ at Site C (Fig. 2.4d). After herbicide application at Site T, the $NDVI$ plummeted from 0.6 to 0.3 over the 24-day measurement period, whereas the $NDVI$ index at Site C varied in response to the natural leaf development (Fig. 2.4f). The vegetation removal resulted in a decrease in the value of u_* at Site T during the period June to October to 0.25 $\mathrm{m\,s^{-1}}$ (versus 0.28 $\mathrm{m\,s^{-1}}$ at Site C; data not shown).

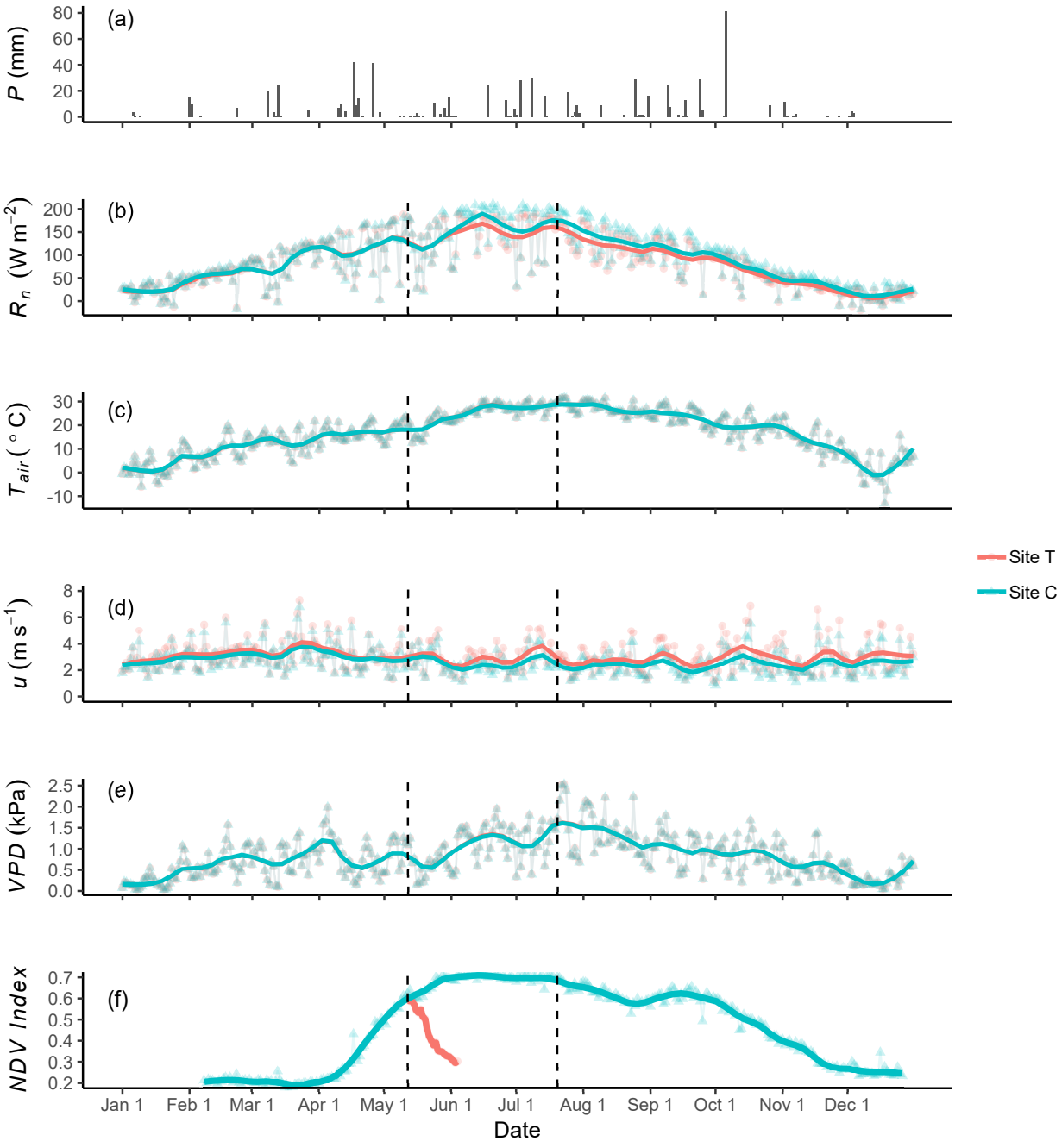

Figure 2.4: Seasonal variations in relevant environmental factors for the two experimental sites. These environmental factors are daily precipitation sum (a) and daily mean values of net radiation (b), air temperature (c), wind speed (d), vapor pressure deficit (e), and *NDVI* (f) for the two sites. Each vertical bar in (a) represents the daily total precipitation; each point in (b–e) represents the daily mean value observed over a 24-h period; each point in (f) represents the mean NDV index between 1200 and 1400 LT. The smoothened curves are fitted via locally weighted regression with a span of 0.1. The two dashed vertical lines represent the dates of the herbicide application to Site T (May 12 and July 20, 2016).

Before the herbicide application, soil-water dynamics across the profile (except for the lowest depth interval) were similar for the two sites, with a substantial divergence in soil water content θ gradually developing following the treatment. The surface and near-surface soils (to a depth of $0.3\,\mathrm{m}$) at both sites exhibited marked and prompt responses to the precipitation inputs, but varied over different ranges during the greater part of the growing season. As the depth increased, these sensitive responses gradually flattened, and the divergence in the values of θ between the two sites progressively developed in these deeper layers until the heaviest rainfall ($81\,\mathrm{mm}$ on October 6) when the discrepancy basically vanished (see Fig. 2.5).

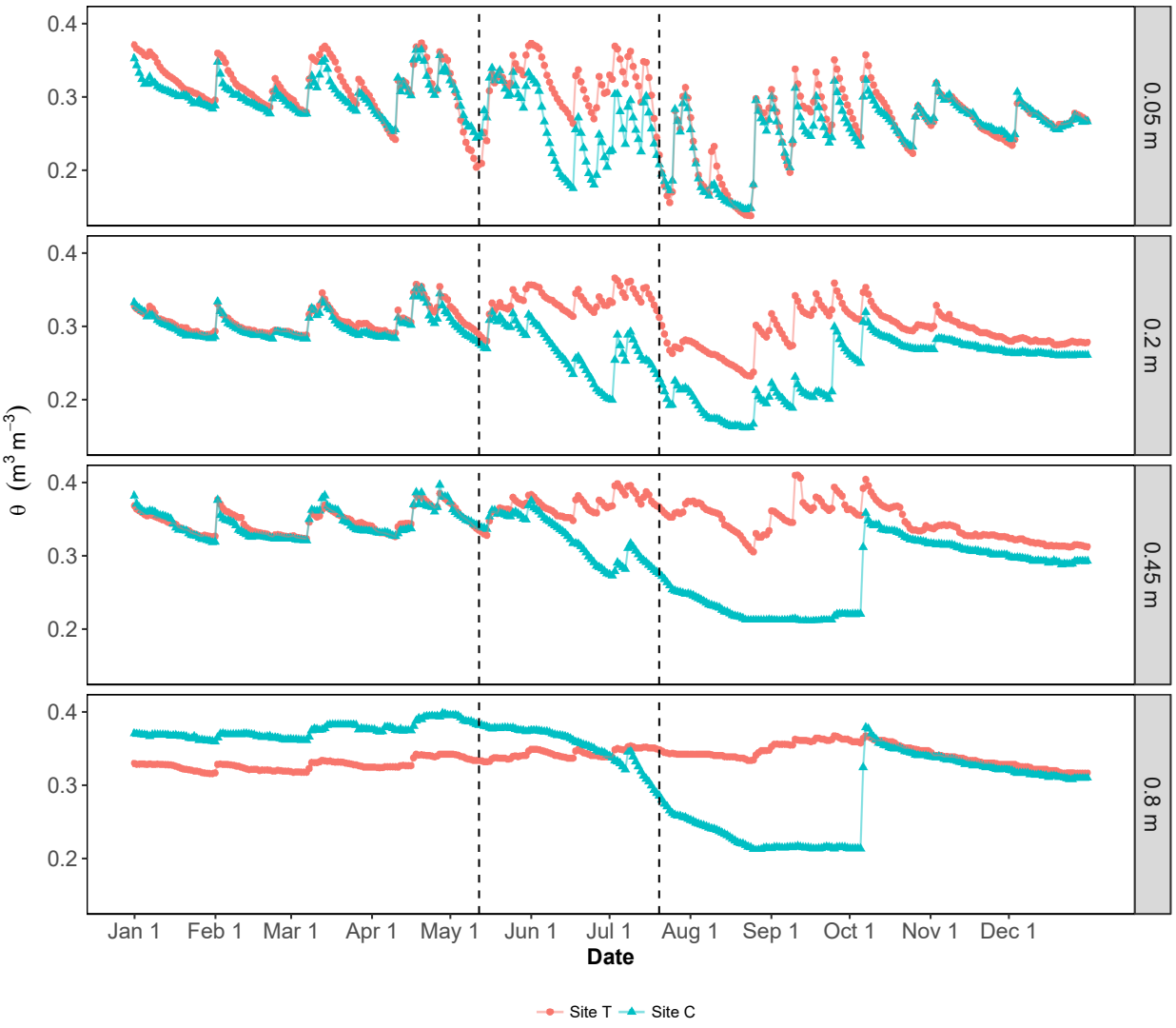

Figure 2.5: Dynamics of volumetric soil moisture (θ) across the soil profiles at the two sites as measured at four depths—0.05 m, 0.20 m, 0.45 m, and 0.80 m—representing, respectively, the soil-water dynamics for the four depth intervals 0–0.1 m, 0.1–0.3 m, 0.3–0.6 m, and 0.6–1.0 m. Each point represents the daily mean value of θ from two measuring stations within each site. Dashed lines indicate the dates of the herbicide treatment.

2.4.2 Footprint Climatology

The yearly flux-footprint climatology and contour lines (10% to 80% with an interval of 10%) show that the flux footprints of the two EC measurements do not overlap (Fig. 2.1), with the nearest separation of the outer boundaries (80% climatology lines) approximately $10\,\mathrm{m}$. The spatial

patterns of these footprints were in line with the prevailing wind directions (Fig. 2.2). The flux footprint of the EC tower of Site T was larger than its counterpart at Site C, coinciding with Site Ts comparatively higher u and lower u_*.

2.4.3 Ground Surface Heat Flux and Energy Balance

The diurnal pattern of ground surface heat flux G_0 has a greater seasonal variation due to the greater difference in the soil heat storage S_{soil} rather than the sub-surface heat flux G_s between our sites (Fig. 2.6). The difference in S_{soil} between the two sites was significant at midday in spring (March 21–June 20), summer (June 21–September 20), and winter (December 21–March 20), while diurnal peaks in the values of S_{soil} varied within narrow ranges at Site T, between 55 ± 5 $\mathrm{W\,m^{-2}}$ (at 1100 LT in spring) and 42 ± 3 $\mathrm{W\,m^{-2}}$ (at 1200 LT in summer), but varied dramatically at Site C, between 88 ± 8 $\mathrm{W\,m^{-2}}$ (at 1130 LT in spring) and 45 ± 5 $\mathrm{W\,m^{-2}}$ (at 1200 LT in autumn; September 21–December 20). Diurnal patterns of the sub-surface heat flux were subdued at both sites, and thus comparable under the dry residual vegetation at one site, and an active canopy at the other. Both sites exhibited a substantial phase lag between the soil heat storage (upper $0.08\,\mathrm{m}$ of the profile) and sub-surface heat flux (depths below $0.08\,\mathrm{m}$), but this lag was especially pronounced at Site T, where S_{soil} peaked between 1100 and 1200 LT, while the values of G_s peaked between 1430 and 1530 LT. The greater magnitudes and more marked variation in the value of S_{soil} show the importance of its role in quantifying G_0, both temporally and in magnitude.

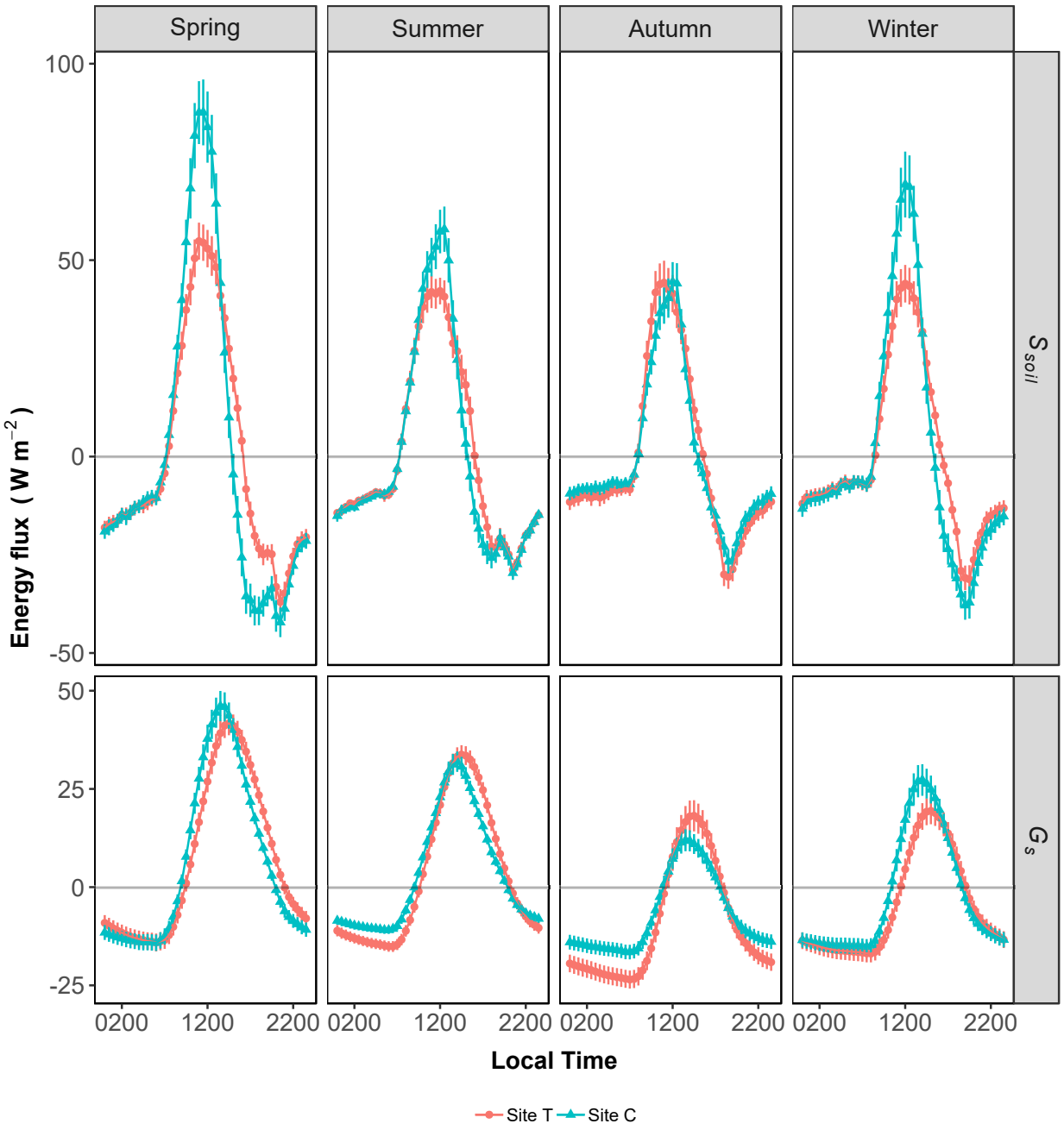

Figure 2.6: Diurnal variations of the two components of ground surface heat flux (G_0), namely S_{soil} in the upper $0.08\,\mathrm{m}$ of the soil profile, and G_s in the deeper levels, for the two sites during the four seasons. Seasons are defined according to the amount of solar radiation received: spring (March 21–June 20), summer (June 21–September 20), autumn (September 21–December 20), and winter (December 21–March 20). Each point is a 30-min ensemble mean for its corresponding flux during that entire season, with a 95% confidence interval. Negative values represent upwards diffusion of heat lost from the surface, and positive values represent downwards absorption through the ground.

Taking the value of S_{soil} into account, the slope of the energy-balance regression is 0.83 for Site T and 0.86 for Site C (Fig. 2.7), implying the measured surface turbulent fluxes are approximately 15% lower than the available energy for both sites. The monthly series of the energy-closure slopes are found to be different between the two sites (paired t-test, p-value <0.01, Table 2.1), with the energy balance typically lower, and intercepts typically higher at Site T, where wind speeds were usually greater, and the friction velocity was lower as a result of the herbicide treatment. The energy balance weakened during the growing season at Site C the control site when the photosynthesis activity and energy storage within and under the developed vegetation canopy, namely the above-ground heat storage, probably enhanced to a non-negligible amount (see Figs. 2.4b & 2.7).

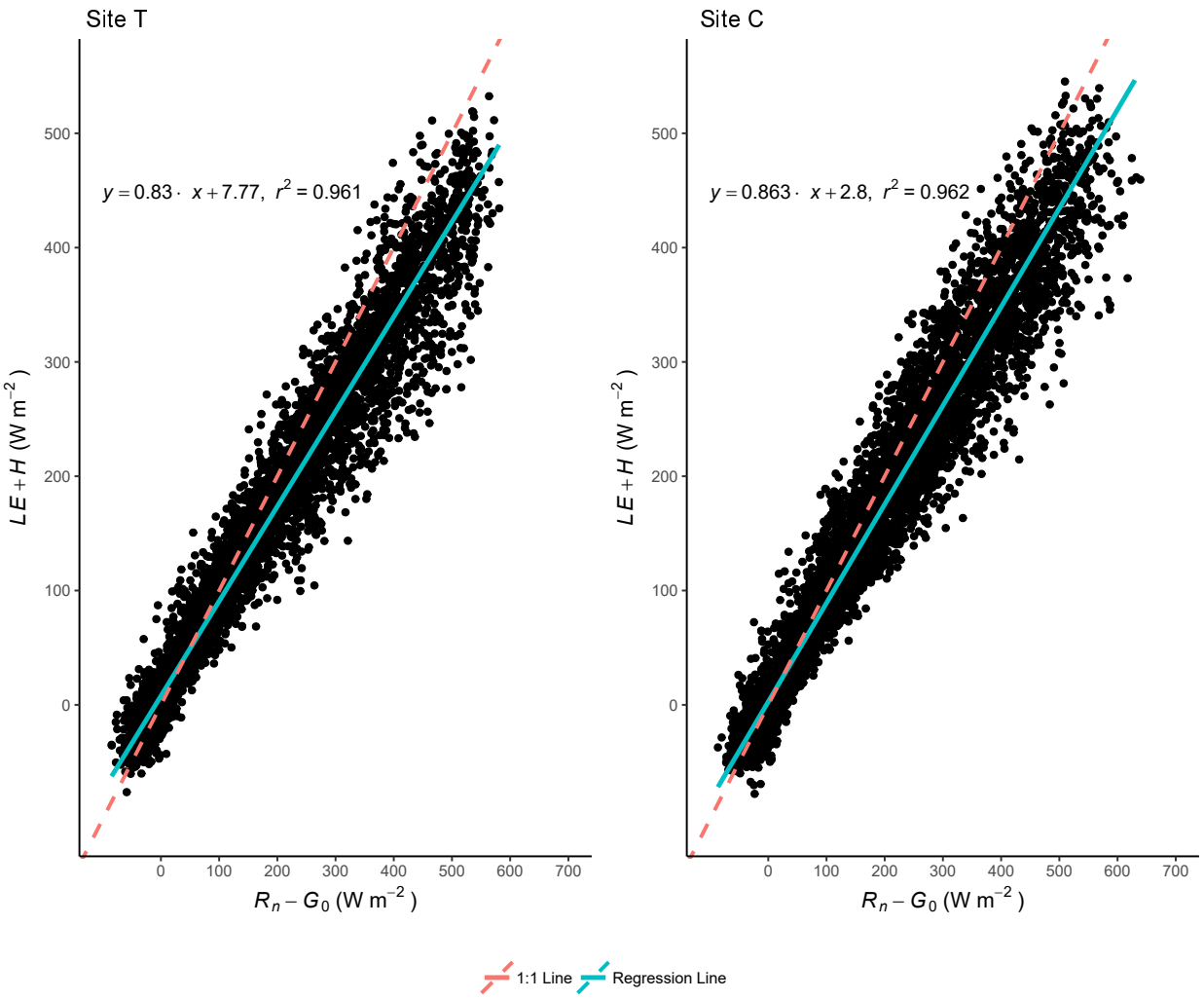

Figure 2.7: Scatter plots of the measured half-hourly series of available energy ($R_n - G_0$) versus the sum of the turbulent fluxes ($H + LE$) for the two sites. The solid line (teal) represents the best linear regression. The numbers of data points are 7026 for Site T and 9133 for Site C.

2.4.4 Energy Partitioning under Contrasting Types of Vegetation Cover

After the vegetation removal, the net radiation R_n became lower at Site T than at Site C (Fig. 2.8, summer and autumn graphics), but the timing of the diurnal peak values of R_n of the two sites is similar (1230 LT during summer and autumn, and 1300 LT during winter and spring). The diurnal patterns of the ground surface heat flux G_0 has a greater seasonal fluctuation at Site C than at Site T (Fig. 2.8), which agrees with the seasonal difference in S_{soil} between the two

Table 2.1: Monthly linear regression coefficients (slope and intercept) between the available energy ($R_n - G_0$) and surface energy fluxes ($H + LE$) for Site T and Site C.

Month	Slope		Intercept		R^2	
	Site T	Site C	Site T	Site C	Site T	Site C
Jan	0.814	0.920	2.96	3.23	0.951	0.967
Feb	0.821	0.927	3.63	-2.15	0.959	0.937
Mar	0.792	0.923	5.02	-1.00	0.943	0.940
Apr	0.820	0.861	6.75	1.49	0.952	0.942
May	0.856	0.865	6.37	2.28	0.953	0.953
Jun	0.871	0.841	16.4	0.83	0.961	0.972
Jul	0.823	0.866	14.0	4.08	0.975	0.976
Aug	0.822	0.860	13.3	2.77	0.965	0.969
Sep	0.835	0.866	11.9	2.49	0.969	0.969
Oct	0.847	0.897	7.53	2.34	0.966	0.974
Nov	0.818	0.879	8.17	3.58	0.965	0.968
Dec	0.823	0.914	3.55	5.12	0.945	0.958
Yearly	0.830	0.863	7.77	2.80	0.961	0.962

sites (Fig. 2.6). At both sites, the diurnal patterns of G_0 are mainly controlled by the diurnal patterns of S_{soil}, which in turn is mainly controlled by the diurnal patterns in the value of ΔT_s (data not shown). The generally higher midday magnitude of G_0 at Site C compared with Site T is in accordance with the contrast in the values of R_n between the two sites. When the value of S_{soil} is taken into consideration, the diurnal patterns of G_0 and R_n become largely synchronous, with phase shifts usually occurring within 30 min.

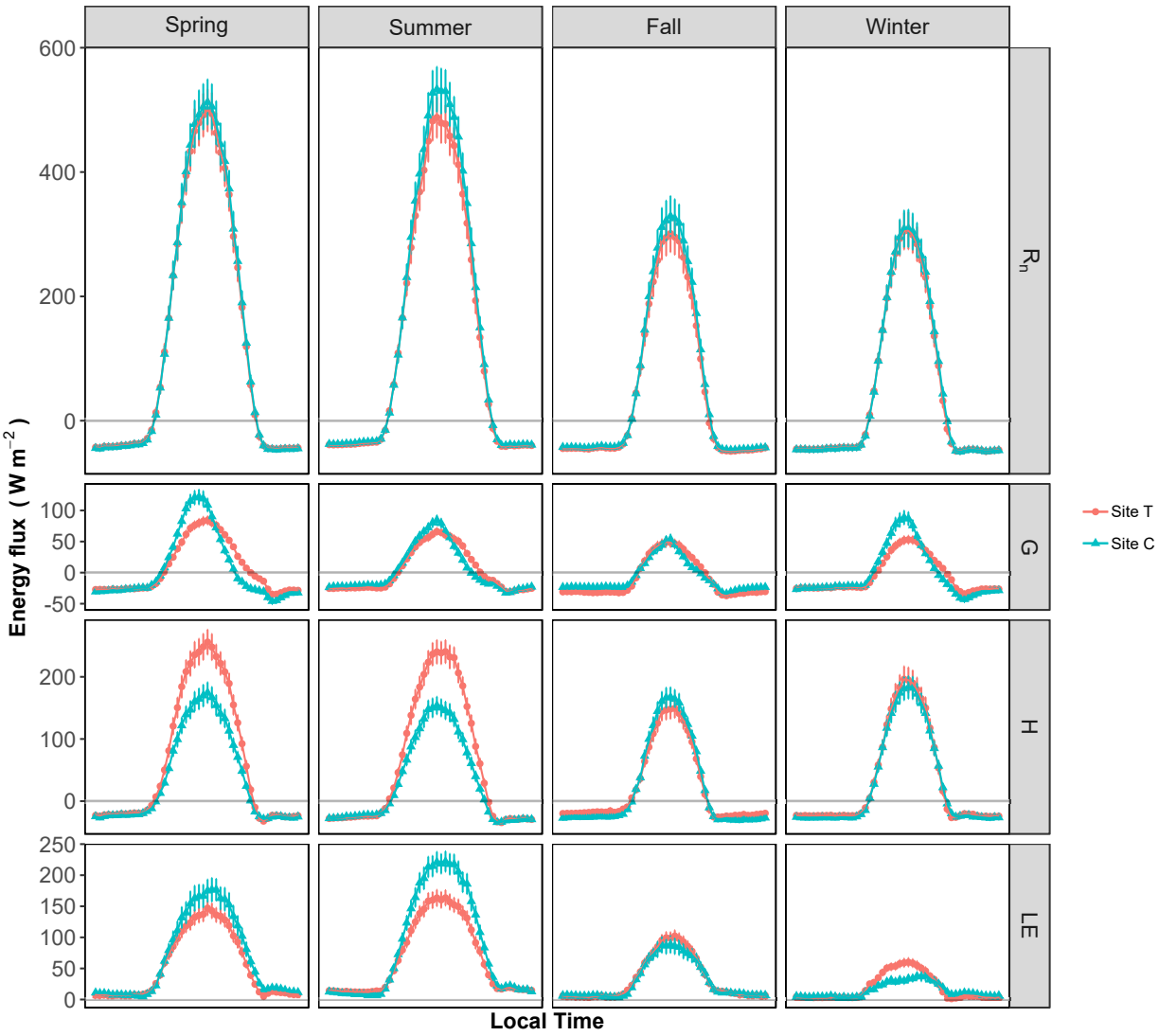

Figure 2.8: Diurnal patterns of energy partitioning for the two sites during the different seasons. Each point represents the ensemble mean value of that energy component during the season, with a 95% confidence interval. The sign of the energy fluxes (R_n and G_0) is positive when moving downwards into the ground, while that of the surface turbulent fluxes (H and LE) is positive when directed from the ground towards the atmosphere.

As shown in Fig. 2.8, the patterns of energy partitioning of the H and LE fluxes for the diurnal processes at the two sites are generally comparable in the autumn and winter (largely matching the non-growing season), but are dramatically different in spring and summer (roughly the growing season), especially during the early afternoon (1200–1400 LT) when the H is consistently higher

at Site T, whereas LE is higher at Site C. A difference in the energy partitioning at the seasonal scale is also evident in the monthly values (Fig. 2.9). During the peak growing season (June to July), average early-afternoon H and LE fluxes at Site C were 133 ± 6 and 280 ± 8 $\mathrm{W\,m^{-2}}$, respectively, and 246 ± 10 and 173 ± 5 $\mathrm{W\,m^{-2}}$, respectively, at Site T. These differences in energy partitioning are mirrored by the H and LE fluxes normalized by the available energy at the daily temporal resolution (Fig. 2.10). Thus, the increase in H that resulted from the vegetation treatment at Site T triggered a rise in the Bowen ratio (H/LE, which is a measure of energy partitioning) during the major part of the growing season.

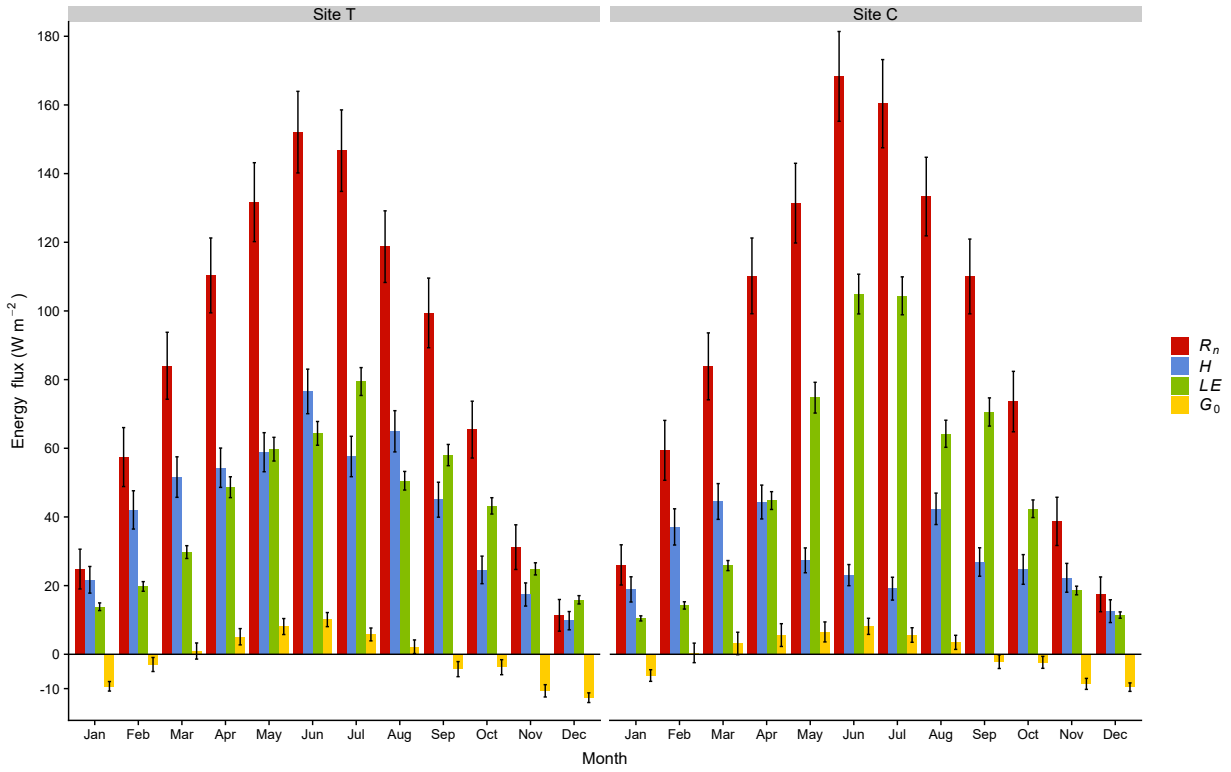

Figure 2.9: Monthly means of all energy and turbulent fluxes (R_n, H, LE, and G_0) for the two sites. The bars on each column represent the 95% confidence intervals.

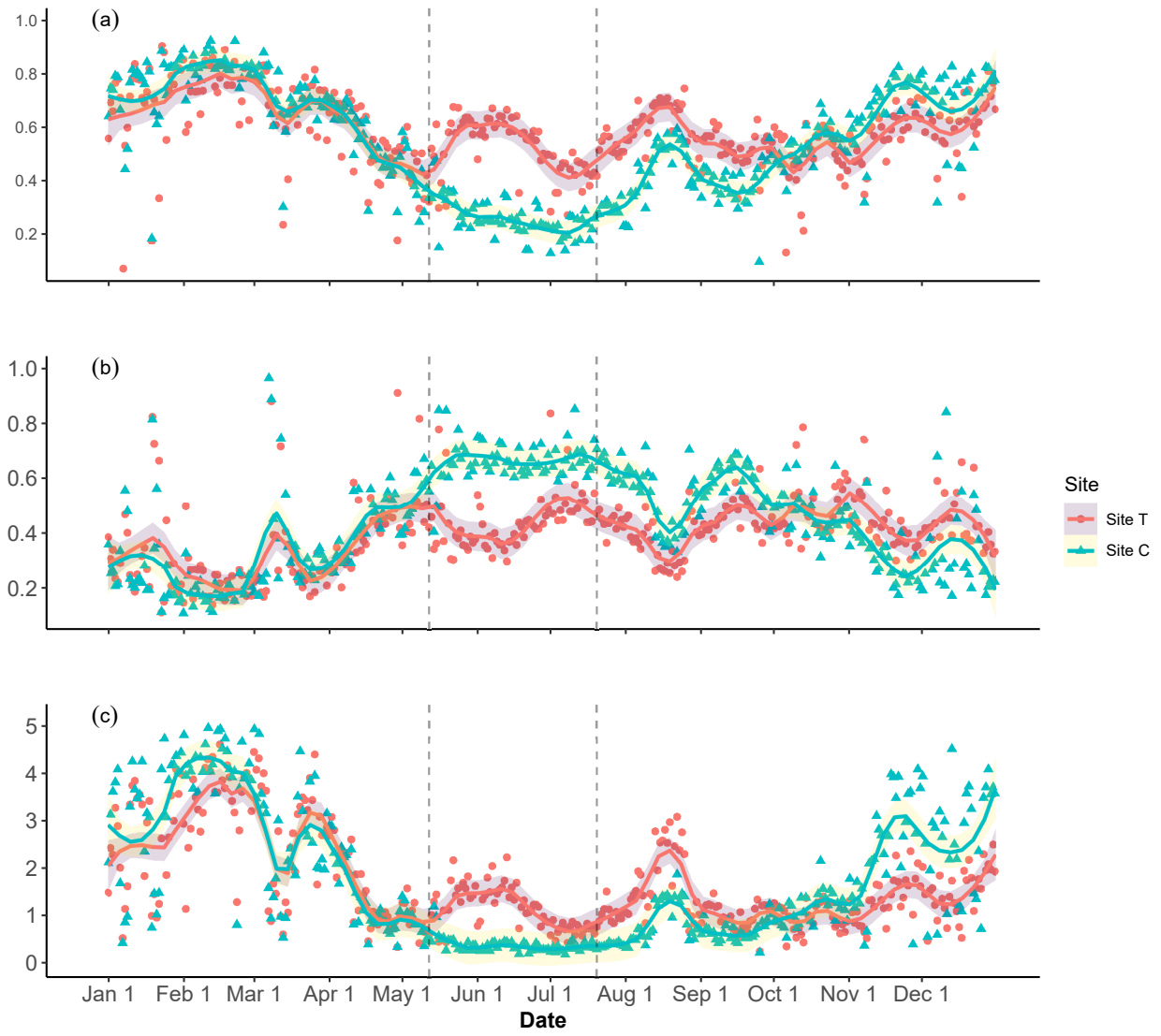

Figure 2.10: Variations in daily H (a) and LE (b) fluxes normalized by the $R_n - G_0$ and Bowen ratios (c). Each point in the normalized value and Bowen ratio represents the daytime average when the global radiation is higher than $20\,\mathrm{W\,m^{-2}}$. All three series were smoothed by a locally weighted regression (span = 0.1). The two vertical dashed lines represent the dates of herbicide application.

Together with the greater magnitude of LE, the soil water content θ at Site C is severely depleted across the profile (Figs. 2.11 & 2.5), especially within the upper $0.3\,\mathrm{m}$ ($\theta_{0.3}$) where there is large evaporation from the surface layer, as well as water loss in the lower portions through uptake by roots (transpiration). The depletion of $\theta_{0.3}$ below a critical threshold ($0.17\,\mathrm{m^3\,m^{-3}}$) at

Site C during the height of the drought in the period August 13–24 led to a suppression of plant transpiration, which in turn caused a convergence in the pattern of energy partitioning between the two sites. Namely, once the value of $\theta_{0.3}$ fell below this critical threshold, plant physiological activities became under severe drought stress, and thus the normalized latent heat flux and the Bowen ratio at Site C approached the concurrent average values at Site T (Fig. 2.10).

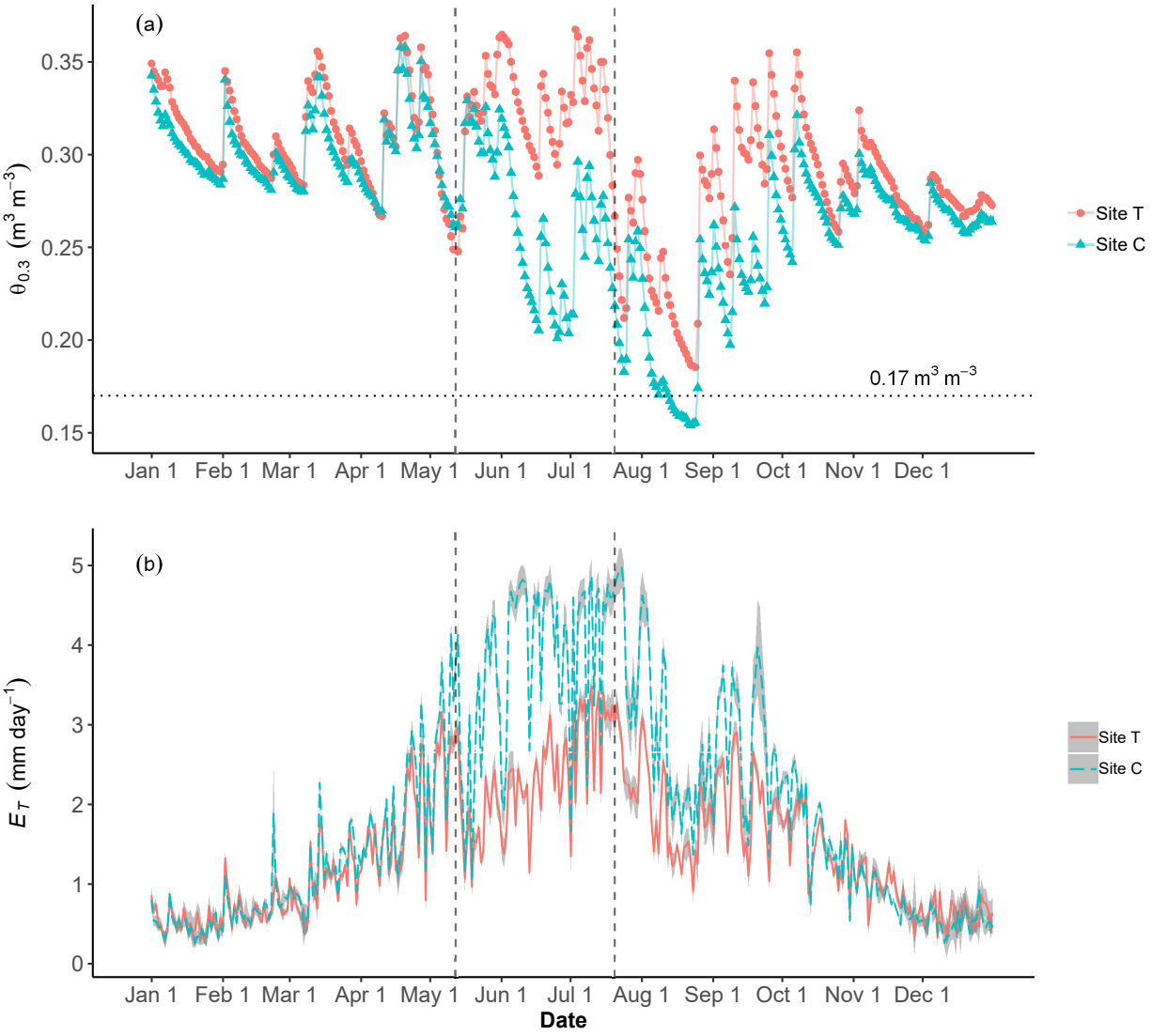

Figure 2.11: Contrasts in soil water content of the upper $0.3\,\mathrm{m}$ ($\theta_{0.3}$, a) and daily ET (b) between the two sites. The lines for the daily evapotranspiration represent sums of $30\,\mathrm{min}$ ET from either the measurements or gap-filling in that day, surrounded by the 95% confidence interval (grey shaded ribbons) derived from the uncertainty analysis in the random sampling and gap-filling. The two vertical dashed lines represent the dates of herbicide application. The horizontal dotted line represents the $\theta_{0.3}$ threshold at which a change in the pattern of energy partitioning is triggered.

2.4.5 Seasonal and Diurnal Variations in Evapotranspiration

The ET exhibits a clear seasonal pattern at both sites, attaining its maximum values during the peak growing season, and generally dropping below $1\,\mathrm{mm\,d^{-1}}$ during the winter (Fig. 2.11).

Following the vegetation treatment, the daily ET at Site T was typically much lower than at Site C, with the peak daily ET at Site T approaching $3.5\,\mathrm{mm\,d^{-1}}$ on July 10, 2016, but reaching close to $5\,\mathrm{mm\,d^{-1}}$ from mid-June to nearly the end of July at Site C. Figure 2.12 shows that the daytime ET was significantly lower at Site T than at Site C from May to September, which is particularly noticeable around midday (1200–1400 LT) during the peak growing season when ET averaged $0.11\,\mathrm{mm\ 30\ min^{-1}}$ at in Site T vs $0.18\,\mathrm{mm\ 30\ min^{-1}}$ at Site C.

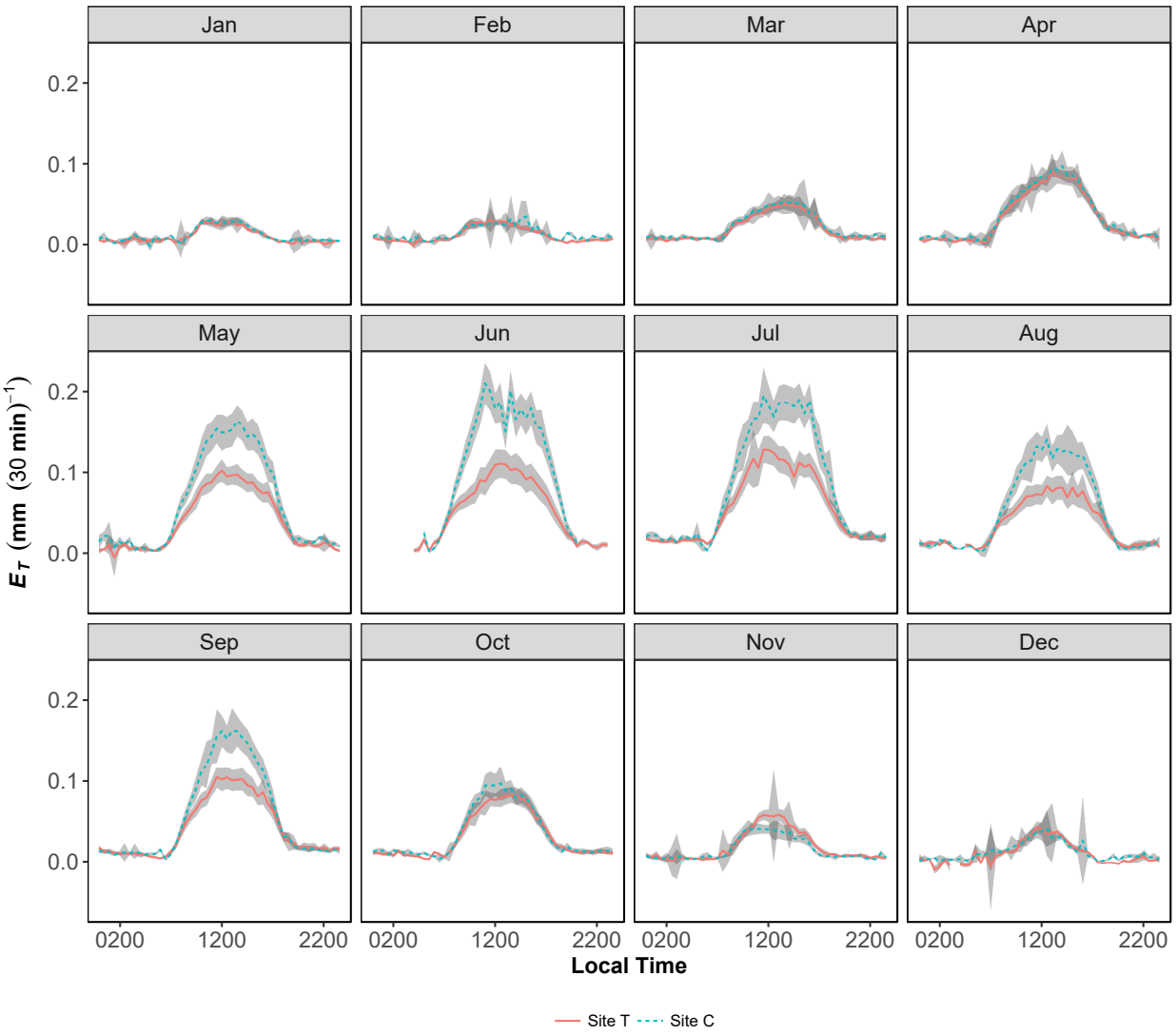

Figure 2.12: Diurnal ET during each month for the two sites. The curves represent binned ensemble means of measured ET values (without gap-filling) at that site for the entire month with the 95% confidence interval (grey shaded ribbons) for only from the uncertainty in the random sampling (the larger uncertainties reflect less data availability for those times).

The cumulative ET readings for the paired sites were similar prior to treatment before diverging substantially afterwards (Fig. 2.13). At Site T, the cumulative ET remained consistently lower than the cumulative precipitation from early March, while the cumulative ET at Site C began to exceed the cumulative precipitation on July 21, reaching 429 ± 2 mm, and remaining so until the heaviest daily rain on October 6, 2016. The yearly cumulative ET for Site C is 728 ± 3 mm, which

is about $181\,\mathrm{mm}$ higher than for Site T ($547 \pm 2\ \mathrm{mm}$), and was close to the yearly precipitation ($721\,\mathrm{mm}$). For Site T, the absence of active vegetation since early in the growing season resulted in a 25% drop in yearly ET.

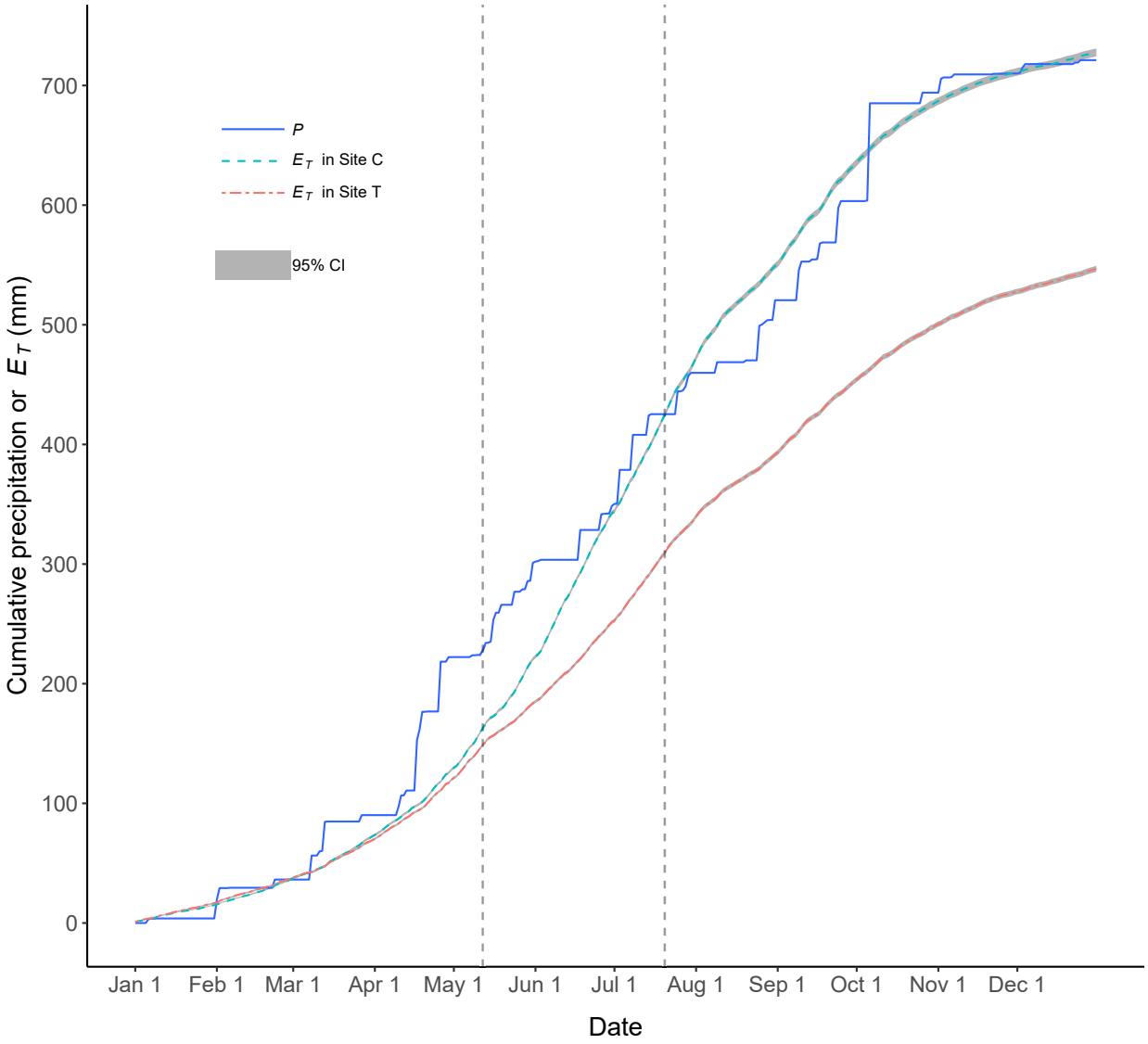

Figure 2.13: Comparison of cumulative precipitation with cumulative ET for the two sites. The two vertical dashed lines represent the dates of herbicide application. The narrow shaded areas surrounding the cumulative evapotranspiration data represent the small 95% confidence interval derived from random sampling error and gap-filling uncertainty.

2.4.6 Bulk Surface Parameters and the Vegetation Index

Differences in bulk surface parameters between the two sites reveal that different factors control the seasonal ET variations (Fig. 2.14). The aerodynamic conductance above the canopy g_a was generally lower at Site T (yearly mean of 27 ± 1 $\mathrm{mm\,s^{-1}}$) than at Site C (yearly mean of 34 ± 1 $\mathrm{mm\,s^{-1}}$), which is consistent with the higher u values and lower u_* values at Site T than at Site C (Eq. 2.6), with this difference not substantially influenced by the vegetation removal. However, the surface conductance g_s, which was similar at the two sites before the treatment, diverged substantially afterwards. From June to October, the mean values of g_s were 8 ± 1 $\mathrm{m\,s^{-1}}$ at Site T and 22 ± 2 $\mathrm{mm\,s^{-1}}$ at Site C. Except for some periods during the first half of the growing season (mainly in May and June) at Site C, the value of g_s was generally less than the value of g_a for both sites, with the result that ET were more constrained by g_s than by g_a. Consequently, during the greater part of the growing season following treatment, the decoupling factor Ω was usually lower at Site T than at Site C—especially during the peak growing season when the mean value of Ω was 0.5 and 0.8 at Site T and Site C, respectively. Thus, during the greater part of the growing season, ET at Site T was more coupled with the meteorological conditions and controlled by the abiotic factors (g_s and VPD), whereas ET at Site C was more decoupled from the near-surface atmosphere and more controlled by vegetation physiological processes, which are regulated by the R_n. However, during the height of the drought (August 13–24, with $\theta_{0.3} \leq 0.17\mathrm{m^3\,m^{-3}}$), the mean daytime value of g_s at Site C fell below $10\,\mathrm{mm\,s^{-1}}$, approaching the concurrently low levels at Site T, and the value of Ω fell below 0.5 for both sites, indicating a strong and similar coupling with the ambient atmosphere for both sites during the drought stress.

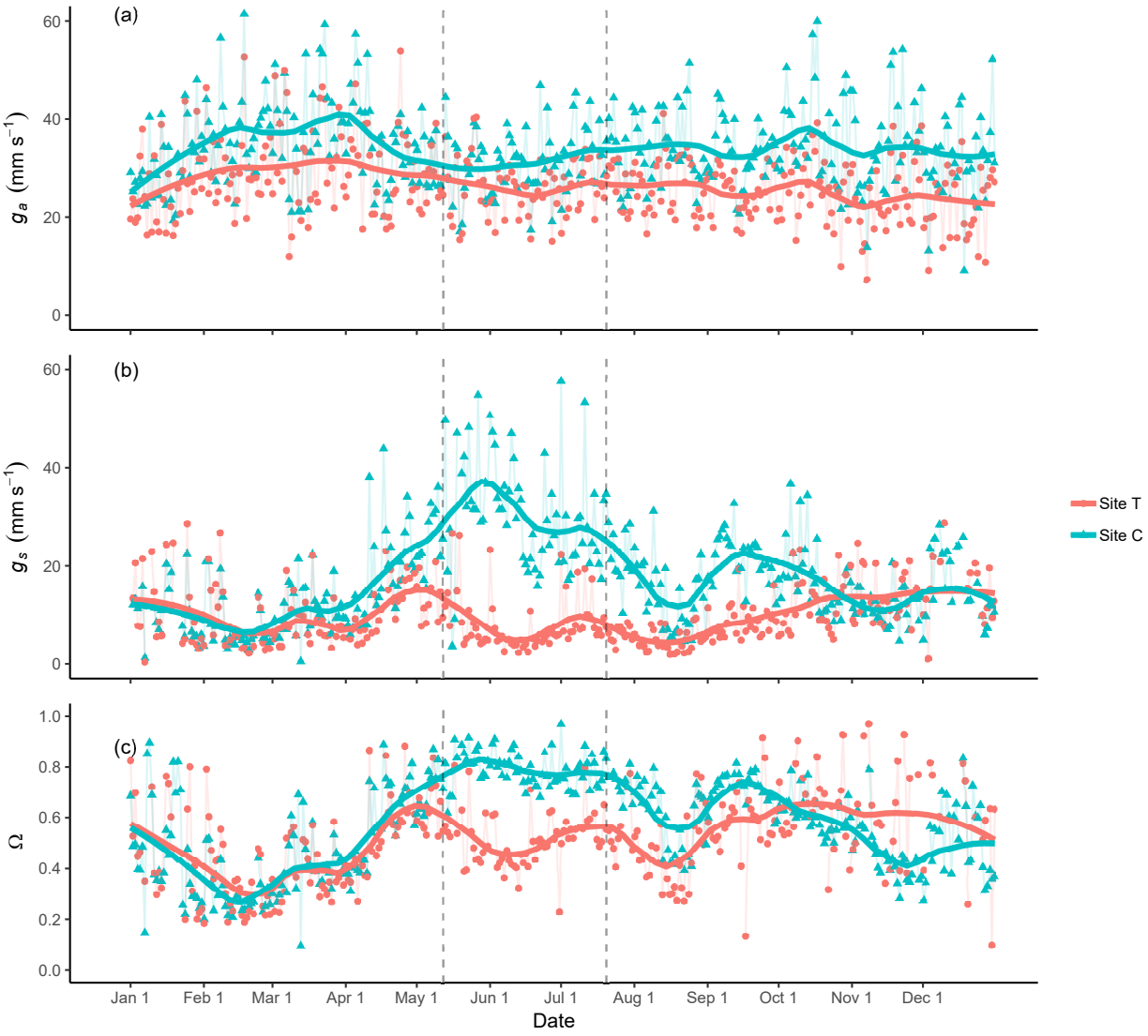

Figure 2.14: Variations in aerodynamic conductance (g_a, in a), surface conductance (g_s, in b), and the decoupling factor (Ω, in c) for the two sites. Each point represents the mean daytime (0800–1700 LT) value, and the curves are locally weighted regression regressions with a span of 0.2. The two vertical dashed lines represent the dates of herbicide application.

2.5 Discussion

2.5.1 Soil Heat Storage and Energy-Balance Closure

Because the magnitude of the soil heat storage S_{soil} increases as the vegetation height (or cover) declines [183], S_{soil} is indispensable for accurate quantification of the ground surface heat flux for

areas with low vegetation [123]. Going beyond several studies that reported the value of S_{soil} could to be as large as the sub-surface heat flux [123, 184, 130], we reveal that the magnitude of S_{soil} could be even greater than the sub-surface heat flux and could regulate the diurnal pattern of ground surface heat flux at both our tallgrass prairie sites. The range of variation (42.2 to 87.6 $\mathrm{W\,m^{-2}}$) and typical peak times (between 1130 and 1230 LT) of S_{soil} values at Site C were in reasonable agreement with those found elsewhere. For example, data from a maize crop site in south-west Oklahoma showed that mean value of S_{soil} peaks around 0900 LT at $40\,\mathrm{W\,m^{-2}}$, and decreases to $-15\,\mathrm{W\,m^{-2}}$ at around 1700 LT [177]. In the semi-arid Loess Plateau of north-west China, the value of S_{soil} ranged from 40 to 75 $\mathrm{W\,m^{-2}}$, with the peak time around 1000 LT [185], while at a desert-edge site sparsely vegetated with desert reeds, a range of 50 to 100 $\mathrm{W\,m^{-2}}$ was observed [186]. Thus, omitting the soil heat storage would result in an underestimation of the ground surface heat flux, which would lead to an overestimation of the available energy, and thereby weakening the energy-balance closure [187]. Further, ignoring the soil heat storage may cause timing errors or phase differences in the diurnal measurements, which may also reduce the energy-balance closure based on 30-min averages [183]. Another study in rice paddy fields found similar differences between sub-surface heat flux and the ground surface heat flux in terms of both the diurnal patterns and phase lags, showing an 9% increase in the slope of the energy-balance closure when the value of S_{soil} was considered [128]. A study on a semi-arid grassland in the Loess Plateau also showed that the integration of S_{soil} into the calculation of the ground surface heat flux increased the budget closure from 76% to 83% [132].

Our yearly energy-balance slopes (0.83 and 0.86) are higher than the value of 0.79 reported by a comprehensive FLUXNET evaluation comprising 22 sites and 50 site-years [131], while the values of the intercepts of 7.8 and 2.8 $\mathrm{W\,m^{-2}}$ at Site T and Site C, respectively, are comparable to the mean intercept of 3.7 ± 2.0 $\mathrm{W\,m^{-2}}$ from that study. Another study carried out on a switchgrass field in Chickasha, Oklahoma, during the growing season of 2011, found a closure ratio of 0.77 [188], but our closure ratios are better and comparable to the ratio of 0.83 from the same Chickasha site during the growing seasons of 2012 and 2013 [146]. Similar closure levels were also reported

for other grasslands [189, 190].

However, accurately determining the value of S_{soil} (and thus the value of the ground surface heat flux) at an ecosystem or field scale is problematic for the EC method as heat-flux plates are typically 0.05–0.1 m in diameter and sample only a tiny area, making it difficult to detect the spatial variability in the soil water content and soil heat storage across a site [127]. The high variations in the value of S_{soil} between our two sites exemplified this spatial heterogeneity, which may not have resulted solely from the difference in vegetation coverage. Quantification of the value of ΔT_s, which is the controlling factor in the value of S_{soil}, involves consideration of the active hydrothermal dynamics within this thin soil layer above the heat-flux plates. Many factors related to these hydrothermal processes may contribute to the spatial heterogeneity in the value of S_{soil}, including the surface-cover conditions, the ambient atmosphere, geomorphological characteristics, the soil-water dynamics, and biogeochemical characteristics. Thus, the fact that the measurements of the turbulent and soil heat fluxes are based on different footprints [154] may to some degree explain the energy imbalance at both our sites.

A dissimilar footprint is probably not the only cause for the energy imbalance, with other factors including the unmeasured advective fluxes and stationary secondary circulations due to landscape heterogeneity [123, 124, 126]. Landscape heterogeneity (engendered by the vegetation treatments) and the consistently higher wind speed at Site T may facilitate the development of strong advection and complicated circulation patterns near the ground, which is a plausible reason for the typically lower monthly closure ratios for Site T. At most of the FLUXNET sites (including those with flat terrain and low vegetation), the energy-balance closure is seldom achieved, but is achievable at homogeneous sites (such as a desert) under all conditions [124].

Photosynthesis and canopy storage are consequential factors, and should be accounted for in situations where there is a fully developed tall canopy, such as a maize field [129]. Even in situations where the canopy is typically relatively short, such as at our sites, these energy fluxes can be substantial during the height of the growing season as evidenced by the steady decrease in monthly energy-closure ratios observed at Site C during the middle of the growing season.

In summary, although consideration of the value of S_{soil} considerably increases the magnitude of G_0 and reduces the phase shift, it does not ensure complete energy-balance closure [191]. Other issues, such as footprint mismatches, landscape heterogeneity, and the canopy heat storage should also be taken into account when attempting to achieve complete energy closure.

2.5.2 Effects of Active Vegetation on Energy Partitioning

The vegetation treatment produced a divergence in the net radiation R_n between the two sites, being significantly reduced during the summer at Site T, probably because the high reflectance of the grass litter and dead biomass increases the albedo [192]. A similar decrease in the value of R_n is caused by the high albedo for an overgrazed grassland with sparse vegetation coverage [193]. During the growing season, the diurnal variation in the value of G_0 at Site C is positively skewed or peaks in advance of the value of R_n, which is in good agreement with other investigations [194, 195].

During the growing season, the dissipation pattern of available energy showed considerable differences between the two sites as a result of the vegetation treatment. Compared with Site T, the sensible heat flux at Site C is substantially subdued (owing to the shading effect of the leaves) and the latent heat flux is enhanced (because of plant transpiration fed by deeper soil moisture). Similar seasonal patterns of energy partitioning were reported for switchgrass and sorghum fields in Chickasha, Oklahoma [146]. At Site C during the peak growing season (June to July), the magnitude of the latent heat flux at midday is roughly double that of the sensible heat flux. This twofold relation was also reported for a mature switchgrass stand in southern Ontario, Canada [196]. Unlike Site T, a switch in the pattern of the energy partitioning (dominance of the sensible heat flux over the latent heat flux) occurred at Site C during the periods of March–April and October–November (coinciding with the leaf emergence and senescence; Fig. 2.9). A similar concurrence between phenological cycles and a switch in the dominance of the energy fluxes has also been observed in other grassland studies [197, 154].

The vegetation treatment at Site T also caused a substantial discrepancy between the two sites in soil water content θ across the profiles, which may alter the divergence in the patterns of energy

partitioning between the two sites. The differences in the values of $\theta_{0.3}$ were especially relevant because the highest concentration (70%–80%) of the root biomass of these grasses is distributed within the top $0.3\,\mathrm{m}$ [198]. Compared with Site T, the value of $\theta_{0.3}$ at Site C was substantially reduced during the peak growing season (Fig. 2.11), during which $\theta_{0.3}$ varied dramatically (between 0.18 and 0.32 $\mathrm{m^3\,m^{-3}}$), but remained above the critical threshold of $0.17\,\mathrm{m^3\,m^{-3}}$. At the same time, the normalized latent heat flux maintained a stable high level (between about 0.60 and 0.75, Fig. 2.10). This steady dominance of the latent heat flux ensured a consistently low Bowen ratio, without regard to the fluctuations in the soil moisture, with similar findings reported for a switchgrass stand in Canada [196], and for a temperate grassland in the northern Great Plains [154]. However, during the severe drought (August 13–24, when the value of $\theta_{0.3}$ at Site C dropped below $0.17\,\mathrm{m^3\,m^{-3}}$), the normalized latent heat flux plunged below 0.5 (between 0.33 and 0.48), approaching the low values observed at Site T for the same period. Because the permanent wilting point of surface soils (within $0.15\,\mathrm{m}$ in depth) at Site C is $0.14\,\mathrm{m^3\,m^{-3}}$ given their loam texture [199], the drought stress produced when the value of $\theta_{0.3}$ dropped below the critical threshold, and approached the wilting point, substantially suppressing the plant physiological activities. During this drought period, the sensible heat flux became the dominant flux (Fig. 2.10), which agrees with the results from the Oklahoma switchgrass field during a severe drought [188]. Similar thresholds were also reported from other studies, including $0.15\,\mathrm{m^3\,m^{-3}}$ for a California annual grassland [200], $0.14\,\mathrm{m^3\,m^{-3}}$ for a Mediterranean grassland in southern Portugal [201], and $0.12\,\mathrm{m^3\,m^{-3}}$ for a tussock grassland in New Zealand [202]. An earlier study of native tallgrass prairie in north-central Oklahoma reported that, under conditions of abundant soil moisture, the evaporative fraction (LE/R_n) was controlled by the leaf area index, but when the value of θ fell below a critical threshold, the evaporative fraction instead became controlled by the soil moisture [145]. Our study, therefore, has further quantified this critical threshold of soil moisture in the root zone of our study sites.

2.5.3 Evapotranspiration Dynamics and Soil Water Storage

The seasonal and diurnal patterns of ET were typical at both sites. Under the same cumulative precipitation ($604\,\mathrm{mm}$) during the growing season, the daily ET at Site T ranged between 0.65 and 3.5 $\mathrm{mm\,d^{-1}}$, with an accumulation of $430\,\mathrm{mm}$, and between 0.55 and 5 $\mathrm{mm\,d^{-1}}$ at Site C, with an accumulation of $613\,\mathrm{mm}$. By way of comparison, a study done in the native tallgrass prairie of north-central Oklahoma during the growing seasons of 1996–2000 [145] found comparable magnitudes of ET (3.5–5 $\mathrm{mm\,d^{-1}}$), while the study carried out on the switchgrass field in Chickasha, Oklahoma, during the growing seasons of 2011, 2012, and 2013 reported daily ET ranges of, respectively, 0.5–4.8, 1.0–6.2, and 1.0–6.7 $\mathrm{mm\,d^{-1}}$, with accumulations of 450, 653, and 740 mm under cumulative rainfall amounts of 432, 635, and $742\,\mathrm{mm}$ [188, 146]. Additionally, the instantaneous maximum at Site C ($0.25\,\mathrm{mm}$ 30 $\mathrm{min^{-1}}$) lay between those of the Chickasha site in the dry growing season of 2011 ($0.18\,\mathrm{mm}$ 30 $\mathrm{min^{-1}}$) and the wet growing season of 2013 ($0.31\,\mathrm{mm}$ 30 $\mathrm{min^{-1}}$) [188, 146]. Similar seasonal trends in ET (but lower in magnitude) were also observed at a northern Great Plains site [154] and in a switchgrass field in Pennsylvania [203].

The difference in vegetation cover after treatment brought about dramatic differences in the magnitudes of ET as well as differences in soil-moisture variability between the two sites, implying that the presence of active vegetation strongly influences ET, and showing the importance of deep soil moisture for plant transpiration. Cumulative ET exceeded cumulative precipitation at Site C during the peak growing season (July 21), which was also observed in the Chickasha switchgrass site in two of the three years [188]. Then, with the arrival of the drought, the grasses at Site C were no longer able to reliably access deep soil water, with the bottom soil layer (0.8-m depth) reaching a stable state of depletion between late August and early October (Fig. 2.5). Clearly, the soil water stored and accumulated prior to the growing season served as an important reservoir for meeting peak evapotranspiration demands during the growing season, as was also reported in other studies [204, 205]. Once the stored soil water had been exhausted, ET became more dependent on precipitation patterns. Because the magnitude of ET, and thus the productivity of the ecosystem, are strongly influenced by precipitation patterns and canopy development [146], extreme hydro-

logical events predicted by climate-change scenarios and/or woody plant encroachment threaten the sustainability of this endangered tallgrass prairie [206, 207, 115].

2.5.4 Environmental and Biological Controls on Surface Conductance

Variations in daily ET correspond closely to those of the surface conductance g_s (Figs. 2.11 & 2.14), which is more dependent on the soil conductance at Site T, and is thus controlled by the near-surface soil moisture. As shown at Site C, with wet soils, the initial leaf expansion early in the growing season could have contributed to an increase in the value of g_s [119]. Leaf expansion and the reliable access to deep soil moisture at Site C maintained a greater value of the $NDVI$ and higher g_s until the end of May, consistent with that observed in the steppe ecosystems of Inner Mongolia, China [208]. After complete leaf expansion, the value of g_s becomes controlled more by the environmental conditions [154, 119]. For example, at Site C, a lower soil moisture and a higher vapor pressure deficit during the two dry intervals in June and August caused decreases in g_s, but of a magnitude greater than the values reported (10–25 $\mathrm{mm\,s^{-1}}$) in tallgrass prairie [209], which is possibly due to the wetter soils and consequently higher $NDVI$ during late May and early June at our sites.

The seasonal fluctuation of the decoupling factor Ω above and below 0.5 at Site C was also reported for the steppe ecosystems in Inner Mongolia [208], as well as for the annual grassland in California [210]. From mid-May to late August, the value of Ω at Site C gradually declined in response to the seasonal leaf development, the reductions in soil moisture, and an increase in the vapor pressure deficit, with similar trends reported by others [211, 154]. Furthermore, in the same way as for the trends in the energy partitioning and the normalized latent heat flux, the trends in the values of g_s and Ω are affected by the value of the threshold of the soil-water content $\theta_{0.3}$ ($0.17\,\mathrm{m^3\,m^{-3}}$), which determines the controlling factors for ET flux. Above this threshold, differences in ET between the two sites are mainly explained by the differences in vegetation cover, whereas they are more explainable by differences in g_s and the vapor pressure deficit below the threshold.

2.6 Summary and Conclusions

To improve understanding of the effect of active vegetation on the energy balance, soil-water dynamics, and the water–vapor exchange between the surface and atmosphere, one year of observations of the turbulent fluxes and evapotranspiration were collected within two collocated tallgrass prairie sites having contrasting vegetation cover, including a site treated with herbicide spraying and mowing, and a control site left undisturbed. One striking finding of our measurements is the greater importance of the soil heat storage above the heat-flux plates (set at $0.08\,\mathrm{m}$ below the ground) than the sub-surface heat flux for quantifying ground surface heat flux, both temporally and in magnitude. Though integration of the soil heat storage is of major importance in calculating the magnitude and temporal phase of the ground surface heat flux for both our sites, the soil heat storage is also highly variable and difficult to quantify because of the active hydro-thermal processes within the thin soil layer above the heat-flux plates. The problem of the energy-balance closure at short time scales remains a challenge, and the achievement of an improved closure requires further work on the spatial extrapolation of the soil heat storage, as well as taking into account the error sources due to landscape heterogeneity.

During the growing season, following the removal of active vegetation, the seasonal and diurnal patterns of energy partitioning at the treated site diverged dramatically from those at the control site where the vegetation remained intact. The increase in albedo after the vegetation treatment at the treated site caused a decrease in the net radiation, while the shading effect of the vegetation canopy substantially reduced the magnitude of the sensible heat flux at the control site, with the greater plant transpiration (fed by soil moisture in the root zone) leading to the increase and eventual dominance of the latent heat flux. However, during the severe dry spell in August, the soil water content in the root zone at the control site was depleted below a critical threshold ($0.17\,\mathrm{m^3\,m^{-3}}$), resulting in a drought stress, which suppressed plant physiological activities, and brought about a convergence in the energy-partitioning patterns between the two sites.

As for the energy partitioning, the time series of the evapotranspiration flux at the paired sites were similar prior to the treatment, but diverged afterwards, with different meteorological and bio-

logical controlling factors coming into play. The active vegetation and higher surface conductance at the control site led to higher rates of evapotranspiration during the early growing season, when net radiation was the controlling factor. With the gradual depletion of soil moisture to below the critical threshold, the vegetation underwent drought suppression, substantially reducing the latent heat flux and evapotranspiration, so that the vapor pressure deficit and surface conductance became the constraining factors. Thus, the canopy growth and soil water availability are two crucial factors in modulating the energy partitioning, surface conductance, and evapotranspiration. Clearly, any land-cover change or vegetation-management action that alters these two factors, such as woody plant encroachment, may significantly alter the energy and water budgets in the endangered tall-grass prairie.

3. ISOTOPIC PARTITIONING OF EVAPOTRANSPIRATION IN A MESIC GRASSLAND DURING TWO WETTING—DRYING EPISODES

3.1 Introduction

The tallgrass prairie in the Great Plains of North America is an important but endangered ecosystem. This mesic grassland are characterized with high biodiversity [212, 213], and is central to agronomical development and biodiversity conservation [214]. As a result of historical agricultural conversion [114] and recent woody plant encroachment [117, 215, 116], tallgrass prairie is now designated as an endangered ecosystem. Understanding the ecohydrologic processes is fundamental for evaluating the ecophysiological properties and sustainability of this endangered ecosystem under land use/cover change and climate change [216, 217].

A clear understanding of ecohydrologic processes in water-limited ecosystems demands accurate quantification of evapotranspiration (ET) and its partitioning [19, 6, 7]. Evapotranspiration is the largest water-loss flux in tallgrass prairie [116, 218, 219]. The bulk ET flux consists of soil evaporation (E) within the soil-atmosphere continuum, plant transpiration (T) along the soil-plant-atmosphere continuum, and direct evaporation of water intercepted within the atmosphere by the plant canopy (I). These three components differ in their diffusive pathways, temporal dynamics, and water use implications [220]. Because biological water use is inexorably coupled with ecosystem productivity [221], ET partitioning is critical for quantifying biological water demand [7] and water-use efficiency [62], thus contains important implication for predicting ecosystem functioning and sustainability in the context of changing environment [222]. The results of ET partitioning are usually expressed as the ratio T/ET, representing the role of plant physiological processes in the hydrologic cycle.

Soil water availability, as a key link between hydrologic and ecological processes, strongly controls the dynamics of ET partitioning in water-limited ecosystems. Recharged by infiltrated precipitation, soil water supplies both E and T flux, with E depletes soil water in the upper layer

while T withdraw water across the active rooting zone [223]. The affect of total precipitation on T/ET was found not obvious over annual or growing-season scale [224, 225, 226, 227, 28]. Besides long-term (seasonal, annual, and interannual) variation, soil moisture varies over short-term (sub-daily, daily, weekly) due to high stochastic precipitation [7, 228] and strong atmospheric water demand. Thus ET partitioning during these dynamic wetting and drying episodes following individual water pulses warrants more attention for a mechanistic understanding of water diffusion from terrestrial ecosystems to atmosphere. A few short-term studies have investigated ET partitioning in water-limited regions—*e.g.* grasslands [49, 47] and winter wheat [20] following irrigation. But to our knowledge, no such study has been carried out in the native tallgrass prairie grassland.

Measuring E and T fluxes separately is methodologically challenging [11]. For this reason, the isotopic two-source mixing model, which is based on the fact that the isotopic composition of soil-evaporation water is distinct from that of plant-transpired water, has become an indispensable tool for ET partitioning [19, 229, 79, 88]. Because one isotope is sufficient for solving the two-source mixing model, most studies on ET partitioning have used only one isotope: either δ^2H [47, 8, 230, 49] or δ^{18}O [106, 52, 55, 50, 88]. Only a few studies have presented results based on both isotopes [48, 51, 12]. In addition, the criteria for selecting one isotope over the other (*e.g.* the applicability and uncertainties associated with each) have not been thoroughly investigated and evaluated.

The overarching question of this study is, how the shallow soil moisture, recharged by precipitation events, return to the atmosphere via different pathways? Using the isotopic approach with both δ^2H and δ^{18}O, we investigated ET partitioning during two drying episodes following precipitation pulses. Our objectives are

- to compare the performance of δ^2H with that of δ^{18}O as a basis for isotopic ET partitioning;
- to determine the pattern of daily T/ET during the two drying episodes;
- to investigate the effects on the temporal pattern of ET partitioning of (a) soil water avail-

ability at different depths and (b) atmospheric processes.

3.2 Materials and Methods

Our study consisted of two intensive field campaigns at a grassland site that is part of the tallgrass prairie ecosystem. An eddy covariance (EC) system, coupled with various biometeorological sensors, was set up to measure the bulk ET flux, atmospheric processes, and soil hydrothermal properties. In close proximity to the EC system, we also sampled waters from various ecohydrologic pools for isotopic analysis. We assumed the same contributing footprint for the flux turbulence measurement as for the isotopic sampling of atmospheric water vapor. All the measurements were recorded in local time (LT = UTC -6 h), disregarding daylight saving time. All isotopic data were reported in δ-notation as per mil units (‰), namely, as concentration ratios related to the Vienna Standard Mean Ocean Water (VSMOW).

3.2.1 Study site

This study was conducted at the Range Research Station ($36°3'24.6''$N,$97°11'28.3''$W, elevation about $330\,\mathrm{m}$ above sea level) of Oklahoma State University, located in north-central Oklahoma, USA (Fig. 3.1). Long-term climate data (1997–2016) from the nearby Marena weather station ($1.9\,\mathrm{km}$ from our study site) shows a subhumid climate, with an average air temperature of 15.63 ± 0.83 °C (mean ± standard deviation; all mean values are expressed this way unless otherwise specified) and mean annual precipitation of 875 ± 206 mm.

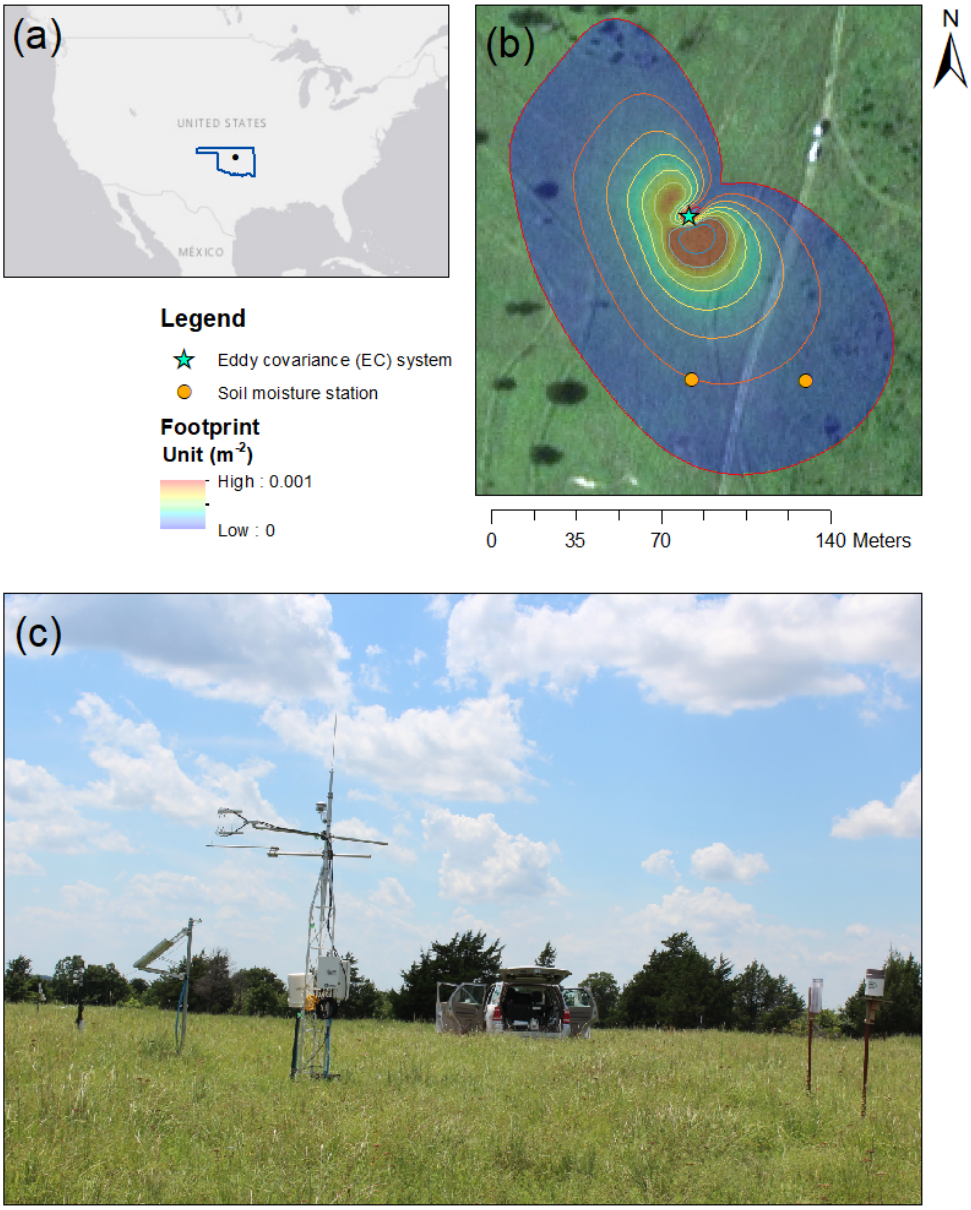

Figure 3.1: (a) Location of study site in central Oklahoma; (b) map of contributing footprint for flux turbulence measurements (from [218]; reprinted with permission); (c) 3- m tower equipped with the eddy covariance system and *in situ* sampling of water vapor using laser spectrometer (placed in the vehicle).

The terrain is mostly flat, with slopes ranging from 1% to 8%, and the soil type is a mosaic of Coyle loam and Stephenville–Darnell complex (https://websoilsurvey.sc.egov.usda.gov/). Our

analysis showed a loamy soil texture for the top 15-cm layer at our site. The grassland is dominated by perennial, warm-season (C4) grasses, including little bluestem (*Schizachyrium scoparium* [Michx.] Nash), big bluestem (*Andropogon gerardii* Vitman), Indiangrass (*Sorghastrum nutans* [L.] Nash), switchgrass (*Panicum virgatum* L.), and tall dropseed (*Sporobolus asper* [Michx.] Kunth) [156].

3.2.2 Micro–meteorological measurements

An eddy covariance system with a standard suite of biometeorological sensors was installed to measure the energy and mass exchange between the ground surface and atmosphere (Fig. 3.1). An integrated CO_2 and H_2O open-path gas analyzer and a three-dimensional sonic anemometer (EC100, IRGASON, Campbell Scientific Inc., Logan, Utah) was mounted $3\,\mathrm{m}$ above the ground for high–frequency measurement on turbulence fluxes. Low–frequency measurements include net radiation (R_n), air temperature (T_{air}), and relative humidity (h_{air}) at this height. The average soil temperature (T_{soil}) for the layer above $8\,\mathrm{cm}$ was measured with an averaging soil thermocouple (TCAV, Campbell Scientific Inc., Logan, Utah). Above-canopy precipitation (P) was also recorded. Detailed information on the configuration of these measurement devices and on data processing are described in Chapter 2.

In close proximity to the EC tower, an array of additional biometeorological sensors were installed on a steel post: a photo-synthetically active radiation (PAR) sensor (model QSO-S, Decagon Devices Inc., Pullman, WA) for measuring photosynthetic photon flux density ($PPFD$) above the plant canopy ($\mathrm{mmol\,m^{-2}\,s^{-1}}$ at approximately 1.5 m); a pair of spectral reflectance sensors (SRS, Decagon Devices Inc., Pullman, WA) for measuring the Normalized Difference Vegetation Index (NDVI); and a leaf wetness sensor (model LWS, Decagon Devices Inc., Pullman, WA), positioned $30\,\mathrm{cm}$ above the leaf surface and at an angle of $45°$ to the horizontal. Data from these sensors were stored in a datalogger (EM50, Decagon Devices Inc., Pullman, WA) with a frequency of $5\,\mathrm{min}$), from which 30-min averages were subsequently calculated. In addition, the leaf area index (LAI) was recorded with a line ceptometer (AccuPAR LP-80, Decagon Devices Inc., Pullman, WA) along three transects under direct solar radiation (July 29, 2016).

3.2.3 Soil moisture dynamics and soil hydraulic parameters

Two soil-moisture stations were established within the footprint of the eddy covariance tower (Fig. 3.1b) to measure the volumetric soil water content (θ_{soil}). Probes (ECH_2O EC-5, Decagon, Pullman, WA) were inserted at depths of 5, 20, 45, and 80 cm for four depth intervals across the profile: 010 cm, 10–30 cm, 30–60 cm, and 60–100 cm (Fig. 1). For each depth interval, we calculated daily changes in soil water storage (ΔS_i, $\mathrm{mm\,d^{-1}}$) as follows:

$$\Delta S_i = \int \Delta\theta_i \mathrm{d}z_i = \Delta\theta_i \cdot z_i, \tag{3.1}$$

where, for layer i, $\Delta\theta_i$ is the variation in θ, and z_i is depth for each interval.

Soil samples were collected from locations the soil moisture stations with coil from three depth intervals (0–5 cm, 5–10 cm, and 10–15 cm) for analysis of soil texture and hydraulic conductivity (such as θ_{res} and θ_{sat}).

3.2.4 Isotopic sampling

During the tallgrass prairie peak growing season, we carried out two intensive field campaigns following precipitation events. Isotopic sampling was done at two-day intervals during Campaign 1 (June 4, 2016 —June 12, 2016), and at daily intervals for Campaign 2 (June 27, 2016 —June 30, 2016). Each sampling session, which lasted throughout most of the daylight hours, consisted of sampling waters of different ecohydrologic pools (atmospheric vapor in the ecosystem boundary layer, bulk leaf and root xylems of grasses, and shallow soil layers) for analysis. The only exceptions wer June 4, 2016 and June 27, 2016, when for logistic reasons measurements began at 1:30pm.

3.2.4.1 Sampling of atmospheric water vapor

To determine the isotopic composition of atmospheric water vapor (δ_V), we employed an *in situ* high temporal-temporal-resolution (about 0.13 Hz) sampling system (Fig. 3.2). Air samples were continuously drawn off (by means of Gelman 1-$\mu\mathrm{m}$ filters, part # 9967-008, LI-COR, Nebraska)

through the system's three inlets, which were located at heights of $1\,\mathrm{m}$, $2\,\mathrm{m}$, and $3\,\mathrm{m}$ on the EC mast. The system uses a computer-controlled, multiport rotary valve (EMT2SC10MWE, VICI, Houston, Texas) configured to draw an air sample into the measuring system from each of the three inlets in turn, while air from all other two inlets was pumped out as mixed exhaust via the common outlet. This bypass configuration was designed to ensure the "freshness" of the air samples from all inlets. A diaphragm pump (part #286-04198, LI-COR, Lincoln, Nebraska) was employed to remove the mixed exhaust at a flow rate of < $3.5\,\mathrm{L\,min^{-1}}$. Next, each selected air sample were routed to the sampling system for $9\,\mathrm{min}$. During switch between two heights, air samples from a desiccant column was interposed for $1\,\mathrm{min}$ as separation signal to label air samples from different heights. Thus, each three-level sampling cycle took $30\,\mathrm{min}$, corresponding to the 30-min cycle of ET data output from the eddy covariance system.

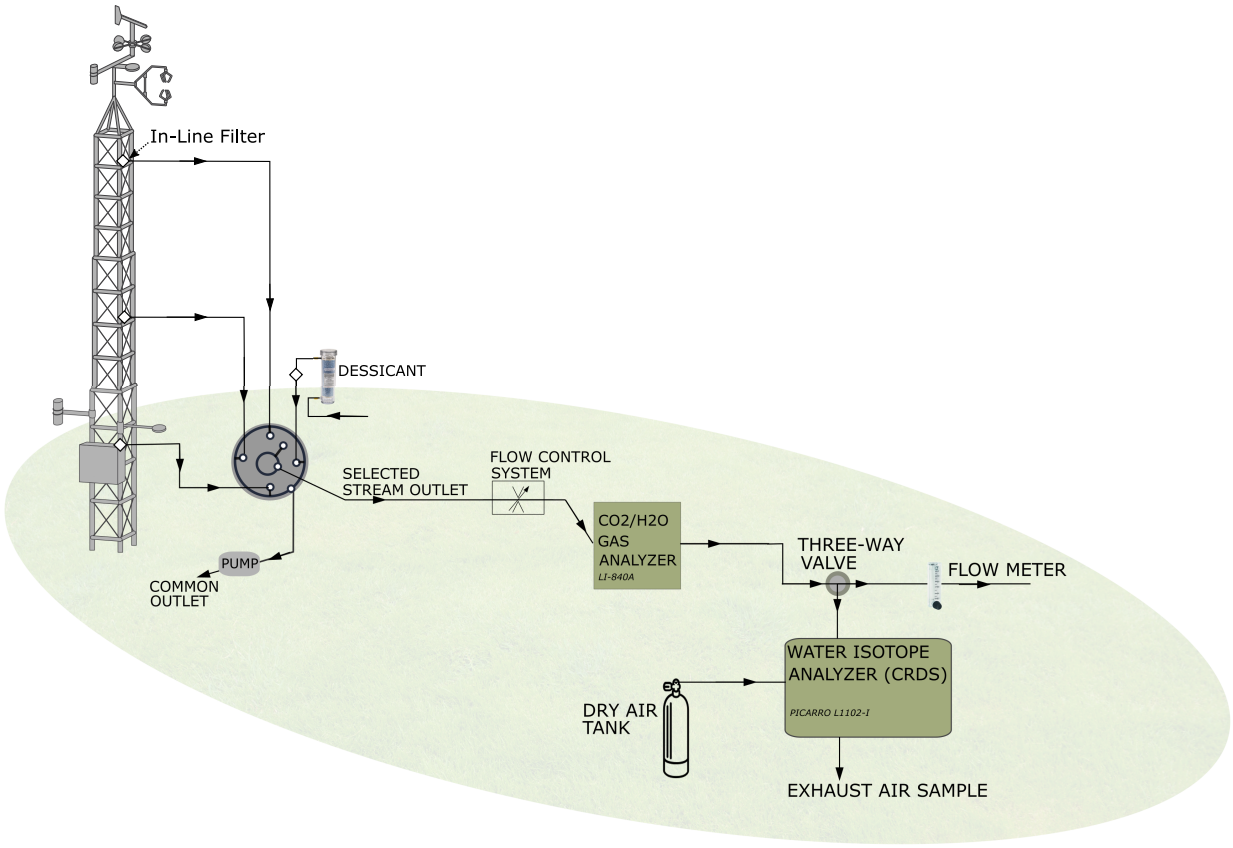

Figure 3.2: Schematic of the field set-up for measuring the isotopic composition of atmospheric water vapor, including automatic valve switching sources of water vapor from different heights, water vapor concentration analyzer used for calibration, and the laser spectrometer. The three inlets for this sampling system is positioned at the eddy covariance mast.

Each selected air sample was then drawn through a flow control unit (LI-670, LI-COR, Lincoln, Nebraska) to an infrared gas analyzer (Li840A, LI-COR, Lincoln, Nebraska). The air sample was then split via a three-way valve and fed into the water isotope analyzer—an infrared wavelength-scanned cavity ring-down spectroscopy (CRDS) (L1102-i, WS-CRDS, Picarro Inc., Santa Clara, California) at a rate of $<0.4\,\mathrm{L\,min^{-1}}$ at one standard atmosphere.

High-density polytetrafluoroethylene (PTFE) tubing (1/8-in outer diameter, 1/16-in inner diameter) was used for this sampling system, because of its minimal memory effect [231] and its high thermal stability. To minimize wind distortion for the eddy covariance measurements, the

sampling system was placed about $8\,\mathrm{m}$ downwind along the prevailing wind direction (Fig. 3.1). Each sampling day, after completing δ_V measurement, we calibrated the WS-CRDS analyzer with the evaporator using two liquid working standards bracketing the range of the obtained δ_V values. The purge carrier gas used in calibration of the laser spectrometer was supplied by a high-pressure, zero-air gas cylinder.

The laser spectrometer measured the mixing ratio (w in $\mathrm{mmol\,mol^{-1}}$) and δ_V of atmospheric water vapor. We selected the middle 6-min data from 10-min interval for each height because the w signal reached high stability in two minutes after the switch from one inlet height to the next. The w measurement from the CRDS analyzer was crosschecked and calibrated by the parallel results of the online infrared gas analyzer. The δ_V data were corrected and calibrated in four steps: (1) outliers having values two standard or more from mean values (account for $\approx 8.5\%$)) were removed for each 30-min interval; (2) correction for vapor concentration effects [232]; (3) correction for instrument drift; and (4) standardization to the international VSMOW–Standard Light Antarctic Precipitation (SLAP) scale. For the repeated measurement of working standards, the drift was less than 5 ‰ and 0.5 ‰ for δ^2H and δ^{18}O, respectively, and the analytical uncertainty (standard deviation) was less than 1.74 ‰ and 0.17 ‰ for δ^2H and δ^{18}O, respectively.

3.2.4.2 Sampling of water in surface soil, vegetation, and precipitation

During the two *in situ* sampling campaigns, we collected soil and plant samples three times each day (morning, noon, and afternoon) for subsequent extraction of water via cryogenic vacuum distillation. Using a shovel, we collected soil sample from the 15–cm depth, because in loamy soils, this depth interval usually best reflects the effect of bare-soil evaporation [233]. One study in temperate grassland found that $15\,\mathrm{cm}$ is also a reasonable sampling depth for δ_E [50]. To better capture the δ_{soil} at the evaporation front, the considerably dried upper few centimeters of soil (if present) were excluded from the samples. In addition, from areas in close proximity to the sampled soils, we collected samples (randomly selected) of the dominant grasses—upper root crowns and whole leaves from the upper canopy. We took samples of the thick, fleshy root crowns because this plant tissue is the least variable and best represents isotopic values of a well-mixed root water

uptake from different depths [76, 234]. We did not differentiate between grass species because there is no difference in the isotopic composition of the plant-root xylem water (δ_X) [235] and no complementary water use [236] among the major specifies. Finally, along with the bulk leaf sampling, we used an infrared laser thermometer to manually measure the temperature of the leaf surface facing sunlit.

All soil and plant samples were quickly transferred into gas-tight, screw-capped 12–mL glass vials (Fisherbrand, catalog No. 14-955-310, Pittsburgh, PA), wrapped with Parafilm®, and stored in a dark, cool box in the field until they could be transferred to a laboratory refrigerator ($4\,^{\circ}\mathrm{C}$) to await vacuum extraction. Because of the large number of samples and the laborious process of cryogenic distillation, we did not collect replicates for soil and plant samples.

In addition to these intensive field campaigns, throughout 2016 we collected precipitation samples following rainfall events at the campus of Oklahoma State University ($11\,\mathrm{km}$ from the study site).

3.2.4.3 Analysis of water samples

Cryogenic vacuum distillation [237, 238] was used to extract water from the plant and soil samples, at the Stable Isotopes for Biosphere Science Laboratory at Texas A&M University. The soil and plant samples were heated under vacuum (< 0.04 hPa) with water baths of 90°C–100°C. The water vapor from the sample matrix was condensed and collected at the other end immersed in a cryogenic liquid nitrogen cold trap. Any extracted water with a noticeable smell or cloudy appearance was filtered through a 0.22–$\mu\mathrm{m}$ filter (Catalog No.09-720-002, Fisherbrand, Fisher Scientific, Pittsburg, PA). The condensed water was thawed and quickly transferred into a 2–mLvial, which was sealed with minimal air in the headspace and stored at 4 $^{\circ}\mathrm{C}$ before isotopic analysis. Within 2 weeks after storage, isotopic analysis was carried out with a mass spectrometry system, consisting of a high-temperature reactor (Temperature Conversion/Elemental Analyzer) coupled on-line to an isotope ratio mass spectrometer (Delta VTM IRMS) via a Conflo IV interface(all components from Thermo Fisher Scientific, Bremen, Germany). The analyzed results from this mass spectrometric system were considered not affected by organic contaminants, and this spectral contamination, es-

pecially by organic substances in plants, could be a serious concern for laser spectrometer analysis [239, 240, 241]. Each batch of 30–40 samples was calibrated against accompanying three in-lab working standards for isotope normalization and quality assurance; the standard deviations were 1.3‰ for δ^2H and 0.14‰ for δ^{18}O.

The precipitation samples were analyzed for isotopic composition (δ_P) by means of the same laser spectrometer in liquid mode. The working standards were used to cross-check the CRDS and IRMS analyses.

3.3 The isotopic two-source mixing model for *ET* partitioning

The isotopic approach works on the principle that strong fractionation processes are involved in soil evaporation, but usually not in the uptake of water by plant roots during transpiration [242, 243, 27]. If evaporation of water intercepted by the canopy is not taken into account, the isotopic compositions of bulk ET and of its two constituents (*i.e.*, δ_{ET}, δ_E, and δ_T) can be used to estimate T/ET via a simple, two-source linear mixing model:

$$\frac{T}{ET} = \frac{\delta_{ET} - \delta_E}{\delta_T - \delta_E}. \tag{3.2}$$

Of the terms in Eq. 3.2, only δ_{ET} can be estimated directly via isotopic sampling of atmospheric water vapor (through the use of field-deployable laser spectrometer). The values of δ_E and δ_T are usually calculated indirectly via isotopic sampling of liquid water extracted from plant xylem and soil samples. We aggregated diurnal results of δ_{ET} and δ_E to obtain a mean value for daily T/ET analysis (Eq. 3.2). The bulk ET flux measured by EC was used to calculate the individual fluxes of E and T, both of which are supplied by soil moisture dynamics across the profile.

3.3.1 δ_{ET} via the Keeling-plot method

The value of δ_{ET} in an ecosystem is usually distinct from the isotopic composition of the ambient background air (δ_{bg}) above. The linear mixing of upward ET and downward background air creates a gradient in the isotopic composition of atmospheric water vapor (δ_V) in the turbulent boundary layer [57]. This gradient can be used to extrapolate δ_{ET} via the Keeling-plot method, a

mass balance mixing equation [72]:

$$\delta_V = w_{bg}(\delta_{bg} - \delta_{ET})(\frac{1}{w}) + \delta_{ET}, \tag{3.3}$$

where w_{bg} and w are the water mixing ratios for the background air and the boundary layer, respectively.

Two assumptions are involved: (1) that the values of w_{bg}, δ_{bg}, and δ_{ET} —namely, the slope parameter in Eq. 3.3 —remain constant during the analysis period ($1\ \mathrm{h}$ in this study) [53]; and (2) that water vapor losses come only from turbulent mixing between the two source layers, and not from other factors (*e.g.* condensation). In other words, turbulent mixing is the only process in the upward transport of water vapor [244, 27].

To meet the first assumption, we applied the Keeling-plot method at hourly intervals, because Keeling-plot estimates of δ_{ET} are more robust at shorter time intervals [245]. To better meet the second assumption, δ_V was obtained from three heights (see Section 3.2.4.1) close to the vegetation canopy, where disturbance from advection is minimal [246, 57]. We applied the ordinary least squares regression method for our Keeling-plot a analysis.

3.3.2 δ_E via the Craig–Gordon model

We quantified δ_E with the popular Craig–Gordon model, which takes into accounts both equilibrium fractionation (α_{eq}) at the liquid–vapor interface within the soil matrix and kinetic fractionation (α_k) along the laminar diffusion layer below the "free" atmosphere [74, 75, 247]. The Craig–Gordon equation is:

$$\delta_E = \frac{\frac{\delta_{Se}}{\alpha_{eq}} - h\delta_a - \varepsilon_k - \frac{\varepsilon_{eq}}{\alpha_{eq}}}{1 - h + \varepsilon_k}, \tag{3.4}$$

where δ_{Se} is the isotopic composition of liquid water at the evaporation front (approximated by δ_{soil} of the upper 15–cm depth interval in this study), and δ_a is the isotopic value of the free atmospheric

water vapor, approximated by δ_V measured at $1\,\mathrm{m}$.

3.3.2.1 Equilibrium fractionation at the liquid–vapor interface

The value of α_{eq} (>1) at the liquid–vapor interface was calculated as a function of soil temperature (T'_{soil} in K) at the evaporation front [248, 249], as follows:

$$\text{for } \delta^2\text{H}, \qquad 10^3 \ln \alpha_{eq} = 24.844 \left(\frac{10^6}{{T'_{Soil}}^2}\right) - 76.248 \left(\frac{10^3}{T'_{soil}}\right) + 52.612 \tag{3.5a}$$

$$\text{for } \delta^{18}\text{O} \qquad 10^3 \ln \alpha_{eq} = 1.137 \left(\frac{10^6}{{T'_{Soil}}^2}\right) - 0.4156 \left(\frac{10^3}{T'_{soil}}\right) - 2.0667. \tag{3.5b}$$

These robust empirical relationships (Eqs.3.5a and 3.5b) are still widely used after almost five decades [57, 103, 75]. The deviation of α_{eq} from unity, ε_{eq}, can be defined as $\varepsilon_{eq} = (1 - \frac{1}{\alpha_{eq}}) \times 10^3$ ‰.

3.3.2.2 Kinetic fractionation within the diffusion layer

As the only parameter in Eq. 3.4 that is not readily measurable in field, ε_k—the deviation of α_k from unity —can be calculated as follows [75, 250]:

$$\varepsilon_k = (1-h)\frac{r_M}{r}\left[\left(\frac{D}{D_i}\right)^n - 1\right]. \tag{3.6}$$

We assumed the "weighting term" (r_M/r) in Eq. 3.6 as unity because the atmospheric boundary layer was not strongly perturbed by the soil evaporation efflux. The dominating factor for variability in ε_k is relative humidity (h), which was normalized to the soil temperature (T_{soil} in °C) at the evaporation front [75, 103, 74] using the empirical Tetens equation [251, 252], as follows:

$$h = h_{air}\ \exp\left(\frac{17.502 T_{air}}{240.97 + T_{air}} - \frac{17.502 T_{soil}}{240.97 + T_{soil}}\right), \tag{3.7}$$

where h_{air} is the relative humidity of the ambient air, and T_{air} is the ambient air temperature (°C). Both variables were obtained through biometeorological measurement from the EC system.

The diffusivity ratio of water isotopologues (D/D_i in Eq. 3.6) along the laminar diffusion

layer above the interface is 1.0251 for ^{2}H and 1.0285 for ^{18}O [253]. This ratio can be reduced when the turbulent mixing layer above the laminar layer interacts strongly with the evaporation surface [103]. The aerodynamic parameter n in Eq. 3.6 incorporates the development of laminar flow as volumetric soil water content (θ) changes [17, 254, 245, 255], as follows:

$$n = \frac{0.5(\theta_{soil} - \theta_{res}) + (\theta_{sat} - \theta_{soil})}{\theta_{sat} - \theta_{res}}, \tag{3.8}$$

where θ_{soil}, θ_{res}, and θ_{sat} are, respectively, the observed, residual, and saturated values of θ at the evaporation front. We obtained θ_{res} and θ_{sat} from soil water characteristic curve based on two sampled 15–cm soil columns. We approximated θ_{soil} from the soil water content of the 0–to 10–cm depth interval (average of measured values from the two moisture stations). Here and elsewhere in this paper, δ, ε_{eq}, and ε_k are applicable to both ^{2}H and ^{18}O unless otherwise specified.

3.3.3 δ_T under the isotopic steady–state assumption

Under the isotopic steady-state (ISS) assumption, the isotopic composition of water absorbed by plant roots equals the isotopic composition of water transpired via leaf stomata. Because no isotopic fractionation occurs during root water uptake and upward movement of water to the leaves [45, 88], we were able to use δ_X to approximate daily δ_T in the early afternoon (13:00—15:00) —when, with the stomata fully open, the ISS assumption can be met [19]. Although the isotopic non-steady-state condition could be more accurate for sub-daily analysis in a highly variable environment or for plants with long leaf-water turnover times [256, 47], ISS can be used to approximate integrated daily δ_T [257, 256, 109]—especially for grasses, in which leaf-water turnover time is short [27].

The validity of the ISS assumption for our site was checked in an indirect way: the isotopic composition of leaf water at the evaporation sites (δ_{Le}) within leaf stomata was derived from δ_X under the ISS assumption. Namely, we rearranged Eq. 3.4 with $\delta_T = \delta_X$, which renders the following:

$$\delta_{Le} = \alpha_{eq}\left[(1 - h + \epsilon_k)\delta_x + h\delta_a + \epsilon_k\right] + \epsilon_{eq}. \tag{3.9}$$

For water in plant leaves, the exponent n originally defined in Eq. 3.6 was assumed to reach unity [75] in Eq. 3.9. To check whether overall leaf water reached ISS, we compared sub-daily results of δ_{leaf} with those of δ_{Le}. If ISS holds true for transpiration at noon, the isotopic enrichment of water at the sites of evaporation should cause δ_{Le} to always be greater than total δ_{leaf} owing to leaf-water isotope heterogeneity [258, 96].

3.3.4 Uncertainty in evapotranspiration partitioning

According to Eq. 3.2, the uncertainty in daily T/ET results obtained from the two-source mixing model is derived from uncertainties in δ_E, δ_T, and δ_{ET}. Because all three of these values were measured independently, the variance of T/ET ($\sigma^2_{T/ET}$) can be calculated as follows [259]:

$$\sigma^2_{T/ET} = \frac{1}{(\overline{\delta_T} - \overline{\delta_E})^2}\left[\sigma^2_{\delta_{ET}} + (\frac{T}{ET})^2\sigma^2_{\delta_T} + (1 - \frac{T}{ET})^2\sigma^2_{\delta_E}\right], \tag{3.10}$$

where $\overline{\delta_E}$ and $\overline{\delta_T}$ are daily mean values, and $\sigma^2_{\delta_{ET}}$, $\sigma^2_{\delta_E}$, and $\sigma^2_{\delta_T}$ are the daily variances of δ_{ET}, δ_E, and δ_T, respectively [259]. According to Eq. 3.10, $\sigma^2_{T/ET}$ is not only inversely proportional to the difference between $\overline{\delta_T}$ and $\overline{\delta_E}$, but is also proportional to $\sigma^2_{\delta_{ET}}$, $\sigma^2_{\delta_E}$, and $\sigma^2_{\delta_T}$, and these three variables depend on the analytical precision of the isotopic analyzer and/or the errors involved in the sampling and vacuum distillation procedures [98]. Since only one xylem sample, taken at midday, was used for daily δ_T estimation, the standard error for δ_T was approximated by using the standard deviation of the sample analysis. In accordance with Eq. 3.4, we propagated measurement uncertainties in δ_{Se} and δ_a to σ_{δ_E}.

3.4 Results

3.4.1 Site environmental conditions

3.4.1.1 Long term climate

The long-term daily mean time series of climate data (from 1997–2016, 20 years) at nearby Marena station ($36°3'51''$N, $97°12'45''$W, elevation 327 $\mathrm{m}$above the sea level) exhibited noticeable interannual variability and clear seasonality (Fig. 3.3 and 3.4). In 2016, the weather showed large

variation—daily mean solar radiation was relatively higher during the first half year, while air temperature showed relative higher values only in the second half of the year, and relative humidity showed both high and low records across the year (Fig. 3.3).

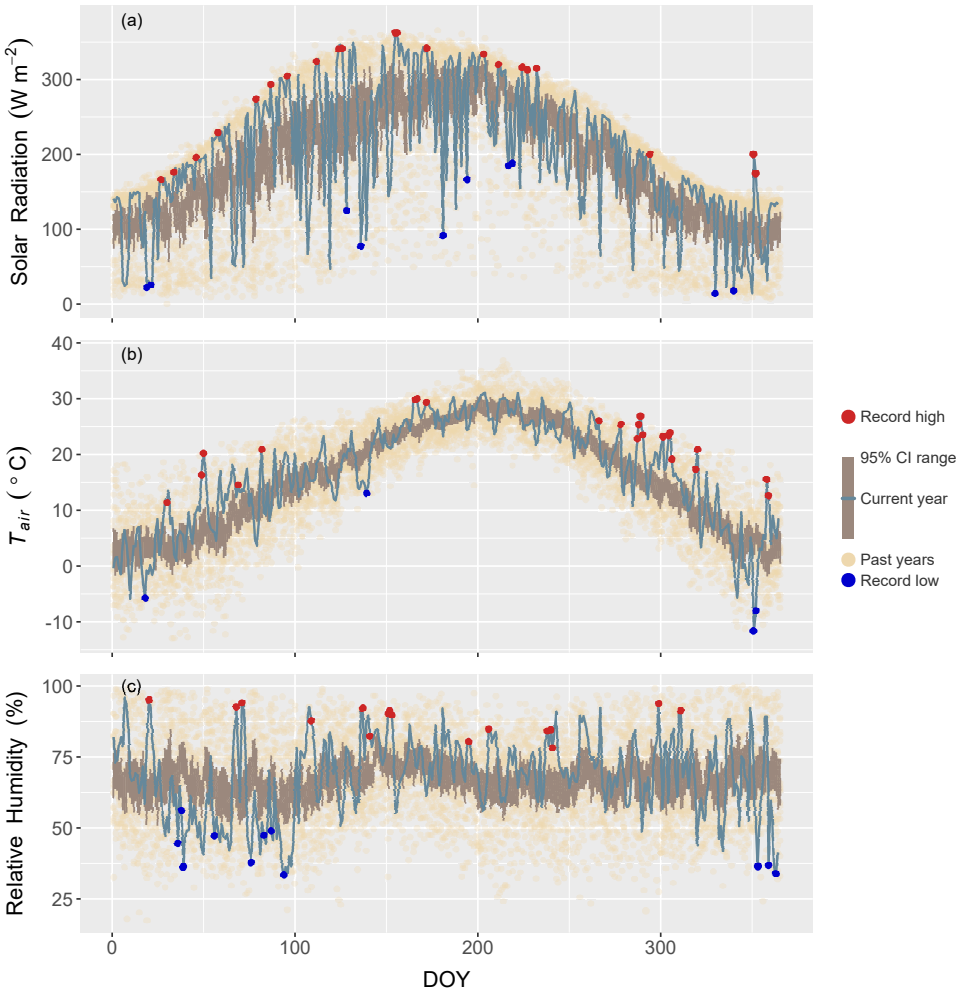

Figure 3.3: Long-term climate data (1997–2016) in Marena, includes global solar radiation (a), air temperature at 1.5 m (b), and relative humidity at 1.5 m (c).

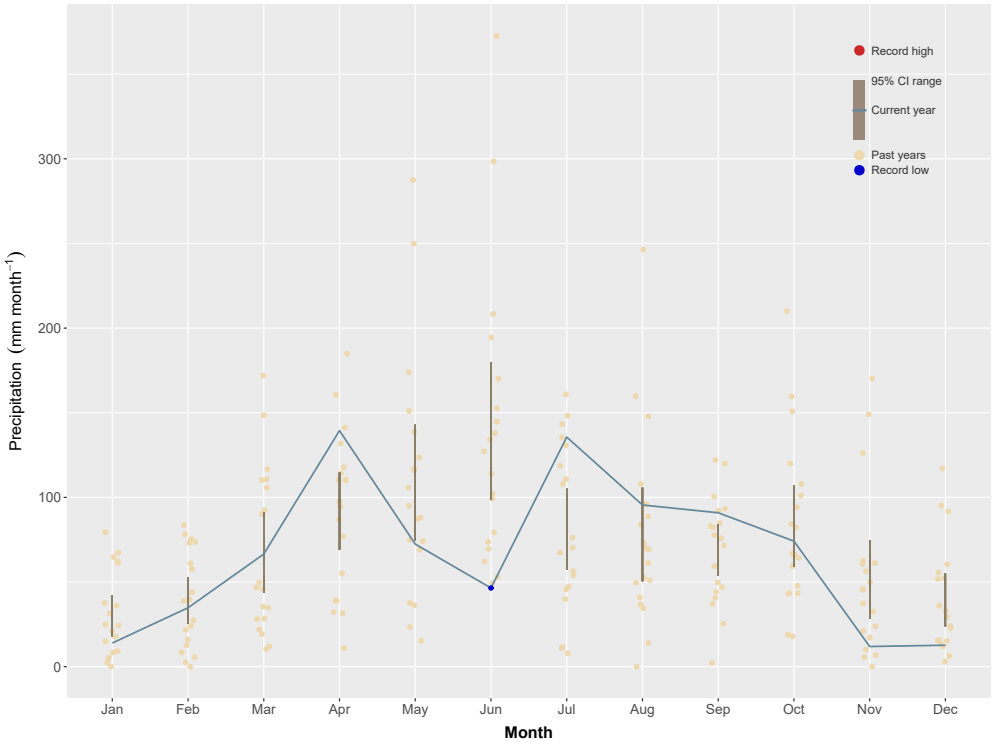

Figure 3.4: Long-term monthly precipitation (1997–2016) in Marena.

In 2016, rainfall was $721\,\mathrm{mm}$, 18% below the long-term mean annual precipitation, with a relatively dry period in early growing season, especially rainfall during June, at $47\,\mathrm{mm}$, was the lowest in 20 years (Fig. 3.4).The LAI measured on July 29, 2016 ranged between 3.75 and 5.40 $\mathrm{m^2\,m^{-2}}$. The daily mean $NDVI$ value was consistently high during the two field campaigns, ranging between 0.62 and 0.64. Short-term weather and soil moisture conditions during the field campaigns were mostly controlled by precipitation and solar radiation (Fig.3.5).

3.4.1.2 Weather conditions and atmospheric processes

Very little rainfall($< 0.25\,\mathrm{mm\,d^{-1}}$) occurred during the two field campaigns. Measured rainfall prior to Campaign 1 (between May 29 and June 3, 2016) was $25\,\mathrm{mm}$; and prior to Campaign 2 (a single event on June 26) was $13\,\mathrm{mm}$ (Fig.3.5a). These few precipitation pulses induced an instant response and high variations in the leaf wetness ratio (LWR, the duration time of leaf wetness as a percentage of a 24–hour period) (Fig.3.5b). During our sampling days, except for June 30, 2016,

leaf wetness (caused by dew or minor night precipitation) was mostly observed during predawn and early morning hours (usually before 9am). No leaf wetness was noted during our *in situ* observations. For this reason, we did not consider evaporation from canopy interception as a factor in our T/ET analysis.

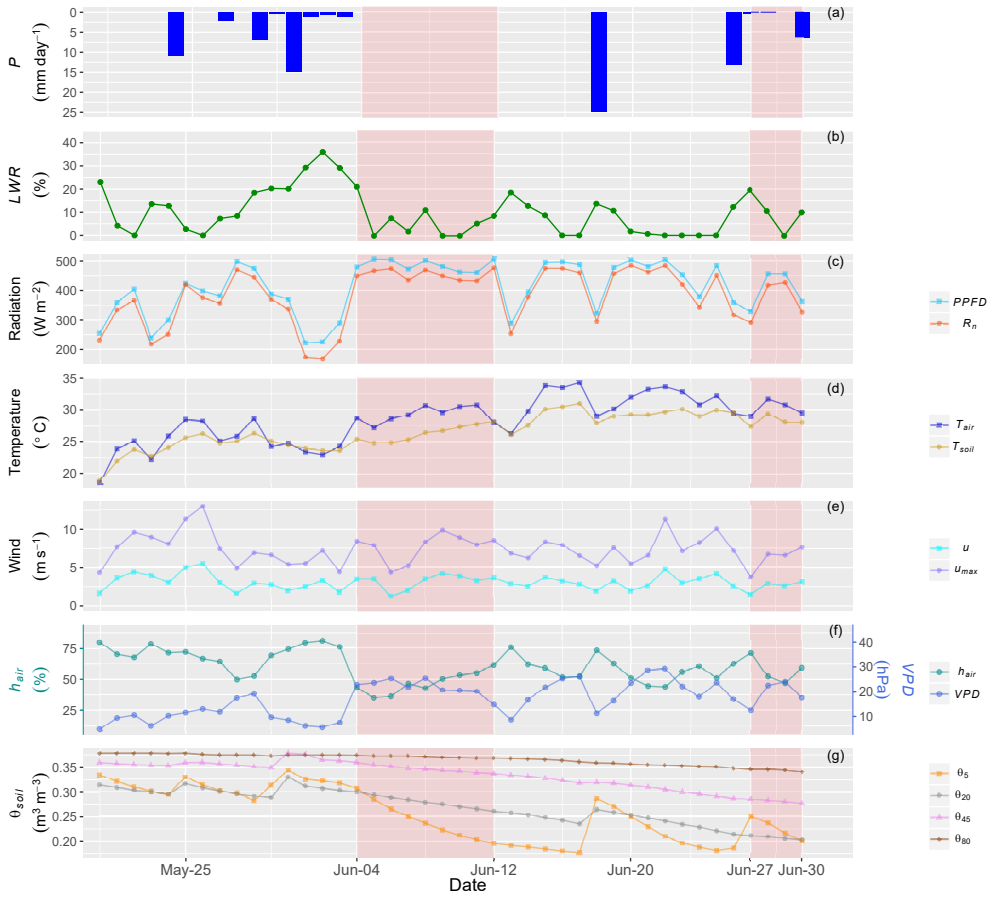

Figure 3.5: *In situ* environmental conditions observed from late May to June, 2016. Except for P and LWR, which are calculated at 24-hour intervals, each point represents the daytime mean value between 9am and 7pm for the corresponding variable. Values for net radiation (R_n), air temperature (T_{air}), wind speed (mean value u and maximum value u_{max}), atmospheric water content (relative humidity h_{air}, and vapor pressure deficit VPD) were obtained from eddy covariance measurements at $3\,\mathrm{m}$ above the ground surface. Variables related to soil processes include soil temperature within the top 8-cm layer (T_{soil}) and volumetric soil water content (θ_{soil}) at various depths. The red-shaded areas represent the two field campaigns.

The values of R_n and $PPFD$ were consistently high during Campaign 1, but showed substan-

tial day-to-day variations during Campaign 2 —especially the low R_n reading on June 27, 2016 (Fig.3.5c). The air temperature (T_{air}, at $3\,\mathrm{m}$) and the surface soil temperature (T_{soil}, in the top $8\,\mathrm{cm}$), both heated by solarradiation, showed similar trends—with T_{soil} averaging 2.50 ± 1.38 °C lower than T_{air} (Fig.3.5d), owing to the shading effect of the vegetation canopy (which showed high values of LAI and $NDVI$). Wind speed was low on June 8 and June 27, 2016, and was particularly stagnant on the latter date, with a mean maximum of $3.72\,\mathrm{m\,d^{-1}}$ (Fig.3.5e). During Campaign 1, the clear weather with high solar radiation resulted in relatively stable day-to-day h_{air} and VPD (Fig.3.5f). In contrast, precipitation on June 27, 2016 and June 30, 2016, accompanied by low solar radiation, brought about high h_{air} and low VPD (especially on June 27).

3.4.1.3 Soil moisture dynamics

Our two field campaigns were characterized with high discrepancy in soil water availability across the profile. This substantial depletion of soil moisture across the profile was caused by the high ET flux during June ($122\mathrm{mm}$) driven by the record low precipitation and intense solar radiation (Fig. 3.5g & 3.6). Dynamics of θ_{soil_5cm} was exceptionally responsive to rainfall pulses. For example, the antecedent θ_{soil_5cm} for both campaigns were rapidly and remarkably replenished following the preceding rainfall events, though the re-wetting was less dramatic because of the weaker precipitation pulses prior to Campaign 2. This recharging effect substantially dampened at $20\,\mathrm{cm}$, and was barely noticeable for θ_{soil_45cm} and θ_{soil_80cm}. As a result of the steady depletion of θ_{soil_20cm}, θ_{soil_45cm}, and θ_{soil_80cm}, the θ_{soil} profile diverged noticeably between the two campaigns (Fig. 3.6).

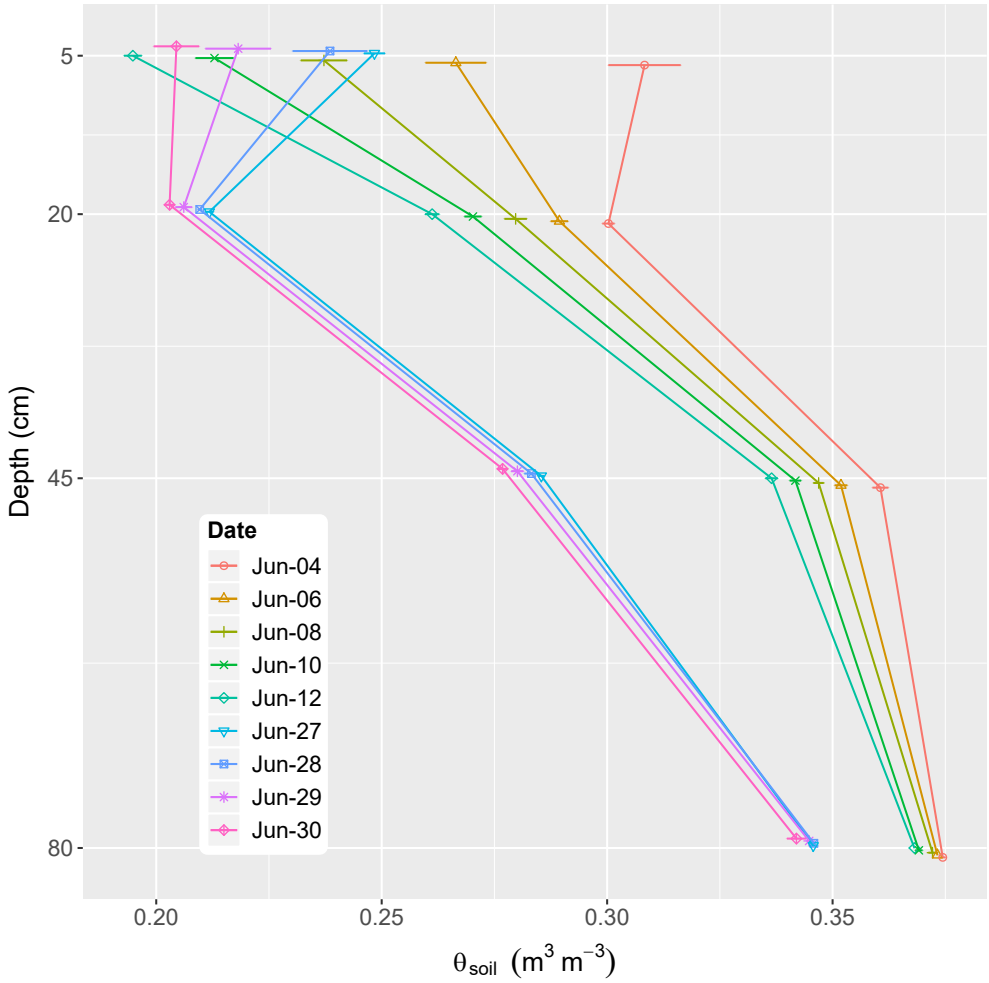

Figure 3.6: Temporal variations in the vertical distribution of volumetric water content (θ_{soil}) over the two campaigns. The dots and solid lines are daily means, and error bars represent one standard deviation.

3.4.2 Stable isotopes as tracers

The depletion of heavier isotopes (^{2}H and ^{18}O) in the meteoric component of ecohydrologic processes (δ_P and δ_V) and the enrichment of heavier isotopes in the evaporative components (δ_{soil} and δ_{leaf}) are illustrated in a dual-isotope plot (Fig. 3.7). The values of δ^{2}H and δ^{18}O are highly correlated (p-value < 0.001) for waters in all these ecohydrologic pools. The slope for δ_P, as observed throughout 2016, was lower than those for the long-term local meteoric water line (LMWL) and the global meteoric water line (GMWL), which may be attributable to strong below-cloud re-

evaporation in this relatively dry year. The values of δ_P showed high storm-to-storm variability during May and June, possibly coinciding with shifts in moisture sources and storm trajectories.

The fact that δ_V was more nagative than δ_P is evidence of isotopic fractionation during the evaporative phase change from liquid to vapor. Because the surface soil layer was strongly recharged by precipitation, the distributions of δ_P and δ_{soil} lies close to each other in the dual-isotope space. But the enrichment of the evaporative component caused δ_{soil} to lie on the right side of δ_P. This soil evaporative fractionation is especially remarkable for δ^{18}O, because kinetic fractionation is greater for δ^{18}O than for δ^{2}H [260]. Because of the absence of fractionation during most root water uptake [261], the distributions of δ_{soil} and δ_X are indistinguishable—and for this reason inter-comparison between δ_{soil} and δ_X is often used to infer depths of root water uptake [98]. The overlapping ofδ_X and δ_{soil} suggests that shallow soil moisture is a major source of the water used by plants in this grassland. The strong evaporative enrichment within the leaf stomata is the reason for the considerably heavier isotopic composition of bulk leaf water (δ_{leaf}), and the associated strong kinetic fractionation caused the regression slope for δ_{leaf} to deviate, becoming substantially lower than that for LMWL and δ_P.

The isotopic depletion of atmospheric water vapor and the isotopic enrichment of the evaporative components were further revealed by obtained data series at the diurnal and daily temporal scales (Fig. 3.8). At the daily interval, δ_V gradually became less negative as each campaign progressed, indicating the increasing contribution of heavier δ_T. An exception was noted on June 12, 2016 —a lighter δ_V with a noticeable diurnal variation. This exception might have been due to a transition in the weather system caused by advection of a different air mass (Fig. 3.5c & d).

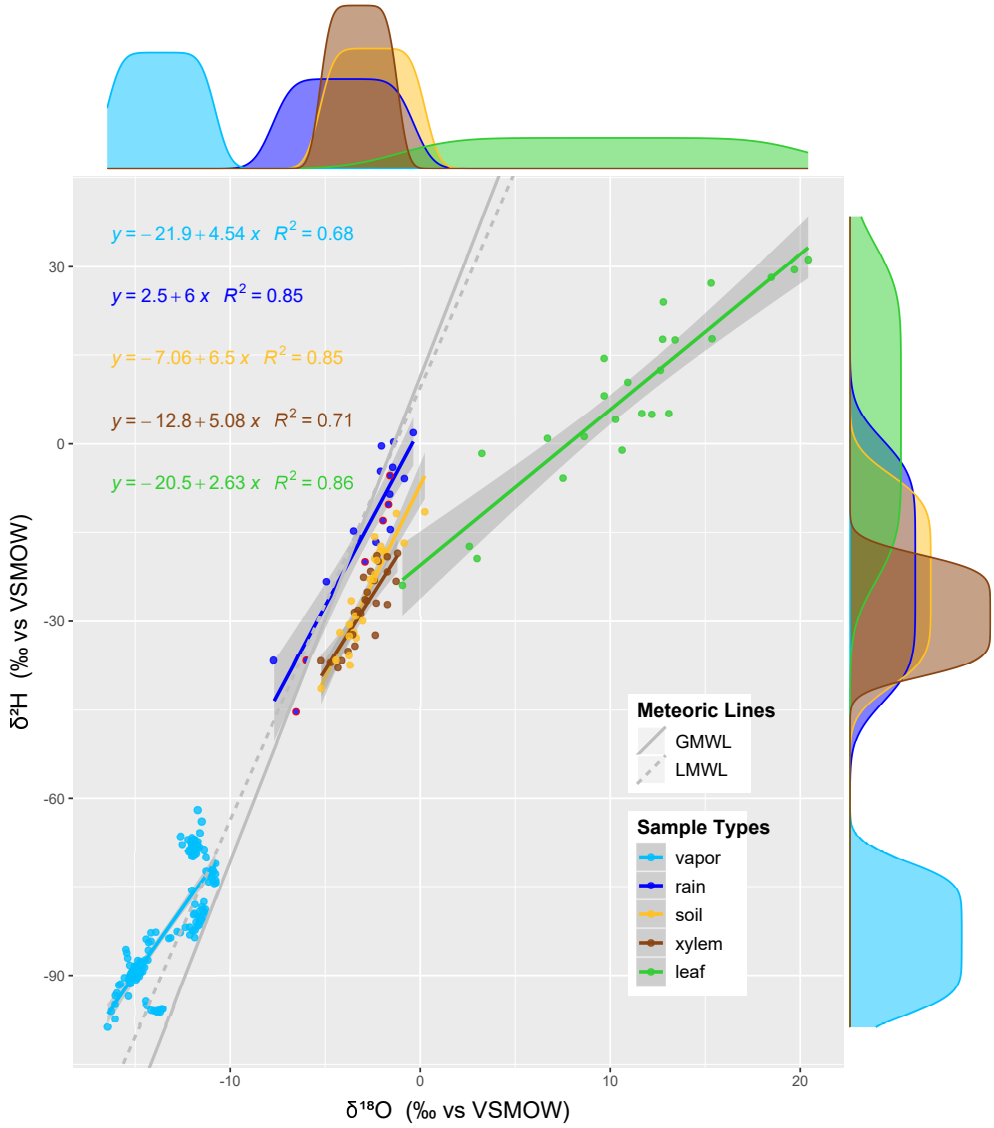

Figure 3.7: Dual-isotope plot of water from various ecohydrologic pools. During the two campaigns, we collected water samples from the upper 15-cm soil layer, plant leaves, root xylem, and the near-ground atmospheric vapor; and we plotted the isotopic composition of rainfall throughout 2016.The plot also includes two meteoric lines: the gray dots represent the Local Meteoric Water Line (LMWL, $\delta^2\mathrm{H} = 7.32\ \delta^{18}\mathrm{O} + 9.5$), from a long-term observation in Norman, OK [262]; and the solid gray line represents the Global Meteoric Water Line (GMWL, $\delta^2\mathrm{H} = 8.20\ \delta^{18}\mathrm{O} + 11.3$) [263]

.

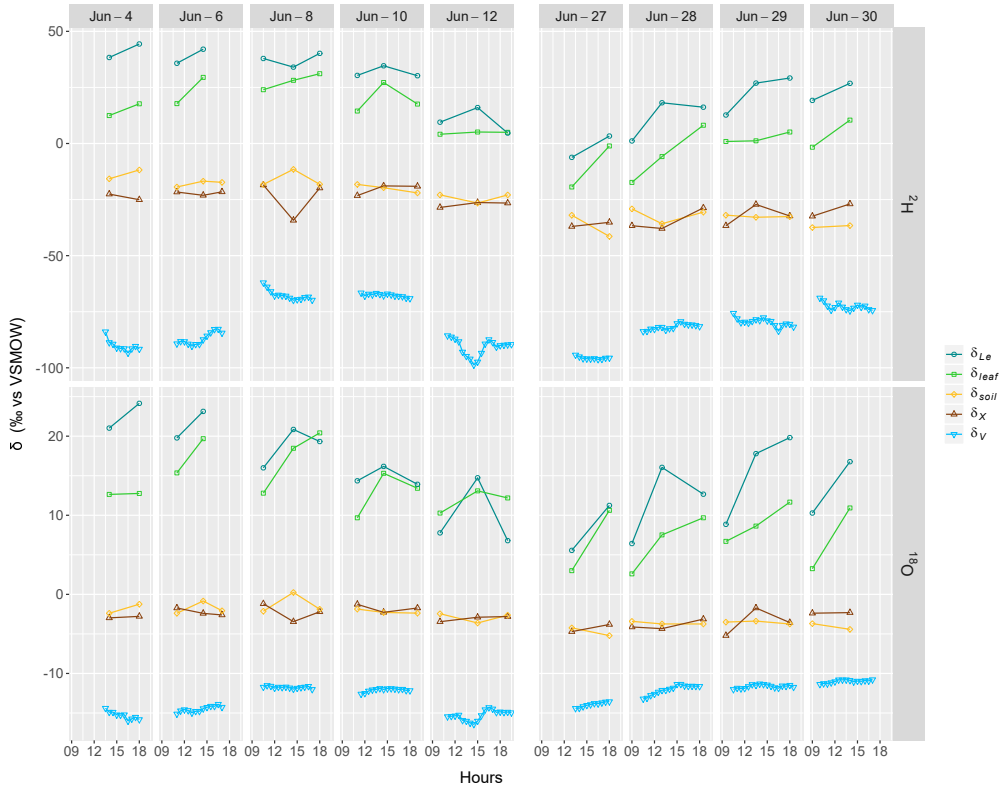

Figure 3.8: Time series of isotopic composition of sampled water in various ecohydrologic pools during the two field campaigns. These pools include atmospheric water vapor (δ_V), liquid water in the surface soil layer (δ_{soil}), plant xylem water (δ_X), bulk leaf water (δ_{leaf}), and simulated leaf water at the evaporation site (δ_{Le}). The analyses for δ_{Le} were done under the isotopic steady state assumption.

3.4.3 Isotopic partitioning of ET flux

3.4.3.1 Determination of δ_{ET} via the Keeling-plot method

The efficacy of Keeling-plot regression was low for both isotopes, especially for δ^{18}O in Campaign 2. The coefficient of determination between high-frequency δ_V and $1/w$ ($R^2_{keeling}$) was 0.48 ± 0.30 for δ^2H and 0.27 ± 0.22 for δ^{18}O during Campaign 1, and was 0.35 ± 0.30 for δ^2H and 0.08 ± 0.13 for δ^{18}O during Campaign 2. The lowest $R^2_{keeling}$ values were seen on June 27, 2016 (0.05 ± 0.07 for δ^2H and 0.03 ± 0.03 for δ^{18}O). The average value of $R^2_{keeling}$ was significantly higher for δ^2H than for δ^{18}O during both campaigns (one-tailed paired-sample t-test, p-value <0.001). The percentage of significant regression (p-value from the F test $\leq$ 0.05) was usually high (>80%),

except for δ^{18}O in Campaign 2 (56.7%).

The efficacy of Keeling-plot regression for δ^{2}H was more explainable than for δ^{18}O by variations in both δ_V and w. Based on Spearmans rank correlation analysis, the correlation between $R^2_{keeling\_^{2}\mathrm{H}}$ and the standard deviation (SD) of $\delta_{V\_^{2}\mathrm{H}}$ was strongly positive (R = 0.73, p-value $\leq$ 0.001), and the correlation between $R^2_{keeling\_^{2}\mathrm{H}}$ and the SD of w was moderately positive (R = 0.56, p-value $\leq$ 0.001). In contrast, the correlation between $R^2_{keeling\_^{18}\mathrm{O}}$ and the SD of $\delta_{V\_^{18}\mathrm{O}}$ was only weakly positive (R = 0.27, p-value $\leq$ 0.05) and that between $R^2_{keeling\_^{18}\mathrm{O}}$ and w was strong negative (R = -0.62, p-value $\leq$ 0.001).

We filtered hourly δ_{ET} solely based on δ^{2}H (p-value threshold from the *F* test $\leq$ 0.05 and $R^2_{keeling\_^{2}\mathrm{H}}$ >0.40), and we removed suspicious outliers showing unusually heavy δ_{ET} values (n = 4). After filtering, 57.1% and 46.7% of raw δ_{ET} data were retained for Campaigns 1 and 2, respectively. Note that this filtering removed all raw δ_{ET} data for June 27, 2016, when weather conditions were static, cloudy, and humid; thus, no data for that date were included in the ET partitioning analysis.

The mean (and range) values of filtered hourly δ_{ET} across the two campaigns were -42.3 ± 13.1 ‰ (from -69.4 ‰ to -16.5 ‰) for δ^{2}H, and was -8.11 ± 3.00 ‰ (from -19.1 ‰ to -3.24 ‰) for δ^{18}O (Fig. 3.9). The standard errors inherited from the linear regression were 1.72 ± 0.84 ‰ and 0.66 ± 0.39 ‰ for ^{2}H and ^{18}O, respectively.

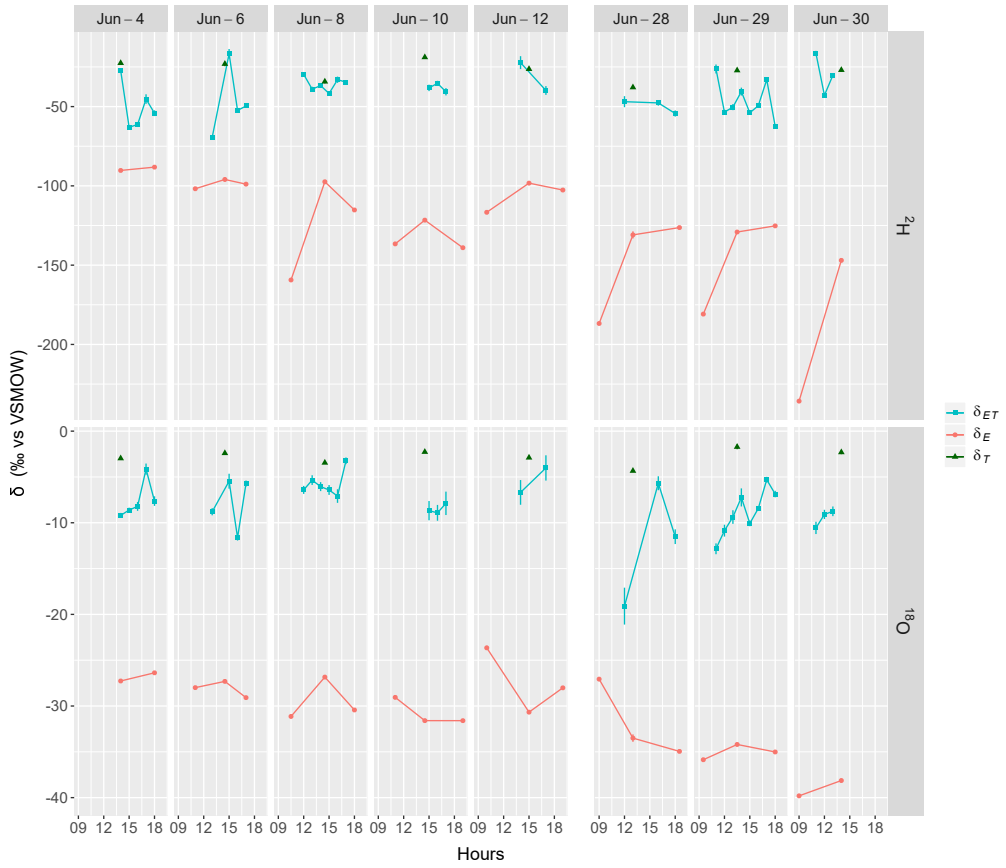

Figure 3.9: Daily averages for δ_{ET}, δ_E, and δ_T during the two field campaigns.

3.4.3.2 Determination of δ_E via the Craig-Gordon model

The proportions of the two fractionation factors (ε_{eq} vs ε_k) were different for the two isotopes (Fig. 3.10). For δ^2H, the values of ε_{eq} and ε_k differed by nearly one order of magnitude, whereas for δ^{18}O they were comparable and thus closely approached to 1:1 line. Diurnal patterns were characterized with higher ε_{eq} in the morning due to low soil temperature (Eq. 3.5a and Eq.. 3.5b), and with higher ε_k (especially for δ^{18}O) during noontime and afternoon due to low relative humidity (and high VPD). These large diurnal variations in ε_{eq} and ε_k resulted in considerable variations in sub-daily δ_E—but the pattern of variation for δ^2H was different from that for δ^{18}O (Fig. 3.9).

The mean (and range) values of δ_E across the two field campaigns were -128 ± 36.4 ‰ (from -236 ‰ to -88.2 ‰) for δ^2H, and -30.9 ± 4.15 ‰ (from -39.8 ‰ to -23.7 ‰) for δ^{18}O. The errors

in δ_E—propagated only from analysis uncertainty—were 0.82 ± 0.45 ‰ for ^{2}H and 0.16 ± 0.08 ‰ for ^{18}O.

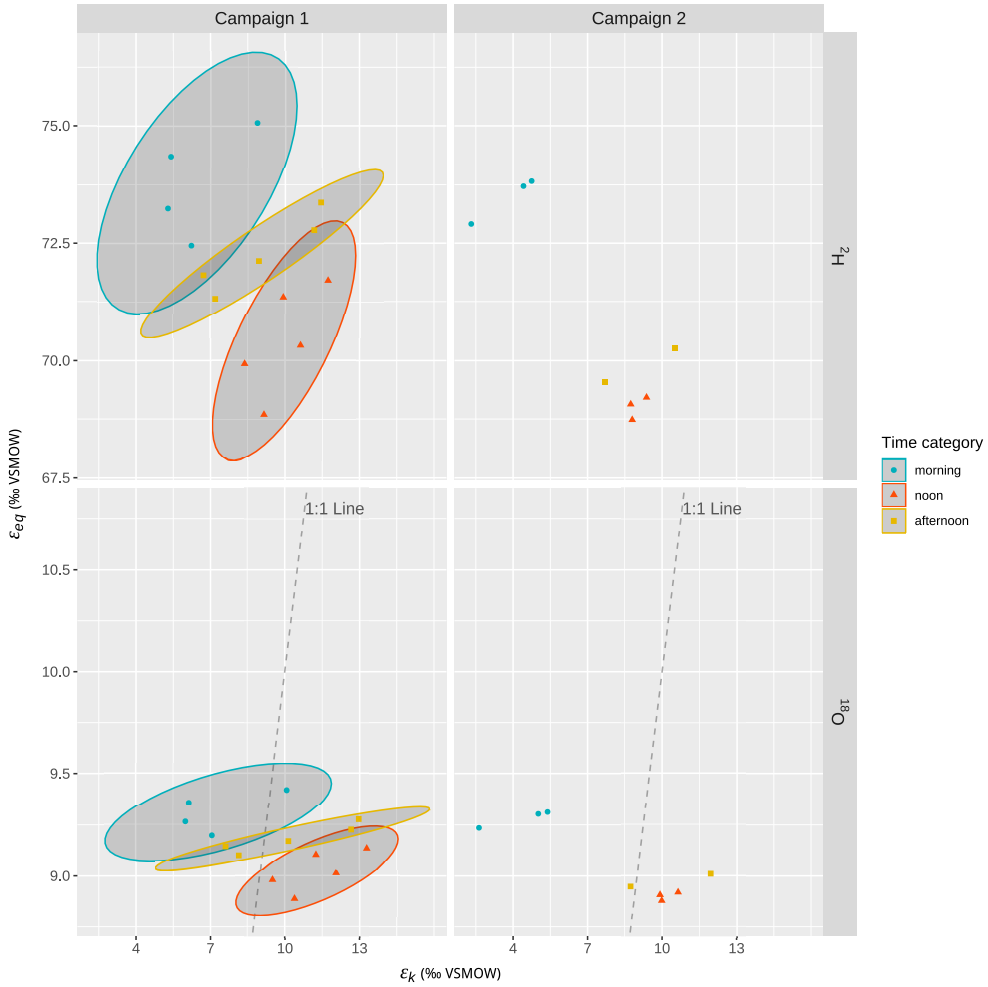

Figure 3.10: Equilibrium fractionation factor ε_{eq} (‰) versus kinetic fractionation factor ε_k (‰) for stable water isotopes δ^2H and δ^{18}O. The confidence level for the ellipses is 0.8. Because of the small data size, ellipses were not drawn for Campaign 2. Data for June 27, 2016 were not included.

3.4.3.3 Determination of δ_T under the isotopic steady state assumption

Comparison of bulk leaf water (δ_{leaf}) and δ_{Le} at the evaporation site within leaf stomata (derived from δ_X under the ISS assumption) indirectly confirmed the validity of our adoption of the ISS approach at midday (Fig. 3.8 and 3.11). We adopted this indirect approach because *in situ*

quantification of δ_T, although essential for assessment on ISS assumption, is technically challenging to obtain. The isotopic enrichment of leaf water at the evaporation site caused δ_{Le} to be heavier than δ_{leaf} (above the 1:1 Line in Fig. 3.11); particularly at noontime, δ_{Le} was consistently heavier than δ_{leaf}, especially for ^{2}H. This isotopic enrichment is clearly to be expected, because the evaporative enrichment took place only at the evaporation sites, not in the vein ribs of leaves [264, 96].

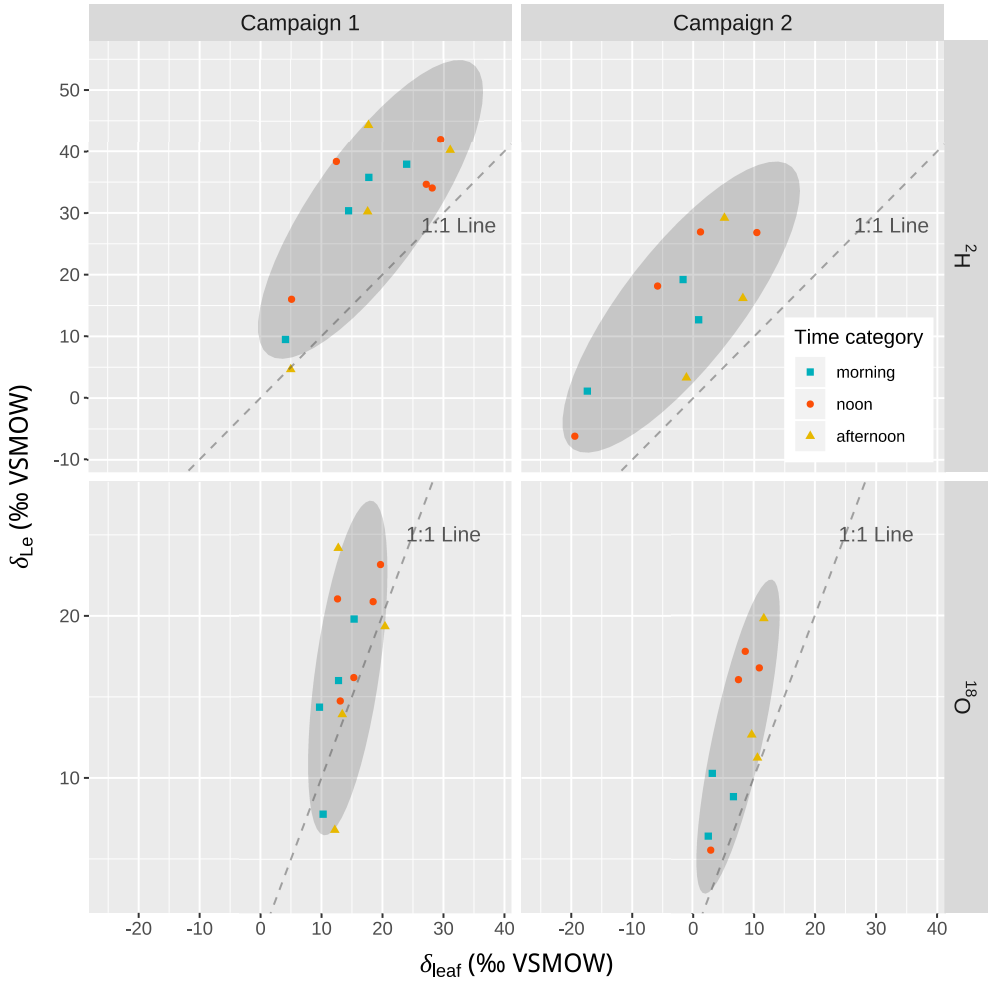

Figure 3.11: Comparison of isotopic compositions δ_{Le} and δ_{leaf} for stable water isotopes δ^2H and δ^{18}O during the two field campaigns.

The daily δ_T value was relatively stable during the two campaigns (Fig. 3.9). The mean (and range) values of δ_T were -27.1 ± 6.23 ‰ (from -18.9 ‰ to -37.9 ‰) for ^{2}H and -2.79 ± 0.82 ‰

(from -1.72 ‰ to -4.34 ‰) for ^{18}O. The errors in δ_T, propagated only from analysis uncertainty, were 0.89 ± 0.27 ‰ for δ^2H and 0.11 ± 0.08 ‰ for δ^{18}O.

3.4.3.4 Dealing with uncertainties involved in isotopic ET partitioning

As expected from the two-source mixing model (Eq. 3.2), δ_{ET} was mostly varied between the isotopically light δ_E and the heavier δ_T at diurnal (Fig. 3.9) and daily scales (Table. 3.1). Over the course of each campaign, daily δ_{ET} values gradually approached those of δ_T while progressively deviating from δ_E —indicating the increasing dominance of plant transpiration.

For partitioning of ET at the daily interval, we used δ^2H rather than δ^{18}O. We obtained a mean daily T/ET value (range) of 0.80 ± 0.06 (from 0.58 to 0.98) during Campaign 1, and of 0.90 ± 0.06 (from 0.83 to 0.97) during Campaign 2. The associated uncertainty levels were 0.13 ± 0.03 and 0.11 ± 0.03 for Campaigns 1 and 2, respectively (Fig. 3.12). The fact that the mean error value for daily δ_{ET} was 1.12 ± 0.69—vs. 0.09 ± 0.09, and 0.74 ± 0.22, for δ_E and δ_T, respectively —shows that the error in daily δ_{ET} is the major source of uncertainty in T/ET results.

Table 3.1: Mean ± standard deviation for daily δ_{ET}, δ_E, and δ_T.

Campaign	Date	^{2}H			^{18}O		
		δ_{ET}	δ_E	δ_T	δ_{ET}	δ_E	δ_T
1	June 4, 2016	-50.6 ± 0.76	-89.2± 0.61	-22.6 ± 0.72	-7.65 ± 0.19	-26.8 ± 0.07	-2.97 ± 0.14
	June 6, 2016	-48.6 ± 0.85	-98.7± 0.57	-23.1 ± 1.41	-8.26 ± 0.24	-28.2 ± 0.06	-2.40 ± 0.04
	June 8, 2016	-35.7 ± 0.58	-119 ± 0.34	-34.2 ± 1.10	-5.80 ± 0.22	-29.2 ± 0.07	-3.45 ± 0.08
	June 10, 2016	-37.9 ± 1.14	-132 ± 0.26	-18.9 ± 0.54	-8.54 ± 0.61	-30.8 ± 0.11	-2.27 ± 0.03
	June 12, 2016	-30.2 ± 2.56	-106 ± 0.59	-26.3 ± 0.77	-5.48 ± 0.97	-27.8 ± 0.11	-2.89 ± 0.08
2	June 28, 2016	-48.3 ± 1.69	-141 ± 1.13	-37.9 ± 0.83	-12.4 ± 0.94	-32.6 ± 0.20	-4.34 ± 0.07
	June 29, 2016	-45.8 ± 0.64	-137 ± 0.43	-27.2 ± 0.94	-8.95 ± 0.22	-34.9 ± 0.09	-1.72 ± 0.25
	June 30, 2016	-30.9 ± 0.74	-176 ± 0.83	-26.9 ± 0.82	-9.45 ± 0.33	-38.7 ± 0.17	-2.31 ± 0.20

1. Values are expressed as mean ± one standard deviation.
2. The uncertainty level for δ_{ET} was derived from the standard error of the OLS regression, and uncertainties in δ_E and δ_T were propagated mainly from the analysis error.

The actual fluxes of E and T exhibited greater variations in Campaign 1 than in Campaign 2 (Fig. 3.13). During Campaign 1, mean daily ET was 4.62 ± 0.04 $\mathrm{mm\,d^{-1}}$, vs. 3.98 ± 0.07 $\mathrm{mm\,d^{-1}}$ during Campaign 2. Within nine days following the precipitation event of June 3, 2016, daily T increased above $4\,\mathrm{mm\,d^{-1}}$, and by the end of Campaign 1 daily E had dropped below $0.25\,\mathrm{mm\,d^{-1}}$. Following the relatively small rainfall events just before Campaign 2, the daily T flux fell below $4\,\mathrm{mm\,d^{-1}}$ and decreased steadily, while the daily E flux dropped to anegligible level at the end of Campaign 2. The uncertainty level for daily T/ET corresponded to those of the daily E and T fluxes, namely 0.55 ± 0.15 $\mathrm{mm\,d^{-1}}$.

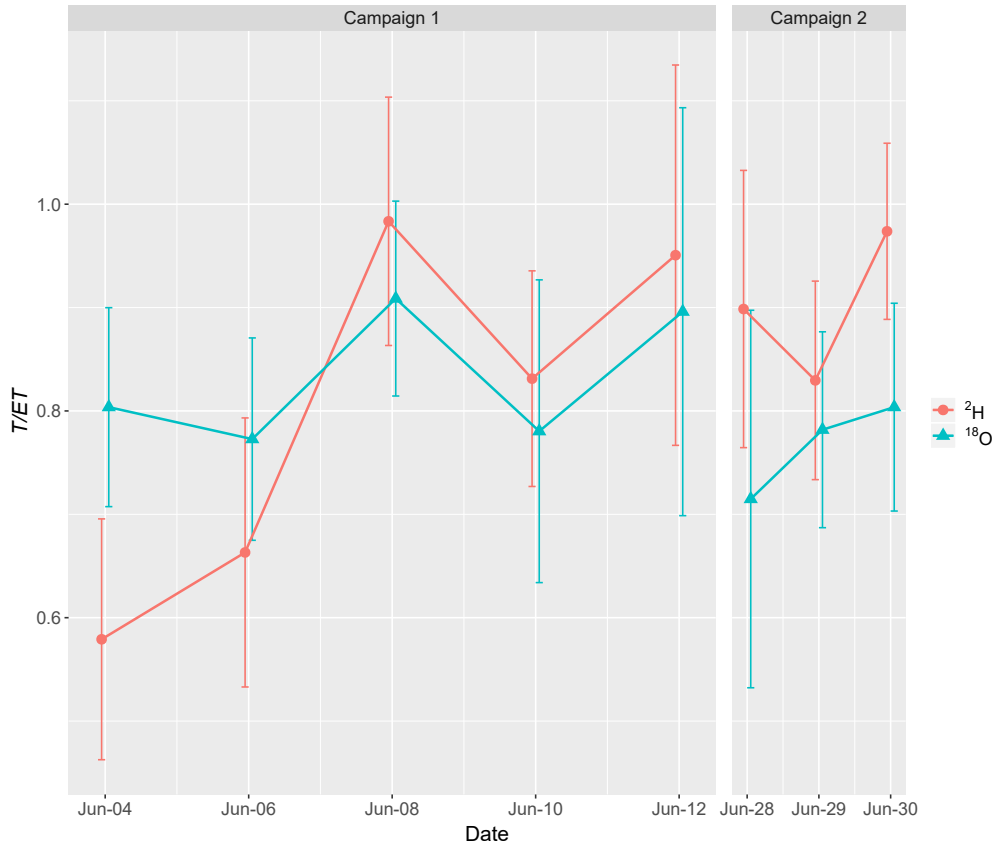

Figure 3.12: Temporal variations in T/ET at the daily interval during the two field campaigns. Each error bar represents the daily standard deviation of T/ET for each sampling day.

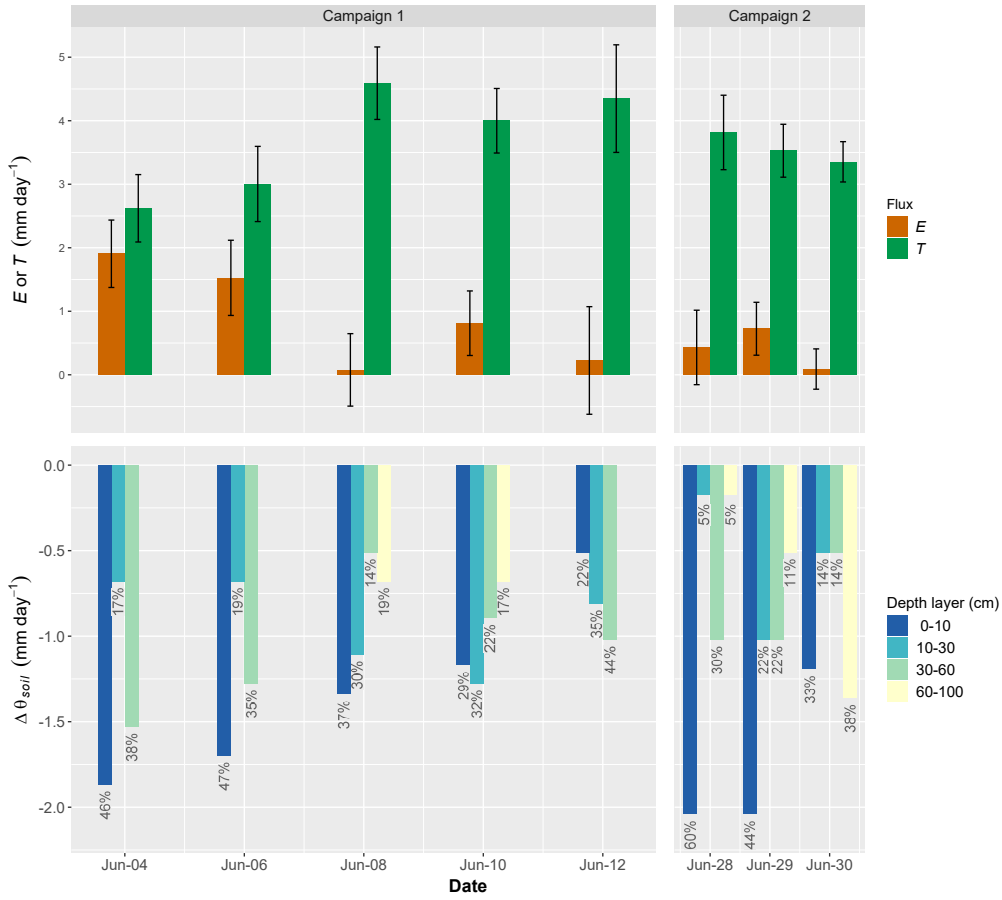

Figure 3.13: Variations in daily fluxes of E and T as shown by partitioning based on δ^2H, and associated variations in volumetric soil water content ($\Delta\theta_{soil}$) at different depths during the two field campaigns. Error bars for E and T represent one standard deviation. Percentages shown for the $\Delta\theta_{soil}$ bars represent the change in water storage change of each layer as a percentage of the total soil column. Note that the $\Delta\theta_{soil}$ bar for June 30, 2016 is derived only from measurements prior to a precipitation event at 5pm that day.

3.4.4 Response of ET partitioning during two drying-up episodes

The variability in daily T/ET was initially driven by an intense drying process of shallow soil water shortly after precipitation, and thereafter was more controlled by micro-meteorological processes. Isotopic analysis based on δ^2H showed a dramatic increase in daily T/ET during Campaign 1—from 0.58 ± 0.12 to 0.98 ± 0.12—within five days following precipitation events (Fig. 3.12). We were unable to observe a similar pattern in daily T/ET during the early part of Campaign 2, because δ_{ET} was unavailable (owing to the low efficacy of Keeling-plot regression

for June 27, 2016). Once the shallow soil moisture had dried up, atmospheric processes became stronger influences on day-to-day variations in T/ET. For example, daily T/ET decreased on both June 10 and June 29, 2016, coincident with the highest T_{air} level for Campaign 1 and the highest VPD level for Campaign 2, respectively.

As shown in Fig. 3.13, the distinct temporal patterns of soil evaporation and plant transpiration caused variations in depletion of soil water storage across the profile. At the beginning of each campaign, soil water availability in the shallow layers was at favorable levels, but this shallow soil moisture became depleted early on as a result of the high E flux, especially for the top 10–cm layer (Fig. 3.6). This thinnest atop layer was the dominant source of E during the first half of Campaign 1 and most of Campaign 2. Then, as $\Delta\theta_{soil}$ for the top 10–cm layer gradually decreased and daily E dropped, T gradually increased, fed by soil moisture from the deeper layers. In particular, the depletion of θ_{soil} from the bottom layer (60–100 cm) was small and intermittent during Campaign 1, but became a major source of T by the end of Campaign 2. This trend of depletion of moisture from deeper level from one campaign to the next concurred with a divergence in the pattern of soil moisture profiles of the two campaigns (Fig. 3.6).

3.5 Discussion

3.5.1 Analysis of uncertainties in the isotopic two-source mixing model

Accurate partitioning of ET depends on clearly distinguishing values between $\overline{\delta_E}$ and $\overline{\delta_T}$ on the one hand, and accurately quantifying δ_{ET}, δ_E, and δ_T on the other hand (Eq. 3.10). Because the result of the partitioning is especially sensitive to δ_{ET}, accurate quantification of this variable is most important—but remains a key challenge [50, 49, 19, 88].

The level of error in estimation of δ_{ET} is the biggest source of uncertainty in our study. The Keeling-plot method optimally applies to sites characterized by substantial temporal variations in δ_V contributed exclusively by a strong ET flux during the short regression period [50]. But such conditions rarely exist in natural environment [246]. The relatively low efficacy shown in our Keeling-plot regression, especially for δ^{18}O, signified that the correlation between δ_V and the recip-

rocal of the molar mixing ratio of water vapor was relatively weak. A similar case was reported for a rice paddy field, where only 24% of the hourly $\delta_{ET\_^2\mathrm{H}}$ data met the filtering standards with a sufficient sample size ($N > 40$) and a sufficiently high coefficient of determination ($R^2_{Keeling} > 0.8$) [265]. One reason for the low regression efficacy could be the existence of highly variable *in situ* micro-meteorological conditions; for example, advection [246] and entrainment [266] processes can be major causes of variations in δ_V at hourly to daily scales. Another reason for this low efficacy might be that the δ_{ET} values are not clearly distinguishable from the isotopic composition of the background atmosphere (δ_{bg}), resulting in a less noticeable gradient in δ_V among the three measurement heights (Fig. 3.8). In particular, on June 27, 2016 characterized with a decreased ET flux and a cloudy, stagnant, and humid weather, such a small vertical gradient in δ_V could appear essentially negligible. For this reason, the Keeling-plot regression was not effective and no satisfactory δ_{ET} results were obtained for that day.

In addition to the uncertainties in estimating δ_{ET}, there are uncertainties involved in the quantification of δ_E and δ_T. For the Craig–Gordon model (Eq. 3.4), identification of the evaporation front is essential for accurate measurement of δ_{Se}, T_{soil}, and h [247, 57]. Substituting δ_{soil} of the bulk surface soil layer for δ_{Se} could introduce large uncertainties into the estimation of δ_E, owing to the high temporal and spatial variability in the isotopic composition of soil water [267, 268]. For example, in a tallgrass prairie pasture, noticeable variations in δ_{soil} was observed in the top $20\,\mathrm{cm}$ of soil [269].

The use of laser spectroscopy for direct, continuous, and non-destructive sampling of pore water (liquid or vapor) in the vadose zone [270, 271, 104, 51, 102] is a promising technique for locating the evaporation front [103] or for direct quantifying δ_E with high temporal and spatial resolution. Although plant transpiration may violate ISS assumption in mornings and evenings [272, 258, 47], assuming ISS are met during the midday hours and deriving δ_T directly from measured δ_X is a widely adopted practice [10, 12, 52, 55]. Our analysis of leaf water at the evaporation site in leaf stomata lends indirect support to our adoption of the ISS assumption for our study.

3.5.2 Selection of an isotope for T/ET analysis (δ^2H vs δ^{18}O)

We selected δ^2H for our T/ET analysis because of its higher efficacy in the Keeling-plot regression and its greater values of equilibrium fractionation involved in evaporation. The higher efficacy we found for δ^2H vs. δ^{18}O in the Keeling-plot regression is consistent with the findings of previous, related investigations [20, 48]. One reason might be that greater variability in the hydrogen-related isotopologues was responsible for the more significant and stronger relationship between $R^2_{Keeling}$ and variations in $\delta_{V\_^2\mathrm{H}}$ that was obtained. The poorer efficacy of δ^{18}O in the Keeling-plot regression was particularly evident during Campaign 2, when conditions were more humid and $R^2_{Keeling}$ was observed to be inversely proportional to w (possibly because $\varepsilon_{k\_^{18}\mathrm{O}}$ declines under high humidity, resulting in smaller gradients in $\delta_{V\_^{18}\mathrm{O}}$ during vapor diffusion). In other words, the robustness of the Keeling-plot regression based on δ^{18}O is jeopardized under humid conditions. The second reason for the higher efficacy of δ^2H might be its lower error level with respect to dependence on water vapor concentrations for laser spectrometer, especially when w is either extremely low or extremely high [270, 273]. The third reason for choosing δ^2H was related to the different sensitivities of δ^2H and δ^{18}O to equilibrium and kinetic fractionation processes [274]: the value of ε_{eq} was dramatically higher for δ^2H than for δ^{18}O, such that analysis based on δ^2H yielded a lighter more lighter δ_E and a pronounced distinction between $\overline{\delta_E}$ and $\overline{\delta_T}$. This pronounced distinction could greatly constrain the uncertainties involved in T/ET analysis (Eq. 3.10). For example, the uncertainty levels for δ^2H and δ^{18}O in our T/ET results were comparable even though the errors involved in δ_{ET}, δ_E, and δ_T were higher for δ^2H than for δ^{18}O.

3.5.3 Pattern of ET partitioning during wetting–drying episodes

A decrease–increase in the T/ET pattern is often observed during the wetting–drying episodes associated with water inputs. For example, a study in an olive plantation revealed that T/ET was 100% during the preceding dry periods but dropped to 0.69–0.85 at midday following precipitation events [10]. Another study, of a semiarid winter wheat cropland, found that average T/ET was 0.80 when the soils were dry and dropped to 0.69 three days after precipitation [20]. This transient

effect of rainfall events on ET partitioning—*i.e.*, suppression of T and enhancement of E —were also observed in a cornfield in the immediate aftermath of rainfall events (up to several days) [223]. During Campaign 1 of our study, the transient decrease in T/ET was followed by an increase, from 0.58 to 0.98 during the five-day drying periods. A similar trend was also observed in a semiarid grassland in southeastern Arizona, USA, where mean daily T/ET increased from 0.35 on day 1 to 0.43 on day 3 following a 39–mm irrigation event [47]. Overall short-term T/ET results for our study (which ranged from 0.80 to 0.90 for our two campaigns) were consistent with those of other pertinent studies. For example, a six-day study in a temperate grassland reported an average T/ET of 0.83 [50]. In grassland ecosystems having a dense canopy, daily T/ET can increase to a maximum value of 0.9 ($LAI > 3\,\mathrm{m}^2\,\mathrm{m}^{-2}$) [90].

3.5.4 Soil water availability and root water uptake

in the mesic tallgrass prairie, most of the soil evaporation comes from water storage in shallow (10–20 cm depth) soils [260], while the majority of C4 grasses roots that are functionally significant in water uptake and leaf transpiration are distributed within the 1–m depth [198]. Though our mere observation of changes in water storage across the profile could not discriminate between water losses from E and those from T, the similarities in isotopic composition of plant xylem water and soil water in the 15-cm-depth layer, as well as the great variability in availability of shallow soil water, are evidence that the shallow soil layers (especially the top $10\,\mathrm{cm}$, until depletion) were the major sources for both E and T. As shallow soil moisture became depleted, root uptake gradually shifted to deeper soil layers (as deep as $1\mathrm{m}$) to supply plant transpiration. A study in an irrigated winter wheat cropland found similar deepening trend in root water uptake [275].

The mechanisms involved in root water uptake reflect the plant's survival strategy [276]. Because of methodological limitation, our study —was not able to fully describe the dynamics and mechanisms of root water uptake across the profile in response to changes in water availability —which would require high-resolution probing of stable water isotopes in soil and transpiration water using laser spectroscopy [277, 270]. Our short-term results were able to identify a certain flexibility in root water uptake; but given that the timescales at which vegetation is observationally

affected by drought in semiarid and subhumid biomes is relatively long [278], longer-term investigations of ET partitioning and vegetation responses will be needed to assess the sustainability of the tallgrass prairie under climate change—especially with the predicated decreases in soil water availability [228, 279] due to precipitation changes and drier summers [280].

3.6 Conclusions

The process of evapotranspiration involves complex biophysical mechanisms that drive the energy and mass exchanges between ground and atmosphere. The partitioning of ET is critical for elucidating these complex mechanisms, and it is also essential for assessing water use efficiency, which enables monitoring of ecosystem functioning and of ecosystem hydrologic response to climate change and land cover change. To help advance our knowledge of ET processes, we carried out an isotopic ET partitioning study on a mesic grassland in tallgrass prairie, during two dynamic wetting—drying episodes. We employed an isotopic two-source mixing model, for which (1) δ_{ET} was obtained by applying the Keeling-plot regression to high-frequency isotopic data of atmospheric water vapor measured by a field-deployable laser spectrometer; (2) δ_E was calculated by applying the Craig—Gordon model to the isotopic value of bulk surface soil water; and (3) δ_T was estimated from the isotopic composition of root xylem water during midday under the isotopic steady-state assumption. Daytime integrated values were calculated for δ_{ET}, δ_E and δ_T were calculated at daily interval. The actual fluxes of E and T was calculated on the basis of the ET partitioning results and eddy covariance measurements of the bulk ET flux. As an additional, parallel analysis, we examined the dynamics of changes in soil water storage for different layers across the soil profile.

We found low efficacy in our Keeling-plot regression analysis, but this low efficacy was explainable (more so for δ^2H than for δ^{18}O) by variations in both the molar mixing ratio and the isotopic composition of atmospheric water vapor. For δ_E, the equilibrium fractionation process was dramatically stronger for δ^2H and than for δ^{18}O, resulting in greater differences between mean values of δ_E and δ_T. For this reason, we selected δ^2H for the two-source mixing model. During Campaign 1, we observed a dramatic increase in daily T/ET (from 0.58 to 0.98) within five days

following precipitation, but a similar pattern was not observed during Campaign 2 —probably because the initial quantification of δ_{ET} was poor. The mean values of daily T/ET were 0.80 ± 0.06 and 0.09 ± 0.06 for Campaigns 1 and 2, respectively. The difference is possibly attributable to the dissimilar soil water availability across the profile. Although our methodology was somewhat limited and our observation only short-term, our findings did reveal a certain plasticity in root water uptake to a depth of $1\,\mathrm{m}$. But a more in-depth understanding of the interplay between soil water availability and ET partitioning will require further investigations—longer term and more detailed—to serve as a foundation for sustainable management of the endangered tallgrass prairie and its ecosystem services under current and predicted environmental conditions.

4. EFFECTS OF WOODY PLANT ENCROACHMENT ON ISOTOPIC COMPOSITION OF EVAPORATIVE WATER VAPOR FLUXES IN TALLGRASS PRAIRIE

4.1 Introduction

Woody plant encroachment (WPE) —the increase in the density and cover of woody plants into open grasslands and woodlands—is a global phenomenon over the past 100–200 years, especially in rangelands of the Americas, Australia, and southern Africa [215, 7, 281]. Few other regions have been altered by WPE as dramatic as in Southern Great Plains of North America [282]. The tallgrass prairies, especially th cross timbers eco-region, occupies a tension zone between humid deciduous forest and semiarid grassland, and has been quite sensitive to shifts in climate, land management and fire regime historically [283, 284]. Specifically, the prime causes for WPE appear to be the high and constant levels of grass herbivory by domestic animals with a concomitant reduction in fire frequency in globe [285, 284].

The extensive and accelerating encroachment by eastern redcedar (*Juniperus Virginiana*) in tallgrass prairie could substantially alter many ecohydrologic processes. For example, WPE could cause rainfall redistribution [286], reduction in both stream flow [287] and deep drainage [288]. Shrub invasion might affect ET due to the change of ecosystem structure and function in four aspects: lower LAI in shrublands than in grassland; deeper roots of shrubs; the phenology of C4 grasses only transpire during growing season while C3 shrubs transpire year wide; and soil erosion in shrublands promotes spatially heterogeneous and deeper infiltration by altering the soil texture [3].

The ecohydrologic implications of shrub encroachment still uncertain [289, 276]. Given that ET is the largest water-loss flux in the endangered tallgrass prairie [218, 219], accurate quantification of ET and detailed description of various diffusive pathways is one of the key topics for investigating the water budget under woody plant encroachment. Water vapor exchange and ecosystem water usage are mainly controlled by plant transpiration (T) and constraint of shallow

soil moisture. The biometeorological factors controlling ET variability, such as photosynthetic active radiation (PAR), vapor pressure deficit (VPD), and temperature, are different from sub-daily to inter-annual scales in tallgrass prairie [219].

The bulk ET flux during woody plant encroachment might keep constant [3, 290] (especially in arid regions) or increase [34]. But T/ET could vary greatly among ecosystem types because of variations in interactions among plant morphology, environmental conditions, and stomatal regulation [13]. Studies are inclined to conclusion that the conversion from herbaceous-dominated rangeland to redcedar woodland enhance canopy interception and vegetation transpiration [291, 292]. The mean rooting depth or depths of active root water uptake might vary along the woody plant encroachment, so do pattern of ET partitioning because plant available water is depended on the soil water potential and the vertical location of water in the soil column [33, 32]. A mechanistic understanding the controlling effects of biological and non–biological processes on ET and its partitioning is the key to evaluate the consequences of woody plant encroachment on water and carbon cycling [106, 39, 34].

Stable isotopologues of water (^{2}H and ^{18}O) at natural abundance levels has been widely used to study plant-water relations and patterns of root water uptake, and to trace evaporative water flux among different diffusion pathways in terrestrial ecosystems [256, 27]. The various diffusive pathways of evaporation and plant transpiration from ecosystems are difficult to determine using traditional hydrometric observation. While no fractionation is assumed for most root water uptake processes for plant transpiration [261], strong fractionation effects occur during phase change involved in physical soil evaporation processes. Distinction in these diffusion pathways are the basis for using stable water isotopes to trace the different evaporative water fluxes. Recent advancement in field deployable laser spectroscopy, which enables continuous measurements of δ_v with high temporal resolution, providing a promising opportunity not only for determining δ_E [74, 75] and δ_{ET} at ecosystem level [293, 294], but also in evaluating the effect of plant transpiration on atmospheric water vapor within the ecosystem boundary layer [295, 272, 10].

Few investigations on isotopic ecohydrologic processes have been reported in the region of

tallgrass prairie. Using a methodology that combines micro-meteorologic measurements with intensive isotopic sampling, we aimed to investigate the effects of woody plants encroachment on the pattern of evaporative diffusion processes. Our isotopic sampling includes high-temporal resolution measurement on δ_V, accompanied by δ_{leaf}, δ_X, and δ_{soil} among three ecosystems in an Oklahoma tallgrass prairie-oak woodland mosaic undergoing eastern redcedar encroachment. We focused on three questions:

- how the isotopic composition of water in various ecohydrologic pools effected by WPE?
- which evaporative pathways are altered by WPE from an isotopic perspective?
- What's the implication on ET and its partitioning along WPE based upon results of δ_{ET} and δ_E?

4.2 Materials and Methods

4.2.1 Study area

This study was conducted at the Range Research Station ($36°2'34.1''$N—$36°4'19.1''$N, $97°9'27.9''$W—$97°11'37.8''$W, elevation about $330\,\mathrm{m}$ above sea level) of Oklahoma State University in north-central Oklahoma, USA (Fig. 4.1). Located at the western edge of the Cross Timbers ecoregion, the landscape in our study site is characterized by a mosaic of upland deciduous forest dominated by blackjack (*Quercus marilandica*) and post oak (*Quercus stellata*) on coarse-textured soils, and tallgrass prarie occurring on fine-textured soils. Eastern redcedar started to encroach into this station in the 1970s and encroached shrubland or savanna patches has been formed [296].

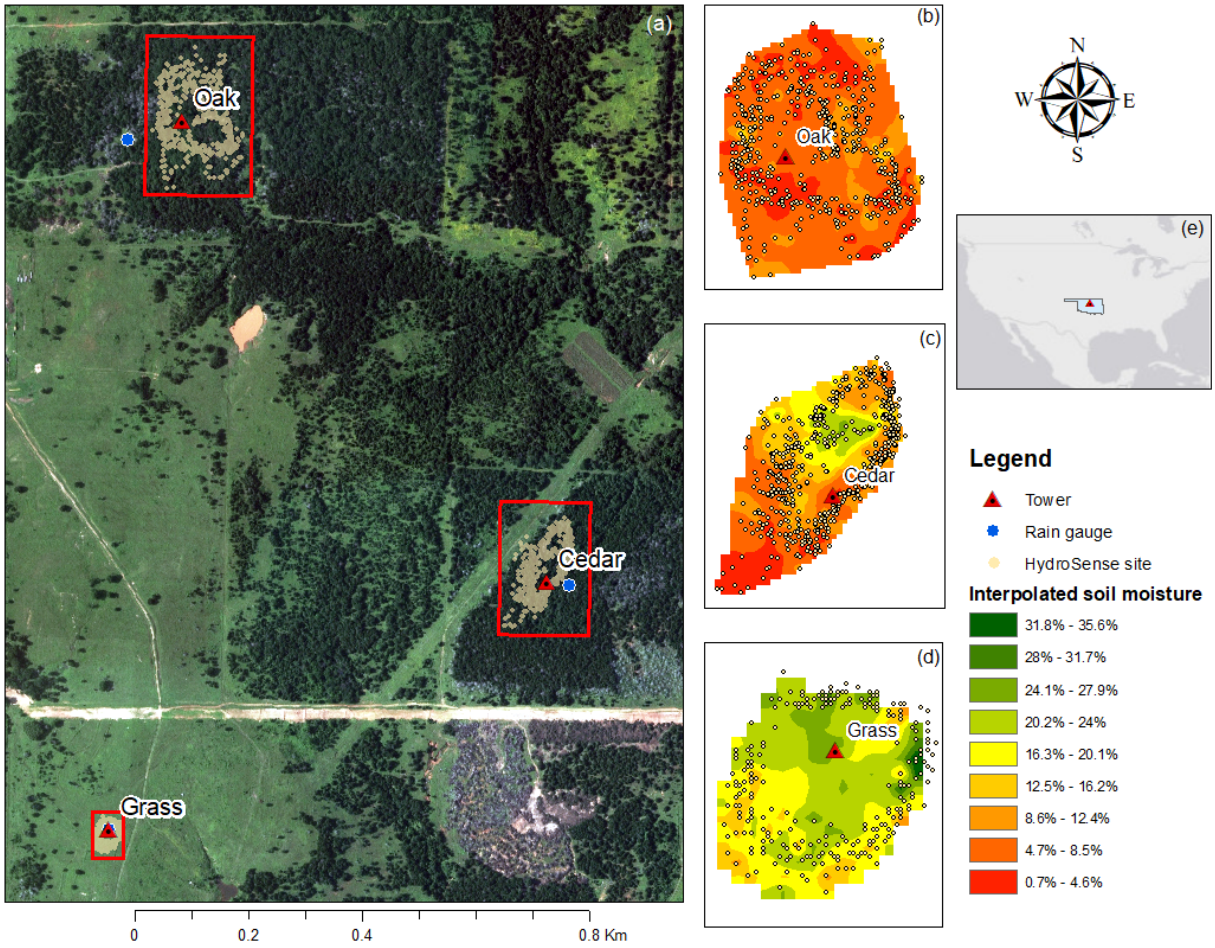

Figure 4.1: Study site showing the three ecosystems in a mosaic landscape in tallgrass prairie: grassland, oak woodland, and juniper woodland. The background image in (a) was obtained by the National Agriculture Imagery Program on June 23, 2015 (https://earthexplorer.usgs.gov/).

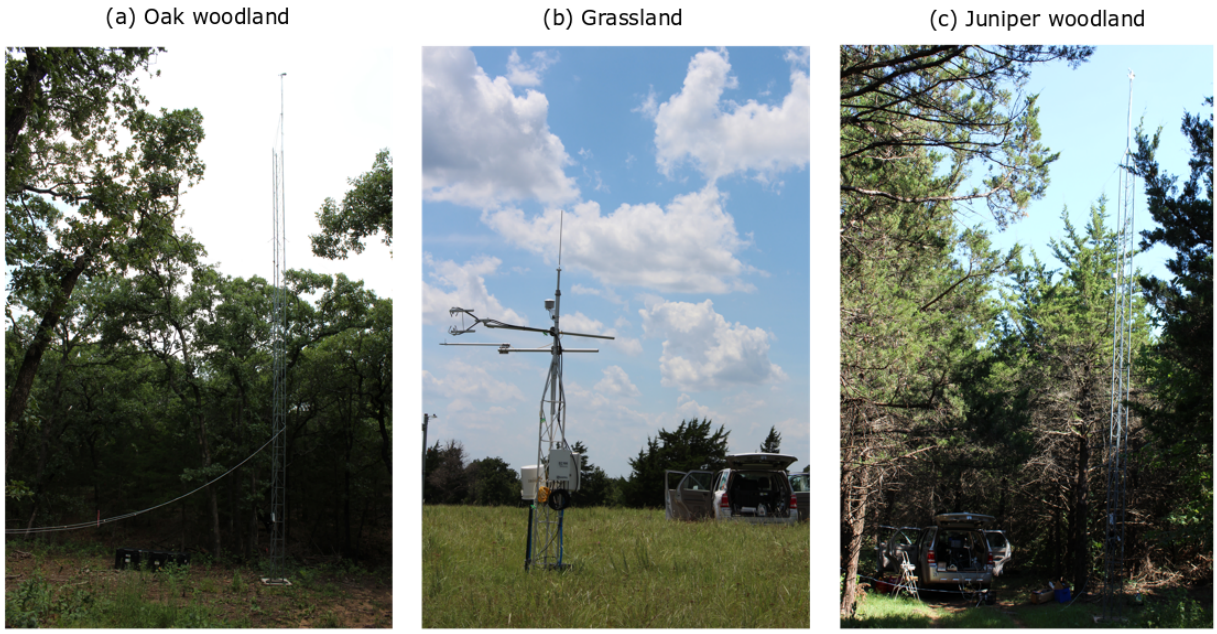

Figure 4.2: Three ecosystem types.

Grassland site were dominated by big bluestem (*Andropogon gerardii*), Little bluestem (*Schizachyrium scoparium*), indiangrass (*Sorghastrum nutans*), and switchgrass (*Panicum virgatum*). Oak site were dominated by post oak (*Quercus stellata*) and blackjack oak (*Quercus marilandica*), with developed understory vegetation. The understory herbaceous layer was also developed in small gaps and hardly existed under dense cedar canopy. We selected three major types of ecosystems (Fig. 4.2)—native tallgrass prairie grassland (hereafter "Grass"), encroached redcedar woodland ("Cedar"), and oak woodland ("Oak").

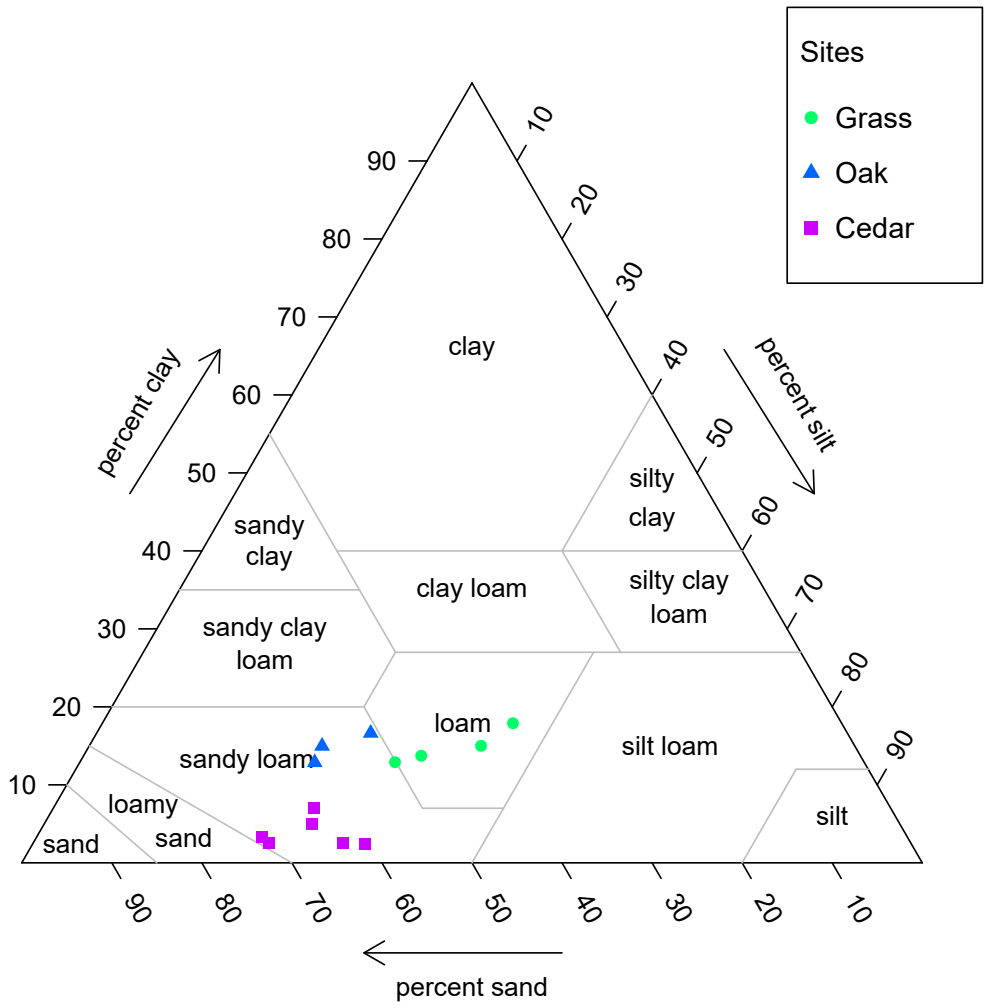

Figure 4.3: Soil texture for surface soils in 15 cm-depth for grassland, juniper woodland, and oak woodland.

The soil texture for the shallow layer (within 15-cm) is loam in grassland and sandy loam in two woodlands (Fig. 4.3). The terrain in grassland is mostly flat (with slopes of 1% to 8%), and the major (74%) and minor (26%) soil type are Coylem loam and Stephenville-Darnell complex; and in oak woodland, the dominant type of soil was Stephenville fine sandy loam, with slopes between

3% and 5%; and in juniper woodland, the dominant soil type (93%) is also Stephenville-Darnell complex, rocky with slopes of 3% to 8%. The minor type of soil type for oak and juniper site is Harrah-Pulaski frequently flooded complex, very rocky with slopes between 0% and 12% [155].

4.2.2 Bio-meteorologic measurements and isotopic water sampling

Besides long-term measurement on vegetation characteristics and micro-meteorologic processes, we carried out an intensive field campaign in July of 2016 on isotopic composition of waters in various ecohydrologic pools among these ecosystems.

4.2.2.1 Biometeorology measurement

An arrange of micro-climate sensors were installed close or upon the towers within these three sites. A photo-synthetically active radiation (PAR) sensor (model: QSO-S, Decagon Devices Inc., Pullman, WA, USA) was installed above the canopy (approximately $1.5\,\mathrm{m}$ in grassland, and 12-15m in woodlands) to measure photosynthetic photon flux density ($PPFD$, in $\mathrm{mmol\,m^{-2}\,s^{-1}}$) from a field of view of 180°. At the same heights, a pair of spectral reflectance sensors (SRS, Decagon Devices Inc., Pullman, WA) were also set up to measure the Normalized Difference Vegetation Index ($NDVI$). We also positioned a leaf wetness sensor (model LWS, Decagon Devices Inc., Pullman, WA) close to foliage (positioned close to foliage with a distance of about $30\,\mathrm{cm}$ with an angle of 45 °to the horizontal). Micro-climate was measured at $3\,\mathrm{m}$ at grassland (above canopy) and about 6-8 m in woodlands (beneath the top canopy layer) with an sensor for air temperature (T_{air}, in $^{\circ}\mathrm{C}$), air relative humidity, and atmospheric pressure (P in mbar) (VP-4 , Temp/RH/Barometer, Decagon Devices, Pullman, WA, USA) with radiation shield. The saturation vapor pressure (e_s in mbar) and VPD (an indicator of atmospheric evaporation demand, in mbar) were calculated based on the air temperature (T_{air}, in $^{\circ}\mathrm{C}$) via the Magnus-Tetens equation [252]. Data from these sensors were stored in a datalogger (EM50, Decagon Devices Inc., Pullman, Washington) with a frequency of $5\,\mathrm{min}$), and 30-min averages were consequently calculated.

4.2.2.2 Soil moisture measurement

Around the measurement tower within each site, volumetric water content (θ in $\mathrm{m^3\,m^{-3}}$) of surface soil layer was manually measured using a portable time-domain reflectometry (HydroSense-II sensor paired with CS659 $12\,\mathrm{cm}$ soil water rods, Campbell Scientific Inc., Utah, USA). The area of the minimum convex hull for each site are 2.26×10^3, 14.0×10^3, and 30.4×10^3 for Grass, Juniper, and Oak sites, respectively (Fig.4.1).

4.2.2.3 Intensive campaign on isotopic composition of water

In June of 2016, we carried out an intensive field campaign to sample the isotopic composition of waters in various ecohydrological pools. The *in situ* sampling was rotated among the three sites (Oak, Juniper, and Grass) from July 9, 2016 to July 24, 2016, except interruption in July 14, 2016 due to precipitation events. A field-deployable laser spectrometer was used to measure the isotopic composition of atmospheric water vapor (δ_V), from which δ_{ET} can be calculated via the Keeling-plot approach. Liquid water was sampled from surface soils ($15\,\mathrm{cm}$-depth) and plants, *i.e.*, bulk leaves (δ_{leaf}) and xylem (δ_X, grass roots or tree stems).

Isotopic composition of soil water (δ^2H and δ^{18}O) across the profile were collected at the end of our field campaigns, which was July 22, 2016 in Oak, July 23, 2016 in Cedar, and July 24, 2016 in Grass; The sampling depth was $70\,\mathrm{cm}$, $120\,\mathrm{cm}$, $110\,\mathrm{cm}$, respectively.

Isotopic sampling of water vapor was carried out mostly between 10am and 6pm, except July 6, 2016 when the measurement only carried out after 3:30pm due to logistic issues. Isotopic sampling of waters in grassland was same as in Section 3.2.4. Instead of root crowns in grassland, randomly selected tree stems were sampled from the top twig under sunlit for xylem water. The stems were immediately cut into small segments, and then placed in vials $4.3\,\mathrm{L\,min^{-1}}$ (part No. 10D1125-101-1053, Gast Inc., Benton Harbor, MI, USA) and sealed with parafilm®.

We applied same processing procedures (Section 3.2.4.1) for quality control of δ_V, and used the same cryogenic method to extract water and analysis on mass spectroscopy (Section 3.2.4.2). Calculation of δ_{ET} and δ_E were also same as methods in Section 3.3 aforementioned.

4.3 Results

4.3.1 Environmental factors

Within 15 days preceding to the sampling campaigns (June 24, 2016–July 8, 2016), four major precipitation events occurred with accumulated depths around 80 mm in Grass and Cedar sites and $99\,\mathrm{mm}$ in Oak. During our campaign, a rainfall series mainly occurred between midnight of July 13, 2016 and July 14, 2016 with accumulated depths of 17.3–19.8 mm among three sites (Fig. 4.4a). This precipitation event occurred around the midnight in the two woodlands (Oak and Cedar), and was relatively lagged behind in Grass site. Corresponding to this rainfall events were wet leaf period, with maximum value of more than $8\mathrm{h}$ in Grass and $12\mathrm{h}$ in Cedar (Fig. 4.4b). One unique phenomena in Grass is higher frequency of dew before dawn.

Solar radiation exhibited high daily variation as expected by weather change, and $PPFD$ especially dropped at July 11, 2016 and July 14, 2016 due to cloudy weather or rainy events, respectively and (Fig. 4.4c). Air temperature (T_{air}) was relatively stable precedent to the precipitation events, and was gradually increased following the precipitation events (Fig. 4.4d). As expected, daily processes of h_{air} exhibited opposite patterns with relation to T_{air} (Fig. 4.4e), while daily trends of VPD nearly mirrored the T_{air} patterns (Fig. 4.4f). With increasing VPD following the precipitation, all ecosystems gradually experienced enhanced atmospheric water demand.

As anticipated, the $NDVI$ values were dramatically higher in woodlands (about 0.80-0.85) than in grasslands (around 0.70) (Fig. 4.2 and 4.4g), indicating higher above-ground biomass along the woody plant encroachment. However, the shallow soil moisture in grasslands were consistently wetter than in woodlands , while θ_{12} was slightly and steadily wetter in Cedar than in Oak (Fig. 4.1 and 4.4h).

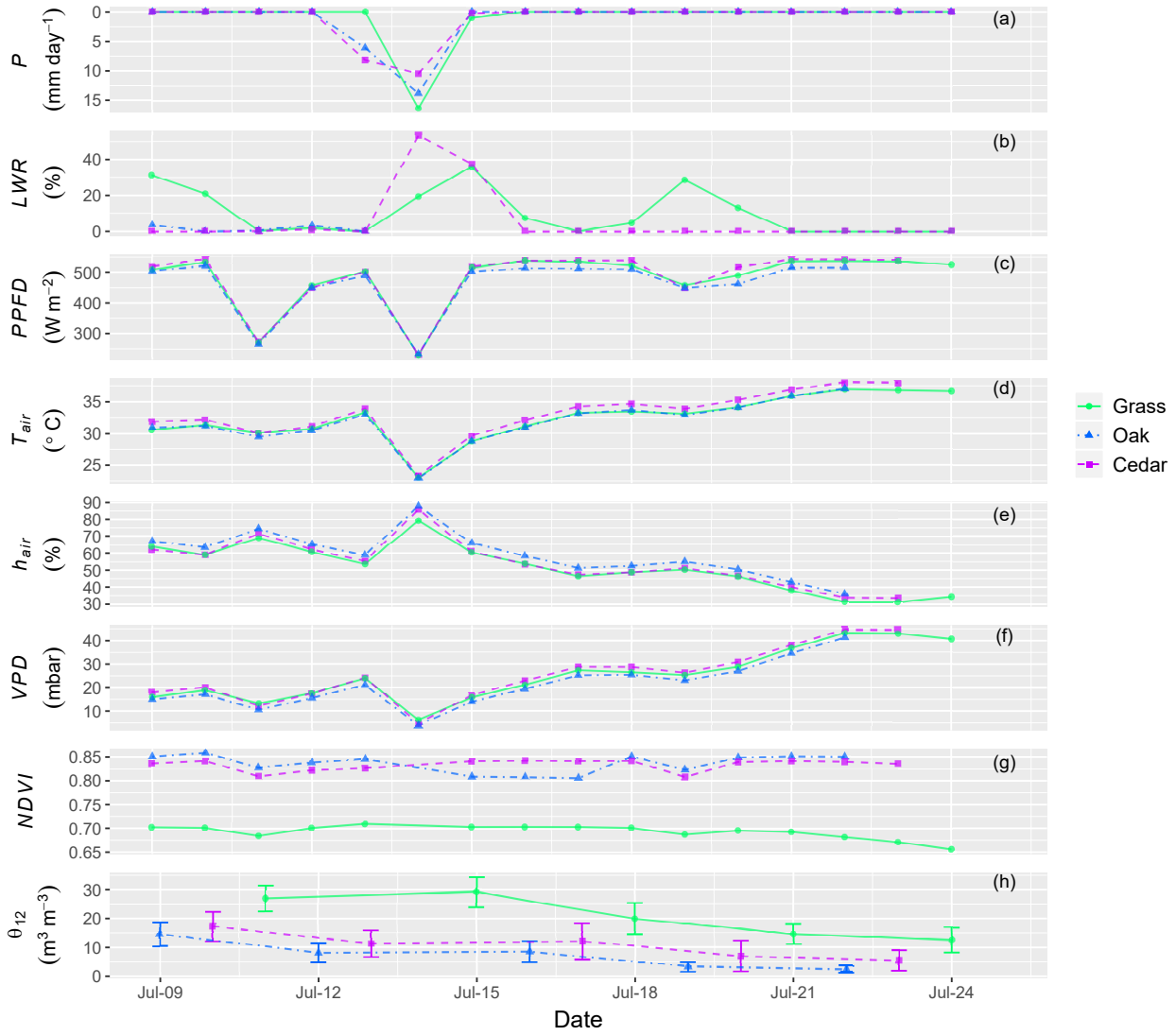

Figure 4.4: Daily processes of environmental factors measured in Grass, Oak, and Cedar sites. Note that daily P and LWR were calculated on 24-hour period. LWR data in Oak following July 14, 2016 were not shown due to sensor malfunctioning. $PPFD$, T_{air}, h_{air}, and VPD were calculated for daytime period between 10am and 6pm. Daily $NDVI$ data were calculated based on data series between noon and 2pm for each day. The $NDVI$ data in July 14, 2016 was not available due to midday raining event. θ_{12} was based on daytime manual sampling of surface soil moisture, with error bar stands for one standard deviation (SD) for daily measurement.

4.3.2 Stable isotopes as tracers

As expected, the dual-isotope plot (Fig. 4.5) revealed isotopically lighter water vapor and isotopically heavier residual water in soils and leaves for all the three ecosystems. Especially for the

leaf water highly enriched in heavier isotopes (^{2}H and ^{18}O) with deviated slopes, indicating strong kinectic fractionation effect at the evaporation sites within the leaves. Maximum enrichment of δ^{2}H and δ^{18}O in leaf water was observed in dry air and minimum enrichment occurred in wet air after precipitation in July 14, 2016. Highly enriched leaf water relative to xylem and soil water has been reported from various ecosystems [297]. In Fig. 4.5, δ_{soil} and δ_X are closely distributed in the grassland, while separately distributed in the two woodlands. For the oak and cedar, δ_X is isotopically lighter than δ_{soil} in the shallow layer, implying that tree had access to deeper soil water with lighter isotopic composition. As shown in Fig. 4.6, deeper soil layers exhibited lighter isotopic composition while shallow soil moisture was substantially enriched in heavier isotopes due to evaporative enrichment effect. These phenomena, including isotopically lighter δ_V, isotopically heavier δ_{leaf} and δ_{soil}, and comparison between δ_{soil} and δ_X, were also displayed in time series in δ^{2}H of these isotopic values (Fig. 4.7).

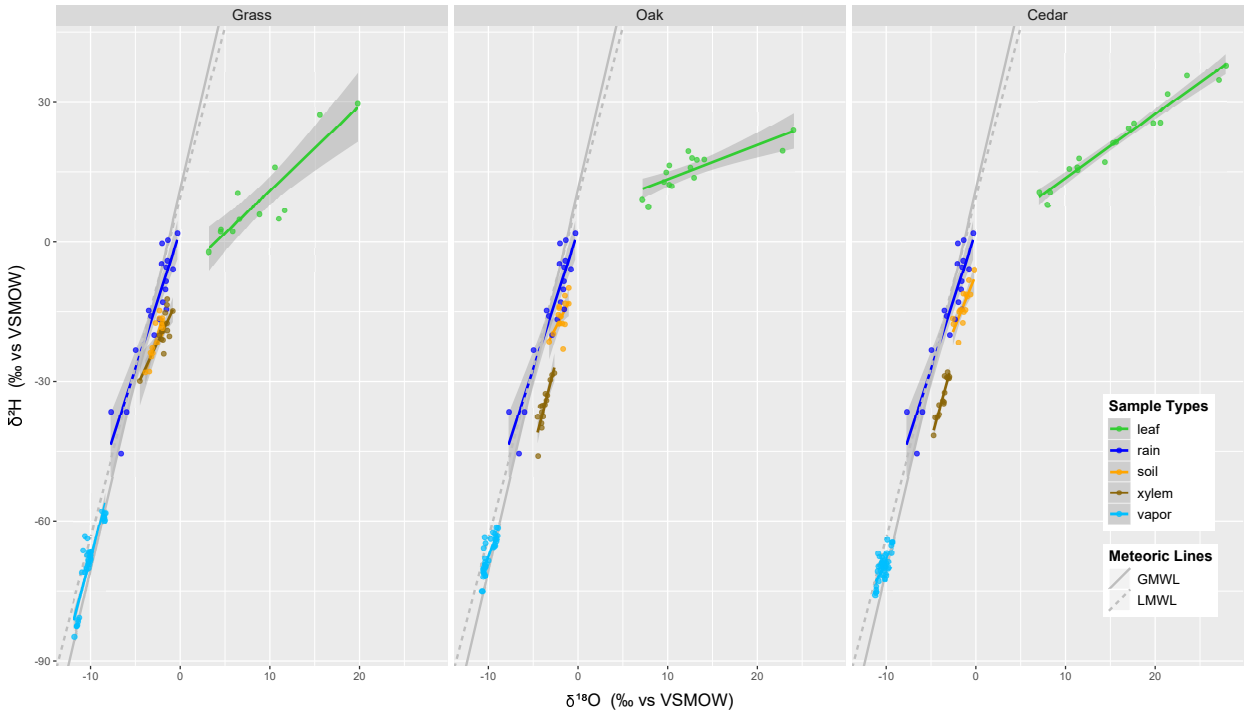

Figure 4.5: Dual-isotope space for waters sampled from various ecohydrologic pools during the intensive field campaigns. These water pools include the upper $15\,\mathrm{cm}$ soil layer, plant leaves, xylem (tree stems or grass roots), and hourly near-ground atmosphere. Isotopic composition of rainfall throughout 2016 was plotted against Local Meteoric Water Line (LMWL, dotted, $\delta^2\mathrm{H} = 7.32\,\delta^{18}\mathrm{O} + 9.5$) from a long-term observation in Norman, Oklahoma [262], and Global Meteoric Water Line (GMWL, solid, $\delta^2\mathrm{H} = 8.20\,\delta^{18}\mathrm{O} + 11.3$) [263].

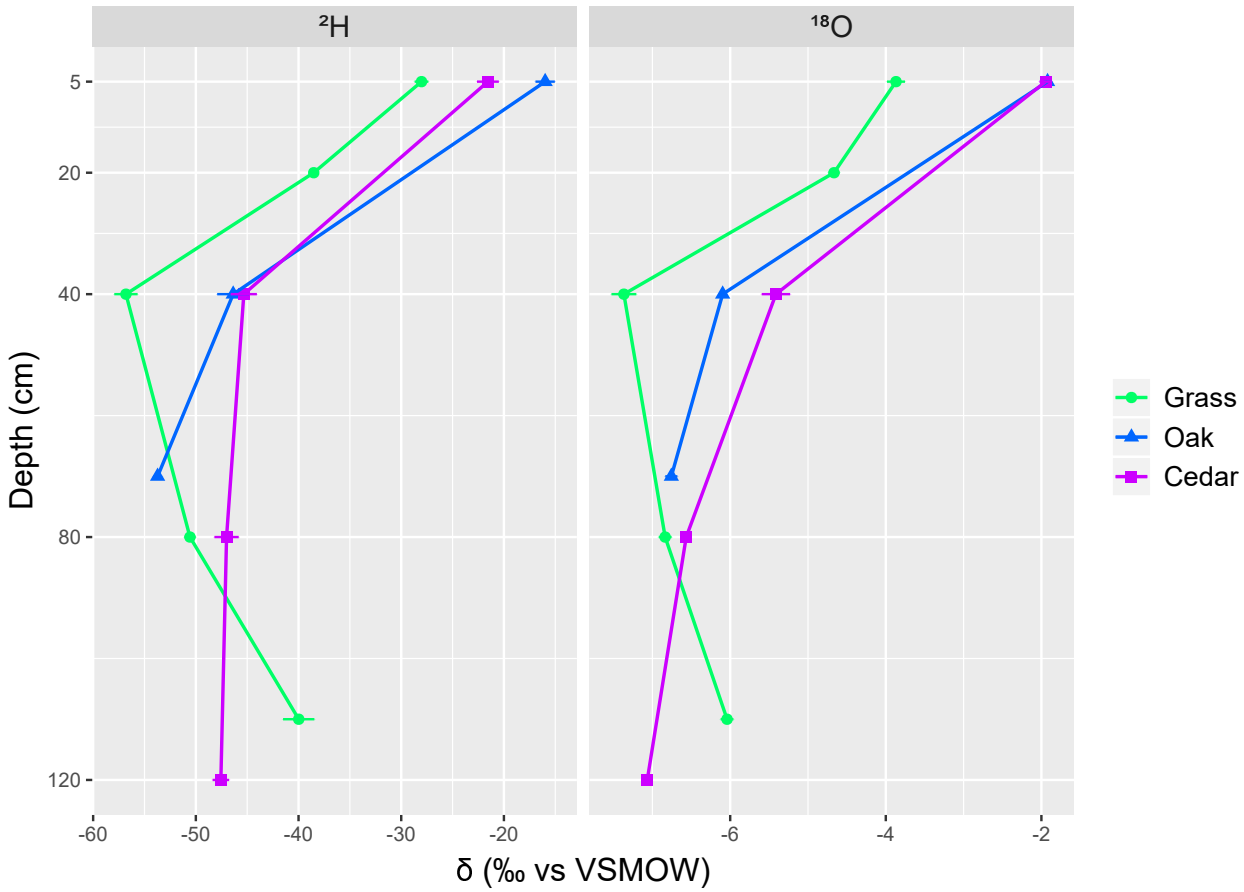

Figure 4.6: Isotopic composition (δ^2H and δ^{18}O) of soil water across the profile in the three types of ecosystem.

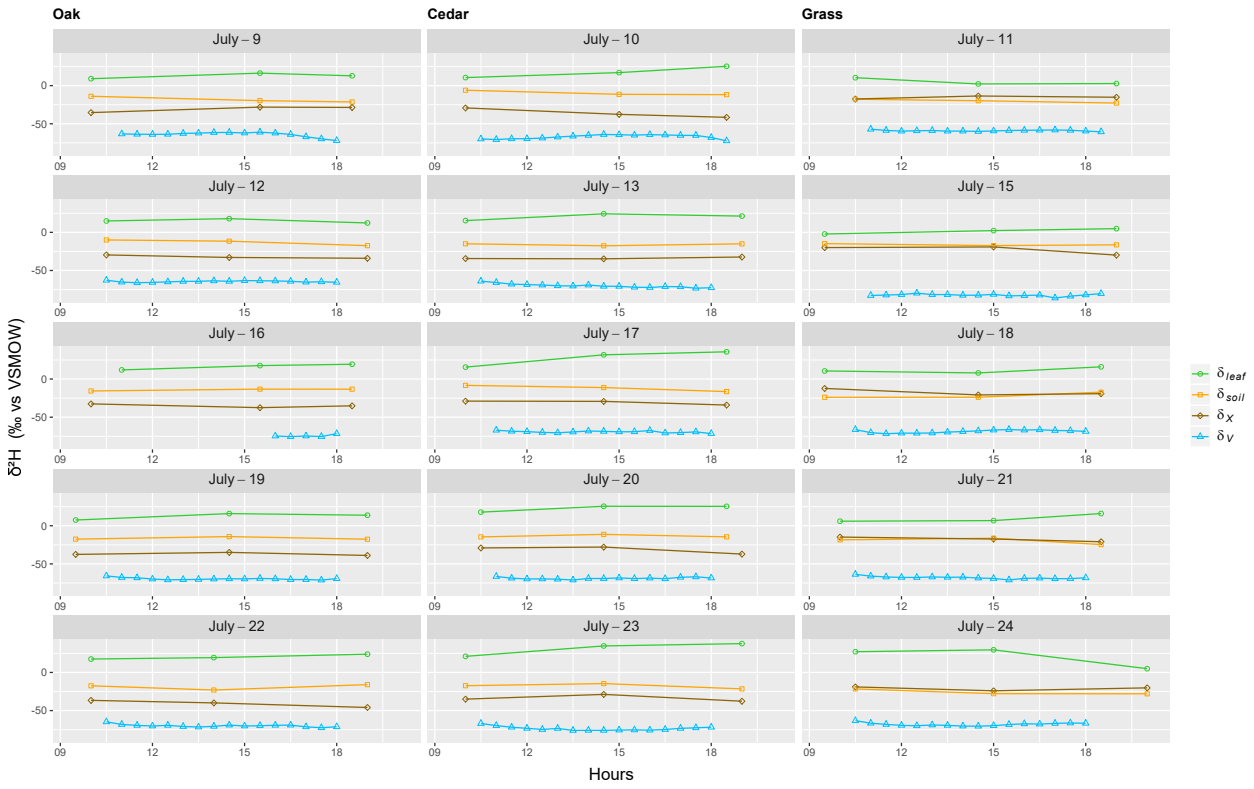

Figure 4.7: Diurnal variation of δ^2H Time series of δ^2H of sampled waters in various ecohydrologic pools. half-hourly δ_V

4.4 Discussion

In dryland ecosystems, a tight coupling exists between ecosystem productivity, surface energy balance, biogeochemical cycles, and water resource availability [16], because temporal variation in water availability drives pulses of high and low biotic activity in these arid and semi-arid systems [87]. Partitioning of ET is essential for understanding how woody plant encroachment will alter water and carbon cycling [289]. The mean rooting depth or depths of active root water uptake might vary along the woody plant encroachment, so do ET partitioning because plant available water is depended on the soil water potential and the vertical location of water in the soil column [49, 103].

4.4.1 Environment

Our results on soil moisture (Fig. 4.1 and 4.4h) echoed the widely reported depletion of soil moisture under WPE, especially the subsurface soil layer [298, 292]. This difference in soil moisture is mainly resulted by high interception at the canopy layer [286] and litter layer [299] with comparison to grassland. Juniper forests were mainly distributed in sandy and loamy soils with low top soil water availability [300].

4.4.2 Two-layer hypothesis and niche complementary

Competition between different functional types (such as shrubs and grasses) can be avoided vertically by different rooting depths of plants, namely two-layer hypothesis [301], or by keying on particular window of moisture availability via difference in phenologies [302], namely temporal partitioning. Two-layer hypothesis proposes that differences in rooting depth (thus root water uptakes) between trees and grasses result in niche partitioning (and therefore tree-grass coexistence), with grasses exploiting soil moisture in shallow layers while trees have exclusive access to deep water [301]. This hypothesis was developed for drier savannas (*i.e.*, $\leq 500\,\mathrm{mm}$ annual precipitation), but it is often applied to a wide range of arid and semi-arid ecosystems [303]. Based on an analysis of a global dataset of more than 1300 observations for individual plants for deserts, scrublands, grasslands and savannas with annual precipitation (MAP) less than 1000 mm mean, the twolayer hypothesis might be most appropriate in drier regimes ($\leq 500\,\mathrm{mm}$ MAP) and in regions with substantial winter precipitation [304].

Stable isotopes of soil water across the profile and vegetation (xylem) water can be used to test these hypothesis. For a subalpine shrubland, stem waters of the dominated *Quercus aquifolioides* in shrub layer and dominated Cystopteris montana in herbage layer show different isotopic composition, indicating different depths of root water uptake [48]. Study with stable isotopes of water in semi-arid grassland revealed that two C4 grasses extracted most of their water from the upper soil profile (0.05-0.5 m), *Pinus ponderosa* acquired a large fraction of water from both the 0.050.5 and 0.50.9 m soil layer, while J. *virginiana* showed more plasticity in tracking the general increase in

soil water content within the 0.50.9 meter profile and was less responsive to growing season precipitation events [235]. Studies using the isotopic composition of xylem water of C4 grasses, C3 forbs and C3 shrubs in tallgrass prairie support soil water partitioning as a mechanism for species coexistence, as C4 species is consistently rely on shallow soil water, while C3 species show niche differentiation in water use strategies across the soil profile to avoid competition with C4 grasses [305]. Woody plant encroachment may continue in the future should precipitation intensity increase, because increase in precipitation intensity can push soil water deeper [306]. In addition, the sandy soil in many dryland ecosystems has good infiltration conditions, which is favorable for deep-rooted shrubs than herbaceous layer. Shrubs are also more resistant to high temperature [307].

Rooting depth in grassland and shrubland is usually shallower than depth in cropland and woodland based on results retrieved in synthesis, so does root water uptake. 70% of the total fine root mass is confined within $0.15\,\mathrm{m}$ of the surface for Chihuahuan Desert shrubland [34], 87% of the root are distributed within 20 cm of soil for a typical dry land perennial grass eld with a sparse cover of a C4 herbaceous layer dominated by species from the Cynodon genus [49], more than 80% root biomass is distributed in the first 30 cm soil layer at fenced temperate grassland dominated with C3 species [50], the main root zone of was reported to be between 20 cm and 40 cm for an open semi-arid forest dominated with Aleppo pine (*Pinus halepensis* Mill.) [36], the active rooting depth for wheat can reaches its maximum of 50 cm at maturity stage [46] and much more concentrated above $40\,\mathrm{cm}$ [5]. The Root Water Uptake model should be parameterized with isotopic composition of xylem water during labeling experiments, and the incorporation of isotopic transport through soils and roots could provide insights into the existence of niche complementarity between tree and grass species [98]. More knowledge of how roots grow and function for different functional groups of vegetation is needed to predict how woody plant encroachment involves under climate change, because soil moisture and belowground nutrient resources become more limiting to plant groowpth in dryland ecosystems.

4.4.3 Evapotranspiration partitioning under woody plant encroachment

Woody plant encroachment often results in a decrease in vegetation cover and increase in bare-soil surfaces [34], and the fractional contribution of bare soil evaporation might increase in semi-arid ecosystems but is negligible in sub-humid and arid ecosystems [289]. Modeling results from experimental tree mosaics showed that total ET increased with woody cover, but T/ET deviated below 1:1 proportionality due to suppression in transpiration with increasing tree cover but not due to differences in soil evaporation [93]. The small precipitation events (ranging from 5 cm to 15 cm) in arid savannas only wet the upper centimeters of the soil and inaccessible to the shrub roots [235], thus grasses are showed much more effective in water uptake from the uppermost centimeters of the topsoil [305]. For example, T/ET was higher for the grass-dominated site than for the shrub-dominated site in southeast Arizona, USA, may related to the higher water use efficacy for grasses [58].

On the other side, woody vegetation showed strong tolerance to long droughts, transpiring at rates close to potential even during the driest conditions, while grass is much less tolerant to soil moisture and withdraw after rainy season in semiarid Mediterranean regions [308]. An isotopic ET partitioning in eastern Mongolia showed that the T/ET was 60-73% at the forest site and 35%-59% at the grassland site [309]. For a California oak savanna, variability in annual ET under different level of precipitation (dry vs wet years) was primarily attributable to the variability in grass transpiration and soil evaporation rather than to that of tree transpiration [86]. Modelling results in sub-tropical savanna also showed that shallow grass root distributions absorbed 32% less water than slightly deeper tree root distributions when grasses and trees were assumed to have equal water demands [310]. Even under the shallow infiltration and the large amount of bare soil, shrubs in a Chihuahua desertthe majority (70%) of fine root is found within 15 cmshowed great capacity (after recovering from dormant state in drought) to access much of the available soil moisture [34]. Thus, temporal variation in water availability may create positive feedbacks to facilitate encroachment of C3 woody species into grasslands dominated by C4 grasses [87]. An ecosystem model driven by long-term meteorological data showed that inter-annual variability in

precipitation enabled shrubs to be more competitive than grasses in semi-arid shrub communities [307]. A dynamic vegetation model reported that fire was required for the coexistence of trees and grasses when deep soil water was available to trees [143].

While T/ET studies under woody plant encroachment is very limited [7], especially for *in situ* studies, understanding of the mechanism and trends of ET and its partitioning is still largely unknown. We are inclined to believe that the dynamics of T/ET along woody plant encroachment might depend on types of plant structural attributes (including LAI) [93], climate variability and differential plant functional responses [34]. The partitioning method and spatial-temporal scales should also be congruent for comparison.

5. CONCLUSION

In drylands, ET is the dominant ecohydrologic process. For this reason, partitioning of ET, determining the relative importance of interception (I), soil evaporation (E), and plant transpiration (T), is critical, but remains a challenge. Recently, however, advances in measurement technologies and data availability have triggered an upsurge in *in situ* studies focused on quantifying T/ET. We carried out a meta–analysis of 38 datasets drawn from 31 studies done in drylands worldwide. This analysis showed that over the growing season, E and T are roughly equivalent for most natural ecosystems, whereas T/ET is higher in irrigated agro-ecosystems. With respect to factors controlling variations in T/ET, we found that:

- no clear correlation for annual precipitation, soil texture, or ecosystem type;
- leaf area index is a more significant controlling factor than fractional cover;
- T/ET varies most during dynamic wettingdrying episodes.

We also found that controlling factors are different for E and T. Because these two processes differ in temporal dynamics, the factors controlling ET partitioning vary with temporal scale. Further, when interception and shallow groundwater are substantial, including these factors is essential for accurate T/ET quantification. The isotopic approach, especially using laser spectroscopy, is now indispensable for such studies. However, issues related to sampling protocols and quality assurance still must be resolved. We propose three promising topics for future studies in drylands:

- isotopic sampling of vadose-zone water vapor using laser spectroscopy;
- improved definition/identification of diffusive pathways;
- robust upscaling from incongruent hydrometric and isotopic measurements.

We carried out a paired study in tallgrass prairie to evaluate the influence of vegetation on the energy exchange and ET. Two eddy–covariance systems were installed over two adjoining

sites, one of which was denuded of vegetation, with the adjacent, control site kept undisturbed. Our year-long investigation shows that, for quantifying the ground surface heat flux, the soil heat storage above the soil plates is more important than the sub-surface soil heat flux, both temporally and in magnitude. The incorporation of the soil heat storage, therefore, is indispensable for energy balance closure in areas with short vegetation. At our control site, we observed a critical threshold of $0.17\,\mathrm{m^3\,m^{-3}}$ in the surface (top $0.3\,\mathrm{m}$) soil water content, whereby the energy partitioning is significantly affected by the presence of the photosynthetically active vegetation when the surface soil water content is higher than this critical threshold. The pattern of energy partitioning approaches that of the treated site when the surface soil water content is lower than this threshold (during drought), because of the suppression of plant physiological activities. This threshold also applies to the surface conductance for water vapour at the control site, where yearly evapotranspiration is $728 \pm 3\ \mathrm{mm}$ (versus $547 \pm 2\ \mathrm{mm}$ for the treated site). Thus, the soil water content and presence of active vegetation are the key determinants of energy partitioning and evapotranspiration. Any land-cover changes or vegetation-management practices that alter these two factors may change the energy and water budgets in tallgrass prairie.

We applied a two-source isotopic mixing model to partition the bulk ET flux in a tallgrass prairie site. Two field campaigns were conducted in the summer, one for relatively wet antecedent soil conditions and the other for drier antecedent conditions before the precipitation events. The isotopic compositions of ET, E, and T (δ_{ET}, δ_E, and δ_T) were determined by the Keeling-plot method, the Craig—Gordon model, and plant xylem water sampled during midday, respectively. We determined that proportions of the components of ET could be more accurately determined with ^{2}H than with ^{18}O, because of

- its higher efficacy and robustness in the Keeling–plot regression
- its higher values of equilibrium fractionation factors during soil evaporation.

Using ^{2}H, we found that T/ET was 0.80 for campaign 1 with wet antecedent soil condition and 0.90 for campaign 2 with relatively dry antecedent soil conditions. Soil water in the shallow soil

layer (especially the top $10\,\mathrm{cm}$) responded actively during these two wetting–drying episodes and was the major source for the ET flux during the initial dynamic drying periods. Only after shallow soil moisture had become substantially depleted did deeper soil layers (up to $1\,\mathrm{m}$) increasingly become the major source for the T flux, while the E flux declined more and more.

We carried out an intensive campaign for sampling and measuring isotopic composition of waters in various ecohydrologic pools over grasslands and encroached oak and juniper (*Juniperus Virginiana*) woodlands in the region of tallgrass prairie. Waters in plant and soils were sampled discretely, extracted via cryogenic vacuum distillation, and analyzed using traditional isotope mass ratio spectroscopy (cold trap/mass spectrometer analysis). We used the same high temporal–resolution laser spectroscopy for isotopic sampling of atmospheric water vapor, and then derived the isotopic composition of evapotranspiration (ET) or δ_{ET} via Keeling-plot approach. These results suggest that as grasslands are gradually shifted into woody plants in tallgrass prairie, soil moisture from deeper layers are more easily be consumed by trees with deeper roots. The shallow soil moisture in woods (especially the oak site) are more depleted than in grasslands, probably because of higher interception and thus less replenishment of surface soil layer in the two woodlands. The value of δ_X is higher than δ_{ET} The isotopic values of xylem water (δ_X) and δ_{ET} are close among these three ecosystems, implying that T is the dominate evaporative water flux during this peak growing season.

REFERENCES

[1] U. Safriel, Z. Adeel, D. Niemeijer, J. Puigdefabregas, R. White, R. Lal, M. Winslow, J. Ziedler, S. Prince, E. Archer, C. King, B. Shapiro, K. Wessels, T. Nielsen, B. Portnov, I. Reshef, J. Thornell, E. Lachman, and D. McNab, *Dryland systems*, vol. 1, pp. 623–662. Island Press, 2005.

[2] S. L. Berry, G. D. Farquhar, and M. L. Roderick, *Co-Evolution of Climate, Soil and Vegetation*, ch. 12. American Cancer Society, 2006.

[3] S. A. Kurc and E. E. Small, "Dynamics of evapotranspiration in semiarid grassland and shrubland ecosystems during the summer monsoon season, central new mexico," *Water Resources Research*, vol. 40, sep 2004.

[4] B. Wilcox, D. Breshears, and M. Seyfried, "The water balance on rangelands, encyclopedia of water science, edited by: Stewart, ba and howell, ta," *Encyclopedia of water science*, pp. 791–794, 2003.

[5] Y. Zhang, Y. Shen, H. Sun, and J. B. Gates, "Evapotranspiration and its partitioning in an irrigated winter wheat field: A combined isotopic and micrometeorologic approach," *Journal of Hydrology*, vol. 408, pp. 203–211, oct 2011.

[6] D. Kool, N. Agam, N. Lazarovitch, J. Heitman, T. Sauer, and A. Ben-Gal, "A review of approaches for evapotranspiration partitioning," *Agricultural and Forest Meteorology*, vol. 184, pp. 56–70, jan 2014.

[7] B. D. Newman, B. P. Wilcox, S. R. Archer, D. D. Breshears, C. N. Dahm, C. J. Duffy, N. G. McDowell, F. M. Phillips, B. R. Scanlon, and E. R. Vivoni, "Ecohydrology of water-limited environments: A scientific vision," *Water Resources Research*, vol. 42, jun 2006.

[8] L. Wang, K. K. Caylor, J. C. Villegas, G. A. Barron-Gafford, D. D. Breshears, and T. E. Huxman, "Partitioning evapotranspiration across gradients of woody plant cover: Assess-

ment of a stable isotope technique," *Geophysical Research Letters*, vol. 37, pp. n/a–n/a, may 2010.

[9] X. Lu, L. L. Liang, L. Wang, G. D. Jenerette, M. F. McCabe, and D. A. Grantz, "Partitioning of evapotranspiration using a stable isotope technique in an arid and high temperature agricultural production system," *Agricultural Water Management*, vol. 179, pp. 103–109, jan 2017.

[10] D. Williams, W. Cable, K. Hultine, J. Hoedjes, E. Yepez, V. Simonneaux, S. Er-Raki, G. Boulet, H. de Bruin, A. Chehbouni, O. Hartogensis, and F. Timouk, "Evapotranspiration components determined by stable isotope, sap flow and eddy covariance techniques," *Agricultural and Forest Meteorology*, vol. 125, pp. 241–258, oct 2004.

[11] J. R. Brooks, "Water, bound and mobile," *Science*, vol. 349, pp. 138–139, jul 2015.

[12] E. A. Yepez, D. G. Williams, R. L. Scott, and G. Lin, "Partitioning overstory and understory evapotranspiration in a semiarid savanna woodland from the isotopic composition of water vapor," *Agricultural and Forest Meteorology*, vol. 119, pp. 53–68, oct 2003.

[13] N. Raz-Yaseef, D. Yakir, G. Schiller, and S. Cohen, "Dynamics of evapotranspiration partitioning in a semi-arid forest as affected by temporal rainfall patterns," *Agricultural and Forest Meteorology*, vol. 157, pp. 77–85, may 2012.

[14] A. T. Austin, L. Yahdjian, J. M. Stark, J. Belnap, A. Porporato, U. Norton, D. A. Ravetta, and S. M. Schaeffer, "Water pulses and biogeochemical cycles in arid and semiarid ecosystems," *Oecologia*, vol. 141, pp. 221–235, feb 2004.

[15] S. Jasechko, "Plants turn on the tap," *Nature Climate Change*, vol. 8, pp. 562–563, jun 2018.

[16] L. Wang, P. D'Odorico, J. P. Evans, D. J. Eldridge, M. F. McCabe, K. K. Caylor, and E. G. King, "Dryland ecohydrology and climate change: critical issues and technical advances," *Hydrology and Earth System Sciences*, vol. 16, pp. 2585–2603, aug 2012.

[17] I. Braud, T. Bariac, J. Gaudet, and M. Vauclin, "SiSPAT-isotope, a coupled heat, water and stable isotope (HDO and h218o) transport model for bare soil. part i. model description and first verifications," *Journal of Hydrology*, vol. 309, pp. 277–300, jul 2005.

[18] J. Kroes, , J. van Dam, R. Bartholomeus, P. Groenendijk, M. Heinen, R. Hendriks, H. Mulder, I. Supit, P. van Walsum, , , , and and, "SWAP version 4," tech. rep., 2017.

[19] S. J. Sutanto, B. van den Hurk, P. A. Dirmeyer, S. I. Seneviratne, T. Röckmann, K. E. Trenberth, E. M. Blyth, J. Wenninger, and G. Hoffmann, "Hess opinions "a perspective on isotope versus non-isotope approaches to determine the contribution of transpiration to total evaporation"," *Hydrology and Earth System Sciences*, vol. 18, pp. 2815–2827, aug 2014.

[20] G. Aouade, J. Ezzahar, N. Amenzou, S. Er-Raki, A. Benkaddour, S. Khabba, and L. Jarlan, "Combining stable isotopes, eddy covariance system and meteorological measurements for partitioning evapotranspiration, of winter wheat, into soil evaporation and plant transpiration in a semi-arid region," *Agricultural Water Management*, vol. 177, pp. 181–192, nov 2016.

[21] T. E. Wong, J. Nusbaumer, and D. C. Noone, "Evaluation of modeled land-atmosphere exchanges with a comprehensive water isotope fractionation scheme in version 4 of the c ommunity l and m odel," *Journal of Advances in Modeling Earth Systems*, vol. 9, pp. 978–1001, apr 2017.

[22] D. M. Lawrence, P. E. Thornton, K. W. Oleson, and G. B. Bonan, "The partitioning of evapotranspiration into transpiration, soil evaporation, and canopy evaporation in a GCM: Impacts on land–atmosphere interaction," *Journal of Hydrometeorology*, vol. 8, pp. 862–880, aug 2007.

[23] Y. Zhang, J. L. Peña-Arancibia, T. R. McVicar, F. H. S. Chiew, J. Vaze, C. Liu, X. Lu, H. Zheng, Y. Wang, Y. Y. Liu, D. G. Miralles, and M. Pan, "Multi-decadal trends in global terrestrial evapotranspiration and its components," *Scientific Reports*, vol. 6, jan 2016.

[24] R. E. Dickinson, G. Wang, X. Zeng, and Q. Zeng, "How does the partitioning of evapotranspiration and runoff between different processes affect the variability and predictability of

soil moisture and precipitation?," *Advances in Atmospheric Sciences*, vol. 20, pp. 475–478, may 2003.

[25] H. H. G. Savenije, "The importance of interception and why we should delete the term evapotranspiration from our vocabulary," *Hydrological Processes*, vol. 18, pp. 1507–1511, may 2004.

[26] M. Falkenmark, J. Rockstrom, and J. Rockström, *Balancing water for humans and nature: the new approach in ecohydrology*. Earthscan, 2004.

[27] D. Yakir and L. da S. L. Sternberg, "The use of stable isotopes to study ecosystem gas exchange," *Oecologia*, vol. 123, pp. 297–311, may 2000.

[28] W. H. Schlesinger and S. Jasechko, "Transpiration in the global water cycle," *Agricultural and Forest Meteorology*, vol. 189-190, pp. 115–117, jun 2014.

[29] L. Wang, S. P. Good, and K. K. Caylor, "Global synthesis of vegetation control on evapotranspiration partitioning," *Geophysical Research Letters*, vol. 41, pp. 6753–6757, oct 2014.

[30] Z. Wei, K. Yoshimura, L. Wang, D. G. Miralles, S. Jasechko, and X. Lee, "Revisiting the contribution of transpiration to global terrestrial evapotranspiration," *Geophysical Research Letters*, vol. 44, pp. 2792–2801, mar 2017.

[31] R. L. Scott and J. A. Biederman, "Partitioning evapotranspiration using long-term carbon dioxide and water vapor fluxes," *Geophysical Research Letters*, vol. 44, pp. 6833–6840, jul 2017.

[32] Y. T. Yimam, T. E. Ochsner, and V. G. Kakani, "Evapotranspiration partitioning and water use efficiency of switchgrass and biomass sorghum managed for biofuel," *Agricultural Water Management*, vol. 155, pp. 40–47, jun 2015.

[33] J. M. Ham, J. Heilman, and R. Lascano, "Determination of soil water evaporation and transpiration from energy balance and stem flow measurements," *Agricultural and Forest Meteorology*, vol. 52, pp. 287–301, sep 1990.

[34] R. L. Scott, T. E. Huxman, W. L. Cable, and W. E. Emmerich, "Partitioning of evapotranspiration and its relation to carbon dioxide exchange in a chihuahuan desert shrubland," *Hydrological Processes*, vol. 20, no. 15, pp. 3227–3243, 2006.

[35] P. J. Mitchell, E. Veneklaas, H. Lambers, and S. S. Burgess, "Partitioning of evapotranspiration in a semi-arid eucalypt woodland in south-western australia," *Agricultural and Forest Meteorology*, vol. 149, pp. 25–37, jan 2009.

[36] N. R. Yaseef, D. Yakir, E. Rotenberg, G. Schiller, and S. Cohen, "Ecohydrology of a semi-arid forest: partitioning among water balance components and its implications for predicted precipitation changes," *Ecohydrology*, pp. n/a–n/a, 2009.

[37] M. L. Cavanaugh, S. A. Kurc, and R. L. Scott, "Evapotranspiration partitioning in semi-arid shrubland ecosystems: a two-site evaluation of soil moisture control on transpiration," *Ecohydrology*, vol. 4, pp. 671–681, aug 2010.

[38] A. Montoro, F. Mañas, and R. López-Urrea, "Transpiration and evaporation of grapevine, two components related to irrigation strategy," *Agricultural Water Management*, vol. 177, pp. 193–200, nov 2016.

[39] R. López-Olivari, S. Ortega-Farías, and C. Poblete-Echeverría, "Partitioning of net radiation and evapotranspiration over a superintensive drip-irrigated olive orchard," *Irrigation Science*, vol. 34, pp. 17–31, nov 2015.

[40] D. Kool, W. Kustas, A. Ben-Gal, N. Lazarovitch, J. Heitman, T. Sauer, and N. Agam, "Energy and evapotranspiration partitioning in a desert vineyard," *Agricultural and Forest Meteorology*, vol. 218-219, pp. 277–287, mar 2016.

[41] W. Zhao, B. Liu, X. Chang, Q. Yang, Y. Yang, Z. Liu, J. Cleverly, and D. Eamus, "Evapotranspiration partitioning, stomatal conductance, and components of the water balance: A special case of a desert ecosystem in china," *Journal of Hydrology*, vol. 538, pp. 374–386, jul 2016.

[42] L. Wang, H. Liu, and C. Bernhofer, "Grazing intensity effects on the partitioning of evapotranspiration in the semiarid typical steppe ecosystems in inner mongolia," *International Journal of Climatology*, vol. 36, pp. 4130–4140, jan 2016.

[43] E. Balugani, M. Lubczynski, L. Reyes-Acosta, C. van der Tol, A. Francés, and K. Metselaar, "Groundwater and unsaturated zone evaporation and transpiration in a semi-arid open woodland," *Journal of Hydrology*, vol. 547, pp. 54–66, apr 2017.

[44] D. Wang and L. Wang, "Dynamics of evapotranspiration partitioning for apple trees of different ages in a semiarid region of northwest china," *Agricultural Water Management*, vol. 191, pp. 1–15, sep 2017.

[45] J. Brunel, G. Walker, J. Dighton, and B. Monteny, "Use of stable isotopes of water to determine the origin of water used by the vegetation and to partition evapotranspiration. a case study from HAPEX-sahel," *Journal of Hydrology*, vol. 188-189, pp. 466–481, feb 1997.

[46] D. F. Ferretti, E. Pendall, J. A. Morgan, J. A. Nelson, D. LeCain, and A. R. Mosier, "Partitioning evapotranspiration fluxes from a colorado grassland using stable isotopes: Seasonal variations and ecosystem implications of elevated atmospheric co2," *Plant and Soil*, vol. 254, pp. 291–303, Jul 2003.

[47] E. A. Yepez, T. E. Huxman, D. D. Ignace, N. B. English, J. F. Weltzin, A. E. Castellanos, and D. G. Williams, "Dynamics of transpiration and evaporation following a moisture pulse in semiarid grassland: A chamber-based isotope method for partitioning flux components," *Agricultural and Forest Meteorology*, vol. 132, pp. 359–376, oct 2005.

[48] Z. Xu, H.-B. Yang, F.-D. Liu, S.-Q. An, J. Cui, Z.-S. Wang, and S.-R. Liu, "Partitioning evapotranspiration flux components in a subalpine shrubland based on stable isotopic measurements," *Botanical Studies*, vol. 49, no. 4, pp. 351–361, 2008.

[49] S. P. Good, K. Soderberg, K. Guan, E. G. King, T. M. Scanlon, and K. K. Caylor, "δ2H isotopic flux partitioning of evapotranspiration over a grass field following a water pulse and subsequent dry down," *Water Resources Research*, vol. 50, pp. 1410–1432, feb 2014.

[50] Z. Hu, X. Wen, X. Sun, L. Li, G. Yu, X. Lee, and S. Li, "Partitioning of evapotranspiration through oxygen isotopic measurements of water pools and fluxes in a temperate grassland," *Journal of Geophysical Research: Biogeosciences*, vol. 119, pp. 358–372, mar 2014.

[51] M. Gaj, M. Beyer, P. Koeniger, H. Wanke, J. Hamutoko, and T. Himmelsbach, "In situ unsaturated zone water stable isotope (2h and 18o) measurements in semi-arid environments: a soil water balance," *Hydrology and Earth System Sciences*, vol. 20, pp. 715–731, feb 2016.

[52] X. Wen, B. Yang, X. Sun, and X. Lee, "Evapotranspiration partitioning through in-situ oxygen isotope measurements in an oasis cropland," *Agricultural and Forest Meteorology*, vol. 230-231, pp. 89–96, dec 2016.

[53] Y. Wu, T. Du, R. Ding, L. Tong, S. Li, and L. Wang, "Multiple methods to partition evapotranspiration in a maize field," *Journal of Hydrometeorology*, vol. 18, pp. 139–149, jan 2017.

[54] X. Guo, L. Tian, L. Wang, W. Yu, and D. Qu, "River recharge sources and the partitioning of catchment evapotranspiration fluxes as revealed by stable isotope signals in a typical high-elevation arid catchment," *Journal of Hydrology*, vol. 549, pp. 616–630, jun 2017.

[55] S. Zhang, J. Zhang, B. Liu, W. Zhang, C. Gong, M. Jiang, and X. Lv, "Evapotranspiration partitioning using a simple isotope-based model in a semiarid marsh wetland in northeastern china," *Hydrological Processes*, vol. 32, pp. 493–506, jan 2018.

[56] H. Laudon, J. Seibert, S. Köhler, and K. Bishop, "Hydrological flow paths during snowmelt: Congruence between hydrometric measurements and oxygen 18 in meltwater, soil water, and runoff," *Water Resources Research*, vol. 40, mar 2004.

[57] W. Xiao, Z. Wei, and X. Wen, "Evapotranspiration partitioning at the ecosystem scale using the stable isotope method—a review," *Agricultural and Forest Meteorology*, vol. 263, pp. 346–361, dec 2018.

[58] M. Moran, R. Scott, T. Keefer, W. Emmerich, M. Hernandez, G. Nearing, G. Paige, M. Cosh, and P. O'Neill, "Partitioning evapotranspiration in semiarid grassland and shrubland ecosys-

tems using time series of soil surface temperature," *Agricultural and Forest Meteorology*, vol. 149, pp. 59–72, jan 2009.

[59] T. M. Scanlon and W. P. Kustas, "Partitioning evapotranspiration using an eddy covariance-based technique: Improved assessment of soil moisture and land–atmosphere exchange dynamics," *Vadose Zone Journal*, vol. 11, no. 3, p. 0, 2012.

[60] T. Skaggs, R. Anderson, J. Alfieri, T. Scanlon, and W. Kustas, "Fluxpart: Open source software for partitioning carbon dioxide and water vapor fluxes," *Agricultural and Forest Meteorology*, vol. 253-254, pp. 218–224, may 2018.

[61] W. Wang, J. A. Smith, P. Ramamurthy, M. L. Baeck, E. Bou-Zeid, and T. M. Scanlon, "On the correlation of water vapor and CO2 : Application to flux partitioning of evapotranspiration," *Water Resources Research*, vol. 52, pp. 9452–9469, dec 2016.

[62] S. Zhou, B. Yu, Y. Zhang, Y. Huang, and G. Wang, "Partitioning evapotranspiration based on the concept of underlying water use efficiency," *Water Resources Research*, vol. 52, pp. 1160–1175, feb 2016.

[63] S. Allen and V. Grime, "Measurements of transpiration from savannah shrubs using sap flow gauges," *Agricultural and Forest Meteorology*, vol. 75, pp. 23–41, jun 1995.

[64] S. S. O. Burgess, M. A. Adams, N. C. Turner, C. R. Beverly, C. K. Ong, A. A. H. Khan, and T. M. Bleby, "An improved heat pulse method to measure low and reverse rates of sap flow in woody plants," *Tree Physiology*, vol. 21, pp. 589–598, jun 2001.

[65] A. Granier, "Evaluation of transpiration in a douglas-fir stand by means of sap flow measurements," *Tree Physiology*, vol. 3, pp. 309–320, dec 1987.

[66] R. Poyatos, V. Granda, R. Molowny-Horas, M. Mencuccini, K. Steppe, and J. Martínez-Vilalta, "SAPFLUXNET: towards a global database of sap flow measurements," *Tree Physiology*, vol. 36, pp. 1449–1455, nov 2016.

[67] R. W. Pearcy, E.-D. Schulze, and R. Zimmermann, "Measurement of transpiration and leaf conductance," in *Plant physiological ecology*, pp. 137–160, Springer, 2000.

[68] D. I. Stannard and M. A. Weltz, "Partitioning evapotranspiration in sparsely vegetated rangeland using a portable chamber," *Water Resources Research*, vol. 42, feb 2006.

[69] N. Raz-Yaseef, E. Rotenberg, and D. Yakir, "Effects of spatial variations in soil evaporation caused by tree shading on water flux partitioning in a semi-arid pine forest," *Agricultural and Forest Meteorology*, vol. 150, pp. 454–462, mar 2010.

[70] O. Perez-Priego, T. S. El-Madany, M. Migliavacca, A. S. Kowalski, M. Jung, A. Carrara, O. Kolle, M. P. Martín, J. Pacheco-Labrador, G. Moreno, and M. Reichstein, "Evaluation of eddy covariance latent heat fluxes with independent lysimeter and sapflow estimates in a mediterranean savannah ecosystem," *Agricultural and Forest Meteorology*, vol. 236, pp. 87–99, apr 2017.

[71] P. Widmoser and G. Wohlfahrt, "Attributing the energy imbalance by concurrent lysimeter and eddy covariance evapotranspiration measurements," *Agricultural and Forest Meteorology*, vol. 263, pp. 287–291, dec 2018.

[72] C. D. Keeling, "The concentration and isotopic abundances of atmospheric carbon dioxide in rural areas," *Geochimica et Cosmochimica Acta*, vol. 13, pp. 322–334, jan 1958.

[73] T. Griffis, J. Baker, S. Sargent, B. Tanner, and J. Zhang, "Measuring field-scale isotopic CO2 fluxes with tunable diode laser absorption spectroscopy and micrometeorological techniques," *Agricultural and Forest Meteorology*, vol. 124, pp. 15–29, jul 2004.

[74] H. Craig and L. I. Gordon, "Deuterium and oxygen 18 variations in the ocean and the marine atmosphere," 1965.

[75] J. Horita, K. Rozanski, and S. Cohen, "Isotope effects in the evaporation of water: a status report of the craig–gordon model," *Isotopes in Environmental and Health Studies*, vol. 44, pp. 23–49, mar 2008.

[76] R. L. Barnard, F. de Bello, A. K. Gilgen, and N. Buchmann, "Theδ18o of root crown water best reflects source water δ18o in different types of herbaceous species," *Rapid Communications in Mass Spectrometry*, vol. 20, no. 24, pp. 3799–3802, 2006.

[77] L. B. Flanagan and J. R. Ehleringer, "Stable isotope composition of stem and leaf water: Applications to the study of plant water use," *Functional Ecology*, vol. 5, no. 2, p. 270, 1991.

[78] X.-F. Wang and D. Yakir, "Temporal and spatial variations in the oxygen-18 content of leaf water in different plant species," *Plant, Cell and Environment*, vol. 18, pp. 1377–1385, dec 1995.

[79] S. Zhang, X. Wen, J. Wang, G. Yu, and X. Sun, "The use of stable isotopes to partition evapotranspiration fluxes into evaporation and transpiration," *Acta Ecologica Sinica*, vol. 30, pp. 201–209, aug 2010.

[80] G. A. Barron-Gafford, E. P. Sanchez-Cañete, R. L. Minor, S. M. Hendryx, E. Lee, L. F. Sutter, N. Tran, E. Parra, T. Colella, P. C. Murphy, E. P. Hamerlynck, P. Kumar, and R. L. Scott, "Impacts of hydraulic redistribution on grass-tree competition vs facilitation in a semi-arid savanna," *New Phytologist*, vol. 215, pp. 1451–1461, jul 2017.

[81] L.-F. Han, M. Gröning, P. Aggarwal, and B. R. Helliker, "Reliable determination of oxygen and hydrogen isotope ratios in atmospheric water vapour adsorbed on 3a molecular sieve," *Rapid Communications in Mass Spectrometry*, vol. 20, no. 23, pp. 3612–3618, 2006.

[82] B. R. Helliker, J. S. Roden, C. Cook, and J. R. Ehleringer, "A rapid and precise method for sampling and determining the oxygen isotope ratio of atmospheric water vapor," *Rapid Communications in Mass Spectrometry*, vol. 16, no. 10, pp. 929–932, 2002.

[83] E. S. F. Berman, N. E. Levin, A. Landais, S. Li, and T. Owano, "Measurement of δ18o, δ17o, and 17o-excess in water by off-axis integrated cavity output spectroscopy and isotope ratio mass spectrometry," *Analytical Chemistry*, vol. 85, pp. 10392–10398, oct 2013.

[84] H. X. Wang and C. M. Liu, "Soil evaporation and its affecting factors under crop canopy," *Communications in Soil Science and Plant Analysis*, vol. 38, no. 1, pp. 259–271, 2007.

[85] J. T. Ritchie and E. Burnett, "Dryland evaporative flux in a subhumid climate: II. plant influences1," *Agronomy Journal*, vol. 63, no. 1, p. 56, 1971.

[86] A. Sepaskhah and S. Ilampour, "Effects of soil moisture stress on evapotranspiration partitioning," *Agricultural Water Management*, vol. 28, pp. 311–323, dec 1995.

[87] K. Snyder and S. Tartowski, "Multi-scale temporal variation in water availability: Implications for vegetation dynamics in arid and semi-arid ecosystems," *Journal of Arid Environments*, vol. 65, pp. 219–234, apr 2006.

[88] X.-F. Wang and D. Yakir, "Using stable isotopes of water in evapotranspiration studies," *Hydrological Processes*, vol. 14, no. 8, pp. 1407–1421, 2000.

[89] S. R. Evett, W. P. Kustas, P. H. Gowda, M. C. Anderson, J. H. Prueger, and T. A. Howell, "Overview of the bushland evapotranspiration and agricultural remote sensing EXperiment 2008 (BEAREX08): A field experiment evaluating methods for quantifying ET at multiple scales," *Advances in Water Resources*, vol. 50, pp. 4–19, dec 2012.

[90] Z. Hu, G. Yu, Y. Zhou, X. Sun, Y. Li, P. Shi, Y. Wang, X. Song, Z. Zheng, L. Zhang, and S. Li, "Partitioning of evapotranspiration and its controls in four grassland ecosystems: Application of a two-source model," *Agricultural and Forest Meteorology*, vol. 149, pp. 1410–1420, sep 2009.

[91] T. E. Huxman, K. A. Snyder, D. Tissue, A. J. Leffler, K. Ogle, W. T. Pockman, D. R. Sandquist, D. L. Potts, and S. Schwinning, "Precipitation pulses and carbon fluxes in semiarid and arid ecosystems," *Oecologia*, vol. 141, pp. 254–268, aug 2004.

[92] F. Laio, A. Porporato, L. Ridolfi, and I. Rodriguez-Iturbe, "Plants in water-controlled ecosystems: active role in hydrologic processes and response to water stress," *Advances in Water Resources*, vol. 24, pp. 707–723, jul 2001.

[93] J. C. Villegas, F. Dominguez, G. A. Barron-Gafford, H. D. Adams, M. Guardiola-Claramonte, E. D. Sommer, A. W. Selvey, J. F. Espeleta, C. B. Zou, D. D. Breshears, and T. E. Huxman, "Sensitivity of regional evapotranspiration partitioning to variation in woody plant cover: insights from experimental dryland tree mosaics," *Global Ecology and Biogeography*, vol. 24, pp. 1040–1048, jul 2015.

[94] G. R. Miller, X. Chen, Y. Rubin, S. Ma, and D. D. Baldocchi, "Groundwater uptake by woody vegetation in a semiarid oak savanna," *Water Resources Research*, vol. 46, oct 2010.

[95] E. A. Yepez, R. L. Scott, W. L. Cable, and D. G. Williams, "Intraseasonal variation in water and carbon dioxide flux components in a semiarid riparian woodland," *Ecosystems*, vol. 10, pp. 1100–1115, aug 2007.

[96] L. A. Cernusak, M. M. Barbour, S. K. Arndt, A. W. Cheesman, N. B. English, T. S. Feild, B. R. Helliker, M. M. Holloway-Phillips, J. A. Holtum, A. Kahmen, F. A. McInerney, N. C. Munksgaard, K. A. Simonin, X. Song, H. Stuart-Williams, J. B. West, and G. D. Farquhar, "Stable isotopes in leaf water of terrestrial plants," *Plant, Cell & Environment*, vol. 39, pp. 1087–1102, mar 2016.

[97] J. S. Roden, G. Lin, and J. R. Ehleringer, "A mechanistic model for interpretation of hydrogen and oxygen isotope ratios in tree-ring cellulose," *Geochimica et Cosmochimica Acta*, vol. 64, pp. 21–35, jan 2000.

[98] Y. Rothfuss and M. Javaux, "Reviews and syntheses: Isotopic approaches to quantify root water uptake: a review and comparison of methods," *Biogeosciences*, vol. 14, pp. 2199–2224, may 2017.

[99] M. Bittelli, F. Ventura, G. S. Campbell, R. L. Snyder, F. Gallegati, and P. R. Pisa, "Coupling of heat, water vapor, and liquid water fluxes to compute evaporation in bare soils," *Journal of Hydrology*, vol. 362, pp. 191–205, dec 2008.

[100] S. K. Deb, M. K. Shukla, P. Sharma, and J. G. Mexal, "Coupled liquid water, water vapor, and heat transport simulations in an unsaturated zone of a sandy loam field," *Soil Science*, vol. 176, pp. 387–398, aug 2011.

[101] B. Herbstritt, B. Gralher, and M. Weiler, "Continuous in situ measurements of stable isotopes in liquid water," *Water Resources Research*, vol. 48, mar 2012.

[102] E. J. Oerter, A. Perelet, E. Pardyjak, and G. Bowen, "Membrane inlet laser spectroscopy to measure h and o stable isotope compositions of soil and sediment pore water with high

sample throughput," *Rapid Communications in Mass Spectrometry*, vol. 31, pp. 75–84, nov 2016.

[103] K. Soderberg, S. P. Good, L. Wang, and K. Caylor, "Stable isotopes of water vapor in the vadose zone: A review of measurement and modeling techniques," *Vadose Zone Journal*, vol. 11, no. 3, p. 0, 2012.

[104] T. H. M. Volkmann and M. Weiler, "Continual in situ monitoring of pore water stable isotopes in the subsurface," *Hydrology and Earth System Sciences*, vol. 18, pp. 1819–1833, may 2014.

[105] C. Stumpp, N. Brüggemann, and L. Wingate, "Stable isotope approaches in vadose zone research," *Vadose Zone Journal*, vol. 17, no. 1, p. 0, 2018.

[106] M. Dubbert, A. Piayda, M. Cuntz, A. C. Correia, F. C. e Silva, J. S. Pereira, and C. Werner, "Stable oxygen isotope and flux partitioning demonstrates understory of an oak savanna contributes up to half of ecosystem carbon and water exchange," *Frontiers in Plant Science*, vol. 5, oct 2014.

[107] B. D. Newman, D. D. Breshears, and M. O. Gard, "Evapotranspiration partitioning in a semiarid woodland: Ecohydrologic heterogeneity and connectivity of vegetation patches," *Vadose Zone Journal*, vol. 9, no. 3, p. 561, 2010.

[108] J. C. Villegas, J. E. Espeleta, C. T. Morrison, D. D. Breshears, and T. E. Huxman, "Factoring in canopy cover heterogeneity on evapotranspiration partitioning: Beyond big-leaf surface homogeneity assumptions," *Journal of Soil and Water Conservation*, vol. 69, pp. 78A–83A, may 2014.

[109] P. Wang, T. Yamanaka, X.-Y. Li, and Z. Wei, "Partitioning evapotranspiration in a temperate grassland ecosystem: Numerical modeling with isotopic tracers," *Agricultural and Forest Meteorology*, vol. 208, pp. 16–31, aug 2015.

[110] M. Boval and R. M. Dixon, "The importance of grasslands for animal production and other functions: a review on management and methodological progress in the tropics," *animal*, vol. 6, pp. 748–762, feb 2012.

[111] F. P. OMara, "The role of grasslands in food security and climate change," *Annals of Botany*, vol. 110, pp. 1263–1270, sep 2012.

[112] R. Tyrl, T. Bidwell, R. Masters, R. Elmore, and J. Weir, "Oklahomas native vegetation types," *Oklahoma State University. Oklahoma Cooperative Extension Service Publication No. E-993*, 2007.

[113] T. H. Ricketts, E. Dinerstein, D. M. Olson, W. Eichbaum, C. J. Loucks, K. Kavanaugh, P. Hedao, P. Hurley, D. DellaSalla, R. Abell, *et al.*, *Terrestrial ecoregions of North America: a conservation assessment*, vol. 1. Island Press, 1999.

[114] F. B. Samson, F. L. Knopf, and W. R. Ostlie, "Great plains ecosystems: past, present, and future," *Wildlife Society Bulletin*, vol. 32, pp. 6–15, mar 2004.

[115] J. Ge and C. Zou, "Impacts of woody plant encroachment on regional climate in the southern great plains of the united states," *Journal of Geophysical Research: Atmospheres*, vol. 118, no. 16, pp. 9093–9104, 2013.

[116] C. B. Zou, D. J. Turton, R. E. Will, D. M. Engle, and S. D. Fuhlendorf, "Alteration of hydrological processes and streamflow with juniper (juniperus virginiana) encroachment in a mesic grassland catchment," *Hydrological Processes*, vol. 28, pp. 6173–6182, dec 2013.

[117] D. C. McKinley and J. M. Blair, "Woody plant encroachment by juniperus virginiana in a mesic native grassland promotes rapid carbon and nitrogen accrual," *Ecosystems*, vol. 11, pp. 454–468, mar 2008.

[118] G. G. Katul, R. Oren, S. Manzoni, C. Higgins, and M. B. Parlange, "Evapotranspiration: A process driving mass transport and energy exchange in the soil-plant-atmosphere-climate system," *Reviews of Geophysics*, vol. 50, jul 2012.

[119] K. B. Wilson and D. D. Baldocchi, "Seasonal and interannual variability of energy fluxes over a broadleaved temperate deciduous forest in north america," *Agricultural and Forest Meteorology*, vol. 100, pp. 1–18, jan 2000.

[120] G. Burba, *Eddy covariance method for scientific, industrial, agricultural and regulatory applications: A field book on measuring ecosystem gas exchange and areal emission rates*. LI-Cor Biosciences, 2013.

[121] D. Baldocchi, E. Falge, L. Gu, R. Olson, D. Hollinger, S. Running, P. Anthoni, C. Bernhofer, K. Davis, R. Evans, J. Fuentes, A. Goldstein, G. Katul, B. Law, X. Lee, Y. Malhi, T. Meyers, W. Munger, W. Oechel, K. T. Paw, K. Pilegaard, H. P. Schmid, R. Valentini, S. Verma, T. Vesala, K. Wilson, and S. Wofsy, "FLUXNET: A new tool to study the temporal and spatial variability of ecosystem–scale carbon dioxide, water vapor, and energy flux densities," *Bulletin of the American Meteorological Society*, vol. 82, pp. 2415–2434, nov 2001.

[122] R. G. Anderson and D. Wang, "Energy budget closure observed in paired eddy covariance towers with increased and continuous daily turbulence," *Agricultural and Forest Meteorology*, vol. 184, pp. 204–209, jan 2014.

[123] T. Foken, "The energy balance closure problem: an overview," *Ecological Applications*, vol. 18, no. 6, pp. 1351–1367, 2008.

[124] T. Foken, M. Aubinet, J. J. Finnigan, M. Y. Leclerc, M. Mauder, and K. T. Paw U, "Results of a panel discussion about the energy balance closure correction for trace gases," *Bulletin of the American Meteorological Society*, vol. 92, no. 4, pp. ES13–ES18, 2011.

[125] H. H. Franssen, R. Stöckli, I. Lehner, E. Rotenberg, and S. I. Seneviratne, "Energy balance closure of eddy-covariance data: A multisite analysis for european fluxnet stations," *Agricultural and Forest Meteorology*, vol. 150, no. 12, pp. 1553–1567, 2010.

[126] Z. Gao, H. Liu, G. G. Katul, and T. Foken, "Non-closure of the surface energy balance explained by phase difference between vertical velocity and scalars of large atmospheric

eddies," *Environmental Research Letters*, vol. 12, no. 3, p. 034025, 2017.

[127] R. Leuning, E. van Gorsel, W. J. Massman, and P. R. Isaac, "Reflections on the surface energy imbalance problem," *Agricultural and Forest Meteorology*, vol. 156, pp. 65–74, apr 2012.

[128] X. Liu, , S. Yang, J. Xu, J. Zhang, J. Liu, , , and and, "Effects of soil heat storage and phase shift correction on energy balance closure of paddy fields," *Atmósfera*, vol. 30, pp. 39–52, jan 2017.

[129] D. Masseroni, C. Corbari, and M. Mancini, "Limitations and improvements of the energy balance closure with reference to experimental data measured over a maize field," *Atmósfera*, vol. 27, pp. 335–352, oct 2014.

[130] E. S. Russell, H. Liu, Z. Gao, D. Finn, and B. Lamb, "Impacts of soil heat flux calculation methods on the surface energy balance closure," *Agricultural and Forest Meteorology*, vol. 214-215, pp. 189–200, dec 2015.

[131] K. Wilson, A. Goldstein, E. Falge, M. Aubinet, D. Baldocchi, P. Berbigier, C. Bernhofer, R. Ceulemans, H. Dolman, C. Field, A. Grelle, A. Ibrom, B. Law, A. Kowalski, T. Meyers, J. Moncrieff, R. Monson, W. Oechel, J. Tenhunen, R. Valentini, and S. Verma, "Energy balance closure at FLUXNET sites," *Agricultural and Forest Meteorology*, vol. 113, pp. 223–243, dec 2002.

[132] J. Zuo, J. Wang, J. Huang, W. Li, G. Wang, and H. Ren, "Estimation of ground heat flux for a semi-arid grassland and its impact on the surface energy budget," *Plateau Meteorology*, vol. 29, pp. 840–848, 08 2010.

[133] F. Eder, F. De Roo, E. Rotenberg, D. Yakir, H. P. Schmid, and M. Mauder, "Secondary circulations at a solitary forest surrounded by semi-arid shrubland and their impact on eddy-covariance measurements," *Agricultural and Forest Meteorology*, vol. 211, pp. 115–127, 2015.

[134] P. C. Stoy, M. Mauder, T. Foken, B. Marcolla, E. Boegh, A. Ibrom, M. A. Arain, A. Arneth, M. Aurela, C. Bernhofer, A. Cescatti, E. Dellwik, P. Duce, D. Gianelle, E. van Gorsel, G. Kiely, A. Knohl, H. Margolis, H. McCaughey, L. Merbold, L. Montagnani, D. Papale, M. Reichstein, M. Saunders, P. Serrano-Ortiz, M. Sottocornola, D. Spano, F. Vaccari, and A. Varlagin, "A data-driven analysis of energy balance closure across FLUXNET research sites: The role of landscape scale heterogeneity," *Agricultural and Forest Meteorology*, vol. 171-172, pp. 137–152, apr 2013.

[135] K. Xu, S. Metzger, and A. R. Desai, "Surface-atmosphere exchange in a box: Space-time resolved storage and net vertical fluxes from tower-based eddy covariance," *Agricultural and Forest Meteorology*, vol. 255, pp. 81–91, may 2018.

[136] J. M. Frank, W. J. Massman, and B. E. Ewers, "Underestimates of sensible heat flux due to vertical velocity measurement errors in non-orthogonal sonic anemometers," *Agricultural and Forest Meteorology*, vol. 171, pp. 72–81, 2013.

[137] T. W. Horst, S. R. Semmer, and G. Maclean, "Correction of a non-orthogonal, three-component sonic anemometer for flow distortion by transducer shadowing," *Boundary-Layer Meteorology*, vol. 155, pp. 371–395, feb 2015.

[138] J. Kochendorfer, T. P. Meyers, J. Frank, W. J. Massman, and M. W. Heuer, "How well can we measure the vertical wind speed? implications for fluxes of energy and mass," *Boundary-Layer Meteorology*, vol. 145, pp. 383–398, jun 2012.

[139] S. P. Oncley, T. Foken, R. Vogt, W. Kohsiek, H. A. R. DeBruin, C. Bernhofer, A. Christen, E. van Gorsel, D. Grantz, C. Feigenwinter, I. Lehner, C. Liebethal, H. Liu, M. Mauder, A. Pitacco, L. Ribeiro, and T. Weidinger, "The energy balance experiment EBEX-2000. part i: overview and energy balance," *Boundary-Layer Meteorology*, vol. 123, pp. 1–28, mar 2007.

[140] P. Yue, Q. Zhang, S. Niu, H. Cheng, and X. Wang, "Effects of the soil heat flux estimates on surface energy balance closure over a semi-arid grassland," *Acta Meteorologica Sinica*,

vol. 25, pp. 774–782, dec 2011.

[141] G. Wohlfahrt, K. Klumpp, and J.-F. Soussana, "Eddy covariance measurements over grasslands," in *Eddy Covariance*, pp. 333–344, Springer Netherlands, nov 2011.

[142] C. Ammann, C. Flechard, J. Leifeld, A. Neftel, and J. Fuhrer, "The carbon budget of newly established temperate grassland depends on management intensity," *Agriculture, Ecosystems & Environment*, vol. 121, pp. 5–20, jun 2007.

[143] D. J. Bremer and J. M. Ham, "Effect of spring burning on the surface energy balance in a tallgrass prairie," *Agricultural and Forest Meteorology*, vol. 97, pp. 43–54, sep 1999.

[144] M. L. Fischer, M. S. Torn, D. P. Billesbach, G. Doyle, B. Northup, and S. C. Biraud, "Carbon, water, and heat flux responses to experimental burning and drought in a tallgrass prairie," *Agricultural and forest meteorology*, vol. 166, pp. 169–174, 2012.

[145] G. G. Burba and S. B. Verma, "Seasonal and interannual variability in evapotranspiration of native tallgrass prairie and cultivated wheat ecosystems," *Agricultural and Forest Meteorology*, vol. 135, pp. 190–201, dec 2005.

[146] P. Wagle, V. G. Kakani, and R. L. Huhnke, "Evapotranspiration and ecosystem water use efficiency of switchgrass and high biomass sorghum," *Agronomy Journal*, vol. 108, no. 3, p. 1007, 2016.

[147] K. B. Arnold, *Eddy Covariance in a Tallgrass Prairie: energy balance closure, water and carbon budgets, and shrub expansion*. PhD thesis, Kansas State University, 2010.

[148] K. Novick, R. Oren, P. Stoy, M. Siqueira, and G. Katul, "Nocturnal evapotranspiration in eddy-covariance records from three co-located ecosystems in the southeastern u.s.: Implications for annual fluxes," *Agricultural and Forest Meteorology*, vol. 149, pp. 1491–1504, sep 2009.

[149] R. L. Scott, T. E. Huxman, G. A. Barron-Gafford, G. D. Jenerette, J. M. Young, and E. P. Hamerlynck, "When vegetation change alters ecosystem water availability," *Global Change Biology*, vol. 20, pp. 2198–2210, apr 2014.

[150] T. P. Meyers, "A comparison of summertime water and CO2 fluxes over rangeland for well watered and drought conditions," *Agricultural and Forest Meteorology*, vol. 106, pp. 205–214, feb 2001.

[151] J. Kidston, C. Brümmer, T. A. Black, K. Morgenstern, Z. Nesic, J. H. McCaughey, and A. G. Barr, "Energy balance closure using eddy covariance above two different land surfaces and implications for CO2 flux measurements," *Boundary-Layer Meteorology*, vol. 136, pp. 193–218, may 2010.

[152] A. K. Knapp, "Variation among biomes in temporal dynamics of aboveground primary production," *Science*, vol. 291, pp. 481–484, jan 2001.

[153] E. Schulze, F. M. Kelliher, C. Korner, J. Lloyd, and R. Leuning, "Relationships among maximum stomatal conductance, ecosystem surface conductance, carbon assimilation rate, and plant nitrogen nutrition: A global ecology scaling exercise," *Annual Review of Ecology and Systematics*, vol. 25, pp. 629–662, nov 1994.

[154] L. A. Wever, L. B. Flanagan, and P. J. Carlson, "Seasonal and interannual variation in evapotranspiration, energy balance and surface conductance in a northern temperate grassland," *Agricultural and Forest Meteorology*, vol. 112, pp. 31–49, jul 2002.

[155] Soil Survey Staff, "Web soil survey," *URL http://www. websoilsurvey. ncsc. usda. gov-/app/[accessed 01/06/2017]*, 2003.

[156] R. F. Limb, D. M. Engle, A. L. Alford, and E. C. Hellgren, "Tallgrass prairie plant community dynamics along a canopy cover gradient of eastern redcedar (juniperus virginiana l.)," *Rangeland Ecology & Management*, vol. 63, pp. 638–644, nov 2010.

[157] F. V. Brock, K. C. Crawford, R. L. Elliott, G. W. Cuperus, S. J. Stadler, H. L. Johnson, and M. D. Eilts, "The oklahoma mesonet: A technical overview," *Journal of Atmospheric and Oceanic Technology*, vol. 12, pp. 5–19, feb 1995.

[158] R. A. McPherson, C. A. Fiebrich, K. C. Crawford, J. R. Kilby, D. L. Grimsley, J. E. Martinez, J. B. Basara, B. G. Illston, D. A. Morris, K. A. Kloesel, A. D. Melvin, H. Shrivastava,

J. M. Wolfinbarger, J. P. Bostic, D. B. Demko, R. L. Elliott, S. J. Stadler, J. D. Carlson, and A. J. Sutherland, "Statewide monitoring of the mesoscale environment: A technical update on the oklahoma mesonet," *Journal of Atmospheric and Oceanic Technology*, vol. 24, pp. 301–321, mar 2007.

[159] Mesonet, "Mesonet long-term averagesmaps," 2016.

[160] S. Conant and P. G. Risser, "Canopy structure of a tall-grass prairie.," *Rangeland Ecology & Management/Journal of Range Management Archives*, vol. 27, no. 4, pp. 313–318, 1974.

[161] D. Vickers and L. Mahrt, "Quality control and flux sampling problems for tower and aircraft data," *Journal of Atmospheric and Oceanic Technology*, vol. 14, pp. 512–526, jun 1997.

[162] J. M. Wilczak, S. P. Oncley, and S. A. Stage, "Sonic anemometer tilt correction algorithms," *Boundary-Layer Meteorology*, vol. 99, pp. 127–150, apr 2001.

[163] T. Foken, M. Göckede, M. Mauder, L. Mahrt, B. Amiro, and W. Munger, "Post-field data quality control. handbook of micrometeorology: A guide for surface flux measurement and analysis, x. lee, w. massman, and b. law," 2004.

[164] J. Moncrieff, R. Clement, J. Finnigan, and T. Meyers, *Averaging, Detrending, and Filtering of Eddy Covariance Time Series*, pp. 7–31. Dordrecht: Springer Netherlands, 2005.

[165] J. Moncrieff, J. Massheder, H. de Bruin, J. Elbers, T. Friborg, B. Heusinkveld, P. Kabat, S. Scott, H. Soegaard, and A. Verhoef, "A system to measure surface fluxes of momentum, sensible heat, water vapour and carbon dioxide," *Journal of Hydrology*, vol. 188-189, pp. 589–611, feb 1997.

[166] E. K. Webb, G. I. Pearman, and R. Leuning, "Correction of flux measurements for density effects due to heat and water vapour transfer," *Quarterly Journal of the Royal Meteorological Society*, vol. 106, pp. 85–100, jan 1980.

[167] M. Mauder and T. Foken, "Impact of post-field data processing on eddy covariance flux estimates and energy balance closure," *Meteorologische Zeitschrift*, vol. 15, pp. 597–609, dec 2006.

[168] N. Kljun, P. Calanca, M. W. Rotach, and H. P. Schmid, "A simple two-dimensional parameterisation for flux footprint prediction (FFP)," *Geoscientific Model Development*, vol. 8, pp. 3695–3713, nov 2015.

[169] K. Heidbach, H. P. Schmid, and M. Mauder, "Experimental evaluation of flux footprint models," *Agricultural and Forest Meteorology*, vol. 246, pp. 142–153, nov 2017.

[170] N. Kljun, P. Calanca, M. W. Rotach, and H. P. Schmid, "A simple parameterisation for flux footprint predictions," *Boundary-Layer Meteorology*, vol. 112, pp. 503–523, sep 2004.

[171] D. Papale, M. Reichstein, M. Aubinet, E. Canfora, C. Bernhofer, W. Kutsch, B. Longdoz, S. Rambal, R. Valentini, T. Vesala, and D. Yakir, "Towards a standardized processing of net ecosystem exchange measured with eddy covariance technique: algorithms and uncertainty estimation," *Biogeosciences*, vol. 3, pp. 571–583, nov 2006.

[172] M. Reichstein, E. Falge, D. Baldocchi, D. Papale, M. Aubinet, P. Berbigier, C. Bernhofer, N. Buchmann, T. Gilmanov, A. Granier, T. Grunwald, K. Havrankova, H. Ilvesniemi, D. Janous, A. Knohl, T. Laurila, A. Lohila, D. Loustau, G. Matteucci, T. Meyers, F. Miglietta, J.-M. Ourcival, J. Pumpanen, S. Rambal, E. Rotenberg, M. Sanz, J. Tenhunen, G. Seufert, F. Vaccari, T. Vesala, D. Yakir, and R. Valentini, "On the separation of net ecosystem exchange into assimilation and ecosystem respiration: review and improved algorithm," *Global Change Biology*, vol. 11, pp. 1424–1439, sep 2005.

[173] T. Wutzler, A. Lucas-Moffat, M. Migliavacca, J. Knauer, K. Sickel, L. Šigut, O. Menzer, and M. Reichstein, "Basic and extensible post-processing of eddy covariance flux data with REddyProc," *Biogeosciences Discussions*, pp. 1–39, feb 2018.

[174] S. Moritz and T. Bartz-Beielstein, "imputeTS: Time series missing value imputation in r," *The R Journal*, vol. 9, no. 1, p. 207, 2017.

[175] P. L. Finkelstein and P. F. Sims, "Sampling error in eddy correlation flux measurements," *Journal of Geophysical Research: Atmospheres*, vol. 106, no. D4, pp. 3503–3509, 2001.

[176] Y. Kosugi, S. Takanashi, H. Tanaka, S. Ohkubo, M. Tani, M. Yano, and T. Katayama, "Evapotranspiration over a japanese cypress forest. i. eddy covariance fluxes and surface conductance characteristics for 3years," *Journal of Hydrology*, vol. 337, pp. 269–283, apr 2007.

[177] T. P. Meyers and S. E. Hollingerb, "An assessment of storage terms in the surface energy balance of maize and soybean," *Agricultural and Forest Meteorology*, vol. 125, pp. 105–115, sep 2004.

[178] T. Twine, W. Kustas, J. Norman, D. Cook, P. Houser, T. Meyers, J. Prueger, P. Starks, and M. Wesely, "Correcting eddy-covariance flux underestimates over a grassland," *Agricultural and Forest Meteorology*, vol. 103, pp. 279–300, jun 2000.

[179] D. D. Baldocchi, "Assessing the eddy covariance technique for evaluating carbon dioxide exchange rates of ecosystems: past, present and future," *Global Change Biology*, vol. 9, no. 4, pp. 479–492, 2003.

[180] M. J., "The state and movement of water in living organisms," in *Proceedings of evaporation and environment, XIXth Symposium*, pp. 205–234, 1965.

[181] J. Monteith and M. Unsworth, *Principles of environmental physics: plants, animals, and the atmosphere*. Academic Press, 2013.

[182] P. Jarvis and K. McNaughton, "Stomatal control of transpiration: Scaling up from leaf to region," in *Advances in Ecological Research*, pp. 1–49, Elsevier, 1986.

[183] T. E. Ochsner, T. J. Sauer, and R. Horton, "Soil heat storage measurements in energy balance studies," *Agronomy Journal*, vol. 99, no. 1, p. 311, 2007.

[184] B. Heusinkveld, A. Jacobs, A. Holtslag, and S. Berkowicz, "Surface energy balance closure in an arid region: role of soil heat flux," *Agricultural and Forest Meteorology*, vol. 122, pp. 21–37, mar 2004.

[185] J. Liang, L. Zhang, X. Cao, J. Wen, J. Wang, and G. Wang, "Energy balance in the semiarid area of the loess plateau, china," *Journal of Geophysical Research: Atmospheres*, vol. 122, pp. 2155–2168, feb 2017.

[186] Y. Li, S. Liu, S. Wang, Y. Miao, and B. Chen, "Comparative study on methods for computing soil heat storage and energy balance in arid and semi-arid areas," *Journal of Meteorological Research*, vol. 28, pp. 308–322, feb 2014.

[187] N. P. Majozi, C. M. Mannaerts, A. Ramoelo, R. Mathieu, A. Nickless, and W. Verhoef, "Analysing surface energy balance closure and partitioning over a semi-arid savanna FLUXNET site in skukuza, kruger national park, south africa," *Hydrology and Earth System Sciences*, vol. 21, pp. 3401–3415, jul 2017.

[188] P. Wagle and V. G. Kakani, "Growing season variability in evapotranspiration, ecosystem water use efficiency, and energy partitioning in switchgrass," *Ecohydrology*, vol. 7, pp. 64–72, sep 2012.

[189] R. L. Scott, "Using watershed water balance to evaluate the accuracy of eddy covariance evaporation measurements for three semiarid ecosystems," *Agricultural and Forest Meteorology*, vol. 150, pp. 219–225, feb 2010.

[190] C. A. Williams, M. Reichstein, N. Buchmann, D. Baldocchi, C. Beer, C. Schwalm, G. Wohlfahrt, N. Hasler, C. Bernhofer, T. Foken, D. Papale, S. Schymanski, and K. Schaefer, "Climate and vegetation controls on the surface water balance: Synthesis of evapotranspiration measured across a global network of flux towers," *Water Resources Research*, vol. 48, jun 2012.

[191] D. Cava, D. Contini, A. Donateo, and P. Martano, "Analysis of short-term closure of the surface energy balance above short vegetation," *Agricultural and forest meteorology*, vol. 148, no. 1, pp. 82–93, 2008.

[192] S. Wang and A. Davidson, "Impact of climate variations on surface albedo of a temperate grassland," *Agricultural and Forest Meteorology*, vol. 142, pp. 133–142, feb 2007.

[193] S. G. Li, Y. Harazono, T. Oikawa, H. L. Zhao, Z. Y. He, and X. L. Chang, "Grassland desertification by grazing and the resulting micrometeorological changes in inner mongolia," *Agricultural and Forest Meteorology*, vol. 102, pp. 125–137, may 2000.

[194] C. Liebethal, *On the determination of the ground heat flux in micrometeorology and its influence on the energy balance closure*. PhD thesis, University of Bayreuth, Bayreuth, 2005.

[195] H.-T. Mengelkamp, F. Beyrich, G. Heinemann, F. Ament, J. Bange, F. Berger, J. Bösenberg, T. Foken, B. Hennemuth, C. Heret, S. Huneke, K.-P. Johnsen, M. Kerschgens, W. Kohsiek, J.-P. Leps, C. Liebethal, H. Lohse, M. Mauder, W. Meijninger, S. Raasch, C. Simmer, T. Spieß, A. Tittebrand, J. Uhlenbrock, and P. Zittel, "Evaporation over a heterogeneous land surface," *Bulletin of the American Meteorological Society*, vol. 87, pp. 775–786, jun 2006.

[196] E. Eichelmann, C. Wagner-Riddle, J. Warland, B. Deen, and P. Voroney, "Evapotranspiration, water use efficiency, and energy partitioning of a mature switchgrass stand," *Agricultural and forest meteorology*, vol. 217, pp. 108–119, 2016.

[197] J. M. Ham and A. K. Knapp, "Fluxes of CO2, water vapor, and energy from a prairie ecosystem during the seasonal transition from carbon sink to carbon source," *Agricultural and Forest Meteorology*, vol. 89, pp. 1–14, jan 1998.

[198] J. B. Nippert, R. A. Wieme, T. W. Ocheltree, and J. M. Craine, "Root characteristics of c4 grasses limit reliance on deep soil water in tallgrass prairie," *Plant and Soil*, vol. 355, pp. 385–394, jan 2012.

[199] K. E. Saxton and W. J. Rawls, "Soil water characteristic estimates by texture and organic matter for hydrologic solutions," *Soil Science Society of America Journal*, vol. 70, no. 5, p. 1569, 2006.

[200] D. D. Baldocchi, L. Xu, and N. Kiang, "How plant functional-type, weather, seasonal drought, and soil physical properties alter water and energy fluxes of an oak–grass savanna and an annual grassland," *Agricultural and Forest Meteorology*, vol. 123, pp. 13–39, may 2004.

[201] L. Aires, C. Pio, and J. Pereira, "The effect of drought on energy and water vapour exchange above a mediterranean c3/c4 grassland in southern portugal," *Agricultural and Forest Meteorology*, vol. 148, pp. 565–579, apr 2008.

[202] J. Hunt, F. Kelliher, T. McSeveny, and J. Byers, "Evaporation and carbon dioxide exchange between the atmosphere and a tussock grassland during a summer drought," *Agricultural and Forest Meteorology*, vol. 111, pp. 65–82, mar 2002.

[203] R. H. Skinner and P. R. Adler, "Carbon dioxide and water fluxes from switchgrass managed for bioenergy production," *Agriculture, Ecosystems & Environment*, vol. 138, pp. 257–264, aug 2010.

[204] G. Sun, K. Alstad, J. Chen, S. Chen, C. R. Ford, G. Lin, C. Liu, N. Lu, S. G. McNulty, H. Miao, A. Noormets, J. M. Vose, B. Wilske, M. Zeppel, Y. Zhang, and Z. Zhang, "A general predictive model for estimating monthly ecosystem evapotranspiration," *Ecohydrology*, vol. 4, pp. 245–255, dec 2010.

[205] P. Valayamkunnath, V. Sridhar, W. Zhao, and R. G. Allen, "Intercomparison of surface energy fluxes, soil moisture, and evapotranspiration from eddy covariance, large-aperture scintillometer, and modeling across three ecosystems in a semiarid climate," *Agricultural and Forest Meteorology*, vol. 248, pp. 22–47, jan 2018.

[206] P. A. Fay, D. M. Kaufman, J. B. Nippert, J. D. Carlisle, and C. W. Harper, "Changes in grassland ecosystem function due to extreme rainfall events: implications for responses to climate change," *Global Change Biology*, vol. 14, no. 7, pp. 1600–1608, 2008.

[207] P. Fay, J. Blair, M. Smith, J. Nippert, J. Carlisle, and A. Knapp, "Relative effects of precipitation variability and warming on tallgrass prairie ecosystem function," *Biogeosciences*, vol. 8, no. 10, pp. 3053–3068, 2011.

[208] S. Chen, J. Chen, G. Lin, W. Zhang, H. Miao, L. Wei, J. Huang, and X. Han, "Energy balance and partition in inner mongolia steppe ecosystems with different land use types," *Agricultural and Forest Meteorology*, vol. 149, no. 11, pp. 1800–1809, 2009.

[209] J. Kim and S. B. Verma, "Components of surface energy balance in a temperate grassland ecosystem," *Boundary-Layer Meteorology*, vol. 51, pp. 401–417, jun 1990.

[210] Y. Ryu, D. D. Baldocchi, S. Ma, and T. Hehn, "Interannual variability of evapotranspiration and energy exchange over an annual grassland in california," *Journal of Geophysical Research*, vol. 113, may 2008.

[211] Y. Hao, Y. Wang, X. Huang, X. Cui, X. Zhou, S. Wang, H. Niu, and G. Jiang, "Seasonal and interannual variation in water vapor and energy exchange over a typical steppe in inner mongolia, china," *Agricultural and Forest Meteorology*, vol. 146, pp. 57–69, sep 2007.

[212] E. M. Steinauer and S. L. Collins, "Prairie ecology: The tallgrass prairie," *Prairie Conservation. Island Press, Washington*, pp. 39–52, 1996.

[213] K. Chapman, M. White, R. Johnson, and Z. Wong, "An approach to evaluate long-term survival of the tallgrass prairie ecosystem," *The Nature Conservancy, Midwest Regional Office, Minneapolis, MN*, vol. 50, 1990.

[214] C. H. Freese, S. D. Fuhlendorf, and K. Kunkel, "A management framework for the transition from livestock production toward biodiversity conservation on great plains rangelands," *Ecological Restoration*, vol. 32, pp. 358–368, nov 2014.

[215] S. R. Archer, E. M. Andersen, K. I. Predick, S. Schwinning, R. J. Steidl, and S. R. Woods, *Woody Plant Encroachment: Causes and Consequences*, pp. 25–84. Cham: Springer International Publishing, 2017.

[216] A. K. Knapp, C. Beier, D. D. Briske, A. T. Classen, Y. Luo, M. Reichstein, M. D. Smith, S. D. Smith, J. E. Bell, P. A. Fay, J. L. Heisler, S. W. Leavitt, R. Sherry, B. Smith, and E. Weng, "Consequences of more extreme precipitation regimes for terrestrial ecosystems," *BioScience*, vol. 58, pp. 811–821, oct 2008.

[217] M. Shafer, D. Ojima, J. M. Antle, D. Kluck, R. A. McPherson, S. Petersen, B. Scanlon, and K. Sherman, "Ch. 19: Great plains. climate change impacts in the united states: the third national climate assessment," tech. rep., 2014.

[218] X. Sun, C. B. Zou, B. Wilcox, and E. Stebler, "Effect of vegetation on the energy balance and evapotranspiration in tallgrass prairie: A paired study using the eddy-covariance method," *Boundary-Layer Meteorology*, vol. 170, pp. 127–160, Jan 2019.

[219] P. Wagle, X. Xiao, P. Gowda, J. Basara, N. Brunsell, J. Steiner, and A. K.C, "Analysis and estimation of tallgrass prairie evapotranspiration in the central united states," *Agricultural and Forest Meteorology*, vol. 232, pp. 35–47, jan 2017.

[220] E. Blyth and R. J. Harding, "Methods to separate observed global evapotranspiration into the interception, transpiration and soil surface evaporation components," *Hydrological Processes*, vol. 25, pp. 4063–4068, dec 2011.

[221] S. P. Good, D. Noone, and G. Bowen, "Hydrologic connectivity constrains partitioning of global terrestrial water fluxes," *Science*, vol. 349, pp. 175–177, jul 2015.

[222] J. B. Fisher, F. Melton, E. Middleton, C. Hain, M. Anderson, R. Allen, M. F. McCabe, S. Hook, D. Baldocchi, P. A. Townsend, A. Kilic, K. Tu, D. D. Miralles, J. Perret, J.-P. Lagouarde, D. Waliser, A. J. Purdy, A. French, D. Schimel, J. S. Famiglietti, G. Stephens, and E. F. Wood, "The future of evapotranspiration: Global requirements for ecosystem functioning, carbon and climate feedbacks, agricultural management, and water resources," *Water Resources Research*, vol. 53, pp. 2618–2626, apr 2017.

[223] T. M. Scanlon and W. P. Kustas, "Partitioning carbon dioxide and water vapor fluxes using correlation analysis," *Agricultural and Forest Meteorology*, vol. 150, pp. 89–99, jan 2010.

[224] M. Berkelhammer, D. C. Noone, T. E. Wong, S. P. Burns, J. F. Knowles, A. Kaushik, P. D. Blanken, and M. W. Williams, "Convergent approaches to determine an ecosystem's transpiration fraction," *Global Biogeochemical Cycles*, vol. 30, pp. 933–951, jun 2016.

[225] S. Fatichi and C. Pappas, "Constrained variability of modeled t:ET ratio across biomes," *Geophysical Research Letters*, vol. 44, pp. 6795–6803, jul 2017.

[226] C. Gu, J. Ma, G. Zhu, H. Yang, K. Zhang, Y. Wang, and C. Gu, "Partitioning evapotranspiration using an optimized satellite-based ET model across biomes," *Agricultural and Forest Meteorology*, vol. 259, pp. 355–363, sep 2018.

[227] X. Li, P. Gentine, C. Lin, S. Zhou, Z. Sun, Y. Zheng, J. Liu, and C. Zheng, "A simple and objective method to partition evapotranspiration into transpiration and evaporation at eddy-covariance sites," *Agricultural and Forest Meteorology*, vol. 265, pp. 171–182, feb 2019.

[228] A. K. Knapp, "Rainfall variability, carbon cycling, and plant species diversity in a mesic grassland," *Science*, vol. 298, pp. 2202–2205, dec 2002.

[229] X. Sun, B. P. Wilcox, and C. B. Zou, "Evapotranspiration partitioning in dryland ecosystems: A global meta-analysis of in situ studies," *Journal of Hydrology*, vol. 576, pp. 123–136, sep 2019.

[230] L. Wang, S. Niu, S. P. Good, K. Soderberg, M. F. McCabe, R. A. Sherry, Y. Luo, X. Zhou, J. Xia, and K. K. Caylor, "The effect of warming on grassland evapotranspiration partitioning using laser-based isotope monitoring techniques," *Geochimica et Cosmochimica Acta*, vol. 111, pp. 28–38, jun 2013.

[231] P. Sturm and A. Knohl, "Water vapor δ^2h and δ^{18}o measurements using off-axis integrated cavity output spectroscopy," *Atmospheric Measurement Techniques*, vol. 3, no. 1, pp. 67–77, 2010.

[232] M. Schmidt, K. Maseyk, C. Lett, P. Biron, P. Richard, T. Bariac, and U. Seibt, "Concentration effects on laser-based δ18o and δ2h measurements and implications for the calibration of vapour measurements with liquid standards," *Rapid Communications in Mass Spectrometry*, vol. 24, pp. 3553–3561, nov 2010.

[233] K. Wythers, W. Lauenroth, and J. Paruelo, "Bare-soil evaporation under semiarid field conditions," *Soil Science Society of America Journal*, vol. 63, no. 5, p. 1341, 1999.

[234] J. Durand, T. Bariac, M. Ghesquière, P. Biron, P. Richard, M. Humphreys, and Z. Zwierzykovski, "Ranking of the depth of water extraction by individual grass plants,

using natural 18o isotope abundance," *Environmental and Experimental Botany*, vol. 60, pp. 137–144, may 2007.

[235] K. D. Eggemeyer, T. Awada, F. E. Harvey, D. A. Wedin, X. Zhou, and C. W. Zanner, "Seasonal changes in depth of water uptake for encroaching trees juniperus virginiana and pinus ponderosa and two dominant c4 grasses in a semiarid grassland," *Tree Physiology*, vol. 29, pp. 157–169, dec 2008.

[236] D. Bachmann, A. Gockele, J. M. Ravenek, C. Roscher, T. Strecker, A. Weigelt, and N. Buchmann, "No evidence of complementary water use along a plant species richness gradient in temperate experimental grasslands," *PLOS ONE*, vol. 10, p. e0116367, jan 2015.

[237] J. R. Ehleringer, J. Roden, and T. E. Dawson, *Assessing Ecosystem-Level Water Relations Through Stable Isotope Ratio Analyses*, pp. 181–198. New York, NY: Springer New York, 2000.

[238] A. G. West, S. J. Patrickson, and J. R. Ehleringer, "Water extraction times for plant and soil materials used in stable isotope analysis," *Rapid Communications in Mass Spectrometry*, vol. 20, no. 8, pp. 1317–1321, 2006.

[239] D. Penna, L. Hopp, F. Scandellari, S. T. Allen, P. Benettin, M. Beyer, J. Geris, J. Klaus, J. D. Marshall, L. Schwendenmann, T. H. M. Volkmann, J. von Freyberg, A. Amin, N. Ceperley, M. Engel, J. Frentress, Y. Giambastiani, J. J. McDonnell, G. Zuecco, P. Llorens, R. T. W. Siegwolf, T. E. Dawson, and J. W. Kirchner, "Ideas and perspectives: Tracing terrestrial ecosystem water fluxes using hydrogen and oxygen stable isotopes – challenges and opportunities from an interdisciplinary perspective," *Biogeosciences*, vol. 15, pp. 6399–6415, oct 2018.

[240] A. G. West, G. R. Goldsmith, P. D. Brooks, and T. E. Dawson, "Discrepancies between isotope ratio infrared spectroscopy and isotope ratio mass spectrometry for the stable isotope analysis of plant and soil waters," *Rapid Communications in Mass Spectrometry*, vol. 24, pp. 1948–1954, jun 2010.

[241] A. G. West, G. R. Goldsmith, I. Matimati, and T. E. Dawson, "Spectral analysis software improves confidence in plant and soil water stable isotope analyses performed by isotope ratio infrared spectroscopy (IRIS)," *Rapid Communications in Mass Spectrometry*, vol. 25, pp. 2268–2274, jul 2011.

[242] G. J. Bowen, Z. Cai, R. P. Fiorella, and A. L. Putman, "Isotopes in the water cycle: Regional- to global-scale patterns and applications," *Annual Review of Earth and Planetary Sciences*, vol. 47, feb 2019.

[243] J. R. Gat, "Oxygen and hydrogen isotopes in the hydrologic cycle," *Annual Review of Earth and Planetary Sciences*, vol. 24, pp. 225–262, may 1996.

[244] M. Quade, A. Klosterhalfen, A. Graf, N. Brüggemann, N. Hermes, H. Vereecken, and Y. Rothfuss, "In-situ monitoring of soil water isotopic composition for partitioning of evapotranspiration during one growing season of sugar beet (beta vulgaris)," *Agricultural and Forest Meteorology*, vol. 266-267, pp. 53–64, mar 2019.

[245] S. P. Good, K. Soderberg, L. Wang, and K. K. Caylor, "Uncertainties in the assessment of the isotopic composition of surface fluxes: A direct comparison of techniques using laser-based water vapor isotope analyzers," *Journal of Geophysical Research: Atmospheres*, vol. 117, pp. n/a–n/a, aug 2012.

[246] X. Lee, R. Smith, and J. Williams, "Water vapour 18o/16o isotope ratio in surface air in new england, USA," *Tellus B: Chemical and Physical Meteorology*, vol. 58, pp. 293–304, jan 2006.

[247] M. Dubbert, M. Cuntz, A. Piayda, C. Maguás, and C. Werner, "Partitioning evapotranspiration–testing the craig and gordon model with field measurements of oxygen isotope ratios of evaporative fluxes," *Journal of Hydrology*, vol. 496, pp. 142–153, 2013.

[248] C. D. Cappa, "Isotopic fractionation of water during evaporation," *Journal of Geophysical Research*, vol. 108, no. D16, 2003.

[249] M. Majoube, "Fractionnement en oxygène 18 et en deutérium entre l'eau et sa vapeur," *Journal de Chimie Physique*, vol. 68, pp. 1423–1436, 1971.

[250] H. Craig, "Isotopic variations in meteoric waters," *Science*, vol. 133, pp. 1702–1703, may 1961.

[251] O. Tetens, "Uber einige meteorologische begriffe," *Z. geophys*, vol. 6, pp. 297–309, 1930.

[252] A. L. Buck, "New equations for computing vapor pressure and enhancement factor," *Journal of Applied Meteorology*, vol. 20, pp. 1527–1532, dec 1981.

[253] L. Merlivat, "Molecular diffusivities of $h[2][16]o$, $hd[16]o$, and $h[2][18]o$ in gases," *The Journal of Chemical Physics*, vol. 69, no. 6, p. 2864, 1978.

[254] I. Braud, T. Bariac, M. Vauclin, Z. Boujamlaoui, J. Gaudet, P. Biron, and P. Richard, "SiSPAT-isotope, a coupled heat, water and stable isotope (HDO and h218o) transport model for bare soil. part II. evaluation and sensitivity tests using two laboratory data sets," *Journal of Hydrology*, vol. 309, pp. 301–320, jul 2005.

[255] R. Mathieu and T. Bariac, "An isotopic study (2h and18o) of water movements in clayey soils under a semiarid climate," *Water Resources Research*, vol. 32, pp. 779–789, apr 1996.

[256] C. tai Lai, J. R. Ehleringer, B. J. Bond, and K. T. P. U, "Contributions of evaporation, isotopic non-steady state transpiration and atmospheric mixing on the delta18O of water vapour in Pacific Northwest coniferous forests," *Plant, Cell and Environment*, vol. 29, pp. 77–94, jan 2006.

[257] M. Dubbert, M. Cuntz, A. Piayda, and C. Werner, "Oxygen isotope signatures of transpired water vapor: the role of isotopic non-steady-state transpiration under natural conditions," *New Phytologist*, vol. 203, no. 4, pp. 1242–1252, 2014.

[258] G. D. Farquhar and L. A. Cernusak, "On the isotopic composition of leaf water in the non-steady state," *Functional Plant Biology*, vol. 32, no. 4, p. 293, 2005.

[259] D. L. Phillips and J. W. Gregg, "Uncertainty in source partitioning using stable isotopes," *Oecologia*, vol. 127, pp. 171–179, apr 2001.

[260] J. D. Marshall, J. R. Brooks, and K. Lajtha, "Sources of variation in the stable isotopic composition of plants," in *Stable Isotopes in Ecology and Environmental Science*, pp. 22–60, Blackwell Publishing Ltd, 2007.

[261] J. R. Ehleringer and T. E. Dawson, "Water uptake by plants: perspectives from stable isotope composition," *Plant, Cell and Environment*, vol. 15, pp. 1073–1082, dec 1992.

[262] J. B. Jaeschke, M. A. Scholl, I. M. Cozzarelli, J. R. Masoner, S. Christenson, and H. Qi, "Stable-isotope ratios of hydrogen and oxygen in precipitation at norman, oklahoma, 1996-2008," 2011.

[263] K. Rozanski, L. Araguás-Araguás, and R. Gonfiantini, "Isotopic patterns in modern global precipitation," *Climate change in continental isotopic records*, vol. 78, pp. 1–36, 1993.

[264] C. A. Aguirre-Gutiérrez, F. Holwerda, G. R. Goldsmith, J. Delgado, E. Yepez, N. Carbajal, M. Escoto-Rodríguez, and J. T. Arredondo, "The importance of dew in the water balance of a continental semiarid grassland," *Journal of Arid Environments*, may 2019.

[265] Z. Wei, K. Yoshimura, A. Okazaki, W. Kim, Z. Liu, and M. Yokoi, "Partitioning of evapotranspiration using high-frequency water vapor isotopic measurement over a rice paddy field," *Water Resources Research*, vol. 51, pp. 3716–3729, may 2015.

[266] X. Lee, J. Huang, and E. G. Patton, "A large-eddy simulation study of water vapour and carbon dioxide isotopes in the atmospheric boundary layer," *Boundary-Layer Meteorology*, vol. 145, pp. 229–248, jul 2011.

[267] E. J. Oerter and G. J. Bowen, "Spatio-temporal heterogeneity in soil water stable isotopic composition and its ecohydrologic implications in semiarid ecosystems," *Hydrological Processes*, apr 2019.

[268] M. Sprenger, D. Tetzlaff, and C. Soulsby, "Soil water stable isotopes reveal evaporation dynamics at the soil–plant–atmosphere interface of the critical zone," *Hydrology and Earth System Sciences*, vol. 21, pp. 3839–3858, jul 2017.

[269] W. J. Riley, C. J. Still, B. R. Helliker, M. Ribas-Carbo, and J. A. Berry, "18o composition of CO2 and h2o ecosystem pools and fluxes in a tallgrass prairie: Simulations and comparisons to measurements," *Global Change Biology*, vol. 9, pp. 1567–1581, nov 2003.

[270] M. Sprenger, B. Herbstritt, and M. Weiler, "Established methods and new opportunities for pore water stable isotope analysis," *Hydrological Processes*, vol. 29, pp. 5174–5192, sep 2015.

[271] Y. Rothfuss, H. Vereecken, and N. Brüggemann, "Monitoring water stable isotopic composition in soils using gas-permeable tubing and infrared laser absorption spectroscopy," *Water Resources Research*, vol. 49, pp. 3747–3755, jun 2013.

[272] L. R. Welp, X. Lee, K. Kim, T. J. Griffis, K. A. Billmark, and J. M. Baker, "δ18o of water vapour, evapotranspiration and the sites of leaf water evaporation in a soybean canopy," *Plant, Cell & Environment*, vol. 31, pp. 1214–1228, sep 2008.

[273] X.-F. Wen, X. Lee, X.-M. Sun, J.-L. Wang, Y.-K. Tang, S.-G. Li, and G.-R. Yu, "Intercomparison of four commercial analyzers for water vapor isotope measurement," *Journal of Atmospheric and Oceanic Technology*, vol. 29, pp. 235–247, feb 2012.

[274] C. Risi, A. Landais, S. Bony, J. Jouzel, V. Masson-Delmotte, and F. Vimeux, "Understanding the17o excess glacial-interglacial variations in vostok precipitation," *Journal of Geophysical Research*, vol. 115, may 2010.

[275] B. Yang, P. Wang, D. You, and W. Liu, "Coupling evapotranspiration partitioning with root water uptake to identify the water consumption characteristics of winter wheat: A case study in the north china plain," *Agricultural and Forest Meteorology*, vol. 259, pp. 296–304, sep 2018.

[276] P. Wang, X.-Y. Li, L. Wang, X. Wu, X. Hu, Y. Fan, and Y. Tong, "Divergent evapotranspiration partition dynamics between shrubs and grasses in a shrub-encroached steppe ecosystem," *New Phytologist*, vol. 219, pp. 1325–1337, jun 2018.

[277] T. H. M. Volkmann, K. Haberer, A. Gessler, and M. Weiler, "High-resolution isotope measurements resolve rapid ecohydrological dynamics at the soil-plant interface," *New Phytologist*, vol. 210, pp. 839–849, feb 2016.

[278] S. M. Vicente-Serrano, C. Gouveia, J. J. Camarero, S. Begueria, R. Trigo, J. I. Lopez-Moreno, C. Azorin-Molina, E. Pasho, J. Lorenzo-Lacruz, J. Revuelto, E. Moran-Tejeda, and A. Sanchez-Lorenzo, "Response of vegetation to drought time-scales across global land biomes," *Proceedings of the National Academy of Sciences*, vol. 110, pp. 52–57, dec 2012.

[279] O. E. Sala, L. A. Gherardi, and D. P. C. Peters, "Enhanced precipitation variability effects on water losses and ecosystem functioning: differential response of arid and mesic regions," *Climatic Change*, vol. 131, pp. 213–227, apr 2015.

[280] N. Raz-Yaseef, D. P. Billesbach, M. L. Fischer, S. C. Biraud, S. A. Gunter, J. A. Bradford, and M. S. Torn, "Vulnerability of crops and native grasses to summer drying in the u.s. southern great plains," *Agriculture, Ecosystems & Environment*, vol. 213, pp. 209–218, dec 2015.

[281] S. Ravi, P. D'Odorico, L. Wang, C. S. White, G. S. Okin, S. A. Macko, and S. L. Collins, "Post-fire resource redistribution in desert grasslands: A possible negative feedback on land degradation," *Ecosystems*, vol. 12, pp. 434–444, feb 2009.

[282] B. P. Wilcox, A. Birt, S. R. Archer, S. D. Fuhlendorf, U. P. Kreuter, M. G. Sorice, W. J. D. van Leeuwen, and C. B. Zou, "Viewing woody-plant encroachment through a social–ecological lens," *BioScience*, vol. 68, pp. 691–705, sep 2018.

[283] J. M. Briggs, A. K. Knapp, and B. L. Brock, "Expansion of woody plants in tallgrass prairie: A fifteen-year study of fire and fire-grazing interactions," *The American Midland Naturalist*, vol. 147, pp. 287–294, apr 2002.

[284] Z. Ratajczak, J. M. Briggs, D. G. Goodin, L. Luo, R. L. Mohler, J. B. Nippert, and B. Obermeyer, "Assessing the potential for transitions from tallgrass prairie to woodlands: Are we operating beyond critical fire thresholds?," *Rangeland Ecology & Management*, vol. 69, pp. 280–287, jul 2016.

[285] O. V. Auken, "Causes and consequences of woody plant encroachment into western north american grasslands," *Journal of Environmental Management*, vol. 90, pp. 2931–2942, jul 2009.

[286] C. B. Zou, G. L. Caterina, R. E. Will, E. Stebler, and D. Turton, "Canopy interception for a tallgrass prairie under juniper encroachment," *PLOS ONE*, vol. 10, p. e0141422, nov 2015.

[287] C. B. Zou, L. Qiao, and B. P. Wilcox, "Woodland expansion in central oklahoma will significantly reduce streamflows - a modelling analysis," *Ecohydrology*, vol. 9, pp. 807–816, sep 2015.

[288] B. S. Acharya, Y. Hao, T. E. Ochsner, and C. B. Zou, "Woody plant encroachment alters soil hydrological properties and reduces downward flux of water in tallgrass prairie," *Plant and Soil*, vol. 414, pp. 379–391, dec 2016.

[289] T. E. Huxman, B. P. Wilcox, D. D. Breshears, R. L. Scott, K. A. Snyder, E. E. Small, K. Hultine, W. T. Pockman, and R. B. Jackson, "Ecohydrological implications of woody plant encroachment," *Ecology*, vol. 86, pp. 308–319, feb 2005.

[290] W. A. Dugas, R. A. Hicks, and R. P. Gibbens, "Structure and function of c3and c4chihuahuan desert plant communities. energy balance components," *Journal of Arid Environments*, vol. 34, pp. 63–79, sep 1996.

[291] G. L. Caterina, R. E. Will, D. J. Turton, D. S. Wilson, and C. B. Zou, "Water use of juniperus virginiana trees encroached into mesic prairies in oklahoma, usa," *Ecohydrology*, vol. 7, no. 4, pp. 1124–1134, 2014.

[292] C. Zou, D. Twidwell, C. Bielski, D. Fogarty, A. Mittelstet, P. Starks, R. Will, Y. Zhong, and B. Acharya, "Impact of eastern redcedar proliferation on water resources in the great plains USA—current state of knowledge," *Water*, vol. 10, p. 1768, dec 2018.

[293] M. Dubbert and C. Werner, "Water fluxes mediated by vegetation: emerging isotopic insights at the soil and atmosphere interfaces," *New Phytologist*, vol. 221, pp. 1754–1763, nov 2018.

[294] R. P. Fiorella, C. J. Poulsen, and A. M. Matheny, "Seasonal patterns of water cycling in a deep, continental mountain valley inferred from stable water vapor isotopes," *Journal of Geophysical Research: Atmospheres*, jul 2018.

[295] M. Moreira, L. Sternberg, L. Martinelli, R. Victoria, E. Barbosa, L. Bonates, and D. Nepstad, "Contribution of transpiration to forest ambient vapour based on isotopic measurements," *Global Change Biology*, vol. 3, pp. 439–450, oct 1997.

[296] P. van Els, R. E. Will, M. W. Palmer, and K. R. Hickman, "Changes in forest understory associated withJuniperusencroachment in oklahoma, USA," *Applied Vegetation Science*, feb 2010.

[297] G. Dongmann, H. W. Nrnberg, H. Frstel, and K. Wagener, "On the enrichment of h2 18o in the leaves of transpiring plants," *Radiation and Environmental Biophysics*, vol. 11, pp. 41–52, mar 1974.

[298] C. B. Zou, D. J. Turton, R. E. Will, D. M. Engle, and S. D. Fuhlendorf, "Alteration of hydrological processes and streamflow with juniper (juniperus virginiana) encroachment in a mesic grassland catchment," *Hydrological Processes*, vol. 28, no. 26, pp. 6173–6182, 2014.

[299] B. S. Acharya, E. Stebler, and C. B. Zou, "Monitoring litter interception of rainfall using leaf wetness sensor under controlled and field conditions," *Hydrological Processes*, vol. 31, pp. 240–249, nov 2016.

[300] J. Wang, X. Xiao, Y. Qin, R. B. Doughty, J. Dong, and Z. Zou, "Characterizing the encroachment of juniper forests into sub-humid and semi-arid prairies from 1984 to 2010 using PALSAR and landsat data," *Remote Sensing of Environment*, vol. 205, pp. 166–179, feb 2018.

[301] H. Walter and J. H. Burnett, *Ecology of tropical and subtropical vegetation*. Van Nostrand Reinhold Company, 1971.

[302] J. F. Reynolds, "Effects of long-term rainfall variability on evapotranspiration and soil water distribution in the chihuahuan desert: A modeling analysis," *Plant Ecology*, vol. 150, no. 1/2, pp. 145–159, 2000.

[303] S. I. Higgins, W. J. Bond, and W. S. W. Trollope, "Fire, resprouting and variability: a recipe for grass-tree coexistence in savanna," *Journal of Ecology*, vol. 88, pp. 213–229, apr 2000.

[304] H. J. Schenk and R. B. Jackson, "Rooting depths, lateral root spreads and belowground/above-ground allometries of plants in water-limited ecosystems," *Journal of Ecology*, vol. 90, pp. 480–494, may 2002.

[305] J. B. Nippert and A. K. Knapp, "Soil water partitioning contributes to species coexistence in tallgrass prairie," *Oikos*, vol. 116, pp. 1017–1029, jun 2007.

[306] A. Kulmatiski and K. H. Beard, "Woody plant encroachment facilitated by increased precipitation intensity," *Nature Climate Change*, vol. 3, pp. 833–837, may 2013.

[307] J. Liu, X. Xu, Y. Zhang, Y. Tian, and Q. Gao, "Effect of rainfall interannual variability on the biomass and soil water distribution in a semiarid shrub community," *Science China Life Sciences*, vol. 53, pp. 729–737, jun 2010.

[308] M. Detto, N. Montaldo, J. D. Albertson, M. Mancini, and G. Katul, "Soil moisture and vegetation controls on evapotranspiration in a heterogeneous mediterranean ecosystem on sardinia, italy," *Water Resources Research*, vol. 42, aug 2006.

[309] M. Tsujimura, L. Sasaki, T. Yamanaka, A. Sugimoto, S.-G. Li, D. Matsushima, A. Kotani, and M. Saandar, "Vertical distribution of stable isotopic composition in atmospheric wa-

ter vapor and subsurface water in grassland and forest sites, eastern mongolia," *Journal of Hydrology*, vol. 333, pp. 35–46, jan 2007.

[310] M. G. Mazzacavallo and A. Kulmatiski, "Modelling water uptake provides a new perspective on grass and tree coexistence," *PLOS ONE*, vol. 10, p. e0144300, dec 2015.

APPENDIX A

SAMPLE R CODE FOR EXTRACTING THE PLANETARY BOUNDARY-LAYER HEIGHT

The sample R code for extracting the planetary boundary-layer height based on the geographical location (latitude and longitude) from the North American Regional Reanalysis data.

```
### Projection information for NCEP North American Regional
   Reanalysis: NARR
### is Northern Lambert Conformal Conic grid.
### Corners of this grid are
### 12.2N; 133.5W,
### 54.5N; 152.9W,
### 57.3N; 49.4W,
### 14.3N; 65.1W (essentially, North America).
### The grid resolution is 349x277, which is approximately 0.3 degrees
   (32km)
### resolution at the lowest latitude
### more details about the coverage can be found here
### https://www.esrl.noaa.gov/psd/data/gridded/data.narr.monolevel.html
#####################################################
######first step is to download the data for the year you interested
###### the data for each year usually quite big, around 700 MB, takes
   time.
#####################################################

############ First way to download data with your internet browser
############ and save locally in your working directory.
############ this is the url:
```

```
   ftp://ftp.cdc.noaa.gov/Datasets/NARR/monolevel/
############ or with "download.file"
############ decide which year's data will be downloaded from "1979 -
   present"
my_year <- 2016 # year of 2016 is just an example
## link example:
   ftp://ftp.cdc.noaa.gov/Datasets/NARR/monolevel/hpbl.1979.nc
URL <-
   paste0("ftp://ftp.cdc.noaa.gov/Datasets/NARR/
   monolevel/hpbl.",my_year,".nc")
download.file(url = URL, destfile = paste0("hpbl.",my_year,".nc"))
############ second way is automatically grab data online with
   "data.table" pacakge
library(data.table)
### decide which year's data will be downloaded from "1979 - present"
my_year <- 2016 # year of 2016 is just an example
hpbl_2016 <- fread(paste0("ftp://ftp.cdc.noaa.gov/Datasets/
                NARR/monolevel/hpbl.",my_year,".nc"))
#######################################################
###### second step is to load the data with package "ncdf4"
#######################################################
library(ncdf4)
obsdata <- nc_open("hpbl.2016.nc")
print(obsdata) # check that dims are lon-lat-time
library(raster)
r <- brick("hpbl_2016.nc", varname = "hpbl")
############
## here you need to find your location information (the variables
   "lon" and "lat")
```

```
## under Lambert Conformal Conic grid.
## you can load the downloade netCDF file in ArcGIS with the tool
   "Make NetCDF Raster Layer"
## to find your location information
## the following number "6538325.863, 3108446.503" is an example for
   my site, you need to revise
## this spatial location according to your site.
############
vals <- extract(r, matrix(c(6538325.863 , 3108446.503), ncol = 2))
dim(vals)
head(vals)
write.csv(vals, "hpbl_site.csv")
########### transpose the output table from wide to long
hpbl <- t(read.csv("hpbl_site.csv"))
hpbl <- as.data.frame(hpbl)
head(hpbl)
names(hpbl)
###### need library "tibble"
hpbl <- tibble::rownames_to_column(hpbl, var = "date_time")
names(hpbl)<- c("date_time", "height")
class(hpbl)
hpbl$date_time <- sub("^X", "", hpbl$date_time)
hpbl$date_time <- as.POSIXct(hpbl$date_time, format =
   "%Y.%m.%d.%H.%M.%S", tz = "UTC")
hpbl <- hpbl[-1,]
hpbl$date_time <- lubridate::ceiling_date(hpbl$date_time, "30 mins" )
### generate a half-hour time series
half_hour_seq <- seq(
from=as.POSIXct("2016-01-01 00:00:00","%Y-%m-%d %H:%M:%S", tz="UTC"),
```

```
to=as.POSIXct("2017-01-01 00:00:00", "%Y-%m-%d %H:%M:%S", tz="UTC"),
by="30 min"
)
half_hour_seq <- as.data.frame(half_hour_seq)
head(half_hour_seq)
head(hpbl$date_time)

library(dplyr)
library(tidyr)
### join with the hpbl data
hpbl_1 <- left_join(half_hour_seq, hpbl, by = c("half_hour_seq" =
   "date_time") )
head(hpbl_1)
tail(hpbl_1)
summary(hpbl_1)
#### interpolate with linear method
hpbl_1$height <- imputeTS::na.interpolation(hpbl_1$height, option =
   "linear")
write.csv(hpbl_1, "hpbl_1_interpolated.csv")
saveRDS(hpbl_1, "hpbl_1_interpolated.rds")
#####################
## the extraction for pbhl is done, then you need to join this value
   to your input dataframe for
## Kljun's model
#########
```

APPENDIX B

R CODE USED FOR ISOTOPIC ET PARTITIONING

These R code were used for application of the two-source mixing model in grassland in Chapter 3.3.

```
**********************************************
**********************************************
**********************************************
Premable: loading packages
**********************************************
**********************************************
**********************************************
# Load packages
   ------------------------------------------------------------
## load fonts must load before ggplot2
suppressMessages(extrafont::loadfonts(device = "postscript"))
library(conflicted)
conflict_prefer("filter", "dplyr")
conflict_prefer("first", "dplyr")
conflict_prefer("last", "dplyr")
library(tidyverse)
conflict_prefer("alpha", "ggplot2")
library(here)
conflict_prefer("here", "here")
library(lubridate)
library(zoo)
```

```
library(rvg)
library(patchwork)
library(emojifont)
library(export)
library(scales)
library(readxl)
library(ggpmisc)
library(Cairo)
library(grid)
library(gridExtra)
windowsFonts(Times=windowsFont("TT Times New Roman"))
library(patchwork)
library(Hmisc)
library(readxl)
library(xtable)
library(ggthemes)
library(ggpubr)
library(PerformanceAnalytics)

## double check time zone
Sys.timezone()


**********************************************
**********************************************
**********************************************
Long-term climate analysis based on MARENA mesonet data
**********************************************
**********************************************
**********************************************
```

```
library(grid)
StatHistorical <- ggproto("StatHistorical", Stat,
compute_group = function(data, scales, params) {
  data <- data %>%
  filter(year != max(year)) %>%
  group_by(x) %>%
  mutate(ymin = Hmisc::smean.cl.normal(y)[3],
  ymax = Hmisc::smean.cl.normal(y)[2]) %>%
  ungroup()
},
required_aes = c("x", "y", "year"))

# Create the layer
stat_historical <- function(mapping = NULL, data = NULL, geom =
   "point",
position = "identity", na.rm = FALSE, show.legend = NA,
inherit.aes = TRUE, ...) {
  list(
  layer(
  stat = "identity", data = data, mapping = mapping, geom = geom,
  position = position, show.legend = show.legend, inherit.aes =
     inherit.aes,
  params = list(na.rm = na.rm, col = "#EED8AE", alpha = 0.3, shape =
     16, ...)
  ),
  layer(
  stat = StatHistorical, data = data, mapping = mapping, geom =
     "linerange",
  position = position, show.legend = show.legend, inherit.aes =
```

```
      inherit.aes,
    params = list(na.rm = na.rm, col = "#9b887d", ...)
    )
    )
}

# Create the stats object
StatPresent <- ggproto("StatPresent", Stat,
compute_group = function(data, scales, params) {
    data <- filter(data, year == max(year))
},
required_aes = c("x", "y", "year"))

# Create the layer
stat_present <- function(mapping = NULL, data = NULL, geom = "line",
position = "identity", na.rm = FALSE, show.legend = NA,
inherit.aes = TRUE, ...) {
    layer(
    stat = StatPresent, data = data, mapping = mapping, geom = geom,
    position = position, show.legend = show.legend, inherit.aes =
      inherit.aes,
    params = list(na.rm = na.rm,col = "#65889b", size = 0.705, ...)
    )
}

# Create the stats object
StatExtremes <- ggproto("StatExtremes", Stat,
compute_group = function(data, scales, params) {
```

```
  present <- data %>%
  filter(year == max(year))
  past <- data %>%
  filter(year != max(year))
  past_extremes <- past %>%
  group_by(x) %>%
  summarise(past_low = min(y),
  past_high = max(y))

  # transform data to contain extremes
  data <- present %>%
  left_join(past_extremes) %>%
  mutate(record = ifelse(y < past_low,
  "#0000CD",
  ifelse(y > past_high,
  "#CD2626",
  "#00000000")))
},
required_aes = c("x", "y", "year"))

# Create the layer
stat_extremes <- function(mapping = NULL, data = NULL, geom = "point",
position = "identity", na.rm = FALSE, show.legend = NA,
inherit.aes = TRUE, ...) {
  layer(
  stat = StatExtremes , data = data, mapping = mapping, geom = geom,
  position = position, show.legend = show.legend, inherit.aes =
     inherit.aes,
  params = list(na.rm = na.rm, ...)
```

```
  )
}
# Finish the function draw_pop_legend
#draw_pop_legend <- function(x = 0.6, y = 0.2, width = 0.2, height =
   0.2, fontsize = 10) default value
draw_pop_legend <- function(x = 0.95, y = 0.5, width = 0.2, height =
   0.2, fontsize = 10) {
  # Finish viewport() function
  pushViewport(viewport(x = x, y = y, width = width, height = height,
     just = "center"))

  legend_labels <- c("Record high",
  "95% CI range",
  "Current year",
  "Past years",
  "Record low")

  legend_position <- c(0.9, 0.7, 0.5, 0.2, 0.1)

  # Finish grid.text() function
  grid.text(label = legend_labels, x = 0.12, y = legend_position,
  just = "left",
  gp = gpar(fontsize = fontsize, col = "grey20"))

  # Position dots, rectangle and line
  point_position_y <- c(0.1, 0.2, 0.9)
  point_position_x <- rep(0.06, length(point_position_y))
  grid.points(x = point_position_x, y = point_position_y, pch = 16,
  gp = gpar(col = c("#0000CD", "#EED8AE", "#CD2626")))
```

```
  grid.rect(x = 0.06, y = 0.5, width = 0.06, height = 0.4,
  gp = gpar(col = NA, fill = "#9b887d"))
  grid.lines(x = c(0.03, 0.09), y = c(0.5, 0.5),
  gp = gpar(col = "#65889b", lwd = 3))

  # Add popViewport() for bookkeeping
  popViewport()
}

**********************************************
**********************************************
**********************************************
Application of Keeling-plot method
**********************************************
**********************************************
**********************************************
library(broom)
picarro_cleaned <-
readRDS(here("delta_ET", "3_output", "3_picarro_cleaned",
   "picarro_cleaned.rds")) %>%
filter(my_date >= lubridate::ymd("2016-06-01")) %>%
select(time_label, my_date, time_decimal, height, water, hydrogen,
   oxygen) %>%
mutate(time_label = lubridate::ceiling_date(time_label, "hour"),
water_reciprocal = 1/water,
time_label = as.character(time_label))

# hydrogen
   ------------------------------------------------------------------
```

```
keeling_hydrogen_analysis <-
picarro_cleaned %>%
split(.$time_label) %>%
map(~ lm(hydrogen ~ water_reciprocal, data = .)) %>%
map(broom::tidy) %>% #
   https://broom.tidyverse.org/reference/tidy.lm.html
map_df(tibble::rownames_to_column, 'var', .id = 'name') %>%
select(-c("statistic", "p.value")) %>%
gather(key = result_type, value = value,
c("estimate", "std.error")) %>%
unite(col = "new_key", c("term", "result_type"), remove = TRUE) %>%
select(- "var") %>%
spread(key = "new_key", value = value) %>%
rename(intercept_estimate = "(Intercept)_estimate",
intercept_se   = "(Intercept)_std.error",
slope_estimate = "water_reciprocal_estimate",
slope_se       = "water_reciprocal_std.error")
###
keeling_hydrogen_statistics <-
picarro_cleaned %>%
split(.$time_label) %>%
map(~ lm(hydrogen ~ water_reciprocal, data = .)) %>%
map(glance) %>%
#https://www.rdocumentation.org/packages/broom/versions/0.5.2/
topics/glance.lm
map_df(tibble::rownames_to_column, 'var', .id = 'name') %>%
rename(F_statistic = statistic, F_test_p.value = p.value) %>%
select(name, r.squared, F_statistic, F_test_p.value, AIC, BIC)
```

```
keeling_hydrogen <-
left_join(keeling_hydrogen_analysis,
  keeling_hydrogen_statistics, by = "name") %>%
mutate(date_time = ymd_hms(name)) %>%
rename_at(vars(- c("name", "date_time")), ~ paste0(., "_hydrogen"))

head(keeling_hydrogen)
# oxygen
   ------------------------------------------------------------------
keeling_oxygen_analysis <-
picarro_cleaned %>%
split(.$time_label) %>%
map(~ lm(oxygen ~ water_reciprocal, data = .)) %>%
map(tidy) %>%
map_df(tibble::rownames_to_column, 'var', .id = 'name') %>%
select(-c("statistic", "p.value")) %>%
gather(key = result_type, value = value,
c("estimate", "std.error")) %>%
unite(col = "new_key", c("term", "result_type"), remove = TRUE) %>%
select(- "var") %>%
spread(key = "new_key", value = value) %>%
rename(intercept_estimate = "(Intercept)_estimate",
intercept_se   = "(Intercept)_std.error",
slope_estimate = "water_reciprocal_estimate",
slope_se       = "water_reciprocal_std.error")

keeling_oxygen_statistics <-
picarro_cleaned %>%
split(.$time_label) %>%
```

```
map(~ lm(oxygen ~ water_reciprocal, data = .)) %>%
map(glance) %>%
map_df(tibble::rownames_to_column, 'var', .id = 'name') %>%
rename(F_statistic = statistic, F_test_p.value = p.value) %>%
select(name, r.squared, F_statistic, F_test_p.value, AIC, BIC)

keeling_oxygen <-
left_join(keeling_oxygen_analysis, keeling_oxygen_statistics, by =
   "name") %>%
mutate(date_time = ymd_hms(name)) %>%
#rename(delta_ET = estimate) %>%
rename_at(vars(- c("name", "date_time")), ~ paste0(., "_oxygen"))

head(keeling_oxygen)

# Combine together
   ------------------------------------------------------
keeling_plot_results <-
left_join(keeling_hydrogen, keeling_oxygen, by = c("date_time",
   "name")) %>%
mutate(my_timestamp = lubridate::ymd_hms(name),
my_date    = lubridate::date(my_timestamp),
my_time    = format(strptime(name, format = "%Y-%m-%d %H:%M:%S", tz =
   "UTC"),
"%H:%M")) %>%
select(- c("date_time", "name"))

keeling_plot_results$time_decimal <-
sapply(strsplit(keeling_plot_results$my_time,":"),
```

```
function(x) {
  x <- as.numeric(x)
  x[1]+x[2]/60
}
)

names(keeling_plot_results)

keeling_plot_results <-
keeling_plot_results %>%
select(names(keeling_plot_results)[19:22],
   names(keeling_plot_results)[1:18])

picarro_cleaned_data_description <-
picarro_cleaned %>%
group_by(time_label) %>%
summarise(air_sample_size = n(),
air_water_mean = mean(water),
air_water_sd = sd(water),
air_hydrogen_mean = mean(hydrogen),
air_hydrogen_sd = sd(hydrogen),
air_oxygen_mean = mean(oxygen),
air_oxygen_sd = sd(oxygen)) %>%
mutate(my_timestamp = lubridate::ymd_hms(time_label)) %>%
select(- time_label)

keeling_plot_results <-
keeling_plot_results %>%
left_join(picarro_cleaned_data_description, by = "my_timestamp")
```

```
saveRDS(keeling_plot_results,
here("delta_ET","3_output", "4_keeling_plot" ,
   "keeling_plot_results_hourly.rds"))


**********************************************
**********************************************
**********************************************
Determination of $\delta_{E}$ based on Craig-Gordon model
**********************************************
**********************************************
**********************************************
############################
##### Input variable ######
############################
#### T_soil, T_air: soil temperature, air temperature (Kelvin)
#### delta_L, delta_air: isotopic composition   (permil)
#### RH_air 0~100: relative humidity percent from 1-100 (%)
#### theta_soil:   soil moisture in decimal (0-1) (decimal, <=1)

#### data from VP-4 Humidity/Temp:
#### celsus degree for Temp and kPa for pressure

#### data from from the weather station:
#### "airTemp","soilT"
#### WS15 for Juniper, and WS18 for grassland

#### Soil properties based on 15cm in depth
```

```
#### Grasland

############################
CG_model_advanced<-
function(delta_L_2H, delta_L_18O, T_soil, T_air, RH_air,
theta_soil, delta_air_2H, delta_air_18O){

  ###_____1_______
  ## Compute equilibrium factionation alpha_L_V for 2H and 18O (>1)
  #### alpha_L_v for 2H
  alpha_equilibrium_2H <-
  exp(0.001*(24.844*10^6/(T_soil^2) - 76.248 * 10^3/T_soil + 52.612))

  epsilon_equilibrium_2H <- 1 - 1/alpha_equilibrium_2H
  #### alpha_L_v for 18O
  alpha_equilibrium_18O <-
  exp(0.001*(1.137*10^6/(T_soil^2) - 0.4156*10^3/T_soil - 2.0667))

  epsilon_equilibrium_18O <- 1 - 1/alpha_equilibrium_18O
  ####_____2______
  ### compute "saturation_WVP", saturation water vapor pressure.
  ## x_temp is stored as in Kelvin degree in data, and here should
     convert to celsus degree
  ## pressure_atm is the atmopsheric pressure in Pascal
  saturation_pressure_component <<- function(soil_temp, air_temp){
    ### temperature conversion
    air_temp_convert <- air_temp - 273.15
    soil_temp_convert <- soil_temp - 273.15
    air_temp_component <- 17.502*air_temp_convert/(240.97 +
```

```
    air_temp_convert)
  soil_temp_component <- 17.502*soil_temp_convert/(240.97 +
    soil_temp_convert)
  exp(air_temp_component - soil_temp_component)
}
saturation_pressure_parameter <-
saturation_pressure_component(soil_temp = T_soil, air_temp = T_air)

###___3___### compute relative humidity

RH_normal = 0.01 * RH_air * saturation_pressure_parameter

###___4___#### compute "kinetic fractionation factor (epsilon_k)"
theta_res <- 0.053
theta_sat <- 0.423
soil_water_normalize <- (theta_soil - theta_res)/(theta_sat -
   theta_res)
n <- 1 - 0.5*soil_water_normalize
Diff_ratio_2H <- 1.0251
Diff_ratio_18O <- 1.0285

epsilon_k_2H <- (1 - RH_normal)*(Diff_ratio_2H^n - 1)
epsilon_k_18O <- (1 - RH_normal)*(Diff_ratio_18O^n - 1)

###_____5_____### get the final computation result for the
   evapiration flux

## for 2H
numerator_2H_first_half <-
```

```
  0.001 * delta_L_2H/alpha_equilibrium_2H - RH_normal * 0.001 *
     delta_air_2H
  numerator_2H_second_half <-
  epsilon_k_2H + (alpha_equilibrium_2H - 1)/alpha_equilibrium_2H^2
  denominator_2H <- 1 - RH_normal + epsilon_k_2H
  delta_E_2H_advanced <-
  (numerator_2H_first_half - numerator_2H_second_half)/denominator_2H

  ### for 18O
  numerator_18O_first_half <-
  0.001 * delta_L_18O/alpha_equilibrium_18O - RH_normal * 0.001 *
     delta_air_18O

  numerator_18O_second_half <-
  epsilon_k_18O + (alpha_equilibrium_18O -1)/alpha_equilibrium_18O^2



  denominator_18O <- 1 - RH_normal + epsilon_k_18O
  delta_E_18O_advanced <-
  (numerator_18O_first_half -
     numerator_18O_second_half)/denominator_18O
  #### return values
  return(dplyr::lst(alpha_equilibrium_2H, 1000 *
     epsilon_equilibrium_2H,
  alpha_equilibrium_18O, 1000 * epsilon_equilibrium_18O,
  RH_normal, n,
  1000 * epsilon_k_2H, 1000 * epsilon_k_18O,
  1000 * delta_E_2H_advanced, 1000 * delta_E_18O_advanced))
}
```

```
**********************************************
**********************************************
**********************************************
Application of Craig-Gordon model
**********************************************
**********************************************
**********************************************
# Import SIBS data
   ----------------------------------------------------
sibs <-
readRDS(file = here("delta_E", "0_raw_data", "sibs", "period_1.rds") )
   %>%
filter(site == "south", sampling == "soil") %>%
select(my_timestamp = date_time, date = Date,
time_category = new_time_category,
soil_hydrogen_value = H2, soil_hydrogen_sd = H2_StDev,
soil_oxygen_value = O18, soil_oxygen_sd = O18_StDev
) %>%
filter(date %in% my_observation_dates_1) %>%
filter(time_category != "night")
dplyr::bind_rows(head(sibs), tail(sibs))
# picarro data preparation
   ------------------------------------------------
picarro_cleaned <-
readRDS(here("delta_ET", "3_output", "3_picarro_cleaned",
   "picarro_cleaned.rds")) %>%
select(time_label, my_date, time_decimal, height, water, hydrogen,
   oxygen) %>%
mutate(water_reciprocal = 1/water,
```

```
time_label = as.character(time_label))

picarro_for_cg <-
picarro_cleaned %>%
group_by(time_label, height) %>%
summarise(air_sample_size = n(),
air_water_mean = mean(water),
air_water_sd = sd(water),
air_hydrogen_mean = mean(hydrogen),
air_hydrogen_sd = sd(hydrogen),
air_oxygen_mean = mean(oxygen),
air_oxygen_sd = sd(oxygen)) %>%
ungroup() %>%
mutate(my_timestamp = lubridate::ymd_hms(time_label)) %>%
select(- "time_label") %>%
select(my_timestamp, colnames(.))

dplyr::bind_rows(head(picarro_for_cg), tail(picarro_for_cg))
saveRDS(picarro_for_cg,
here("delta_E", "3_output", "picarro_for_cg.rds" ))
# import picarro data
   ----------------------------------------------------
cg_input_picarro <-
readRDS(file = here("delta_E","3_output", "picarro_for_cg.rds")) %>%
mutate(my_time = format(strptime(my_timestamp, format = "%Y-%m-%d
   %H:%M:%S", tz = "UTC"),
"%H:%M")) %>%
select(my_timestamp, my_time, height, contains("air"))
```

```
cg_input_picarro$time_decimal <-
sapply(strsplit(cg_input_picarro$my_time,":"),
function(x) {
  x <- as.numeric(x)
  x[1]+x[2]/60
}
)

head(cg_input_picarro)
summary(cg_input_picarro$air_sample_size)

cg_input_picarro <-
cg_input_picarro %>%
rename_at(vars(starts_with("air_")),
list(~ str_replace(., pattern = "air_", replacement = ""))) %>%
gather(key, value, -c("my_timestamp", "my_time","time_decimal",
   "height")) %>%
unite(new_key, key, height) %>%
spread(new_key, value)

names(cg_input_picarro)

cg_input_picarro <-
cg_input_picarro %>%
mutate(air_hydrogen_value = if_else(!is.na(hydrogen_mean_Low),
   hydrogen_mean_Low,
if_else(!is.na(hydrogen_mean_Middle), hydrogen_mean_Middle,
hydrogen_mean_High)),
air_hydrogen_sd = if_else(!is.na(hydrogen_sd_Low), hydrogen_sd_Low,
```

```
if_else(!is.na(hydrogen_sd_Middle), hydrogen_sd_Middle,
hydrogen_sd_High)),
air_oxygen_value = if_else(!is.na(oxygen_mean_Low), oxygen_mean_Low,
if_else(!is.na(oxygen_mean_Middle), oxygen_mean_Middle,
oxygen_mean_High)),
air_oxygen_sd = if_else(!is.na(oxygen_sd_Low), oxygen_sd_Low,
if_else(!is.na(oxygen_sd_Middle), oxygen_sd_Middle,
oxygen_sd_High))
) %>%
select(my_timestamp, my_time, time_decimal, contains("air"))

head(cg_input_picarro)
names(cg_input_picarro)
summary(cg_input_picarro)

saveRDS(cg_input_picarro, here("delta_E","3_output",
   "cg_input_picarro.rds"))
# write.csv(cg_input_picarro, here("delta_E","3_output",
   "cg_input_picarro_1.csv"))

### remeber!
### note this CSV needs to be manaully aligned according to sibs data
### borrow data from nearby time slot
### time at the beginning and end of the day are mannually adjusted
head(cg_input_picarro$my_timestamp)

cg_input_picarro <-
read.csv(here("delta_E","3_output", "cg_input_picarro_1.csv"),
header = TRUE) %>%
```

```
mutate(my_timestamp = lubridate::mdy_hm(my_timestamp),
time_decimal = as.numeric(time_decimal)) %>%
tbl_df()

sibs_picarro <-
left_join(sibs, cg_input_picarro[, -1], by = "my_timestamp") %>%
drop_na()

saveRDS(sibs_picarro, here("delta_E","3_output", "sibs_picarro.rds"))

###
# join sibs_picarro with eddy covariance data
   ------------------------------
# sibs_picarro <- readRDS(here("delta_E","3_output",
   "sibs_picarro.rds"))
eddy_biomet_south <- readRDS(here("EC_ET", "3_output",
   "eddy_biomet_south_rain_soil.rds"))

dplyr::bind_rows(head(sibs_picarro), tail(sibs_picarro))
names(sibs_picarro)
names(eddy_biomet_south)
dplyr::bind_rows(head(eddy_biomet_south), tail(eddy_biomet_south))

sibs_picarro_eddy <-
sibs_picarro %>%
left_join(eddy_biomet_south[, c("my_timestamp", "Tair", "Tsoil", "RH",
   "south_5")],
by = "my_timestamp") %>%
mutate(T_air = Tair + 273.15,
```

```
T_soil = Tsoil + 273.15) %>%
rename(RH_air = "RH", theta_soil = "south_5") %>%
select(-c("Tair", "Tsoil"))

names(sibs_picarro_eddy)
saveRDS(sibs_picarro_eddy, here("delta_E","3_output",
   "sibs_picarro_eddy.rds"))

# apply craig_gordon
   ----------------------------------------------------
## input T_air

cg_results <-
sibs_picarro_eddy %>%
rename(delta_L_2H = soil_hydrogen_value, delta_L_18O =
   soil_oxygen_value,
delta_air_2H = air_hydrogen_value, delta_air_18O = air_oxygen_value)
   %>%
select(delta_L_2H, delta_L_18O, T_soil, T_air, RH_air,
theta_soil, delta_air_2H, delta_air_18O) %>%
mutate(!!!invoke(CG_model_advanced, unname(.)))

head(cg_results)

### join and calculate the uncertainity, Error Propagation
str()
cg <-
sibs_picarro_eddy %>%
rename(delta_L_2H = soil_hydrogen_value, delta_L_18O =
```

```
   soil_oxygen_value,
delta_air_2H = air_hydrogen_value, delta_air_18O = air_oxygen_value)
   %>%
left_join(cg_results,
by = c("delta_L_2H", "delta_L_18O", "delta_air_2H",
"delta_air_18O", "RH_air", "theta_soil", "T_air", "T_soil")) %>%
rename(my_date = date,
soil_hydrogen_value = delta_L_2H,
soil_oxygen_value = delta_L_18O,
delta_air_hydrogen = delta_air_2H,
delta_air_oxygen = delta_air_18O,
alpha_equilibrium_hydrogen = alpha_equilibrium_2H,
epsilon_equilibrium_hydrogen = `1000 * epsilon_equilibrium_2H`,
alpha_equilibrium_oxygen = alpha_equilibrium_18O,
epsilon_equilibrium_oxygen = `1000 * epsilon_equilibrium_18O`,
epsilon_kinetic_hydrogen = `1000 * epsilon_k_2H`,
epsilon_kinetic_oxygen =`1000 * epsilon_k_18O`,
delta_E_hydrogen_value = `1000 * delta_E_2H_advanced`,
delta_E_oxygen_value = `1000 * delta_E_18O_advanced`) %>%
mutate(delta_E_hydrogen_sd =
   sqrt(soil_hydrogen_sd^2/alpha_equilibrium_hydrogen^2 + RH_normal^2
   * air_hydrogen_sd^2),
delta_E_oxygen_sd = sqrt(soil_oxygen_sd^2/alpha_equilibrium_oxygen^2 +
   RH_normal^2 * air_oxygen_sd^2))

**********************************************
**********************************************
**********************************************
Dual-isotope Plot
```

```
**********************************************
**********************************************
**********************************************

library(ggExtra) ## for marginal distribution plot
# Import data for dual-isotope graph
   ------------------------------------

## picarro data for air
picarro_data <-
readRDS(file = here("delta_ET", "3_output", "3_picarro_cleaned",
   "picarro_cleaned_study_1.rds"))
dplyr::bind_rows(head(picarro_data), tail(picarro_data))
water_vapor <-
picarro_data %>%
ungroup() %>%
select(my_timestamp = time_label, hydrogen, oxygen) %>%
group_by(my_timestamp) %>%
summarise(hydrogen = mean(hydrogen),
oxygen = mean(oxygen)) %>%
mutate(type = "vapor") %>%
select(- my_timestamp)
summary(water_vapor)
## rain data
rain_data <-
readRDS(file = here("dual_isotope", "3_output", "delta_rain.rds")) %>%
mutate(type = "rain") %>%
select(hydrogen = hydrogen_mean, oxygen = oxygen_mean, type)
## sibs data
```

```
sibs_data <-
readRDS(file = here("delta_E", "0_raw_data", "sibs", "period_1.rds"))
   %>%
filter(Date %in% my_observation_dates_1) %>%
select(my_timestamp = date_time, type = sampling, hydrogen = H2,
   oxygen = O18) %>%
filter(oxygen < 37) %>% # remove an outlier in June 6 afternoon leaf
   data (heavier isotopic ratios)
mutate(type = as.character(type),
type = if_else(type == "root", "xylem", type)) %>%
select(hydrogen, oxygen, type)

summary(sibs_data)
## combine data in two ways
## full_join

dual_isotope <- bind_rows(water_vapor, rain_data, sibs_data)

dplyr::bind_rows(head(dual_isotope), tail(dual_isotope))

dual_isotope$type <-
factor(dual_isotope$type,
levels = c("vapor", "rain", "soil", "xylem", "leaf"),
ordered = TRUE)

saveRDS(dual_isotope,
here("dual_isotope", "3_output", "dual_isotope.rds"))

# dual_isotope <- readRDS(file = here("dual_isotope", "3_output",
```

```
   "dual_isotope.rds"))
##
# Plot dual_isotope graph
   ------------------------------------------------
rain_may_june <-
readRDS(file = here("dual_isotope", "3_output", "delta_rain.rds")) %>%
mutate(month = lubridate::month(my_date)) %>%
filter(month >=5, month <=6)

my_colors <- c("Deep Sky Blue", "Blue","Goldenrod 1", "Saddle Brown",
   "Lime Green")

met_line <- data.frame(slope = c(7.32, 8.2), intercept = c(9.50, 11.3),
lty =c("dotted", "dashed"), name = c("LMWL", "GMWL"))

formula <- y ~ x

dual_isotope_plot <-
ggplot(data = dual_isotope, aes(x = oxygen, y = hydrogen, color =
   type)) +
geom_smooth(method = "lm", se = TRUE,
show.legend = NA, inherit.aes = TRUE) +
geom_abline(data= met_line,
mapping = aes(slope=slope, intercept=intercept, linetype =
   factor(name)),
col = "gray", size = 0.9) +
geom_point(alpha = 0.8) +
geom_point(data = rain_may_june,
mapping = aes(x = oxygen_mean, y = hydrogen_mean),
```

```
shape = 21, colour = "red",
fill = NA, inherit.aes = FALSE) +
scale_color_manual(name = "Sample Types", values = my_colors) +
scale_linetype(name="Meteoric Lines") +
scale_x_continuous(breaks = seq(-30, 40, 10)) +
scale_y_continuous(breaks = seq(-150, 150, 30)) +
stat_poly_eq(aes(label = paste(..eq.label.., ..rr.label.., sep =
   "~~~")),
label.x.npc = "left", label.y.npc = "top",
formula = formula, parse = TRUE, size = 4) +
#stat_fit_glance(method = "lm",
#            method.args = list(formula = formula),
#            label.x = "middle",
#            label.y = "top",
#            aes(label = paste("italic(P)*\"-value = \"*",
#                        signif(..p.value.., digits = 2), sep = "")),
#            parse = TRUE, size = 3.5) +
xlab("\u03b4\ub9\u2078O (\u2030 vs VSMOW)") +
ylab("\u03b4\u00b2H (\u2030 vs VSMOW)")+
#theme_classic() + ## classic theme
theme(legend.position = c(0.8, 0.25),
legend.title = element_text(face = "bold", size = 12),
legend.text = element_text(size = 11),
axis.title.x = element_text(size = 14, margin = margin(t = 8, r = 0, b
   = 0, l = 0)),
axis.title.y = element_text(size = 14, margin = margin(t = 0, r = 8, b
   = 0, l = 0)))

ggExtra::ggMarginal(dual_isotope_plot, type = "density", margins =
```

```
   "both",
groupColour = TRUE,
groupFill = TRUE)

ggsave(file = here("dual_isotope", "3_figure",
   "dual_isotope_plot_ggsave.eps"),
ggMarginal(dual_isotope_plot, type = "density", margins = "both",
groupColour = TRUE,
groupFill = TRUE),
width = 9.55, height = 9.55, dpi = 1200,
device=cairo_ps)

export::graph2eps(file = here("dual_isotope", "3_figure",
   "dual_plot_isotope_export.eps"),
width = 8.40, height = 9.55)

**********************************************
**********************************************
**********************************************
Application of isotopic two-source mixing model}
**********************************************
**********************************************
**********************************************
# function for isotopic ET partitioning
   ------------------------------------

ET_partitioning_function <-
function(delta_ET, delta_E, delta_T){
  (delta_ET - delta_E)/(delta_T - delta_E)
```

```
}

# function for uncertainity analysis
   ---------------------------------------
## delta_ET_Variance, delta_E_variance, delta_T_variance
## is the variance of delta_ET, delta_E, and delta_T
ET_partitioning_variance <-
function(delta_ET_variance, delta_E_variance, delta_T_variance,
   f_T_ET, delta_E, delta_T){
  first_part <<- 1/(delta_T - delta_E)^2
  second_part <<- delta_ET_variance + f_T_ET^2 * delta_T_variance + (1
     - f_T_ET)^2 * delta_E_variance
  f_variance <<- sqrt(first_part * second_part)
  return(f_variance)
}

# Apply isotopic ET partitioning at daily interval --------
delta_daily_data <-
delta_daily_data %>%
dplyr::mutate(
f_T_ET = purrr::pmap(
list(delta_ET = ET_value, delta_E = E_value, delta_T = T_value),
ET_partitioning_function),
f_variance = purrr::pmap(
list(delta_ET_variance = ET_variance,
delta_E_variance = E_variance,
delta_T_variance = T_variance,
f_T_ET        = f_T_ET,
delta_E       = E_value,
```

```
delta_T       = T_value),

ET_partitioning_variance)

) %>%

tidyr::unnest() %>%

mutate(f_sd = sqrt(f_variance))


dplyr::bind_rows(head(delta_daily_data), tail(delta_daily_data))
```